Acoustofluidics
2024

Table of Contents

Welcome Letter

WELCOME BY THE CONFERENCE CHAIRS

It is with great pleasure that we welcome you to the annual Acoustofluidics conference 2024. It has been more than 10 years since the conference was organized in Sweden and we are very excited to welcome you back. We are pleased to be able to organize the meeting as a fully in-person event although we have maintained the option of live streaming for those members of the international acoustofluidics community that have not been able to make it to Uppsala.

Abstract submissions were again of a high standard, enabling assembly of a conference program of talks spanning advancements in device physics, new phenomena, and applications. The broad coverage of the contributed talks is also reflected in the series of excellent keynote and invited speakers, which point to connections of acoustic force fields with optical fields to developing the technology and combining acoustofluidic devices with additional methodologies.

As introduced last year in St. Louis, we have again a special arrangement in the program prepared by the Young Acoustofluidics Scientist Network (YASN) to strengthen the networking between PhD students and postdocs in the community and equip our future faculty with additional skills needed for a successful career. We are very excited about this panel discussion that we welcome you all, young or old, to attend.

This year, we also see the return of the Acoustofluidic Olympics kindly coordinated by Jeremy Hawkes. We will have four live demonstrations of acoustofluidic devices set up in a lecture room adjacent to the main conference venue. The demos will be running in parallel with the poster session and we hope you will find time to visit both events.

In this welcome note we would also like to address a special thanks to this year's sponsors for their kind contributions to our conference – THANK YOU! Their set-ups will be on display throughout the meeting, and we encourage you all to interact with them.

We will highlight the winner of the previous year's *W. Terence Coakley Award,* Advaith Narayan, with an invited talk on the first day of the conference. This award distinguishes a promising student or postdoctoral researcher in acoustofluidics and is selected from the poster presentations. Additionally, the Royal Society of Chemistry will sponsor an award for Best Research Image in Acoustofluidics. The image will be featured on the cover of an upcoming issue of the Royal Society's prestigious journal *Lab on a Chip.* And this year, we have a new prize introduced, the *CBMS Award* that will be awarded to the best oral presentation by a young researcher where the prize is a waived registration fee to the 2025 µTAS conference!

Finally, we would like to acknowledge the support and feedback provided by members of the Acoustofluidics Society and community, which allow us to maintain the Acoustofluidics conference as an essential venue for dissemination of important results in the field. We greatly appreciate the work of the Scientific Committee to evaluate submitted abstracts that ensures a top-level quality of the conference program. This conference would also not have been possible without the invaluable contribution of PMMI Global with the administrative arrangements of the meeting and the fantastic local organizing committee.

Maria Tenje
Uppsala University, SWEDEN
Conference Chair 2024

Martin Wiklund
Royal Institute of Technology (KTH), SWEDEN
Conference Co-Chair 2024

Per Augustsson
Lund University, SWEDEN
Program Chair 2024

General Information

Meeting Space
All events will be held at the [Ångströmlaboratoriet, House 10](#) (Hus 10) unless otherwise indicated.
- Main Conference Room - Sonja Lyttkens (101121) Room, Floor 1
- Poster Session - Floor 0 (100602)
- Olympiad - Evelyn Sokolowski (101136) Room, Floor 1

Wireless Internet Service
Wireless Internet will be available in the meeting space. As a visitor and guest, you can use the wireless network called UU-Guest, that gives you 24 hrs free access at the time.

The Eduroam network is also available throughout the University campus (as well as at Arlanda Airport).

Cellular Phones and Alarms
As a courtesy to our speakers and other attendees, please turn off any cellular phones and alarms during sessions.

Video Recording
Video recordings are strictly prohibited in the sessions and poster presentations.

Welcome Reception
Wednesday, 14 August
18:00 – 19:00
University Main Building, Biskopsgatan 3, 753 10 Uppsala

The Dean of the Faculty of Science and Engineering will welcome us to Uppsala with some drinks and snacks in the University Main Building. The University guide will also be available to give us a brief overview of the history of this beautiful building and the proud history of Uppsala University from its establishment in 1477. NB! Doors are only open 18:00 – 18:10, please make sure you arrive on time!

Banquet
Thursday, 15 August
18:30 – Late
Norrland's Nation, Västra Ågatan 14, 753 09 Uppsala

No conference is complete without a banquet. Join us on Thursday evening at Norrland's Nation for a delicious meal and a chance to network with colleagues. Norrland's Nation is centrally located by the riverbanks of Fyrisån, a 30-minute walk or a 15-minute bus ride from the Ångström Laboratory.

Conference Officials

Conference Chairs

Maria Tenje **(Chair)** .... Uppsala University, SWEDEN
Martin Viklund **(Co-Chair)** .... KTH, SWEDEN
Per Augustsson **(Program Chair)** .... Lund University, SWEDEN

Advisory Committee

Per Augustsson .... Lund University, SWEDEN
Bruce Drinkwater .... University of Bristol, UK
Xuexin Duan .... Tianjin University, CHINA
Thomas Franke .... University of Glasgow, SCOTLAND
James Friend .... University of California, San Diego, USA
Richard Fu .... Northumbria University, UK
Peter Glynne-Jones .... University of Southampton, UK
Mark Meacham .... Washington University in St. Louis, USA
Ashis Kumar Sen .... Indian Institute of Technology, Madras, INDIA
Tim Segers .... University of Twente, NETHERLANDS
Glauber T. Silva .... Universidade Federal de Alagoas, BRAZIL
Maria Tenje .... Uppsala University, SWEDEN

Scientific Committee

Per Augustsson .... Lund University, SWEDEN
Thierry Baasch .... Lund University, SWEDEN
Michaël Baudoin .... Université de Lille, FRANCE
Philippe Brunet .... Université Paris Diderot, FRANCE
Henrik Bruus .... Technical University of Denmark, DENMARK
Feiyan Cai .... Shenzhen Institute of Advanced Technology, CHINA
Bruce Drinkwater .... University of Bristol, UK
Xuexin Duan .... Tianjin University, CHINA
Gabriel Dumy .... KOLIBRI Lab, FRANCE
Mohamed El Malki .... Mohammed First University, MOROCCO
Thomas Franke .... University of Glasgow, SCOTLAND
James Friend .... University of California, San Diego, USA
Richard Fu .... Northumbria University, UK
Peter Glynne-Jones .... University of Southampton, UK
Feng Guo .... Indiana University, USA
Xiasheng Guo .... Nanjing University, CHINA
Ruchi Gupta .... University of Birmingham, UK
Martin Hill .... University of Southampton, UK
Andreas Lenshof .... Lund University, SWEDEN
Kian-Meng Lim .... National University of Singapore, SINGAPORE
Jikui "Jack" Luo .... Zhejiang University, CHINA
Zhichao Ma .... Shanghai Jiao Tong University, CHINA
Philippe Marmottant .... Université Grenoble Alps, FRANCE
Mark Meacham .... Washington University in St. Louis, USA

Scientific Committee (continued)

Adrian Neild .... Monash University, AUSTRALIA
Jinsoo Park .... Chonnam National University, KOREA
Alen Pavlic .... California Institute of Technology, USA
Wei Qiu .... Lund University, SWEDEN
Stefan Radel .... TU Wien, AUSTRIA
Hagen Schmidt .... IFW Dresden, GERMANY
Tim Segers .... University of Twente, NETHERLANDS
Ashis Kumar Sen .... Indian Institute of Technology, Madras, INDIA
Glauber T. Silva .... Universidade Federal de Alagoas, BRAZIL
Karthick Subramani .... Indian Institute of Information Technology,
Design & Manufacturing Kancheepuram, INDIA
Hyung Jin Sung .... Korea Advanced Institute of Science & Technology, KOREA
Maria Tenje .... Uppsala University, SWEDEN
Zhenhua Tian .... Virginia Tech, USA
Michel Versluis .... University of Twente, NETHERLANDS
Martin Wiklund .... KTH Stockholm, SWEDEN
Likun Zhang .... University of Mississippi, USA

Acoustofluidics Society

The Acoustofluidics Society is an international body that represents and facilitates the interests of researchers and industries in the fields of acoustic particle manipulation, acoustic fluid control, and associated technologies, with particular applications in the Life sciences.
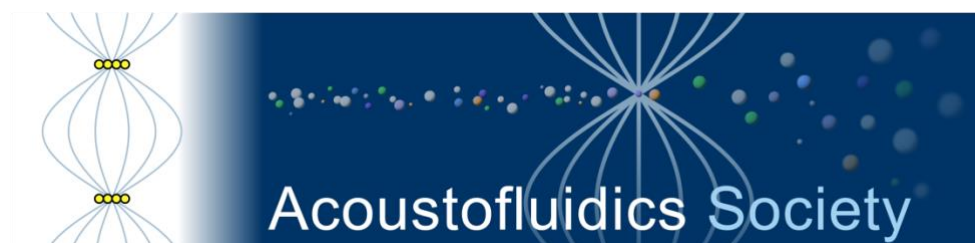
The Acoustofluidics Society is an international body that represents and facilitates the interests of researchers and industries in the fields of acoustic particle manipulation, acoustic fluid control, and associated technologies, with particular applications in the Life sciences.

Executive Committee

Per Augustsson **(President)** .... Lund University, SWEDEN
Maria Tenje **(Vice-President)** .... Uppsala University, SWEDEN
Thomas Franke **(Secretary)** .... University of Glasgow, SCOTLAND
Mark Meacham **(Treasurer)** .... Washington University in St. Louis, USA

Board Members

Feiyan Cai .... Shenzhen Institute of Advanced Technology, CHINA
Alen Pavlic .... California Institute of Technology, USA
Glauber T. Silva .... Universidade Federal de Alagoas, BRAZIL
Tim Segers .... University of Twente, NETHERLANDS
Ashis Kumar Sen .... Indian Institute of Technology, Madras, INDIA

The society developed from USWnet, a network formed in 2003 in the UK led by Clare Selden, UCL. Other founding members included Terry Coakley 1940-2006 (obituary).

Benefactors

Conference Sponsor

Acoustofluidics Society

Supported by:

Chemical and Biological Microsystems Society (CBMS)

W. Terence Coakley Poster Award Sponsor

Acoustofluidics Society

Gold Benefactors

AcouSort

BELEKTRONIG
advancing lab controllers

COMSOL

CtS
Your Partner in
Smart Solutions.

LIQUID
INSTRUMENTS

ROYAL SOCIETY
OF CHEMISTRY

Lab on a Chip

SinePhase
RELIABLE INSTRUMENTATION TECHNOLOGY

Keynote Speakers

OPTICAL AND ACOUSTIC MANIPULATION FOR TOMOGRAPHIC IMAGING
Monika Ritsch-Marte
Medical University of Innsbruck, AUSTRIA

ADVANCING THE FRONTIERS OF ACOUSTIC MICRO-ACTUATORS
Michael Baudoin
Université de Lille, FRANCE

THE PARTICLE SIZE-EFFECT IN OPTICAL AND ACOUSTIC TRAPS
Karen P. Volke Sepulveda
National Autonomous University of Mexico (UNAM), MEXICO

THE EMERGING CONFLUENCE OF ACOUSTIC MICROMANIPULATION, ACOUSTIC HOLOGRAPHY AND 3D PRINTING
David Collins
University of Melbourne, AUSTRALIA

ACOUSTIC STREAMING
James Friend
University of California, San Diego, USA

ELUCIDATING CELL-CELL AND CELL-FIELD INTERACTIONS FOR ACOUSTICALLY CONFINED MICROSWIMMERS
Advaith Narayan
Washington University in St. Louis, USA
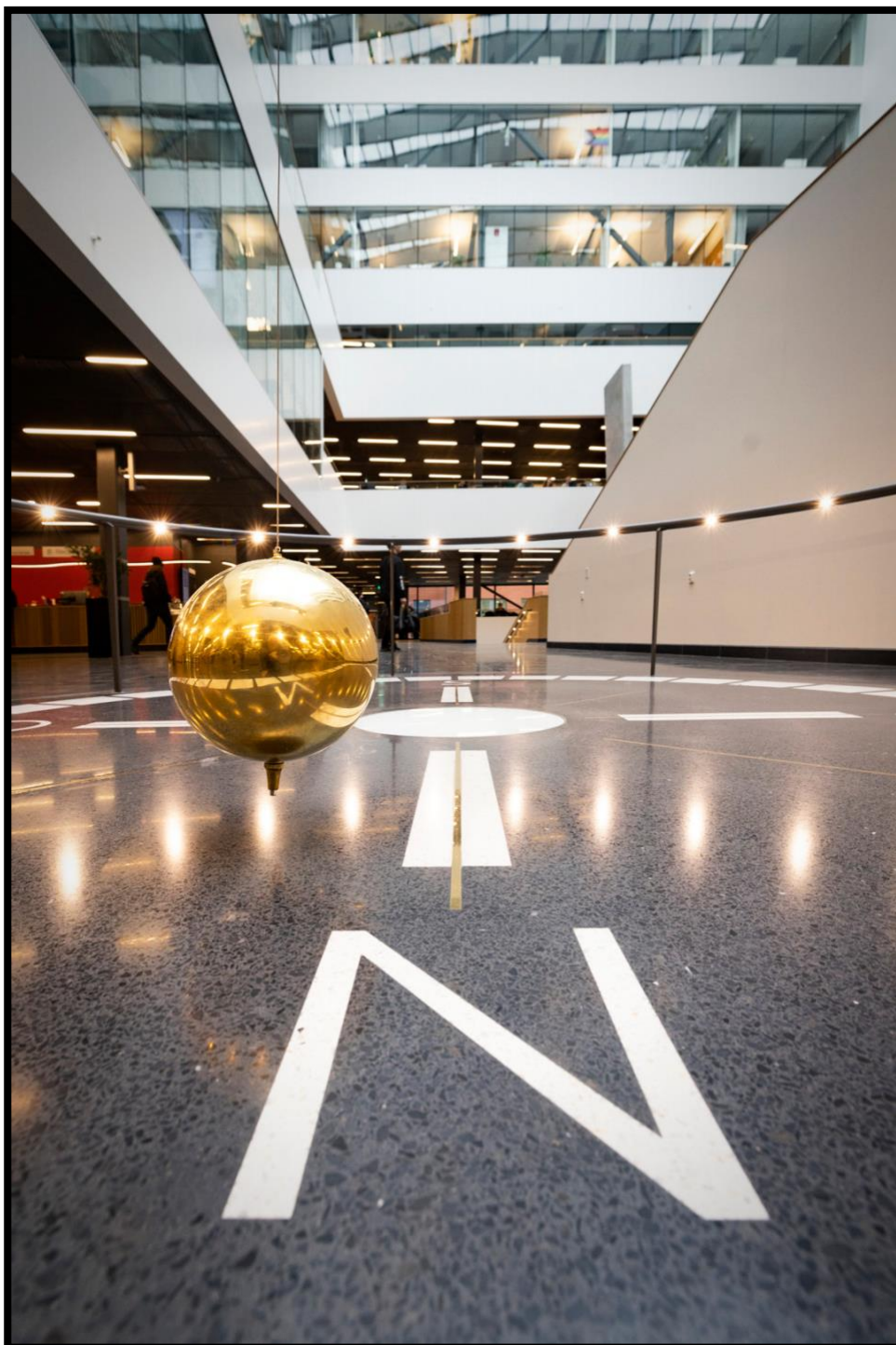
Program Schedule

Wednesday 14 August
All Times are Central European Summer Time (CEST).

08:50 **Welcome and Opening Remarks**
Maria Tenje, *Uppsala University, SWEDEN* (Conference Chair)
Martin Wiklund, *KTH, SWEDEN* (Conference Co-Chair)

Session 1 – Applications of Acoustic Systems 1
Session Chair: Maria Tenje, Uppsala University, SWEDEN

Keynote Speaker 1

09:00 **OPTICAL AND ACOUSTIC MANIPULATION FOR TOMOGRAPHIC IMAGING**
Monika Ritsch-Marte
Medical University of Innsbruck, AUSTRIA

Contributed Talks

09:50 **ACOUSTIC PIPETTE AND BIOFUNCTIONAL NEGATIVE ACOUSTIC CONTRAST MICROPARTICLE SYSTEM FOR RAPID PICOMOLAR-LEVEL BIOMOLECULE DETECTION IN WHOLE BLOOD**
Cooper P. Thome[1], John P. Fowle[1], Parker McDonnell[1], Johanna Zultak[1], Kaushik Jayaram[1], Aaron K. Neumann[2], Gabriel P. López[3], and C. Wyatt Shields IV[1]
[1]University of Colorado Boulder, USA, [2]University of New Mexico School of Medicine, USA, and [3]University of New Mexico, USA

10:05 **ACOUSTOFLUIDIC BLOOD PLASMA SEPARATION FOR NEONATAL CARE**
Amal Nath[1], Wei Qiu[1], Thierry Baasch[1], Andreas Lenshof[1], Marie Larsson[2], Linda Nilsson[3], Magnus Gram[3], David Ley[3], and Thomas Laurell[1]
[1]Lund University, SWEDEN, [2]Hospitals of Halland, SWEDEN, and [3]Skåne University Hospital, SWEDEN

10:20 **RAPID ACOUSTIC ISOLATION UNVEILS PROTEOME OF EXTRACELLULAR VESICLES FROM A MINUTE VOLUME OF HUMAN BLOOD PLASMA**
Megan Havers[1], Aaron Scott[1], Niklas Ortenlöf[1], Marc Isaksson[1], Simon Ekström[1], Charlotte Welinder[1], Thierry Baasch[1], Mikael Evander[2], Andreas Lenshof[1], Magnus Gram[1], and Thomas Laurell[1]
[1]Lund University, SWEDEN and [2]AcouSort AB, SWEDEN

10:35 **Coffee Break**

Session 2 – Applications of Acoustic Systems 2
Session Chair: Thomas Franke, University of Glasgow, UK

Invited Speaker 1 - Coakley Award Winner 2023

11:00 **SYNERGISTIC EXPLORATION OF ACOUSTIC FIELD-MICROSWIMMER INTERACTIONS**
Advaith Narayan
Washington University, St. Louis, USA

Contributed Talks

11:30 **COMPRESSIBILITY-BASED POSITIVE ISOLATION OF BACTERIA FROM PLATELETS USING TILTED-ANGLE STANDING SURFACE ACOUSTIC WAVE**
Song Ha Lee and Jinsoo Park
Chonnam National University, KOREA

11:45 **ECHOGRID: HIGH-THROUGHPUT ACOUSTIC TRAPPING TOWARDS MICRO AND NANOPLASTIC MONITORING**
Martim Costa[1], Björn Hammarström[1], Liselotte van der Geer[1], Selim Tanriverdi[1], Haakan Joensson[1], Martin Wiklund[1], and Aman Russom[1,2]
[1]KTH Royal Institute of Technology, SWEDEN and [2]AIMES - Karolinska Institute and KTH Royal Institute of Technology, SWEDEN

12:00 **REVERSING THE ACOUSTIC CONTRAST FACTOR BY TUNING THE MEDIUM CAN MAKE FOCUSED BEAMS TRAP CELLS IN THREE DIMENSIONS**
Shiyu Li and Zhixiong Gong
Shanghai Jiao Tong University, CHINA

12:15 **Lunch**

Session 3 – Acoustic Manipulation
Session Chair: Martin Wiklund, Royal Institute of Technology (KTH), SWEDEN

Keynote Speaker 2

13:30 **ADVANCING THE FRONTIERS OF ACOUSTIC MICRO-ACTUATORS**
Michael Baudoin
University of Lille, FRANCE

Contributed Talks

14:20 **SIMULTANEOUS FLUORESCENCE AND ABSORBANCE SIGNAL SORTING OF MICROFLUIDIC DROPLETS USING TRAVELING SURFACE ACOUSTIC WAVES (TSAW)**
Esther S. Richter, Andreas Link, Raymond W. Sparrow, and Thomas Franke
University of Glasgow, UK

14:35 **RELAXATION TO FROZEN MODE TRANSITION OF VISCOELASTIC FLUIDS UNDER ULTRASOUND: EFFECTS ON PARTICLE TRANSPORT**
T Sujith, Lokesh Malik, and Ashis K. Sen
Indian Institute of Technology, Madras, INDIA

14:50 **ACOUSTOFLUIDIC PLATFORMS FOR TOMOGRAPHY OF BIOLOGICAL SAMPLES BY ROTATIONAL MANIPULATION**
Mia Kvåle Løvmo[1], Shiyu Deng[2], Simon Moser[1], Franziska Strasser[1], Wolfgang Drexler[2], and Monika Ritsch-Marte[1]
[1]Medical University of Innsbruck, AUSTRIA and
[2]Medical University of Vienna, AUSTRIA

15:05 **Coffee Break**

Young Acoustofluidics Scientists' Network Event

15:45 **Panel Discussion on Research Funding in Different Parts of the World**

Sia Gosheva-Oney, Grants Office, ETH Zurich, SWITZERLAND
Bruce Drinkwater, University of Bristol, UK
NN, National Science Foundation (NSF), USA

17:00 Joint walk from the Ångström Lab to the University Main Building (~30 min)

Welcome Reception

18:00-19:00 Welcome Reception and Guided Tour in the University Main Building

Thursday, 15 August

All Times are Central European Summer Time (CEST).

08:50   **Announcements**

Session 4 - Physics of Acoustic Systems
Session Chair: Per Augustsson, Lund University, SWEDEN

Keynote Speaker 3

09:00   **THE PARTICLE SIZE-EFFECT IN OPTICAL AND ACOUSTIC TRAPS**
Karen P. Volke
National Autonomous University of Mexico, MEXICO

Contributed Talks

09:50   **INFLUENCE OF DIELECTROPHORESIS ON SPHERICAL AND NON-SPHERICAL PARTICLES IN A STANDING SURFACE ACOUSTIC WAVE FIELD**
Sebastian Sachs, Christian Cierpka, and Jörg König
Technische Universität Ilmenau, GERMANY

10:05   **NEAR-FIELD ACOUSTIC RESONANCE EFFECTS AND CAVITATION IN SAW AEROSOL GENERATION**
Mehrzad Roudini[1], Juan Manue. Rosselló[2], Ofer Manor[3], Claus-Dieter Ohl[2], and Andreas Winkler[1]
[1]Leibniz Institute for Solid State and Materials Research Dresden, GERMANY,
[2]Otto-von-Guericke University Magdeburg, GERMANY, and
[3]Technion - Israel Institute of Technology, ISRAEL

10:20   **SUPERHYDROPHOBIC COATING ACTS AS A SHIELD AGAINST ULTRASOUND-INDUCED HEATING**
Alex Drago-González, Maxime Fauconnier, Bhuvaneshwari Karunakaran, Laura Fieber, William S. Y. Wong, Robin H. A. Ras, and Heikki J. Nieminen
Aalto University, FINLAND

10:35   **Coffee Break**

Session 5 - Acoustic Streaming
Session Chair: Andreas Winkler, IFW Dresden, GERMANY

Invited Speaker 2

11:00   **ACOUSTIC STREAMING**
James Friend
University of California, San Diego, USA

Contributed Talks

11:30   **ACOUSTIC MICROSTREAMING AROUND ASYMMETRIC BUBBLES**
Claude Inserra[1], Cyril Mauger[2], Philippe Blanc-Benon[2],
and Alexander A. Doinikov[2]
[1]Université Lyon 1, FRANCE and [2]Ecole Centrale Lyon, FRANCE

11:45   **VESICLE-BASED DRUG LOADING AND INTRACELLULAR DELIVERY BY GIGAHERTZ ACOUSTIC STREAMING**
Haopu Wang, Shuailong Zhang, Huikai Xie, and Yao Lu
Beijing Institute of Technology, CHINA

12:00   **ADVANCING SIZE-SELECTIVE PARTICLE SEPARATION: ULTRASONIC MICROBUBBLE STREAMING FOR AUTOMATED DEPLETION**
Amirabas Bakhtiari and Christian J. Kähler
Bundeswehr University Munich, GERMANY

12:15   **Lunch**

Session 6 - Physics: Two-Phase Acoustofluidics
Session Chair: Jinsoo Park, Chonnam National University, KOREA

Contributed Talks

13:30   **NUMERICAL SIMULATION OF BULK ACOUSTIC WAVES INDUCED DROPLET GENERATION IN AN IMMISCIBLE COFLOW SYSTEM**
Sazid Z. Hoque[1,2] and Ashis K. Sen[1]
*[1]Indian Institute of Technology, Madras, INDIA and
[2]Technical University of Denmark, DENMARK*

13:45   **NUMERICAL STUDY OF ACOUSTIC STREAMING IN SPHERICAL DROPLETS SUSPENDED IN UNCONFINED MEDIA**
Pradipta Kr. Das[1], Carl D. Meinhart[2], and Maria Tenje[1]
[1]Uppsala University, SWEDEN and [2]University of California, Santa Barbara, USA

14:00   **DROPLET DYNAMICS BEYOND THE RAYLEIGH LIMIT UNDER ACOUSTIC-GRAVITY FORCES: A ROUTE TO EXTRACT SPECIFIC DROPLET SIZES FROM A BROAD RANGE**
Jeyapradhap Thirisangu and Karthick S
Indian Institute of Information Technology, Design & Manufacturing, INDIA

14:15   **Coffee Break**

W. Terence Coakley Poster Session

14:30 - 17:30

P01 **ACOUSTIC-DRIVEN LIQUID ATOMIZATION FOR NANOSATELLITE MANEUVERING**
Amihai Horesh[1], William Connacher[2], and James Friend[2]
[1]Agriculture Research Organizing, ISRAEL and [2]University of California, USA

P02 **ACOUSTICALLY LEVITATED DROPLETS FOR CHEMICAL REACTIONS AND BIOASSAYS**
Ruchi Gupta[1] and Nicholas J. Goddard[2]
[1]University of Birmingham, UK and [2]Process Instruments, UK

P03 **ACOUSTOFLUIDIC SORTING OF RED BLOOD CELLS USING REAL-TIME MACHINE VISION**
Raj Kumar Rajaram Baskaran, Andreas Link, and Thomas Franke
University of Glasgow, UK

P04 **ACOUSTOFLUIDIC CHARACTERIZATION OF THE EFFECT OF STAINING ON CELL PROPERTIES**
Qing Wang, Andreas Lenshof, Alexander Edthofer, Thierry Baasch,
Thomas Laurell, and Wei Qiu
Lund University, SWEDEN

P05 **ANALYTICAL SOLUTION OF SOURCE TERM FOR BULK ACOUSTIC STREAMING WITH NONLINEAR PROPAGATION**
Shiyu Li[1], Weiwei Cui[2], Thierry Baasch[3], Bin Wang[1,4], and Zhixiong Gong[1,4]
*[1]Shanghai Jiao Tong University, CHINA, [2]Tianjin University, CHINA,
[3]Lund University, SWEDEN, and
[4]Key Laboratory of Marine Intelligent Equipment and System, CHINA*

P06 **COMPUTATIONAL OPTIMIZATION OF ACOUSTOFLUIDIC DEVICES**
Kirill Kolesnik[1], Vijay Rajagopal[1,2], and David J. Collins[1,2]
[1]University of Melbourne, AUSTRALIA, and [2]Graeme Clark Institute, AUSTRALIA

P07 **CONCEPT OF ACOUSTIC BUOYANCY**
Andreas Fuchsluger[1], Annalisa De Pastina[2], Tina Mitteramskogler[1],
and Bernhard Jakoby[1]
[1]Johannes Kepler University Linz, AUSTRIA and [2]Silicon Austria Labs, AUSTRIA

P08 **DESIGN OPTIMIZATION OF ACOUSTIC CAVITY TRAPS FOR EFFECTIVE MICROPARTICLE TRAPPING**
Pradipta Kr. Das, Gabriel Werr, and Maria Tenje
Uppsala University, SWEDEN

P09 **ELECTROKINETIC INTERACTIONS BETWEEN SURFACE ACOUSTIC WAVES AND ELECTROLYTE SOLUTIONS**

Yifan Li, Sudeepthi Aremanda, Oles Dubrovski, and Ofer Manor
Technion - Israel Institute of Technology, ISRAEL

P10 **ELECTRONICS FOR ACOUSTOFLUIDIC ACTUATORS, VERSATILE VS SPECIFIC**

Raimund Bruenig[1], Melanie Colditz[2], and Andreas Winkler[2]
[1]BelektroniG GmbH, GERMANY and [2]IFW Dresden, GERMANY

P11 **ELUCIDATING FLUID MIXING IN AN ACOUSTIC BIOREACTOR WITH APPLICATION TO YEAST GROWTH**

Gabriel Dumy[1], Thomas Chomette[2], Marin Virey[1], Siriny Laumier[1], and Florian Dittmann[1]
[1]KOLIBRI, FRANCE and [2]ESPCI Paris, FRANCE

P12 **ENRICHMENT OF PROTEIN CRYSTALS IN SERIAL CRYSTALLOGRAPHY USING FLOW CONTROL**

Varun Kumar Rajendran, Björn Hammarström, Martin Vikulnd, and Jonas Sellberg
KTH Royal Institute of Technology, SWEDEN

P13 **EQUILIBRIUM POSITION STABILIZATION OF MULTIMODAL PARTICLE MANIPULATION WITH REINFORCED LEARNING**

Alexander Edthofer, Thomas Laurell, and Thierry Baasch
Lund University, SWEDEN

P14 **EXPERIMENTAL DEMONSTRATION OF LONG-RANGE ACOUSTIC PULLING USING MODE CONVERSION IN WAVEGUIDE**

Feiyan Cai[1], Yanlong Guo[2], Degang Zhao[2], and Hairong Zheng[1]
*[1]Shenzhen Institutes of Advanced Technology, CHINA and
[2]Huazhong University of Science and Technology, CHINA*

P15 **FOCUSED ULTRASOUND INDUCED FLUID FLOW IN A SILICON CAPILLARY DETERMINED VIA MICRO-PIV TREATMENT**

Elisa Ghiringhelli, Carine Guivier-Curien, Philippe Lasaygues, and Cécile Baron
Aix-Marseille Université, CNRS, FRANCE

P16 **GENTLE BLOOD PLASMA SEPARATION WITH SURFACE ACOUSTIC WAVE-BASED MICROFLUIDICS**

Melanie Colditz[1], Armaghan Fakhfouri[1], Romy Kronstein-Wiedemann[2], Kateryna Ivanova[1], Torsten Tonn[2], and Andreas Winkler[1]
*[1]Leibniz-IFW Dresden, GERMANY and
[2]TU Dresden/ DRK-Blutspendedienst Nord-Ost GmbH, GERMANY*

P17 **HIGH THROUGHPUT ACOUSTIC CELL WASHING AND CONCENTRATION FOR CAR T CELL THERAPY**

Anke Urbansky, Karl Westerlund, Raghuraman Srinivasan, Erik Karlsson, Cecilia Magnusson, Erling Nielsen, Julia Alsved, Jessica Congiu, Magnus Hivert, and Pelle Ohlsson
AcouSort AB, SWEDEN

P18   **IDENTIFYING TEMPERATURE GRADIENTS INSIDE ACOUSTOFLUIDIC CHANNELS**
Gabriel Werr, Pradipta Kr Das, Zahra Khaji, and Maria Tenje
Uppsala University, SWEDEN

P19   **INCREASED THROUGHPUT AND CAPACITY OF NM-PARTICLE TRAPPING USING AN ULTRASOUND ACTIVATED PACKED BED**
Michael Gerlt, Ted Bondesson, and Thomas Laurell
Lund University, SWEDEN

P20   **INVESTIGATION OF ACOUSTIC WAVE ATTENUATION IN POLYDIMETHYLSILOXANE FOR ACOUSTOFLUIDIC APPLICATIONS**
Jeongeun Park[1], Beomseok Cha[1], Furkan Ginaz Almus[2], Mehmet Akif Sahin[2], Ghulam Destgeer[2], and Jinsoo Park[1]
[1]Chonnam National University, KOREA, and
[2]Technical University of Munich, GERMANY

P21   **MODES THAT FORM SEVEN TYPES OF NODE**
Jeremy J. Hawkes[1], Sadaf Maramizonouz[2], and Richard Yongqing Fu[3]
[1]Acoustic Machines Ltd, UK, [2]Newcastle University, UK, and
[3]Northumbria University, UK

P22   **MULTI-FREQUENCY ULTRASONIC ATOMIZATION DRIVEN BY BENDING MODE USING A PARABOLIC REFLECTOR**
Weiquan Wang[1], Chikahiro Imashiro[1], Hiroshi Hasegawa[2], Kohsuke Hirano[2], and Takeshi Morita[1]
[1]University of Tokyo, JAPAN and [2]Kaijo Corpration, JAPAN

P23   **MULTICHANNEL ACOUSTOFLUIDIC SEPARATOR FOR HIGH-THROUGHPUT MULTIPLEXED BIOMOLECULE DETECTION ON BIOFUNCTIONAL ELASTOMERIC PARTICLES**
Cooper P. Thome, Creighton T. Tisdale, and C. Wyatt Shields IV
University of Colorado Boulder, USA

P24   **ON THE EVOLUTION OF A NEUTRAL CONFIGURATION OF INHOMOGENEOUS FLUIDS UNDER ACOUSTIC FIELDS**
Sujith Jayakumar[1], Videsh Vk[1], Jeyapradhap T[1], Hemachandran E[2], and Karthick Subramani[1]
[1]Indian Institute of Information Technology, Design and Manufacturing, INDIA, and [2]National Institute of Advanced Manufacturing Technology, Ranchi, INDIA

P25   **ON THE FABRICATION OF A SAW-BASED MICROFLUIDIC DEVICE WITH RAISED ACOUSTIC ENERGY DENSITY AND TAILORED ACOUSTIC PRESSURE FIELD USING DRY FILM RESIST**
Sebastian Sachs, David Schreier, Jörg König, and Christian Cierpka
Technische Universität Ilmenau, GERMANY

P26   **OPTIMIZING TRANSDUCER CONFIGURATIONS FOR 2D ACOUSTIC FOCUSING**
Tuva Eriksson Viklund, Varun Kumar Rajendran, Martin Wiklund, Jonas Sellberg, and Björn Hammarström
KTH Royal Institute of Technology, SWEDEN

P28 PARTICLE RADIATION AND ACOUSTIC MIXING IN A CNC MILLED ALUMINUM-BASED DEVICE

Amaury de Hemptinne, Pierre Gelin, Vyacheslav R. Misko, and Wim De Malsche
Vrije Universiteit Brussel, BELGIUM

P29 PRESSURE CONTROLLED VARIABLE VOLUME ULTRASONIC BIOREACTOR FOR BIOPRODUCTION APPLICATIONS

Gabriel Dumy, Marin Virey, Siriny Laumier, Florian Dittmann, Noémie Cavanna, and Mathilde Maëstrali
KOLIBRI, FRANCE

P31 SMART MICROACOUSTIC SETUP FOR AUTOMATED ICE SENSING AND DEICING USING SURFACE ACOUSTIC WAVES

Kiana Khodakarami[1], Stefan Jacob[2], Atefeh Karmizadeh[1], Uhland Weissker[1], Shilpi Pandey[1], Jaime Del Moral[3], Jorge Gil-Rostra[3], Ana Borrás[3], Agustin R. González-Elipe[3], and Andreas Winkler[1]
[1]Leibniz Institute for Solid State and Materials Research, GERMANY,
[2]Physikalisch-Technische Bundesanstalt, GERMANY, and
[3]Consejo Superior de Investigaciones Científicas, SPAIN

P33 STUDY OF SAW FIELD NONUNIFORMITY FOR OPTIMIZATION OF SAW BASED ACOUSTIC STREAMING MICROPUMP

Chen Wu[1,2], Grim Keulemans[2], Benjamin Jones[2], Veronique Rochus[2], Xavier Rottenberg[2], and Paul Heremans[1,2]
[1]KU Leuven, BELGIUM and [2]Imec, BELGIUM

P34 THE EFFECT OF SPEED OF SOUND MISMATCH ON ACOUSTOPHORETIC FOCUSING QUALITY WITHIN DROPLETS

Qian Shi[1], Thierry Baasch[2], Zhenhua Liu[1], Anna Fornell[1], Gabriel Werr[1], Laurent Barbe[1], and Maria Tenje[1]
[1]Uppsala University, SWEDEN and [2]Lund University, SWEDEN

P35 THE IN-FLOW MOBILITY RATIO METHOD ENABLES OPTIMIZING ACOUSTOPHORESIS SEPARATION QUALITY

Thierry Baasch, Alexander Edthofer, Linda Péroux, Olivia Rengbrandt, Lovisa Silversand, Andreas Lenshof, and Thomas Laurell
Lund University, SWEDEN

P36 TOWARDS LOVE WAVE-BASED IN-SITU MEASUREMENT OF ICE LAYER THICKNESS ON WIND TURBINE ROTOR BLADES

Philipp Schulmeyer and Hagen Schmidt
Leibniz Institute for Solid State and Materials Research Dresden, GERMANY

P37 TRANSIENT BUILDUP AND DECAY OF THERMOACOUSTIC STREAMING

Franziska Martens, Wei Qiu, Ola Jakobsson, and Per Augustsson
Lund University, SWEDEN

P38 TRANSIENT MODEL OF THE OPTO-ACOUSTOPHORETIC EFFECT USING SEPERATION OF TIMESCALES

Jonas H. Jørgensen
Comsol A/S, DENMARK

P39 **TWO-STEP ACOUSTOFLUIDIC CANCER CELL ENRICHMENT**
Cecilia Magnusson, Mahdi Rezyati Charan, and Per Augustsson
Lund University, SWEDEN

P40 **ULTRASONIC ATOMIZATION IN A SUPERHYDROPHOBIC MICROCHANNEL'S PLASTRON.**
Maxime Fauconnier, Bhuvaneshwari Karunakaran, Alex Drago-González, Laura Fieber, William S.Y. Wong, Robin H.A. Ras, and Heikki J. Nieminen
Aalto University, FINLAND

P41 **VOLUMETRIC TEMPERATURE MEASUREMENT IN A MICRO CHANNEL SUBJECTED BY A STANDING SURFACE ACOUSTIC WAVE**
Jörg König and Christian Cierpka
Technische Universität Ilmenau, GERMANY

P42 **ARRAY OF PIEZOELECTRIC MICROMACHINED ULTRASONIC TRANSDUCERS (PMUTS) FOR THE ACOUSTOFLUIDIC MANIPULATION OF PARTICLES AND SPHEROIDS**
Emilie Vuille-dit-Bille[1,2], Sarah Heub[1], Dara Z. Bayat[1], Marc-Alexandre Dubois[1], Thomas Overstolz[1], Gilles Weder[1], Michel Despont[1], and Selman Sakar[2]
[1]CSEM SA, SWITZERLAND, and [2]EPFL, SWITZERLAND
(Presented in Session 8 – Devices)

P43 **BLOOD CELL FOCUSING IN SIMULATION OPTIMIZED MOLDED POLYMER ACOUSTOPHORESIS CHIP**
Mathias Ohlin[1], Fabian Lickert[2], Sazid Zamal Hoque[2], Anke Urbansky[1], Mikael Evander[1], Agnes Michanek[1], Magnus Hivert[1], Henrik Bruus[2], and Pelle Ohlsson[1]
[1]AcouSort AB, SWEDEN and
[2]Technical University of Denmark (DTU), DENMARK
(Presented in Session 8 – Devices)

P45 **ECHOGRID: HIGH-THROUGHPUT ACOUSTIC TRAPPING TOWARDS MICRO AND NANOPLASTIC MONITORING**
Martim Costa[1], Björn Hammarström[1], Liselotte van der Geer[1], Selim Tanriverdi[1], Haakan Joensson[1], Martin Wiklund[1], and Aman Russom[1,2]
[1]KTH Royal Institute of Technology, SWEDEN and [2]AIMES - Karolinska Institute and KTH Royal Institute of Technology, SWEDEN
(Presented in Session 2 - Applications of Acoustic Systems 2)

P46 **LOCALIZED BULK ACOUSTIC TRAPS USING MILLED ALUMINUM DEVICES**
Saumitra Joshi, Dhananjay V. Deshmukh, and Mark W. Tibbitt
ETH Zurich, SWITZERLAND
(Presented in Session 8 – Devices)

P47 **RAPID ACOUSTIC ISOLATION UNVEILS PROTEOME OF EXTRACELLULAR VESICLES FROM A MINUTE VOLUME OF HUMAN BLOOD PLASMA**
Megan Havers[1], Aaron Scott[1], Niklas Ortenlöf[1], Marc Isaksson[1], Simon Ekström[1], Charlotte Welinder[1], Thierry Baasch[1], Mikael Evander[2], Andreas Lenshof[1], Magnus Gram[1], and Thomas Laurell[1]
[1]Lund University, SWEDEN and [2]AcouSort AB, SWEDEN
(Presented in Session 1 - Applications of Acoustic Systems 1)

P48 **VESICLE-BASED DRUG LOADING AND INTRACELLULAR DELIVERY BY GIGAHERTZ ACOUSTIC STREAMING**

Haopu Wang, Shuailong Zhang, Huikai Xie, and Yao Lu
Beijing Institute of Technology, CHINA
(Presented in Session 5 - Acoustic Streaming)

P49 **ACOUSTOFLUIDIC BLOOD PLASMA SEPARATION FOR NEONATAL CARE**

Amal Nath[1], Wei Qiu[1], Thierry Baasch[1], Andreas Lenshof[1], Marie Larsson[2], Linda Nilsson[3], Magnus Gram[3], David Ley[3], and Thomas Laurell[1]
[1]Lund University, SWEDEN, [2]Hospitals of Halland, SWEDEN, and [3]Skåne University Hospital, SWEDEN

P50 **NUMERICAL STUDY OF ACOUSTIC STREAMING IN SPHERICAL DROPLETS SUSPENDED IN UNCONFINED MEDIA**

Pradipta Kr. Das[1], Carl D. Meinhart[2], and Maria Tenje[1]
[1]Uppsala University, SWEDEN and [2]University of California, Santa Barbara, USA

Acoustofluidics Olympics
House 10, First Floor, Room 101136
14:30 - 17:30

THE ECHOGRID – THE WORLD'S FASTEST MICROPLASTIC ENRICHMENT DEVICE!
Martim Costa
KTH, SWEDEN

We will demonstrate the EchoGrid, which is an acoustofluidic chip used for upconcentrating microplastics from dilute liquid samples. The chip is based on a surface displacement transducer combined with a PDMS flow chamber, and utilizes silica seed particles for trapping and enriching microplastics at relatively high flow rates. The device has recently been described in this publication: M. Costa et al., Anal. Chem. 2024, 96, 23, 9493–9502 (https://doi.org/10.1021/acs.analchem.4c00933).

A FRUGAL, SELF-SUSTAINING ACOUSTOFLUIDICS BIOREACTOR DEMONSTRATOR
Gabriel Dumy
KOLIBRI, FRANCE

This is a much simplified version of our bioreactor that was made for education purposes, but that exhibit how the acoustofluidics methods that are exploited in a conference such as ours can be efficiently implemented with quite few material and devices. For less than 400€, this small bioreactor system generates a complete culture column, that can shift its position in space, in accordance to the temperature and constrains imposed to the system. Real time control is achieved on said position, and the fluid cavity (about 30mL) is projected on a large screen.

NM-PARTICLE TRAPPING IN A PACKED BED
Michael Gerlt
Lund University, SWEDEN

We demonstrate trapping of 270 nm fluorescent particles in a capillary filled with 100 μm polystyrene particles. The setup consists of syringe pumps, the trapping device and a dynolite camera for fluorescence analysis.

3 NODE TYPES IN DIFFERENT CHANNELS ON ONE MICROSCOPE SLIDE
Jeremy Hawkes
Acoustic Machines, UK

Liquids in capillary bridge channels run in parallel on a microscope slide. The channel depths range from 0.15 mm to 1 mm and particles simultaneously move to the nodes in each liquid bridge. Different node patterns form at each channel depth. The nodes are produced by resonances in: 1) the top film, 2) the liquid and 3) the glass. The nodes from each resonant source appear independently and separated by the channel depth because at each depth a resonance from only one origin dominates.

Board Meeting of the Acoustofluidics Society (open to all)
House 10, First Floor, Room 101132
16:00 - 17:00

Banquet

18:30 -   **Norrlands Nation**
Late

Norrland's Nation, Västra Ågatan 14, 753 09 Uppsala

No conference is complete without a banquet. Join us on Thursday evening at Norrland's Nation for a delicious meal and a chance to network with colleagues. Norrland's Nation is centrally located by the riverbanks of Fyrisån, a 30-minute walk or a 15-minute bus ride from the Ångström Laboratory.

Friday, 16 August

All Times are Central European Summer Time (CEST).

08:50   Announcements

Session 7 – Applications of Acoustic Systems 3
Session Chair: Thomas Laurell, Lund University, SWEDEN

Keynote Speaker 4

09:00   THE EMERGING CONFLUENCE OF ACOUSTIC MICROMANIPULATION, ACOUSTIC HOLOGRAPHY AND 3D PRINTING
David Collins
University of Melbourne, AUSTRALIA

Contributed Talks

09:50   MICRO-MANIPULATION OF MISCIBLE FLUIDS WITH ACOUSTIC TWEEZERS
Samir Almohamad[1], Gustav K. Modler[2], Ravinder Chutani[1], Udita Gosh[1], Sarah Cleve[1], Henrik Bruus[2], and Michael Baudoin[1]
[1]Université de Lille, FRANCE and [2]Technical University of Denmark, DENMARK

10:05   APPLICATIONS OF HIGH-POWER BULK WAVE ACOUSTOFLUIDICS
Enrico Corato, Wei Qiu, and Per Augustsson
Lund University, SWEDEN

10:20   HIGH-POWER BULK-WAVE-ACOUSTOPHORESIS DEVICES UTILIZING AN ELLIPTICAL REFLECTOR FOCUSING TRANSDUCER
Zhirui Chen[1], Chikahiro Imashiro[1], Wei Qiu[2], and Takeshi Morita[1]
[1]University of Tokyo, JAPAN and [2]Lund University, SWEDEN

10:35   Coffee Break

Session 8 – Devices
Session Chair: Martyn Hill, University of Southampton, UK

Contributed Talks

11:00   BLOOD CELL FOCUSING IN SIMULATION OPTIMIZED MOLDED POLYMER ACOUSTOPHORESIS CHIP
Mathias Ohlin[1], Fabian Lickert[2], Sazid Zamal Hoque[2], Anke Urbansky[1], Mikael Evander[1], Agnes Michanek[1], Magnus Hivert[1], Henrik Bruus[2], and Pelle Ohlsson[1]
[1]AcouSort AB, SWEDEN and
[2]Technical University of Denmark (DTU), DENMARK

11:15 **LOCALIZED BULK ACOUSTIC TRAPS USING MILLED ALUMINUM DEVICES**
Saumitra Joshi, Dhananjay V. Deshmukh, and Mark W. Tibbitt
ETH Zurich, SWITZERLAND

11:30 **ARRAY OF PIEZOELECTRIC MICROMACHINED ULTRASONIC TRANSDUCERS (PMUTS) FOR THE ACOUSTOFLUIDIC MANIPULATION OF PARTICLES AND SPHEROIDS**
Emilie Vuille-dit-Bille[1,2], Sarah Heub[1], Dara Z. Bayat[1], Marc-Alexandre Dubois[1], Thomas Overstolz[1], Gilles Weder[1], Michel Despont[1], and Selman Sakar[2]
[1]CSEM SA, SWITZERLAND, and [2]EPFL, SWITZERLAND

11:45 **Award Announcements**

12:00 **Announcement of Acoustofluidics 2025**

12:15 **Conference Adjourns**

Acoustic pipette and biofunctional negative acoustic contrast microparticle system for rapid picomolar-level biomolecule detection in whole blood

Cooper P. Thome[1,*], John P. Fowle[1], Parker McDonnell[2], Johanna Zultak[2], Kaushik Jayaram[2,3], Aaron K. Neumann[4], Gabriel P. López[5], and C. Wyatt Shields IV[1,3]

[1]Department of Chemical and Biological Engineering, University of Colorado Boulder, Boulder, USA
[2]Paul M. Rady Department of Mechanical Engineering, University of Colorado Boulder, Boulder, USA
[3]Biomedical Engineering Program, University of Colorado Boulder, Colorado, USA
[4]Department of Pathology, University of New Mexico School of Medicine, New Mexico, USA
[5]Department of Chemical and Biological Engineering, University of New Mexico, New Mexico, USA
[*]E-mail: cooper.thome@colorado.edu

Introduction

Biosensing is an essential part of patient diagnosis, pandemic response, and disease management; however, many biosensing techniques require laborious preparation and processing steps. For example, enzyme-linked immunosorbent assay (ELISA) is considered the gold standard for quantitative biomarker detection due to its high sensitivity and specificity, but the assay includes numerous blocking, labeling, and washing steps that require significant user engagement for large portions of the assay (up to several hours). Here, we present a simple microparticle-based assay to rapidly isolate and purify biomarkers from whole blood in a handheld pipette for sensitive and streamlined biomarker detection in under 1 hour and 15 minutes. A key aspect of this technology is the preparation and use of functional negative acoustic contrast particles (fNACPs), a unique set of acoustically responsive and modularly functionalized microparticles. fNACPs can be decorated with a range of biorecognition motifs (e.g., antigens, antibodies, aptamers) for the specific capture of target biomarkers from whole blood. After capture, targets can be labeled *in situ* by fluorescent secondary antibodies (Abs). Here, we show analysis of fNACP fluorescence by both a custom, portable fluorimeter and standard flow cytometer. The second key aspect of this technology is the handheld acoustic pipette, which contains an acoustofluidic trapping channel. The trapping channel establishes a half-wavelength acoustic standing wave across the width of the channel, yielding a pressure node along the center of the channel and antinodes along the walls. Cells have positive acoustic contrast factors and thus experience primary acoustic radiation forces that guide their displacement toward the node of the standing wave. However, fNACPs are forced toward the antinodes of the standing wave due to their negative acoustic contrast, where they are trapped. Due to their large sizes (25 μm) and compressibilities, the fNACPs robustly trap along the pressure antinodes of the standing wave and separate from blood components in under 60 seconds with >99% efficiency. We demonstrate the detection of a model antibody biomarker, anti-ovalbumin (anti-OVA), from blood at picomolar levels (35-60 pM) with integrated controls showing minimal non-specific adsorption.

Theory and Experimental Procedure

When a half-wavelength standing wave is established within a microfluidic channel, such as a glass capillary, positive acoustic contrast particles (PACPs) with diameters much smaller than the wavelength (e.g., cells) move towards the pressure node, which is located along the middle of the channel [1]. Alternatively, NACPs undergo acoustophoresis to the antinodes along the walls of the channel. In addition to the primary radiation force, particles and cells in the channel also experience a secondary radiation force, which is attractive between particles at close distances [2,3]. Therefore, when NACPs undergo acoustophoresis, they are forced to the channel walls and subsequently aggregate. Finally, beyond the axial component of the acoustic radiation force, particles in an acoustofluidic channel experience a lateral acoustic radiation force that originates from gradients in the local acoustic potential along the channel and acts parallel to the channel, toward regions of local acoustic minima or maxima. In certain conditions, such as at high acoustic radiation forces, this can result in acoustic trapping, which we define as the immobilization of NACPs along the pressure antinodes in the presence of an applied flow, due to both the lateral component of the primary acoustic radiation force and the secondary acoustic radiation force exceeding the force on NACPs from Stokes' drag [3,4]. In this work, NACPs were synthesized via homogenization of a Sylgard 184 and triethoxyvinylsilane polymer precursor and subsequent heating to facilitate crosslinking. Following crosslinking, we isolated a low-polydispersity fraction of the NACPs by sequential vortexed filtration through 40, 30, and 20 μm filters, collecting the NACPs retained by the 20 μm filter. This process yields NACPs with a low polydispersity with a mean size of 24.3 μm (coefficient of variance (CV) = 12.4%). The surfaces of NACPs were functionalized by conjugating a biotin-polyethylene glycol (PEG)-silane linker, streptavidin, and biotinylated OVA, in that order. To evaluate the fNACP assay performance and limit of detection (LOD), anti-OVA Abs were spiked into 100 μL buffer or porcine blood containing 10^4 nonfluorescent fNACPs and 10^4 green fluorescent nonfunctionalized NACPs as an internal control. After target capture, the fNACPs and NACPs were incubated with fluorescently tagged secondary

Abs, washed, and analyzed via flow cytometry. Trapping channels were fabricated by bonding a piezoelectric transducer, actuated by an applied AC signal at 750 kHz, to a square glass capillary. To assess trapping performance, $5x10^4$ NACPs were mixed with 100 µL porcine blood and diluted to 1 mL with buffer. The mixture was passed through the trapping channel at varied flow rates, and NACPs were trapped, yielding waste and enriched samples. Samples were analyzed via flow cytometry to quantify NACP retention and sample purity. Using primarily CAD and 3D printing, we created the ergonomic, handheld acoustic pipette (Fig. 1a). To accommodate all necessary assay components, the pipette was designed with two main parts: i) the main pipette body, which contains three syringe chambers to store wash buffer and fluorescent secondary antibody, and ii) the trapping tip, which contains the acoustofluidic trapping channel and related components (Fig. 1b).
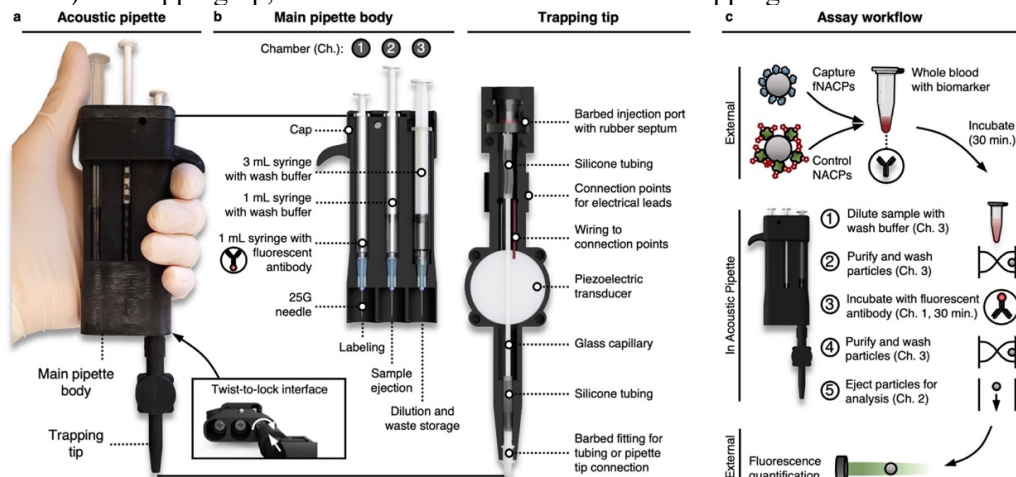
Figure 1: Acoustic pipette overview. a Image of acoustic pipette. Inset shows mechanism for movement and locking of trapping tip. **b** Schematic illustration of acoustic pipette internals, including the main pipette body and trapping tip. **c** Schematic illustration of general pipette-facilitated fNACP assay.

Results and Discussion

The discriminant forces acting on fNACPs and blood cells enabled their efficient (over 99% retention and purity) separation from blood components in short timescales (under 40 sec, Fig. 2a and b). Further, decoration of fNACPs with OVA enabled the capture and detection of anti-OVA immunoglobulin G Abs at picomolar levels (LOD = 0.06 nM) when analyzed by flow cytometry, a sensitivity competitive with commercial ELISAs (e.g., ~0.013 nM, Fig. 2c). Due to the PEG linkers between the particle surfaces and capture antigen, nonspecific adsorption of biomarkers and secondary Abs was extremely low at physiological levels. The pipette design enables a simple workflow that eliminates the many cumbersome steps associated with traditional immunoassays; by integrating the trapping channel and multiple assay buffer chambers into the pipette, all fNACP-based assay steps can be carried out with minimal user engagement in 75 minutes. Beyond this, we developed a portable, custom benchtop fluorimeter for analysis of samples processed in the acoustic pipette. Following labelling of fNACPs in a modified fNACP-based assay, we detected anti-OVA at 100 nM in seconds using the fluorimeter.
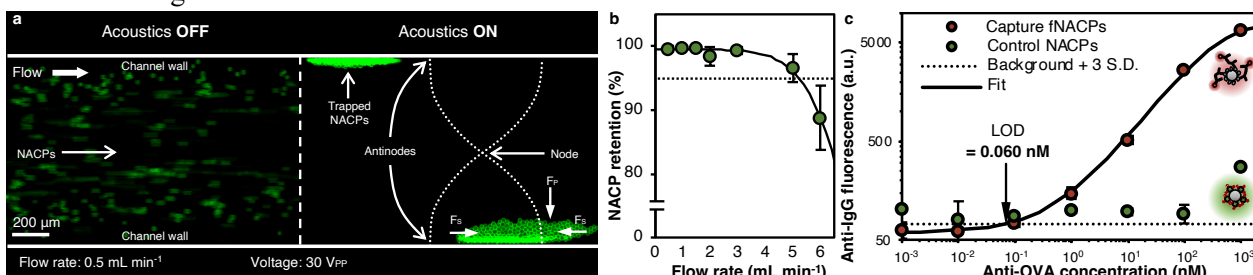
Figure 2: a Acoustic trapping of NACPs within a glass capillary supporting a half-wavelength standing wave. NACPs, shown in green, were coated with fluorescent streptavidin. **b** NACP retention over a range of flow rates through the acoustofluidic trapping channel, N = 5. **c** Fluorescence of anti-IgG on capture fNACPs and control NACPs over range of anti-OVA concentrations spiked in whole blood. Data was fit to a 5-parameter logistic curve to determine the assay LOD. Dotted line indicates baseline fluorescence of fNACPs without fluorescent anti-IgG. Data is presented as mean MFI ± standard deviation. N = 3.

Conclusion

We demonstrate an NACP-based, acoustic pipette-enabled assay that isolates biomarkers from whole blood for rapid and sensitive detection in a simple, ergonomic, and handheld acoustofluidic device. By integrating the pipette and fluorimeter, thereby eliminating the need for flow cytometry, we show the ability for the NACP-based, acoustics-enabled assay to be simplified for biomarker detection in areas with limited resources.

References

[1] Gao, L. *et al. Biomicrofluidics* **9**, 014105 (2015).
[2] Laurell, T., Petersson, F. & Nilsson, *Chem. Soc. Rev.* **36**, 492–506 (2007).
[3] Evander, M. & Nilsson, J., *Lab. Chip* **12**, 4667–4676 (2012).
[4] Hammarström, B., Laurell, T. & Nilsson, *Lab. Chip* **12**, 4296–4304 (2012).

Acoustofluidic Blood Plasma Separation for Neonatal Care

Amal Nath[1], Wei Qiu[1], Thierry Baasch[1], Andreas Lenshof[1], Marie Larsson[2,3], Linda Nilsson[3], Magnus Gram[3], David Ley[3], Thomas Laurell[1]

[1]Department of Biomedical Engineering, Lund University, Lund, Sweden
[2]Clinical Chemistry, Hospitals of Halland, Varberg/ Halmstad, Sweden
[3]Department of Clinical Sciences, Pediatrics, Lund University, Skåne University Hospital, Sweden
*E-mail: amalnath.manindranath@bme.lth.se

Introduction

Many newborn babies require intensive care right after birth due to complications arising from premature birth, infection, malformations, or other diseases. To monitor the health of the neonate, blood is sampled every few hours and routine blood tests are performed. Neonates born prematurely may weigh as low as 0.5-0.6 kg, and have a circulating blood volume as low as only 50-60 ml. The current neonatal blood sampling procedures are unfortunately adapted from techniques used for adult patients with mature cardiovascular systems. As the immune system in neonates is not fully developed, loss of blood from sampling poses significant risk of disease [1]. Additionally, manual intervention in the sampling procedure needs to be minimized as it potentially increases the risk of infection. In this work, we propose a closed-loop on-line blood sampling method using an acoustofluidic system where blood is drawn from the neonate, blood plasma is separated from the whole blood for clinical analyses while the blood cells are returned to the neonate. The whole system is envisaged to be in the form of a compact device placed inside the incubator, which minimizes the risk of infection. The initial experiments with blood samples from adult donors to assess separation performance show that the number of blood cells in the collected blood plasma are well within the guideline limits prescribed by the European Directorate for the Quality of Medicines & HealthCare (EDQM), indicating high quality of separation.

Methods

The experimental setup developed for the study is shown in Fig. 1. Briefly, a side-actuated two-stage glass acoustofluidic device is used to focus the blood cells and separate blood plasma from whole blood. Three DC motor-driven peristaltic micro pumps are connected at the channel outlets operating in suction mode to draw the blood into the plasmapheresis chip. Peristaltic pumps are chosen because of their safe and reliable operation in existing medical applications, including apheresis and dialysis machines. To dampen pulsations in the flow caused by the peristaltic pumps, PDMS-based flow dampeners consisting of an array of air chambers transverse to a main channel, are connected between the device outlets and the pumps. The lead-free BNT-BT-BNMN transducers glued to the sides of the first and second channels are excited by sinusoidal signals with a linear frequency sweep (duty cycle: 1 msec) between 1.940 MHz – 1.946 MHz and 1.934 MHz – 1.940 MHz, respectively. The use of frequency sweep ensures focusing of cells across blood samples from different donors having different hematocrit values and compositions and smoothens out irregularities in acoustic focusing across the entire length of the channel.
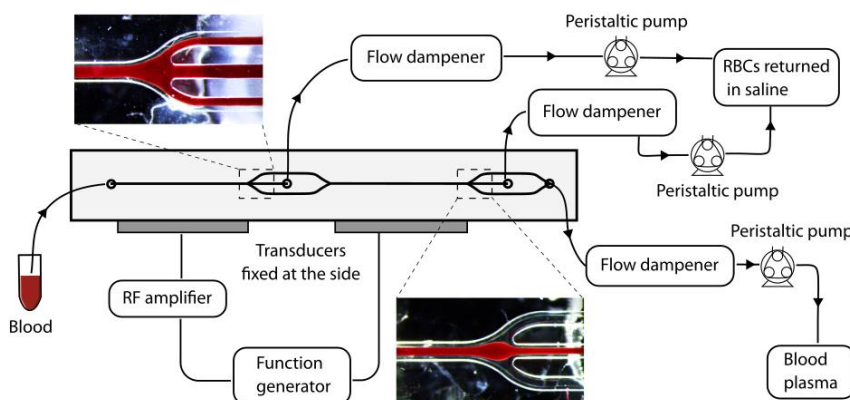
Figure 1: Schematic of the experimental setup. The channels etched in glass have cross sectional dimensions 440 μm × 150 μm and lengths 36.9 mm and 31.6 mm. The transducers mounted to the first and second channels are actuated by sinusoidal signals with peak-to-peak voltages of 22.2 V and 10 V respectively. Experimental images showing focusing of the cells at the end of the two stages of separation are shown in the inset.

Results and Discussion

The experiments described here aimed at developing an integrated device that separates blood plasma from adult whole blood, as a model system that can later be adapted to newborn infants. The high cell concentration necessitates performing the blood plasma separation in two stages. The first transducer is actuated with an amplified voltage signal of 22.2 V_{p-p} to create a strong acoustic field which enables removal of a majority of the cells through the first outlet. As a result, the second stage has a much lower concentration of blood cells. The actuation voltage in the second stage is constrained to 10 V_{p-p} to limit the steady state device temperature

to 30°C. The blood sample input flow rate is set to 115 µl/min, while the flow rates of packed cells through the central outlets at the end of the first and second stages are set to 47 µl/min and 45 µl/min, respectively. Blood plasma is collected from the side outlet at the end of the second stage at a flow rate of 23 µl/min, with a volume efficiency (plasma flow rate/ sample flow rate) of 20%.

The pulsations in the flow arising due to peristaltic pumps necessitates the use of flow dampeners to enable separation of blood cells, without which the cells periodically spill over into the side plasma outlet. Here, a PDMS-based flow dampener is used, consisting of circular air chambers (R = 1 mm) transverse to a 400 µm wide and 200 µm deep main channel and distributed along 50 mm, i.e. introducing an additional dead volume of only 4 µl to the flow path. The compression and relaxation of air in these chambers absorbs a part of the pressure variations, thereby reducing the pulsations in the flow. As shown in Fig. 2a, the pulsations, quantified here by the standard deviation from mean flow rate, are reduced from ±34% to ±15% by using the dampener.

No. of cells/ µl	Whole blood	CEN plasma	AF plasma
RBCs	~10^6	~10^2	~10^2
WBCs	~10^4	~10^1	~10^1
Platelets	~10^5	~10^2	~10^4
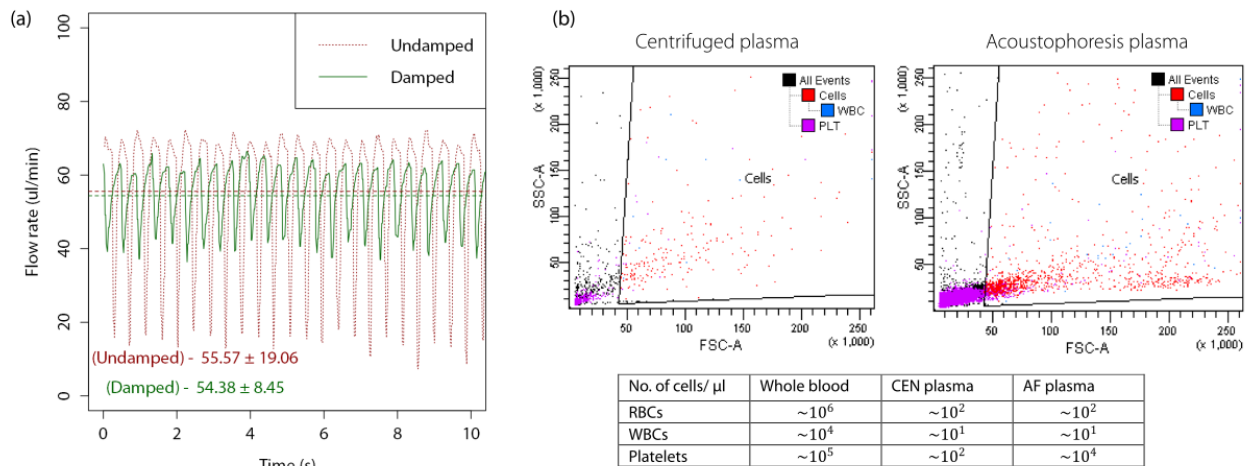
Figure 2: (a) The instantaneous flow rate of PBS using a single peristaltic pump is measured using a flow sensor for both the undamped case, and when the PDMS dampener is connected to the pump. The measured mean flow rate and standard deviation are shown. (b) FACS plots of Sample V (in Table 1) showing the presence of leukocytes (WBC) and platelets (PLT) in the separated blood plasma. Cells in the sample are depleted by several orders of magnitude after the separation process, while the removal of platelets is relatively less efficient due to their lower acoustophoretic mobility.

The separation performance is measured by comparing flow cytometry (FACS) analysis of the blood plasma collected from the device (acoustophoresis plasma) with that obtained from centrifugation of whole blood (2000×g for 10 min) (see Fig. 2b). WBCs and platelets in the blood plasma are labeled by anti-CD-45 antibodies and anti-CD-61 antibodies, respectively. The cell counts measured in different separated samples are shown in Table 1. The acoustophoresis blood plasma is seen to have cell and platelet counts below the guideline limit values prescribed by the European Directorate for the Quality of Medicines & HealthCare (EDQM). Further, the degree of hemolysis induced by the separation is measured using a low Hb photometer and seen to be in the same range for both acoustophoresis and centrifugation, i.e. 0.2-0.3%.

numbers per µl of blood plasma	Sample I		Sample II		Sample III		Sample IV		Sample V		Guideline (EDQM)[b]
	AF	CEN	AF	CEN	AF	CEN	AF	CEN	AF	CEN	
Total events	6311	219	8868	318	25441	680	6728	318	19467	324	
RBCs	153	40	157	16	314	6	233	17	469	70	<6000
WBCs	6	2	2	1	9	0	6	2	16	15	<100
Platelets[a]									17159	133	<50000

Table 1: The number of cells per µl of blood plasma measured by flow cytometry is given in the table. The number of different cells is seen to be significantly lower than the guideline limits. AF: acoustophoresis, CEN: centrifuged.
[a] Platelets are not labeled in the first four samples but are within the guideline limits due to lower total events.
[b] Guideline limits for fresh frozen plasma used for clinical transfusion.

Conclusion
The micro-plasmapheresis system separates blood plasma out of adult whole blood, at an output plasma flow rate of 23 µl/min, with blood plasma quality conforming to the EDQM clinical standards. Forthcoming studies will encompass blood chemistry and coagulation tests to further assess the quality of separated plasma. The operating parameters in the existing design may also need to be tuned to take into consideration the higher hematocrit and difference in composition of neonatal blood as compared to adult blood.

References
[1] Hellström, W., Forssell, L., Morsing, E., Sävman, K., Ley, D., *Acta Paediatrica*, **109 (4),** 2019

Rapid acoustic isolation unveils proteome of extracellular vesicles from a minute volume of human blood plasma

Megan Havers[1], Aaron Scott[3], Niklas Ortenlöf[2],
Marc Isaksson[3], Simon Ekström[3], Charlotte Welinder[3],
Thierry Baasch[1], Mikael Evander[4], Andreas Lenshof[1], Magnus Gram[2], Thomas Laurell[1]

[1] Department of Biomedical Engineering, Lund University, Lund, Sweden, [2] Department of Pediatrics, Lund University Lund, Sweden, [3] Department of Clinical Sciences, Lund University Lund, Sweden, [4] AcouSort AB, Lund, Sweden.
*E-mail: megan.havers@bme.lth.se

Motivation

Acoustic trapping of nanoparticles in a 200x2000 µm $\lambda/2$-resonator (4.1 MHz) has been recently demonstrated with both polystyrene and silica seed particles [1], additionally showing that a high flow rate wash (200 µL/min) can be employed for nanoparticle trapping into silica seed particle clusters without compromising performance. Here we present an experimental study, showing the application of acoustic trapping to the rapid enrichment of biological nanoparticles from a complex mixture. Namely, extracellular vesicles (EVs) from blood plasma - a readily available biofluid in clinics which has a very high dynamic range in protein abundance. Metatla *et al.* recently demonstrated that isolating EVs from plasma enhances protein identification [2], albeit requirng multiple centrifugations over several hours and pooling plasma for sufficient material. Here we capitalize on the benefits of microfluidics and the power of acoustic trapping using silica seed particles, reducing the processing time, by cutting wash time from 7 to 1 min, and volume required as low as 8 µL.

Acoustic isolation and proteomic analysis methodology

Acoustic trapping was performed as previously detailed [1] and outlined in Fig. 1 for EV isolation from diluted plasma. In brief, silica seed particles are acoustically retained against flow as a cluster [1], into which the biological nanoparticles may then be enriched, and free proteins can be washed off. The EVs trapped from plasma are subsequently collected and prepared for proteomic analysis by lysis, purification and proteolytic digestion. Liquid chromatography-mass spectrometry (LC-MS) was performed, followed by protein quantification and data processing using the Uniprot reviewed protein database and gene ontology (GO) terms.
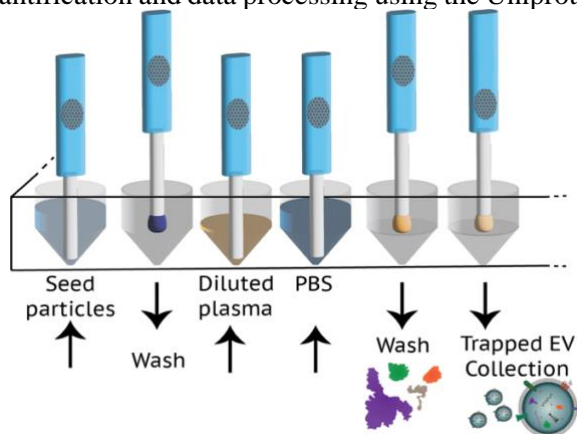
Figure 1: Schematic representation of the acoustic trapping protocol, in which the trapping capillary unit moves to each well of the microplate from left to right. The system performs the following sequence of steps: seed particle trapping, dispensing phosphate buffered saline (PBS) to wash excess seed particles from the cluster, aspirating plasma (8 µL diluted with 17 µL PBS), aspiration of PBS, dispensing PBS to wash away dissolved proteins and then dispensing the seed particle cluster containing trapped EVs in 75 µL PBS. The glass capillary has a cross-section of 200 µm by 2 mm and is mounted, as shown in Fig. 2a, on a piezoelectric transducer, actuated at 4.1 MHz, 10 V_{pp}.

Results and Discussion

Proteomic analysis indicates that the trapped samples are significantly different to the raw plasma samples, Fig. 2. Many proteins are significantly (p-values > 0.05) enriched by trapping (Fig. 2d) and those associated with EVs display several connections (Fig. 2e). The protein rank plots including all proteins detected in trapped samples (Fig. 2f-g) indicate that proteins which have been significantly enriched with a fold change greater than 2.8 were mostly present in low abundance in raw plasma (ranked 200-300), and then enriched by trapping, ranking around 50-200 most abundant in trapped samples. Furthermore, 51 proteins were found consistently only in trapped samples and not in raw plasma (Fig. 2b), half of these trapped proteins have been previously associated with EVs. For example, Pyruvate kinase (a common vesicular protein), was found in most trapped samples but not in raw plasma samples. Here we can see that the dynamic range of mass spectrometry is limited, and that EV proteins present in plasma can be detected better following enrichment by trapping EVs and washing off abundant free proteins. In this work we also found that there is no significant difference in protein abundance despite changing seed particle material and washing flow rate. By replacing the commonly used polystyrene seed particles with silica seed particles, we could increase the washing flow rate, from 30 to 200 µL/min, reducing the total time by 50% without altering the enriched proteome [1]. Thus, we address an unmet need in rapidly growing field of EV biomarker research for fast, cheap, and automated techniques for EV enrichment and purification, with acoustic trapping.

Conclusion

We propose acoustic silica seed particle trapping to purify extracellular vesicles from minute blood plasma samples at an unprecedented speed and unveil the extracellular vesicle proteome by mass spectrometry.
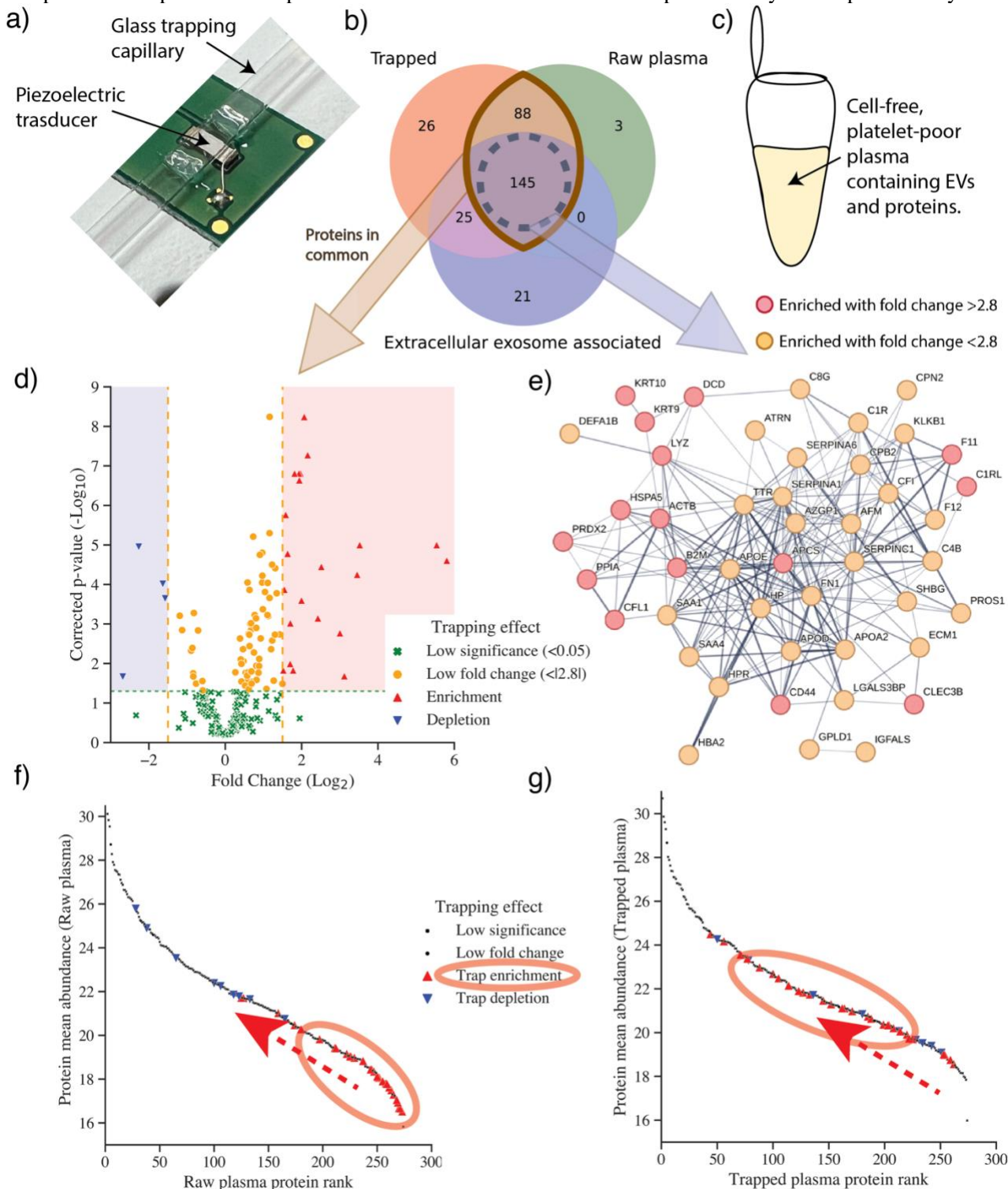
Figure 2 a) Acoustic trapping unit. b) Venn diagram of the proteins detected consistently (>60%) in trapped samples compared with those in the raw plasma samples, compared with a set of proteins which are associated with the gene ontology term 'extracellular exosome' and detected in at least one sample. c) Schematic of raw plasma. d) Significance was characterized for each protein by corrected p-values<0.05 and fold change magnitude above 2.8 e) String association network with edge thickness showing confidence of interaction between detected 'extracellular exosome' genes which were enriched by trapping, red/orange indicates high/low enrichment by trapping. f-g) Protein ranks in raw plasma (f) compared to trapped (g) plasma show that many low abundant proteins were enriched and moved to higher abundance.

References

[1] M. Havers, T. Baasch, A. Lenshof, M. Evander and T. Laurell, *Phys. Rev. Appl.*, **21** 034016 (2024).
[2] I. Metatla, *et al., Clin. Proteomics*, **21** 22 (2024).

Compressibility-based Positive Isolation of Bacteria from Platelets using Tilted-Angle Standing Surface Acoustic Wave

Song Ha Lee[1], and <u>Jinsoo Park</u>[1, *]

[1]Department of Mechanical Engineering, Chonnam National University, Gwangju, Republic of Korea
[*]E-mail: jinsoopark@jnu.ac.kr

Introduction

Sepsis and endocarditis are disorders that arise from bacterial infections circulating in the blood. Sepsis, responsible for one-fifth of global fatalities and resulting in one million deaths each year, prompted the World Health Organization (WHO) to adopt a resolution in 2017 to enhance efforts in preventing, diagnosing, and treating sepsis. The isolation of minute entities like cells and bacteria is a fundamental preparatory step in numerous microfluidic applications across disciplines such as microbiology, chemistry, biology, and biomedicine. The varied methods are limited, not compatible with automated point-of-care testing platforms, and only suitable for samples containing distinct differences in particle size. These constraints have led to the development of advanced automated microfluidic methods for separating bacteria. Platelets (PLTs) pose a technical challenge in separation due to their size similarity to bacteria, unlike red and white blood cells. Current microfluidic separation methods primarily rely on size differentiation [1, 2], which hinders their efficacy in separating samples with similar sizes. This research introduces an acoustofluidic employing a tilted-angle standing surface acoustic wave (taSSAW) for the label-free separation of microscale entities of comparable sizes based on their compressibility. The research findings indicate that Escherichia coli (*E. coli*) can be effectively separated from PLTs using this method. The acoustic radiation force induced by taSSAW on the relatively less compressible *E. coli* was greater than that exerted on the PLTs. Various analytical techniques, including fluorescence microscopy, scanning electron microscopy, hemocytometry, sodium dodecyl sulfate polyacrylamide gel electrophoresis, and polymerase chain reaction.

Methodology

Figure 1(a) shows the design of the acoustofluidic device, which consists of a pair of interdigital transducers (IDTs) positioned on a piezoelectric LiNbO$_3$ substrate. Figure 1(b) schematizes acoustofluidic separation of *E. coli* from PLTs. PDMS microchannel is affixed to the substrate at a 30° angle relative to the direction of flow and wave propagation. The microchannel features one central inlet for introducing sample fluids such as *E. coli* and PLTs, along with two sheath inlets to direct the sample flow away from the microchannel. The microchannel includes two outlets for the separate collection of target *E. coli* (Outlet 1) and non-target PLTs (Outlet 2).

In the presence of taSSAW, objects suspended in a medium exhibit movement towards pressure nodes and antinodes based on their positive and negative acoustic contrast factors (ACF) respectively. Despite similar sizes, the force exerted on these objects by the taSSAW-induced acoustic radiation force (ARF) can vary significantly depending on their compressibility within the taSSAW field.
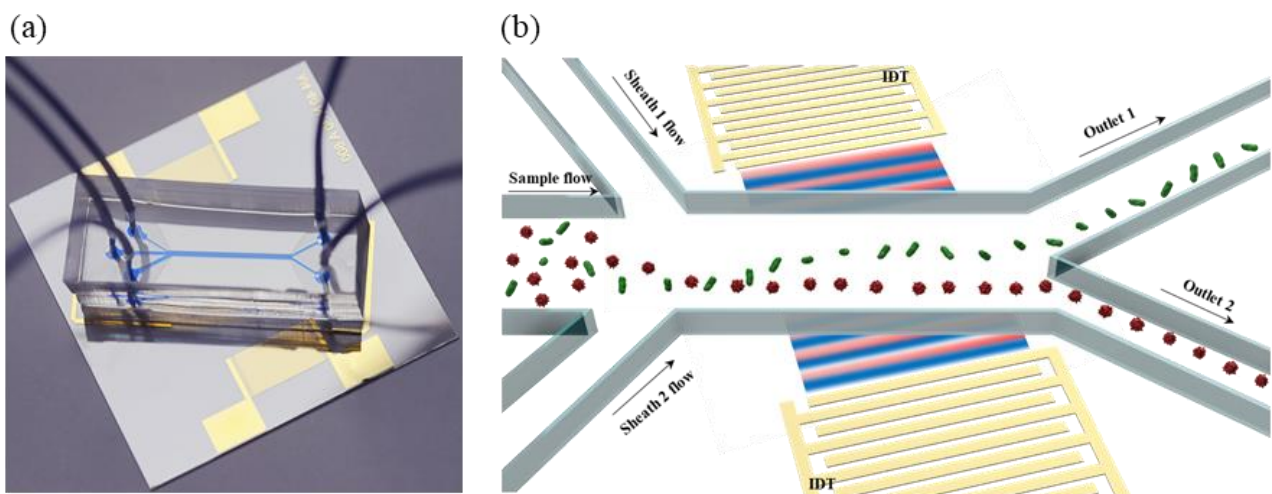
Figure 1: Microfluidic chip and schematic diagram utilizing tilted-angle standing waves for the acoustic separation of bacteria from platelets.

Results and Discussion

In our study, PLTs usually exhibit a spherical shape with an average diameter of around 2 μm, while *E. coli* typically displays a rod-shaped morphology, measuring approximately 2 μm in length and ranging from 0.25 to 1.0 μm in diameter. Despite their similar size and density, the elastic moduli have been reported to significantly differ. When the transverse acoustic surface wave (taSSAW) field was generated at a frequency of 24.8 MHz within the microchannel, distinct trajectories were observed for *E. coli* and PLT as depicted in Figure 2(a). This divergence in paths can be attributed to the varying magnitudes of the taSSAW-induced acoustic radiation force experienced by the two entities, which is influenced by their differing compressibility properties. The fluorescent microscopy was used to distinguish the trajectories of both types of bioparticles. As the trajectories of *E. coli* and PLTs diverge into two separate paths, they can be individually retrieved from the respective outlets. The taSSAW off, Both the *E. coli* (green) and PLTs (red) were observed to pass through the lower outlet. Upon the application of the taSSAW field, the *E. coli* were found to be influenced by the ARF, causing them to migrate towards the upper outlet, while the platelets maintained their original trajectories and continued to flow through the lower outlet. The study found that the compressibility of PLTs was greater than that of *E. coli*, resulting in the ARF generated by taSSAW being insufficient to displace the more compressible PLTs as they moved through the acoustic field. In contrast, the less compressible *E. coli* experienced a significant change in trajectory due to the taSSAW-induced ARF, causing them to move upwards and cross multiple pressure nodes within the acoustic field.

The results of the quantitative measurements depicted in Figure 2(b) demonstrate the successful separation of *E. coli* and PLTs within the proposed device, with *E. coli* and PLTs achieving purities of 96.55% and 94.44% in Outlet 1 and Outlet 2, respectively. The recovery rate was determined by assessing the discharged amount in relation to the initial concentration. *E. coli* displayed a recovery rate of 81.81% from the initial concentration, while PLTs exhibited a recovery rate of 91.89%. Despite the attainment of a high purity separation exceeding 95%, the bacterial recovery rate was relatively lower compared to that of PLTs, primarily attributed to bacterial adherence to the microchannel walls.
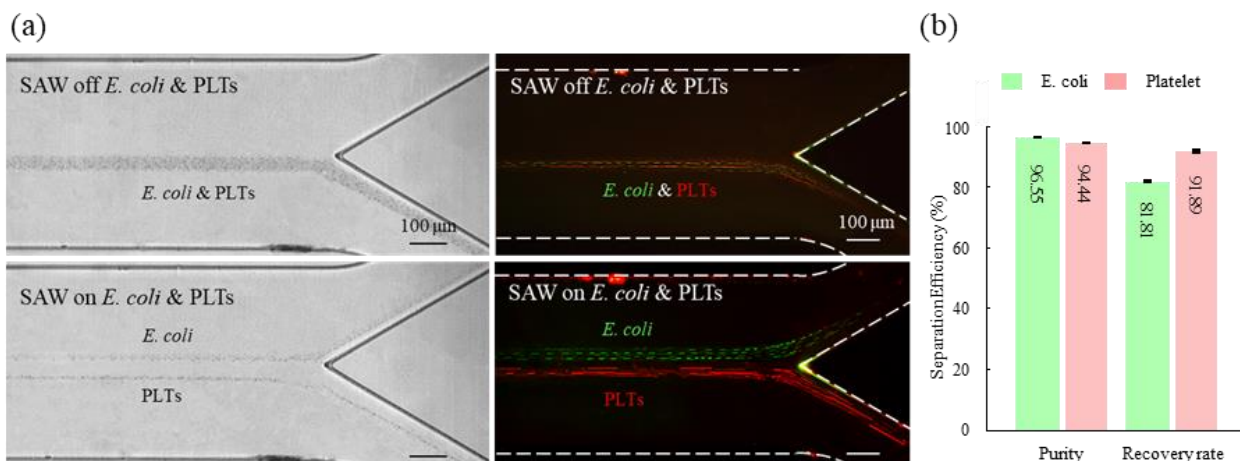
Figure 2: Images showing the separation of *E. coli* and PLTs in the (a) bright-field and fluorescence. (b) Graph of separation efficiency with purity and recovery rates of *E. coli* and PLT separation.

Conclusion

We have created an acoustofluidic technique that enables the separation of *E. coli* from platelets of similar size without the need for labeling. This method relies on the compressibility of the particles and utilizes the taSSAW-derived ARF to achieve high levels of purity and recovery rates. According to the results, it was shown that the *E. coli*, which are relatively less compressible, could be distinguished by ARF from platelets of similar size due to a significant variance in compressibility. The suggested acoustofluidic method for manipulating bacteria is anticipated to be applied in the identification and assessment of illnesses resulting from bacterial infections, such as endocarditis and sepsis.

Acknowledgements

References

[1] S. H. Lee, B. S. Cha, J. G. Ko, and J. Park, *Biomicrofluidics,* **17** 102410 (2023)
[2] S. Li, F. Ma, H. Vachman, C. E. Cameron, X. zeng, and T. J. Huang, *J. Micromech Microeng*, **27** 1(2017)

EchoGrid: High-throughput Acoustic Trapping towards Micro and Nanoplastic Monitoring

Martim Costa[1*], B Hammarström[2], Liesbeth van der Geer[1], Selim Tanriverdi[1], Haakan N. Joensson[1], M Wiklund[2] and A Russom[1,3]

[1] Division of Nanobiotechnology, Department of Protein Science, KTH Royal Institute of Technology, Science for Life Laboratory, Solna, Sweden

[2] Department of Applied Physics, KTH Royal Institute of Technology, Science for Life Laboratory, Solna, Sweden

[3] AIMES – Center for the Advancement of Integrated Medical and Engineering Sciences at Karolinska Institutet and KTH Royal Institute of Technology, Stockholm, Sweden

[*]E-mail: martim.costa@scilifelab.se

Introduction

Since their inception 70 years ago, plastics have become an essential material in human society and its industries, with their production projected to increase exponentially [1]. This can be attributed to the material's advantages in terms of versatility, low-cost, ease of manufacture and resistance to degradation, among others [2]. However, UV radiation, abrasions and improper disposal can lead to the circulation of microplastics into the environment, which may then degrade into nanoplastics. These contaminants have been found in remote ecosystems, in consumer goods [4], and in the human body [5]. This has raised serious questions regarding the potential danger of micro and nanoplastics to human health and highlighted the need for robust monitoring solutions at these size ranges [6]. Our work seeks to fill this need by developing an acoustofluidic device, the EchoGrid, designed to trap micro and nanoplastics at flow rates compatible with the high volumes usually found in environmental and drinking water samples. In this experimental study, we integrate a surface displacement transducer (SDT) with a PDMS microchannel to direct capture these analytes in a stable grid conformation. We have also developed a silica-enhanced seed particle method to allow for indirect capture of low concentration microplastics (10 and 23 µm) at even high flow rates (5 mL/min), which also works for the capture of 50-500 nm nanoplastics (5 mL/min).

Theory and Experimental procedure

The EchoGrid (**Figure 1**) is a device based on the fundamental principles of an acoustic trap and on surface resonance modes [7]. In brief, we maximize the lateral forces emerging from a milled slot in the transducer towards resisting high flow rates, which patterns particles into a grid. The primary acoustic radiation force pushes particles to the nodes and the second acoustic radiation force clusters them strongly. The combination of these two allows for robust direct and indirect (silica-enhanced seed particle method) capture.
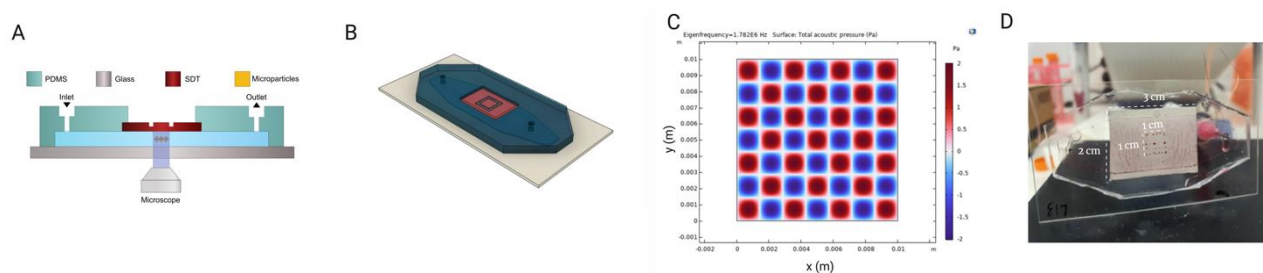
Figure 1: Schematics of the EchoGrid. (A) Side-view diagram. (B) Computer model of the assembly. (C) COMSOL Multiphysics simulation of the acoustic potential. (D) Grid patterning of 10 µm particles

Results and Discussion

After designing and fabricating the chip, its performance was evaluated by using fluorescent polystyrene (PS) beads and collecting the signal of their enrichment as they cluster over the SDT. Representative particles were used for this purpose (10 and 23 µm) at a high concentration (10^6 particles/mL). Two distinct flow rates were used, 20 and 200 µL/min (**Figure 2**).
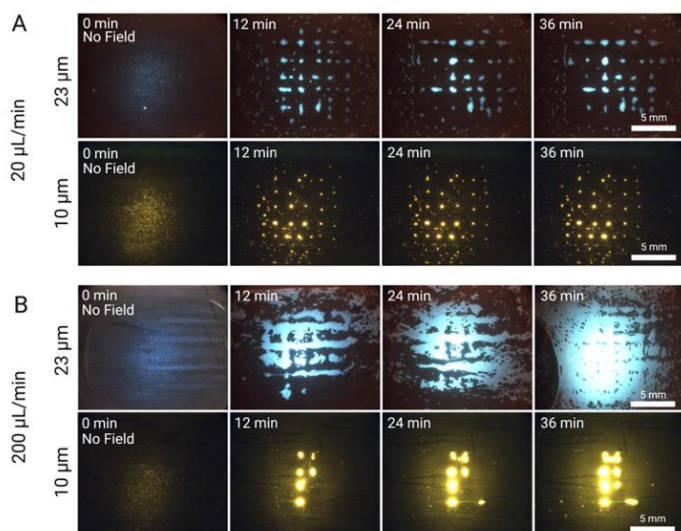
Figure 2: EchoGrid fluorescence images at 10^6 particles/mL (A) Performance of the device at 20 µL/min, with 10 (yellow) and 23 µm (blue) (B) Performance of the device at 200 µL/min, with 10 and 23 µm.
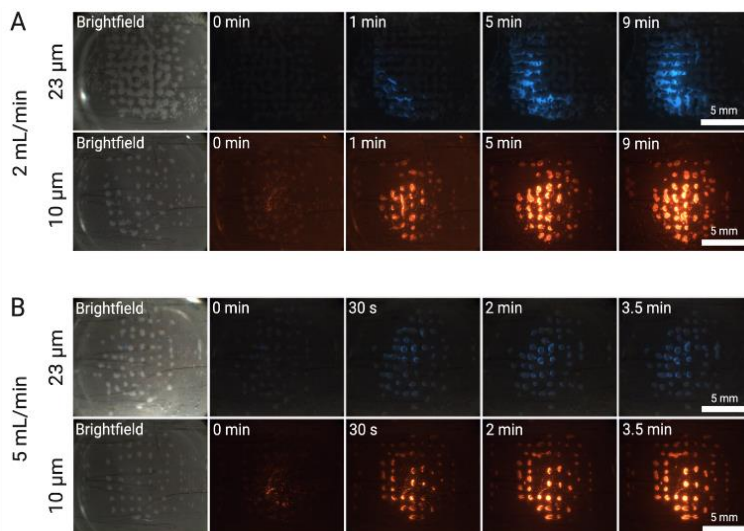
Figure 3: EchoGrid fluorescence images at 10^4 particles/mL using the silica-enhanced seed particle method (A) Performance of the device at 2 mL/min, with 10 (yellow) and 23 µm (blue) (B) Performance of the device at 5 mL/min, with 10 and 23 µm.

While we observed greater enrichment outcomes at higher flow rates, where there were more particles per unit of time, it was necessary to ensure this was the case for lower concentration solutions as well. Other experiments at 10^4 particles/mL showed that the system struggled to capture particles directly under these conditions. For this reason, we pre-seeded the trap with silica particles (able to be maintained up to a flow rate of 50 mL/min) and used these silica clusters as extra anchoring points that could compensate for the lower presence of microplastics in the sample. As a result (**Figure 3**), we observed fluorescence signal increasing in intensity in both particles sizes, even at 25× the original flow rate (200 µL/min to 5 mL/min) and at 100× lower particle concentration (10^6 particles/mL to 10^4 particles/mL). We have also used this method to enrich nanoplastics at various size ranges (50-500 nm) at flow rates of 5 mL/min.

Conclusion

The EchoGrid is an acoustofluidic device capable of capturing micro and nanoplastics at high flow rates. The combination of this platform with the silica-enhanced seed particle methods allows the enrichment of low concentration solutions at flow rates in the order of 5 mL/min, highlighting its potential as a high-throughput monitoring solution for these contaminants in consumer goods such as drinking water. This method of particle immobilization also has potential for integration with endpoint analysis and categorization of plastic type towards accurate policy and regulation of micro and nanoplastics.

Acknowledgements

References

[1] Geyer, Roland, et al. "Production, Use, and Fate of All Plastics Ever Made". Science Advances, vol. 3, n. 7, July 2017, p. e1700782.

[2] Andrady, Anthony L., and Mike A. Neal. "Applications and Societal Benefits of Plastics." Philosophical Transactions of the Royal Society B: Biological Sciences 364, no. 1526 (2009): 1977–84.

[3] Peeken, Ilka, et al. "Arctic Sea Ice Is an Important Temporal Sink and Means of Transport for Microplastic." Nature Communications, vol. 9, no. 1, Dec. 2018, p. 1505.

[4] Oßmann, Barbara E., et al. "Small-Sized Microplastics and Pigmented Particles in Bottled Mineral Water." Water Research, vol. 141, Sept. 2018, pp. 307–16.

[5] Ragusa, Antonio, et al. "Plasticenta: First Evidence of Microplastics in Human Placenta". Environment International, vol. 146, Jan. 2021, p. 106274. DOI.org

[6] McDevitt, Jason P., et al. "Addressing the Issue of Microplastics in the Wake of the Microbead-Free Waters Act—A New Standard Can Facilitate Improved Policy." Environmental Science & Technology, vol. 51, no. 12, June 2017, pp. 6611–17.

[7] Hammarström, Björn, et al. "Acoustic Trapping Based on Surface Displacement of Resonance Modes." The Journal of the Acoustical Society of America, vol. 149, no. 3, Mar. 2021, pp. 1445–53.

Reversing the acoustic contrast factor by tuning the medium can make focused beams trap cells in three dimensions

Shiyu Li[1], Zhixiong Gong[1,*]

[1]State Key Laboratory of Ocean Engineering, Key Laboratory of
Marine Intelligent Equipment and System, School of Ocean and Civil Engineering, Shanghai Jiao Tong
University, Shanghai, 200240, China
*E-mail: zhixiong.gong@sjtu.edu.cn

Introduction
Selective trapping of micro-particles and cells are essential to the field of biomedical analysis, for example, the mechanics measurement of a single cell. Single focused beam is a good candidate to achieve the three-dimensional (3D) trapping because of its simple wave structure and large gradient of intensity in three dimensions. However, the 3D trapping is challenging for focused beams since the acoustic contrast factor of typical human cells in water is generally positive [1]. Hence, an intuitive solution is to reverse the acoustic contrast factor to negative so that the cell could be trapped at the focus of a focused beam with the maximum intensity. In this work, we propose to use a cell-friendly medium (made of iodixanol with water) [2] to make the acoustic contrast factor negative for breast cancer cells (MCF-7). Based on the theory of 3D acoustic radiation forces in terms of the angular spectrum method, numerical simulations are implemented to demonstrate that it is possible to trap a selective MCF-7 cell in three dimensions in the iodixanol medium with a single focused beam.

Numerical model：Acoustic radiation force under a finite-aperture focused beam
An ideal spherical focused beam is truncated by a plane to obtain the two sets of equiphase electrodes, see the blue and red concentric circles on a wafer as shown in Fig. 1, which is used to design the miniaturized acoustical tweezer device. To achieve a 3D trapping, the particle or cell in the medium under the incidence of a focused beam should have the restoring force in all the directions. This is simply illuminated by the lateral and axial radiation forces which will push the particles or cells back to the focus, leading to a 3D trapping. The acoustic radiation force in a realistic acoustic field produced with finite aperture is calculated based on the angular spectrum method (ASM) as listed in Eq. (1) [1,3]. The coefficients in the set of formulas are given in details in Eq. (5) of Ref. [1].
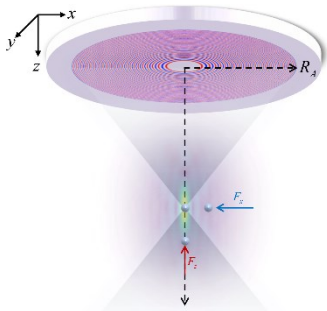
$$F_x = \frac{1}{4\pi^2 \rho_0 k^2 c^2} \mathrm{Re}\left\{\sum_{n=0}^{\infty}\sum_{m=-n}^{n} C_n\left(-b_{n+1}^{-m}H_{nm}H_{n+1,m-1}^* + b_{n+1}^{m}H_{nm}H_{n+1,m+1}^*\right)\right\}$$

$$F_y = \frac{1}{4\pi^2 \rho_0 k^2 c^2} \mathrm{Im}\left\{\sum_{n=0}^{\infty}\sum_{m=-n}^{n} C_n b_{n+1}^{m}\left(H_{n,-m}H_{n+1,-m-1}^* + H_{nm}H_{n+1,m+1}^*\right)\right\} \quad (1)$$

$$F_z = -\frac{1}{2\pi^2 \rho_0 k^2 c^2} \mathrm{Re}\left\{\sum_{n=0}^{\infty}\sum_{m=-n}^{n} C_n c_{n+1}^{m}H_{nm}H_{n+1,m}^*\right\}$$

Figure 1: Schematic diagram of the transducer to produce the focused acoustic field. The gray balls represent cells, and the red and blue concentric circles represent two sets of electrodes with opposite phases.

Results and Discussion
We calculated the 3D acoustic radiation forces of an MCF-7 cell in the iodixanol medium in and beyond the Rayleigh regime separately with the acoustic parameters are shown in Table 1. Due to the uncertainty of the sound speed of MCF-7 cells, we choose the average value for calculation, i.e., c_l=1530 m/s. The working frequency of transducer is f_0=40 MHz. The amplitude of the acoustic pressure in the source plane is set as p_0=1 MPa, and the cells are modeled as fluid spheres [1]. The transducer is designed using acoustic holography as a finite aperture planar sound source, making it convenient for fabrication. The aperture of the transducer is R_A=1.75mm and the focal length is h=1mm.

Table 1: Acoustic parameters of cell and medium

Material	Density (kg/m^3)	Sound speed (m/s)
MCF-7 [5]	1068	1490-1570
Iodixanol [2]	1319.7	1497.7

We consider the first case of 3D trapping in the Rayleigh regime with the ratio of the cell radius over the wavelength as a/λ=0.001. Since the cell size is much smaller than the wavelength, the acoustic radiation force

can be calculated using the classical Gor'kov theory [4], as shown in Figure 2. When taking the iodixanol solution as the medium, the Gor'kov potential U in the beam center is minimum which is opposite compared with that in water [1]. This leads to a restoring force under the corresponding acoustic radiation forces, which can achieve the three-dimensional trapping of MCF-7 cells.
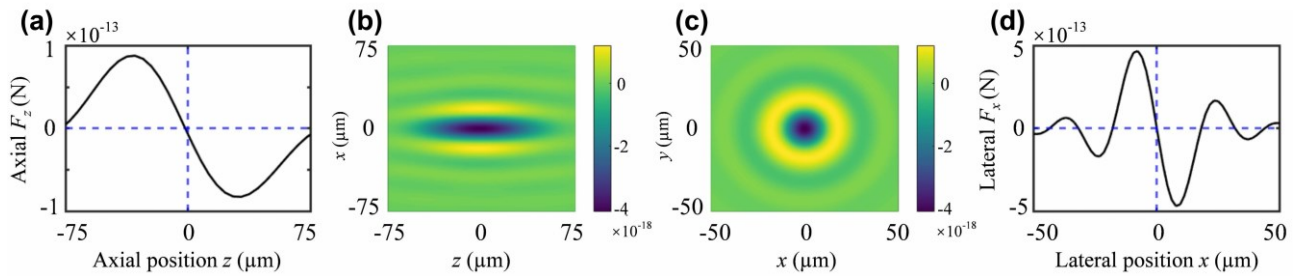
Figure 2: The Gor'kov potential U and the acoustic radiation force for a small MCF-7 cell in the 60% iodixanol medium. (a) and (d) are the variation curves of axial F_z and lateral radiation forces F_x versus spatial locations, respectively. (b) and (c) are the Gor'kov potential in the x-z plane and x-y plane, respectively.

Next, we take the general size into consideration for an MCF-7 cell with the ratio of a/λ up to 1. The 60% iodixanol solution is used as the surrounding medium. As shown in Figure 3(a) and 3(b), both the axial and lateral acoustic radiation forces are negative at $a/\lambda=0.41$. This may ensure a 3D trapping. To further demonstrate the 3D trapping of an MCF-7 cell in the iodixanol medium, we study the axial (Figure 3(c)) and lateral acoustic radiation forces (Figure 3(d)) acting on the cell as a function of distance at $a/\lambda=0.41$, respectively. It can be found that both the axial and lateral acoustic radiation force can push MCF-7 cells that deviate from their equilibrium position back to the trapping spot. Hence, the 3D trapping of an MCF-7 cell in the iodixanol medium is possible beyond Rayleigh regime, which can not be achieved in the medium of water as shown in Ref. [1].
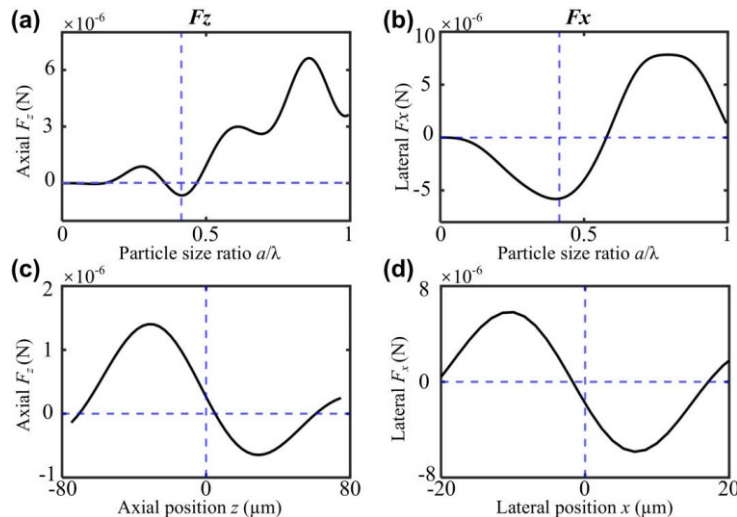
Figure 3: The axial and lateral acoustic radiation forces of cells beyond the Rayleigh regime in the 60% iodixanol medium.

Conclusion
In general, the single focused-beam acoustic tweezers cannot achieve the three-dimensional trapping of MCF-7 cells in the medium of water, neither in nor beyond the Rayleigh regime. In this study, we show that by adding one kind of cell-friendly mediums called iodixanol solution, the three-dimensional trapping of MCF-7 cell both in and beyond the Rayleigh regime can be achieved. This is very inspiring to use a simple focused beam for 3D trapping of typical human cells and may be extended for 3D patterning of cells in space like the precise assembly of atoms in the array of optical tweezer.

References
[1] Z. Gong, and B. Michael, Phys. Rev. Appl., **18** 044033 (2022).
[2] P. Augustsson, et al. Nature commun., 7 11556 (2016).
[3] O. A. Sapozhnikov, and R. B. Michael, J. Acous. Soc. Am., **133** 661 (2013).
[4] L. P. Gor'kov, Sov. Phys.-Doklady, **6**. 773 (1962).
[5] K. E. Cushing, et al. Analytical Chemistry, **89** 8917 (2017).

Simultaneous fluorescence and absorbance signal sorting of microfluidic droplets using traveling surface acoustic waves (TSAW)

Esther S. Richter[1], Andreas Link[1], Raymond W. Sparrow[1] and Thomas Franke[1,*]

[1]Division of Biomedical Engineering, School of Engineering, University of Glasgow, Glasgow, UK
[*]E-mail: thomas.franke@glasgow.ac.uk

Introduction

Microfluidic droplet sorting is a well-established technique in biotechnology, used for various applications s such as directed evolution and drug screening [1,2]. While fluorescence detection is common [2], there is a demand for label-free sorting techniques to enhance screening capabilities [2,3]. Leveraging molecule absorption properties provides a solution, offering better quantifiability than fluorescence [2]. Previous studies showed simultaneous detection of multiple signals, such as fluorescence, absorbance, and scattering [3,4], as well as sorting using dielectrophoresis of multiple signals with low droplet rates (200Hz) [4]. Droplet microfluidics enables rapid screening and sorting of droplets with low sample volumes [1]. Using traveling surface acoustic waves (TSAW), droplets are sorted by a generated change in the streaming inside channel, meaning we do not require responsive particles, magnetic or dielectric labelling [1]. Acoustic sorting has further been proven to be less harmful to cells [1]. We have previously presented an absorbance-based droplet sorting device for label-free sorting at high throughput rates [5] and have now combined this device with established fluorescence detection methods to enable simultaneous sorting of fluorescence and absorbance droplets at kHz rates. We present the sorting of different fluorescent and absorbent dye filled droplets as well as sorting between two E. coli strains.

Methods

Our dual signal sorting device consists of a tapered IDT (TIDT) on piezoelectric LiNbO3 substrate and PDMS micro-channels. The detection of absorbance and fluorescence happens simultaneously. Our previously reported optic fibre with lenses and LED setup [5] is used for absorbance detection, whereas a laser and PMT combination detects fluorescence, see Figure 1.
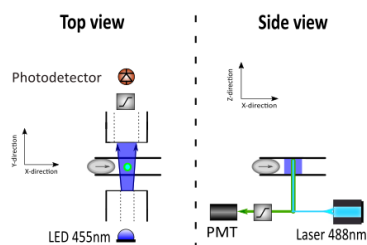
Figure 1: Schematics of the optical detection setup for absorbance and fluorescence signal detection in a microfluidic sorting device. Optical fibers are integrated into the PDMS device and are used to detect absorbance by being coupled into an LED for illumination and a photodetector for detection. Fluorescence is detected using a laser and PMT setup where a laser is focused into the channel and excites the droplets. A photomultiplier tube (PMT) detects the emission.

One optic fibre is connected to an LED (455nm) and illuminates the droplets continuously and a second one attached to a photodetector detects a voltage signal. A laser (488nm) is coupled into the channel from below, exciting the fluorescence which is detected by a photomultiplier tube (PMT). Bandpass filter at both the PMT and photodetector ensure that only either the emitted fluorescence, or the absorbance wavelength are detected. The laser spot needs to be positioned in the path of the LED light beam to avoid time delay between the two signals. Both signals are measured as voltages and analyzed in LabVIEW software. We set threshold conditions for both the absorbance and fluorescence signal. The droplet that fulfills the conditions for both signals causes the acoustics to trigger with a set delay time to deflect the target droplet. We used an operating frequency of 162MHz and 24dBm power to sort droplets with kHz rates. The absorbance signal presents as valleys the signal, the signal for the oil is set to 8V, whereas the fluorescence droplet signals are upwards peaks with a baseline around 0V (0.65V gain PMT, laser 7mW). For simpler overlay we invert the absorbance signal and offset the baseline to coincide with the fluorescence signal baseline, thus droplets then show as peaks in the signal.

We produced a droplet mixture containing four different colorimetric and fluorescent dyes (50μM tartrazine, 50μM fluorescein, 1mM brilliant black, 50μM fluorescein with 1mM brilliant black) resulting in two fluorescent peak populations and two absorbance peak populations, see Figure 2 A. Using these dyes allows the visual distinction in a microscope video. The brilliant black droplets appear black, whereas the tartrazine and fluorescein appear transparent. Droplets were produced in a flow focusing device in HFE Novec 7500 (3M) and 1.8% FluoSurf surfactant (Emulseo). In a second experiment we encapsulated two different E. coli strains (Bl21de3 and ATCC-25922GFP) in LB medium and incubated them for 6 hours at 37℃. ATCC-25922GFP cells produce the fluorescent protein GFP. We then sort the droplets filled with cells that produced

fluorescent protein GFP and a high cell density (absorbance). Droplets filled with cells show a higher absorbance signal than empty droplets.

Results and Discussion

In the first sorting experiment we set the sorting for two different droplet populations, one for the fluorescein with brilliant black droplets using the condition that both the higher absorbance and higher fluorescent peak need to be detected to trigger the sorting, see Figure 2 A and B. For the second population the values are set to trigger the droplets containing only brilliant black, excluding all droplets that have a fluorescent signal. These settings result in the droplets containing brilliant black with fluorescein as well as the ones only containing brilliant black to be sorted. Sorting using two signals works reliably up to 1.5 kHz droplet rates.
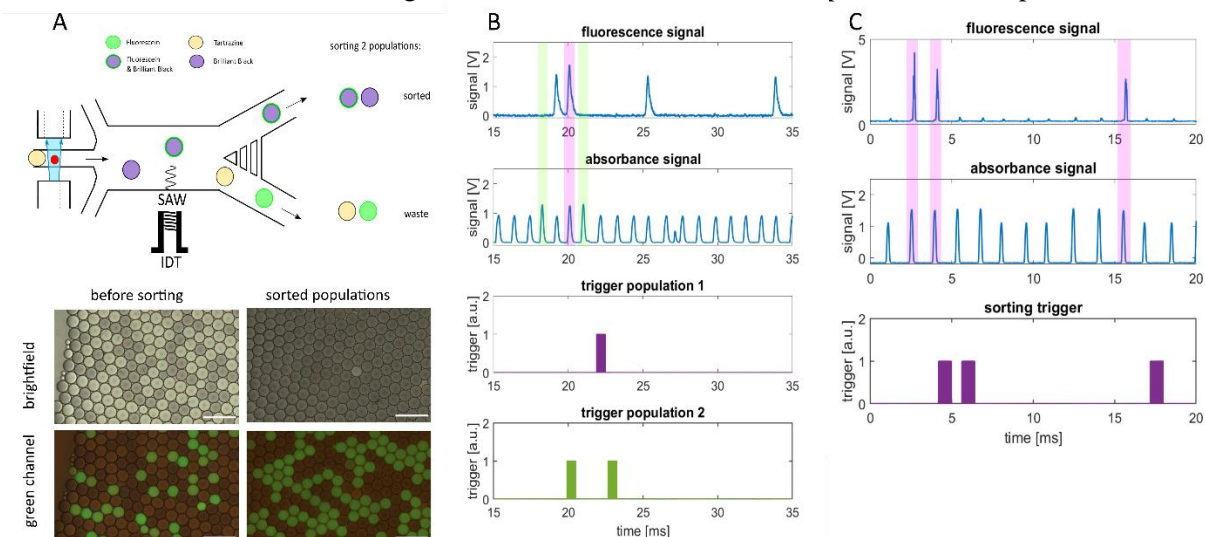
Figure 2: A: Schematic depicting the sorting of absorbent and fluorescent dye filled droplets. Images showing bright field and fluorescent images of the droplet mixture before and after sorting, scale bar 250μm. B: Graphs showing the fluorescence and absorbance signals as well as sorting trigger for the sorting experiment were fluorescein with brilliant black droplets and brilliant black droplets are sorted. Two brilliant black droplets are detected and the sorting of them is triggered (green trigger population 2). One droplet peak shows higher fluorescence and absorbance, triggering the sorting of the droplets that contains fluorescein with brilliant black (purple trigger population 1). C: Graphs showing the fluorescence and absorbance signals, as well as sorting trigger for the sorting experiment of bacteria filled droplets. Three fluorescent peaks are detected in this signal sequence caused by E.coli growth induced GFP production. These droplets have a higher absorption value due to cell growth and fluorescence due to GFP production.

Bacteria growth in droplets can be measured using the absorbance signal. The higher cell density blocks the light which cause a higher absorbance signal. The fluorescent signal shows a peak solely for the droplets filled with the GFP producing strain. We set the sorting parameters to sort for droplets with a fluorescence signal, and a higher absorption. This ensures only droplets filled with ATCC-25922GFP are sorted, see Figure 2 C. This way we guarantee that only cells that grew and produced GFP inside the droplets are sorted and droplets in which growth was inhibited or limited, but produced some fluorescence are excluded. The absorbance signal is used to measure cell growth inside the droplets and the fluorescence signal to measure protein production. This system enables us to sort for the fastest growing and most protein producing cells by setting the sorting values for the highest peak values.

Conclusion

Combining existing absorbance and fluorescence detection methods allows us to sort droplets with two signals as conditions to trigger the acoustic sorting at kHz rates. We show successful sorting for dye filled droplets as well as sorting between two different E. coli strains. This system has the potential for cell viability, antibiotic resistance, strain separation and directed evolution studies that require two parameters for differentiation.

Acknowledgements

References

[1] L. Schmid, D.A.Weitz and T. Franke. Lab on a Chip 19, 3710-3718 (2014).
[2] S. Hengoju, S. Wohlfeil, A. S. Munser, S. Boehme, E. Beckert, O. Shvydkiv, M. Tovar, M. Roth and M. A. Rosenbaum. Biomicrofluidics 14, 2 024109 (2020).
[3] T. Yang, S. Stavrakis, and A. DeMello Anal. Chem. 2017, 89, 23, 12880–12887
[4] J. Panwar, A. Autour, CA. Merten. Nat Protoc. 2023 Apr;18(4):1090-1136
[5] E.S. Richter, A. Link, J.S. McGrath, R.W. Sparrow, M. Gantz, E.J. Medcalf, F. Hollfelder and T. Franke Lab Chip, 2023,23, 195-202

Relaxation to frozen mode transition of viscoelastic fluids under ultrasound: effects on particle transport

T Sujith[1,*], Lokesh Malik[1], and Ashis Kumar Sen[1]

[1]Micro Nano Bio Fluidics Unit, Department of Mechanical
Engineering, Indian Institute of Technology Madras, Chennai-600036, Tamil Nadu, India
[*]E-mail: sujitht996@gmail.com

Introduction

Bio-fluids are crowded suspensions of cells and bio-particles and are extremely diverse. These fluids, such as blood, saliva, sputum, and synovial fluid exhibit viscoelastic properties due to the presence of various cells, structural proteins, and other macromolecules [1]. Among various microfluidic techniques, acoustofluidics has emerged as a promising method for manipulating cells and particles in these fluids for medical diagnostics [2]. Even though earlier studies involve the use of complex bio-fluids, prevailing modeling techniques often oversimplify by presuming Newtonian characteristics, thereby disregarding their inherent viscoelastic properties. To address this gap, we conduct a comprehensive study by investigating the behavior of viscoelastic fluids and suspended particles under the influence of a standing bulk acoustic wave (S-BAW) using numerical simulations, theory, and experiments. Our study investigates the effect of viscoelastic parameters: μ^* (ratio of viscosity of the viscoelastic fluid to the base Newtonian fluid) and De ($= \tau\omega$, product of relaxation time of fluid and angular frequency of actuation) on the acoustic force parameters, which governs the particle migration dynamics. We classify ultrasound responses of fluids into three categories with the transition from viscous to elastic behavior, based on De and α (ratio of dimensionless viscous shear wavelength to acoustic boundary layer thickness, $\lambda_{ve}^*/\delta_{ve}^*$), where the fluid transits from an energy dissipation state, i.e. relaxation mode to an energy storage state, i.e. frozen mode. Further, we examine the effects of this transition on particle migration by decoupling the elastic effects from viscous effects. Our findings reveal that while viscous effects decelerate acoustic particle migration, the elastic effects tend to accelerate the migration process. We observe that acoustic particle migration in viscoelastic fluids is faster than in Newtonian fluids of identical viscous properties. We validate our theoretical and numerical findings, with experimental data and find a very good agreement. Our study could find significance in understanding migration of cells, and extracellular vesicles in bio-fluids.

Methodology

We consider a Glass-Silicon-Glass acoustofluidic chip with a microchannel of dimensions 400 µm×300 µm×20 mm ($W×D×L$). The particles are suspended in a viscoelastic fluid and introduced to the microchannel and the chip is excited by a 2 MHz transducer-signal generator and power amplifier assembly. A 3D and top view of the channel is shown in Fig.1. Here a 1D standing wave is generated along the width of the channel (y-axis) and we numerically explore the response of quiescent viscoelastic fluids to S-BAW by solving the modified perturbations equations across the cross of the channel (y-z plane). Later we relate it with the acoustic energy density (AED) of the fluid. Further, we investigate the effects on particle migration dynamics by theoretically modifying the expression for acoustic radiation force (ARF) using first-order scattering theory [3] and the derived expressions for particle trajectory and velocity as follows

$$y(t) = \frac{1}{k_y}\arctan\left\{\tan[k_y y(0)]\exp\left[\frac{4\Phi(\bar{\kappa},\bar{\rho},\delta_{ve}^*,\lambda_{ve}^*)(k_y a)^2 E_{ac}(\mu^*,De)\,t}{3\mu\xi}\right]\right\} \tag{1}$$

$$V_P = \frac{2\Phi(\bar{\kappa},\bar{\rho},\delta_{ve}^*,\lambda_{ve}^*)k_y a^2 E_{ac}\sin(2k_y y)}{3\mu\xi} \tag{2}$$

To validate our theoretical and numerical findings, we conduct experiments using Polyvinylpyrrolidone (PVP) and Polyethylene oxide (PEO) powder in deionized water (DI) with Polystyrene beads of diameter($2a$) 15 µm.
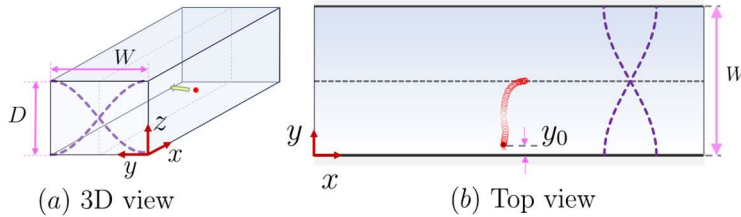
Figure 1: Physical domain used in the problem formulation, (a) 3D view (b) top view of the microchannel with particle suspended in viscoelastic fluid, starting position of the particle in the channel is y_0. The channel is exposed to a 1D standing wave (along the y-axis, shown by dashed violet lines) operating at the first harmonic mode, i.e., half-wave mode.

Results and Discussion

Under S-BAW, a viscoelastic fluid experiences perturbations, as depicted in Fig. 2 (a)-(d), showing variations of first-order pressure (p_1^*) and velocity (v_1^*) along y^* ($y/w/2$) and z^* ($z/w/2$). These variations result in three distinct behaviors under different De, characterized by α ($\lambda_{ve}^*/\delta_{ve}^*$) as shown in Fig. 2 (e). In Class A ($De \ll$

1, $\alpha > 1$), representing viscous behavior, first-order fluid velocity oscillations are less, and pressure amplitude is lower with a moderate boundary layer thickness, where stress relaxation is faster than t_f ($= 1/\omega$, $\tau \ll t_f$). Class B (Intermediate De, $\alpha < 1$) marks a transition from viscous to elastic behavior with increased velocity oscillations and higher-pressure amplitude, accompanied by a thicker boundary layer. Class C ($De \gg 1$, $\alpha > 1$) indicates elastic behavior with reduced velocity oscillations, high-pressure amplitude, and a thin boundary layer, where stress relaxation is slower than t_f ($\tau \gg t_f$). The changes in first-order fields with elasticity of the fluid affect the AED, where fluid transforms from an energy dissipation state (relaxation mode) to a storage state (frozen mode- energy dissipation is frozen) with De, shown in Fig. 2 (e), which in turn changes the ARF.
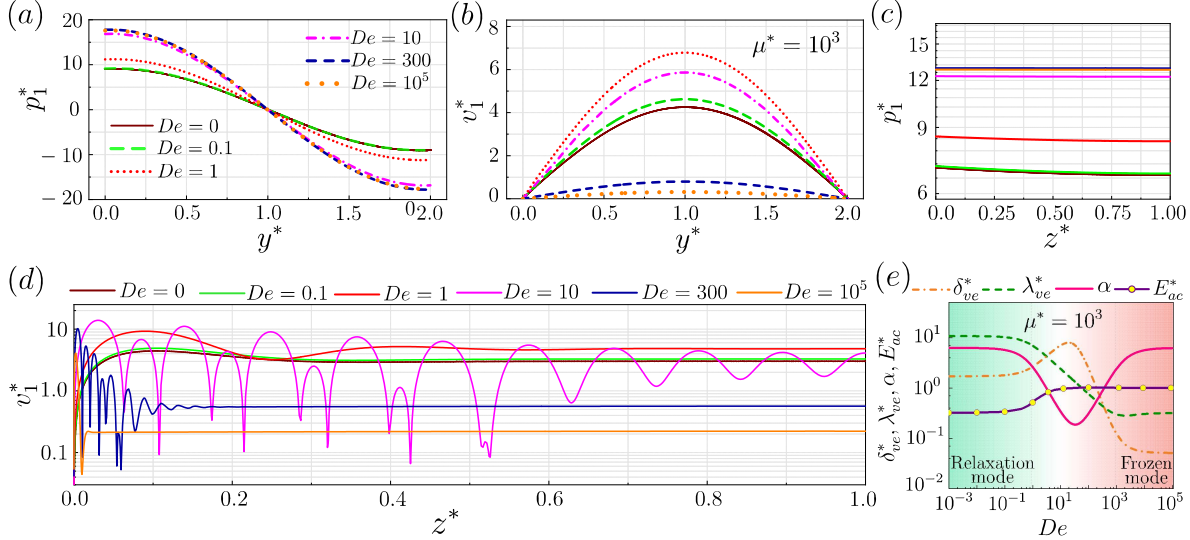
Figure 2: Variation of p_1^* and v_1^* fields in Newtonian ($De = 0$) and viscoelastic fluid ($De = 0.1, 1, 10, 300, 10^5$) at $\mu^* = 1000$, $\mu_s^* = 1$, $\mu_p^* = 999$, $\rho^* = 1$ and $c^* = 1$,(a) p_1^* along y^*,(b) v_1^* along y^*,(c) p_1^* along z^*, (d) v_1^* along z^*. Variation of (e) $\delta_{ve}^*(\delta_{ve}/a)$, $\lambda_{ve}^*(= \lambda_{ve}/a)$, α ($= \lambda_{ve}^*/\delta_{ve}^*$), and $E_{ac}^*(= E_{ac}/E_{ac}^{bf})$ with De.
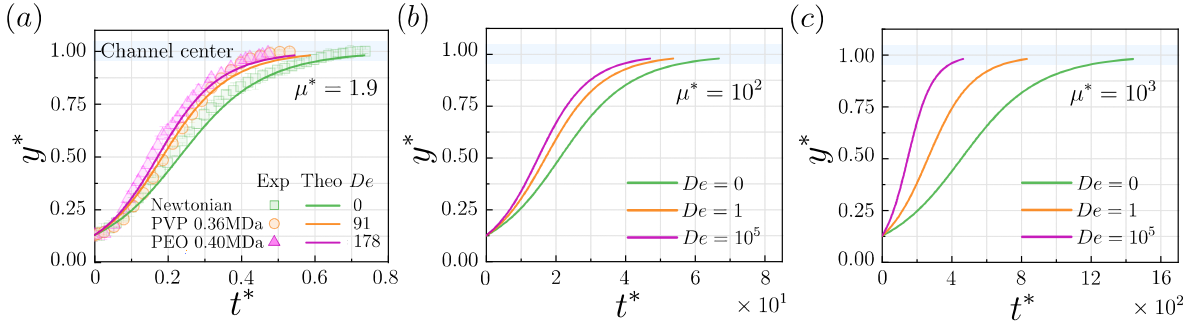
Figure 3: Comparison of theoretical and experimental variation of a particle in PEO 0.4 MDa, PVP 0.36 MDa, and Newtonian (DI Water+0.3% Glycerol) fluid of constant viscosity (a) at $\mu^* = 1.9$. Theoretical variation of Normalized particle trajectory at different De ($De = 0, 1, 10^5$) for (b) $\mu^* = 10^2$ (c) $\mu^* = 10^3$.

The ARF induces particle migration towards the channel center, as illustrated in Fig. 3. To isolate elastic effects, we match the viscosities of Newtonian and viscoelastic fluids while keeping the density and speed of sound constant. Experimental results in Fig. 3(a) show that, with a fixed μ^*, increasing elastic effects (De) enhances particle migration velocity and reduces the migration time due to increased AED and ARF with elasticity, where fluid shows a transition from relaxation mode to frozen mode as shown in Fig. 2 (e) (Class A to B and then to C). Remarkably close agreement between theoretical predictions (Eqn. 1, 2) and experimental results is observed in Fig. 3 (a). In Fig. 3(b) and (c), we extend the effect of varying De on particles for other μ^* values. These findings highlight the importance of understanding and controlling both the viscosity and elasticity of viscoelastic fluids under ultrasound.

Conclusion
We classify the response of a viscoelastic fluid to an ultrasound field into three categories, Class A, B, and C, where the fluid transforms from an energy dissipation state (relaxation mode) to a storage state (frozen mode) with elasticity (De). Our investigation successfully decouples the effects of viscosity and elasticity, the elastic effects of the fluid accelerate and viscous effects retards the particle migration. Moreover, the acoustic particle migration in viscoelastic fluid is faster than in Newtonian fluid with similar viscous properties.

References
[1] M. Brust et al. *Phys. Rev. Lett.* 110, 078305 (2013).
[2] T. Laurell, F. Petersson and A. NilssonO. *Chem. Soc. Rev.* 36, 492-506 (2007).
[3] M. Settnes and H. Bruus *Physical Review E* 85, 016327 (2012)

Acoustofluidic platforms for tomography of biological samples by rotational manipulation

Mia Kvåle Løvmo[1,*], Shiyu Deng[2], Simon Moser[1], Franziska Strasser[1], Wolfgang Drexler[2] and Monika Ritsch-Marte[1]

[1]Institute of Biomedical Physics, Medical University of Innsbruck, Innsbruck, Austria
[2]Center for Medical Physics and Biomedical Engineering, Medical University of Vienna, Vienna, Austria
[*]E-mail: mia.kvale@i-med.ac.at

Introduction

Along with model-organisms, 3D *in vitro* models, such as spheroids and organoids, provide valuable insight into fundamental biological processes and human pathology. The current methods to handle and image these samples are limited and often rely on immobilization in hydrogels and invasive analysis techniques because mature samples are often too opaque for standard phase contrast or fluorescence microscopy. Access to the 3D structure and refractive index (RI) distribution of biological samples offer valuable insight into their morphology, composition and function [1,2], and both non-invasive handling and imaging is crucial to enable long-term monitoring of live and developing tissues. To provide a solution offering both biocompatible manipulation and tomographic reconstruction of biological samples, we have developed acoustofluidic platforms compatible with Optical Diffraction Tomography (ODT) and Optical Coherence Tomography (OCT). To collect multi-angle data, we induce rotations of the sample by generating acoustic torques. Along with our developed reconstruction algorithms to fuse the multi-angle data from *a priori* unknown illumination angles, our approach demonstrates 3D reconstruction of biological samples from single cells to millimeter-sized model-organisms at an enhanced angular coverage and penetration depth compared to illumination scanning ODT and standard OCT imaging.

Theory and Experimental procedure

We couple Bulk Acoustic Waves (BAWs) in two to three orthogonal directions into a fluid-filled chamber that acts as a resonator and generates standing waves for manipulating suspended samples. The geometry of the acoustic platforms is optimized for controlling the strength of the acoustic restoring (radiation) torque and the acoustic spinning torque. While the restoring torque is an effect of acoustic radiation forces acting in individual parts of an extended object to align it to the incident field, the spinning torque can be generated in orthogonal acoustic waves resulting in a vortex field around the particle. The spinning torque includes the effects from acoustic dissipation in the viscous boundary layer and potentially due to absorption in the particle itself [3,4]. To collect tomographic data, we induce sustained object rotations or stepwise reorientations optimal for single-shot or scanning-based imaging, respectively.

For the combination with ODT, which is suitable for high resolution RI reconstruction of single cells and small clusters, we developed the platform shown in Figure 1a [5]. This platform is compatible with high NA illumination and hence suitable for collecting data by angle scanning at multiple stable object orientations or for collecting complex field measurements while inducing sustained object rotation. The three orthogonal transducers are made of optically transparent lithium niobate and the channel lengths are tuned to support orthogonal modes at the same MHz frequency in the vertical and one horizontal direction for inducing rotations orthogonal to the imaging axis.
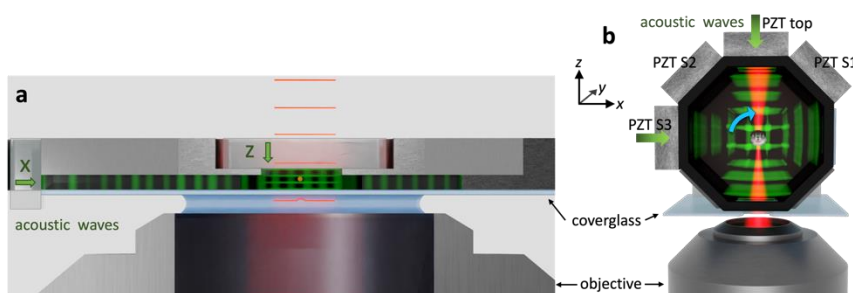
Figure 1: Schematics of the microfluidic chips and the experimental setups. **a)** shows a cross-section of the aluminium-based platform compatible with optical transmission imaging and ODT. **b)** shows a platform based on a 3D printed polymer-frame suitable for OCT imaging. Acoustic waves in green color and imaging light in red. Figure by M. Kvåle Løvmo adapted from [5,6].

OCT can offer a high penetration depth of 1-2 mm in tissue and an excellent optical sectioning, which makes it suitable for imaging larger samples at a resolution of a few μm. OCT is based on low-coherence interferometry where 3D images are generated by raster-scanning the laser beam across the sample while collecting depth information at each point. The platform especially designed for the combination with OCT is shown in Figure 1b [6]. The sample chamber has an octagonal cross-section with 4 transducers and 4 reflectors around the sides. We induce reorientations around the samples major axis by controlling the strength of the acoustic radiation forces between the four transducers in a sequence, or by controlling the relative phase and voltage between only the vertical and its orthogonal transducer. The Lead zirconate titanate (PZT) transducer at 0.6 MHz were chosen to trap samples up to millimeters in size, and the trapping in the center of the large chamber eliminates unwanted back-reflections from coverslip and transducers in the OCT signal.

Results and Discussion

While our non-contact manipulation offers a biocompatible handling of the samples, the price to pay is that the exact illumination angles are *a priori* unknown and need to be recovered to reconstruct the samples. We tackle this problem in our model-based reconstruction algorithms where we fuse the multi-angle ODT or OCT data in a physically consistent manner. Based on complex field data collected by inducing sustained rotations of single cells, also around orthogonal object axes, we demonstrate an enhanced angular coverage allowing for precise and quantitative 3D RI reconstructions. ULtrasound-Induced reorientation for Multi-Angle OCT (ULTIMA-OCT) is a novel strategy and the stepwise rotation of levitated samples to stable orientations 360° around the major axis enables 3D reconstruction with isotropic resolution. We demonstrate enhanced penetration depth in the joint 3D-recovery of reflectivity, attenuation, RI, and position registration for millimeter-sized zebrafish larvae.
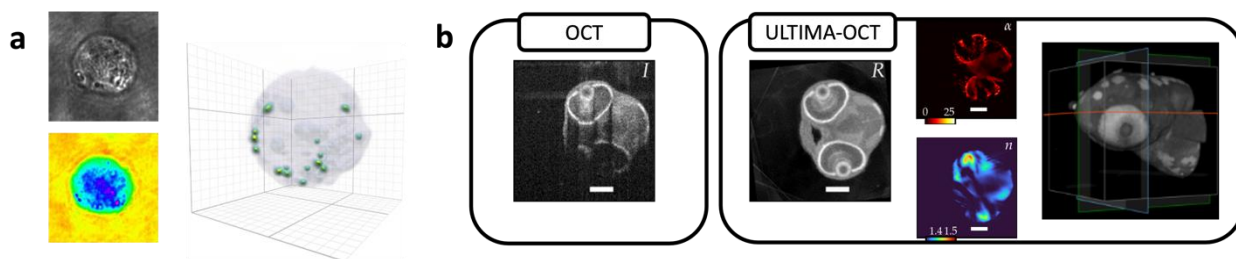
Figure 2: 3D reconstructions based on optical tomographic data collected by acoustically induced object rotations. **a)** shows intensity and phase images of a 12 μm sized neuroblastoma cell under sustained rotation, as well as a 3D RI reconstruction. **b)** shows a comparison between OCT imaging from a single direction and a reconstruction based on multi-angle data with a cross-section of a zebrafish larvae. In addition to the enhanced penetration depth and detail in the 3D reconstruction of reflectivity, the ULTIMA-OCT approach also recovers the attenuation and RI maps. Scalebar: 100 μm. Adapted figure from [6] by S. Moser.

Conclusion

Our acoustofluidic platforms enable non-invasive handling of samples and compatibility with a range of imaging modalities. The rotational manipulation provides an efficient means of collecting multi-angle data to improve the precision and penetration depth in tomographic reconstruction. Our reconstruction algorithms provide a powerful tool for reconstructing samples rotated in any non-contact system where uncertainty of the rotation parameters is inevitable. In total our strategy creates an enabling tool for future applications in microscopic 3D imaging and long-term monitoring of developing cells, organisms and organoids.

Acknowledgements

References

[1] D. Jin et al., *Tomographic phase microscopy: principles and applications in bioimaging,* (JOSA 2017)

[2] K. C. Zhou et al., *Computational 3D microscopy with optical coherence refraction tomography*, (Optica 2022)

[3] A. Lamprecht et al., *Viscous torque on spherical micro particles in two orthogonal acoustic standing wave fields,* (JASA 2015)

[4] D. Baresch et al., *Orbital angular momentum transfer to stably trapped elastic particles in acoustical vortex beams,* (PRL 2018)

[5] M. Kvåle Løvmo et al., *Acoustofluidic trapping device for high-NA multi-angle imaging*, (Front. Phys. 2022)

[6] M. Kvåle Løvmo et al., *Ultrasound-induced reorientation for multi-angle optical coherence tomography*, (Nat. Commun. 2024)

Influence of dielectrophoresis on spherical and non-spherical particles in a standing surface acoustic wave field

Sebastian Sachs[*], Christian Cierpka, and Jörg König

Institute of Thermodynamics and Fluid Mechanics, Technische
Universität Ilmenau, Ilmenau, Germany
[*]E-mail: sebastian.sachs@tu-ilmenau.de

Introduction

The systematic manipulation of suspended micro particles using standing surface acoustic waves (sSAW) is typically predicated on leveraging acoustic phenomena ranging from scattering effects at suspended particles to acoustically induced fluid flows [1]. However, the sSAW is inherently accompanied by an inhomogeneous electric field that couples into the fluid domain of the acoustofluidic device [2]. Hence, the behavior of polarizable particles is additionally affected by dielectrophoresis, which is less explored in sSAW-based devices. In this study, experimental and numerical investigations are combined to shed light on the physical mechanisms underlying the positioning and orientation of spherical and non-spherical particles in an acoustoelectric wave field. By screening the electric field locally using a thin metal layer deposited on the surface of a piezoelectric substrate, the dielectrophoretic impact on the particles can be revealed experimentally. In this way, particles are levitated near the substrate surface in the non-screened region, while they are pushed downwards in the screened region. The impact of dielectrophoresis extends not only to the positioning of focused particles but further affects the unintuitive orientation of prolate spheroids perpendicular to the pressure nodes of the sSAW recently reported [3]. By utilizing a developed 3D numerical model, complementary effects of the acoustic and dielectrophoretic torque for the orientation of the non-spherical particles are revealed, which match the experimental observations. The numerical model promises large progress in the precise prediction of the particle behavior in complex acoustoelectric wave fields.

Methods

The acoustofluidic device used consists of two opposing interdigital transducers (IDTs) to excite an sSAW with a wavelength λ_{SAW} on a substrate of 128° YX LiNbO$_3$ (see Fig. 1a). A thin metal layer (10/10 nm Cr/Au) is deposited centrally between the IDTs, covering half the aperture AP of the IDTs. Located on top of the substrate is a micro channel made of polydimethylsiloxane (PDMS) with a cross-section of $500 \times 180~\mu m^2$ and one inlet and outlet. Particles suspended in aqueous glycerol solution (24% v/v) were pumped through the channel at a flow rate of 1 µl/min using a syringe pump (neMESYS, cetoni GmbH). The acoustofluidic device was mounted on top of an inverted fluorescence microscope (Axio Observer 7, Zeiss GmbH) to observe the particle behavior. The propagation of the acoustic waves and the electric field was calculated with a 3D numerical model including the piezoelectric substrate, the fluid and PDMS domain. Once calculated using the full model, the mechanical displacement and electric potential were used as boundary conditions at the substrate-fluid interface in reduced models comprising only the micro channel. To correctly integrate the acoustic and dielectrophoretic torque, a non-spherical particle was modeled as a solid domain within the fluid.
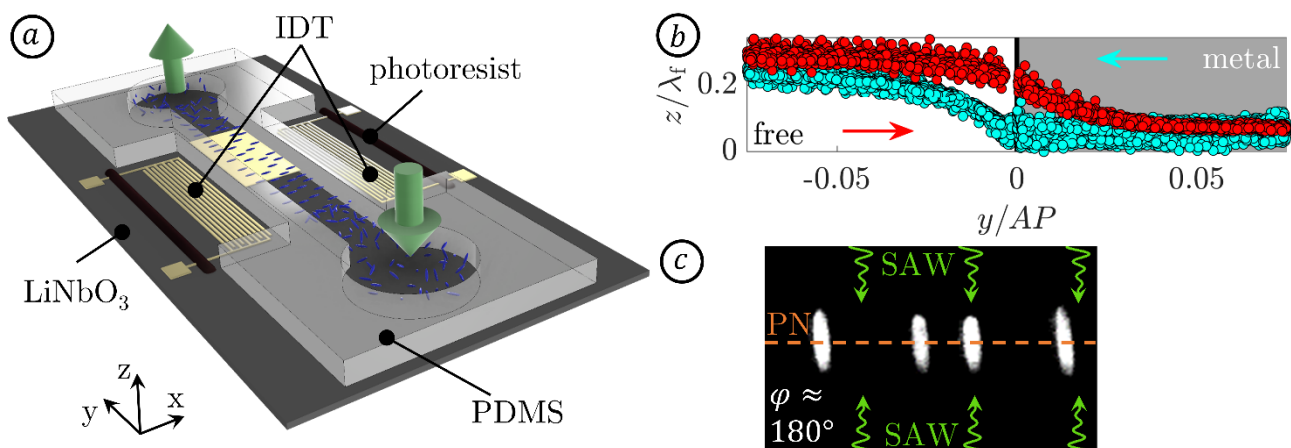
Figure 1: (a) Schematic of the acoustofluidic device. (b) Measured positions of spherical particles in the vicinity of the substrate surface and close to the center of the sSAW at $y/AP = 0$. Main flow direction from left to right (red) and right to left (cyan). (c) Orientation of prolate spheroids at an in-plane angle $\varphi = 180°$ focused at one pressure node (PN) of the sSAW.

Results and discussion

As indicated by measurements and shown in Fig. 1b, spherical polystyrene particles with diameter $d = 5.03\,\mu m$ are levitated in the non-screened region of the substrate surface by approx. $0.22\lambda_f$ due to the dielectrophoretic force $\boldsymbol{F}_{DEP}$ and pushed down above the screened region. Here, the wavelength of the bulk acoustic wave in the fluid is denoted by λ_f. This effect was not present at higher positions as $\boldsymbol{F}_{DEP}$ decays exponentially with the distance to the substrate surface. A similar behavior was observed for prolate spheroids made of polystyrene, which additionally aligned perpendicular to the pressure nodes (PN) of the sSAW (see Fig. 1c). The patterns of the underlying inhomogeneous electric field $\boldsymbol{E}$ and normalized Gor'kov potential $\widetilde{U}$ are revealed by the results of the numerical calculations depicted in Fig. 2a and b, respectively. Field lines of the electric field are connected between neighboring antinodes of the sSAW. However, the dielectrophoretic force consistently acts in the positive z-direction, leading to the levitation of the particles in the non-screened region observed experimentally. The acoustic, dielectrophoretic and sum of both torque components $(T_{AC,z}, T_{DEP,z}, T_z)$ about the z-axis acting on a prolate spheroid located in a pressure node are shown in Fig. 2c as a function of the in-plane angle φ. The torques induced by both effects are complementary and lead to a stable orientation at $180°$ or $0°$, as illustrated in Fig. 2d and e based on the distribution of the local torque components $(T_{AC,z,l}, T_{DEP,z,l})$ on the particle surface. The final orientation of the non-spherical particle is further characterized by an out-of-plane rotation of about $40°$ relative to the x-axis resulting from the pattern of the Gor'kov potential.
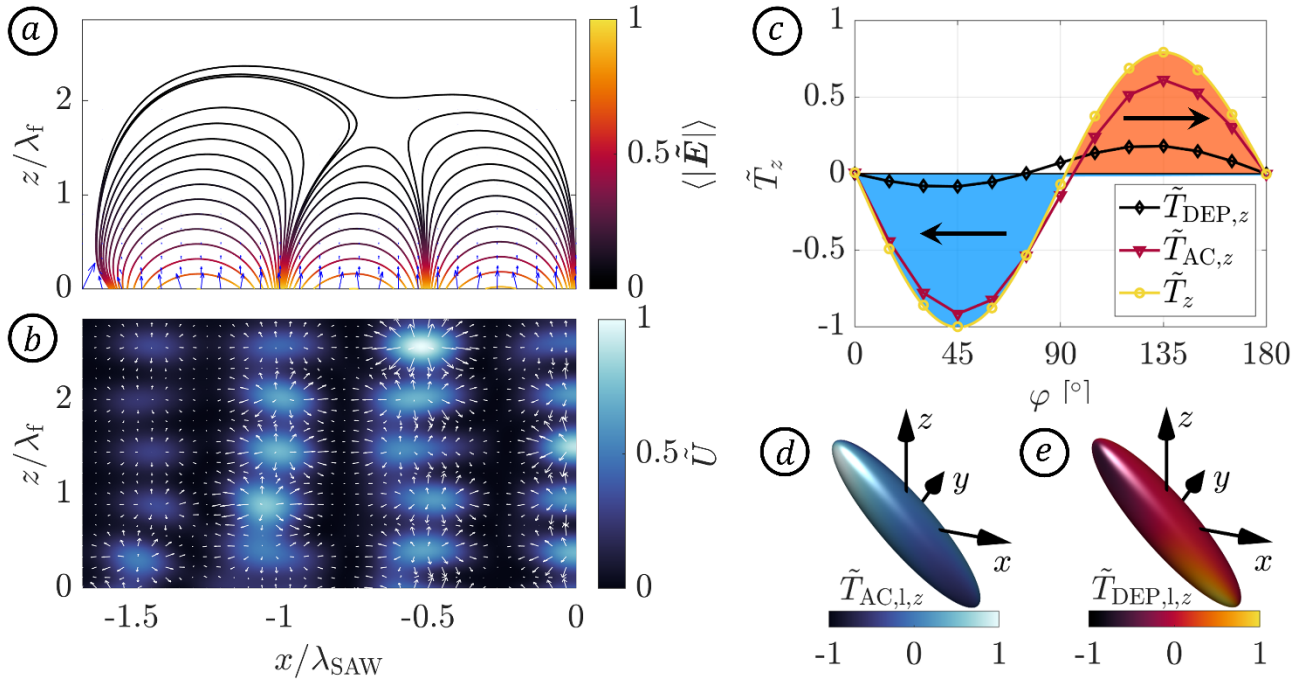
Figure 2: (a) Numerically calculated field lines of the normalized time-averaged electric field with vector representation of the dielectrophoretic force and (b) normalized Gor'kov potential $\widetilde{U}$ in half the channel cross section. Please note that the right edge of the figure ($x/\lambda_{SAW} = 0$) corresponds to the middle of the channel. (c) Normalized dielectrophoretic, acoustic and sum of torque components $(\widetilde{T}_{DEP,z}, \widetilde{T}_{AC,z}, \widetilde{T}_z)$ about the z-axis as a function of the in-plane angle φ. (d) Distribution of the local acoustic and (e) dielectrophoretic torque component $(\widetilde{T}_{AC,l,z}, \widetilde{T}_{DEP,l,z})$ across the particle surface.

Conclusion

The interplay of acoustophoresis and dielectrophoresis for the behavior of spherical and non-spherical particles in an acoustoelectric wave field has been characterized experimentally and numerically. By depositing a thin metal layer at the substrate surface, the electric field accompanying the sSAW was screened locally to reveal the influence of the dielectrophoretic force and torque in the non-screened region. Based on the experimental results, a 3D numerical model was developed to characterize on the underlying acoustic and electric fields. Combining experimental and numerical findings provides a fundamental understanding to facilitate a precise prediction of the particle behavior in complex acoustofluidic devices, which will be presented and discussed on site.

Acknowledgements

References

[1] Z. Chen, X. Liu, M. Kojima, Q. Huang, T. Arai, *Applied Sciences*, **10** 1260 (2020)
[2] D.J. Collins, T. Alan, A. Neild, *Lab on a Chip,* **14** 1595 (2014)
[3] S. Sachs, H. Schmidt, C. Cierpka, J. König, *Microfluidics and Nanofluidics*, **27** 81 (2023)

Near-field Acoustic Resonance Effects and Cavitation in SAW Aerosol Generation

Mehrzad Roudini[1, *], Juan M Rosselló[2], Ofer Manor[3], Claus-Dieter Ohl[2] and Andreas Winkler[1]

[1]Leibniz Institute for Solid State and Materials Research Dresden, Acoustic Microsystems, Germany
[2]Otto-von-Guericke University Magdeburg, Institute for Physics, Germany
[3]Technion - Israel Institute of Technology, Department of Chemical Engineering, Israel
[*]E-mail: m.roudini@ifw-dresden.de

Introduction

Compact surface acoustic wave (SAW) aerosol generators, also known as SAW nebulizers or atomizers, are attracting widespread interest in many technical processes due to their capability to produce directed fine aerosols with adjustable narrow size distribution and low shear forces, making them compatible even with complex biomolecules. This technology was, however, just recently taken to an application-relevant level [1]. Adjusting the aerosol drop size range is a crucial aspect for various applications, including miniaturized inhalation therapy [2], material deposition [3], liquid chromatography/spectroscopy [4], and olfactory displays. However, we show that the large pressure levels (relative to the low-pressure levels used to actuate liquid in SAW microfluidics) further support cavitation [5].

This paper investigates the complex acousto-hydrodynamics associated with standing surface acoustic wave (sSAW) interactions with a liquid film, its acoustic stabilization, patterning, and the droplet breakup mechanisms from the developed liquid pattern by employing analysis techniques with unprecedented high temporal and spatial resolution. Experimentally shown and supported by analytic models are the dynamics of cyclic, spatiotemporal formation of liquid domes understanding SAW excitation and their transformation into acoustic resonators with oscillating pressure amplitudes in which cavitation bubbles may be nucleated. For the first time, the observed fragmentation of liquid domes can be linked to three separate droplet generation mechanisms, including cavitation and capillary-wave instabilities. This work contributes to a deeper understanding of acoustic resonance effects in SAW aerosol generation, enhancing the applicability of such devices in real-world applications.

Experimental procedure

This study uses standing surface acoustic waves (sSAWs) to disintegrate an acoustically stabilized liquid film with a thickness in the order of the SAW wavelength into fine droplets. A microscopic image of the used microfluidic SAW atomization chip including partially open microfluidic channels and interdigital transducers (IDT) is shown in Fig. 1a. A chip holder with an integrated hole was prepared to access the atomization zone optically from below through the transparent chip substrate, as shown in Fig. 1b. The formation process of the liquid domes and the rather fast bubble dynamics were captured using high-speed photography combined with a long-distance optical microscope.
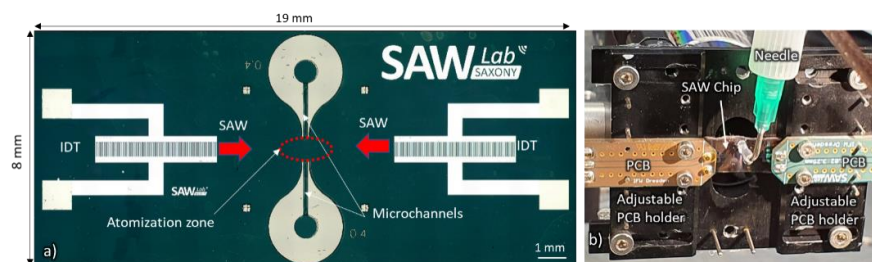
Figure 1: a) microscopy image of saw chip for aerosol generation includes IDTs with a 90 µm wavelength and integrated microchannels located outside the acoustic aperture. b) The assembled chip holder and its components to visualize the atomization zone optically from below through the transparent chip substrate.

Results and Discussion

In this study, the liquid atomization zone on the piezoelectric substrate, i.e., the zone of SAW-liquid interaction and aerosol origin, is optically visualized using a custom SAW aerosol generation microfluidics chip design (Fig. 2a) in an ultra-high-speed camera to gain insight into the hydrodynamics associated with standing SAW liquid interaction. The recorded time series of microscopic images in Fig. 3b show typical cyclic variation in the shape of the liquid patterns induced by standing SAW (Fig. 2b). We observed, that when the liquid dome reaches a specific height value, cavitation bubbles are nucleated in the liquid dome. Cyclic bubble appearance, growth, and collapse events are depicted in Fig. 2c and d. Additionally, the acoustically-induced fragmentation of liquid domes indicates the participation of three droplet generation mechanisms, including cavitation and capillary-wave instabilities as shown in Fig. 2e.
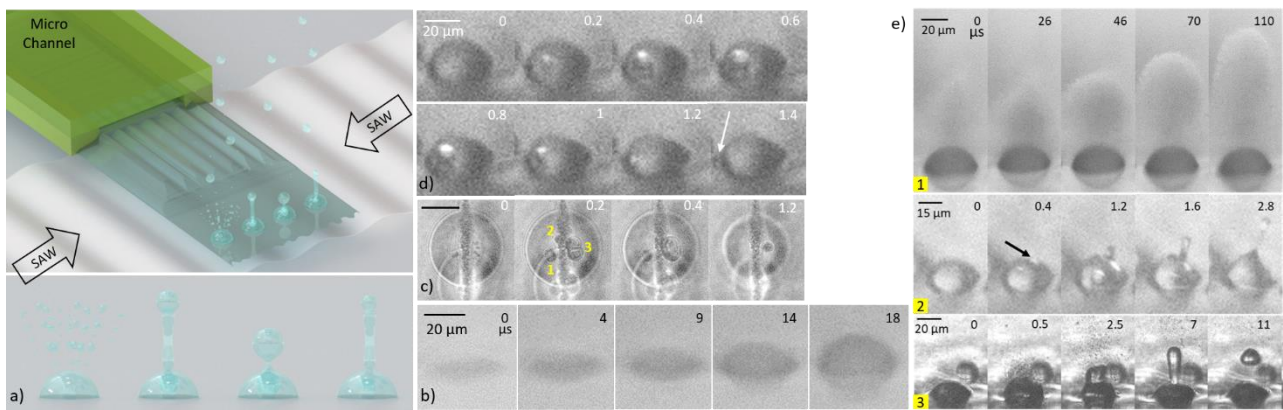
Figure 2: a) schematic representation of the microacoustic aerosol generation platform, where droplets are formed from acoustically induced liquid domes. b) standing SAW induced dome-shaped liquid pattern in the atomization zone appears quasi-static at a frame rate of 2 million fps. microscopic observation of c) multi and d) single-bubble dynamics inside the liquid dome and cavitation bubble dynamics. Droplet formation regimes: d) (1) capillary wave-induced mist generation. (2) microjets in the course of the collapse of cavitation bubbles. (3) atomization followed by a large droplet disintegration.

Conclusion

For the first time, the dynamics of the cyclic, spatiotemporal formation of liquid domes under sSAW are investigated experimentally and supported by analytic models. The acoustics in the domes are modeled by balancing the capillary and acoustic pressures. We speculate that the domes become acoustic resonators with oscillating pressure amplitudes in which cavitation bubbles can be nucleated, grow, and collapse, as observed in the high-speed videos. Photographic evidence reveals that these bubbles are responsible for the ejection of specific droplet fractions from the liquid domes. Interestingly, the locations where cavitation bubble oscillations were observed are identical to the erosion seen on the substrate. This hints at cavitation-based erosion mechanics in aerosol generation SAW devices, which is of high significance for all fields of their application and may limit their applicability in the medical field. The investigations in this study are contributing to a deeper understanding of sSAW atomization, therefore enhancing the predictability and practicality of such devices in real-world applications. Further research is needed to understand the cause of bubble nucleation and the limitation of cavitation erosion, as well as the dynamics of acoustowetting involved.

References

[1] Winkler, A., et al., *Biomedical Microdevices*, 2017. 19(1): p. 9.
[2] Cortez-Jugo, C., et al., *Ultrasonics Sonochemistry*, 2022. 88: p. 106088.
[3] Winkler, A., et al., *Journal of Sol-gel science technology*, 2016. 78(1): p. 26-33.
[4] Kiontke, A., et al., *Scientific reports*, 2021. 11(1): p. 2948-2948.
[5] Roudini, M., et al., *Ultrasonics Sonochemistry*, 2023: p. 106530.

Superhydrophobic coating acts as a shield against ultrasound-induced heating

Alex Drago-González[1, *], Maxime Fauconnier[1],
Bhuvaneshwari Karunakaran[2], Laura Fieber[2], William S.
Y. Wong[2], Robin H. A. Ras[2] and Heikki J. Nieminen[1]

[1]Dept. of Neuroscience and Biomedical Engineering, Aalto University, Espoo, Finland
[2]Dept. of Applied Physics, Aalto University, Espoo, Finland
[*]E-mail: alex.dragogonzalez@aalto.fi

Introduction

High-intensity focused ultrasound (HIFU) allows remote thermal deposition with spatial precision and accuracy [1], finding applications in many fields, *e.g.*, medicine [2,3], industrial cleaning [4] and micro-robotics [5]. However, in applications that do not rely on heating as the primary mechanism, unwanted thermal damage may be induced to delicate tissues [6], heat-sensitive components [7] and superhydrophobic surfaces (SHS). In SHS, thermal damage can lead to deterioration of self-cleaning [8], drag reduction [9] or antibiofouling [10] properties.

This experimental work dives into the capability of plastrons, an air layer encapsulating the SHS when submerged under water, to influence sound propagation and protect the SHS against the adverse thermal effects of ultrasound. Using Schlieren imaging, we first demonstrate ultrasound-induced changes in reflection, transmission, and absorption of a focused US wave by a SHS. The surface is studied while it is in wet (*i.e.*, Wenzel state, W) and fractionally wet (*i.e.*, Cassie-Baxter state, CB) conditions.
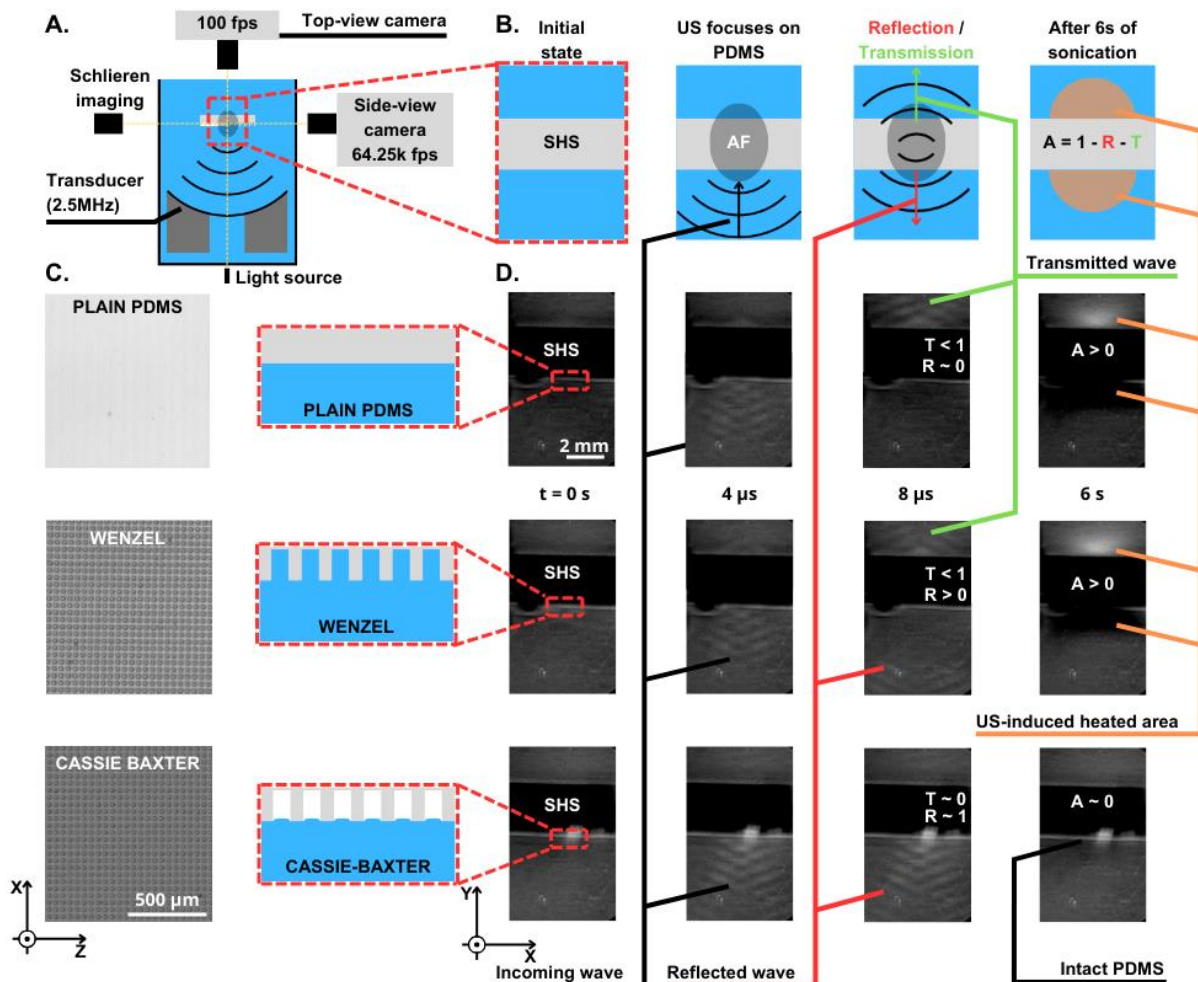
Figure 1: A. Experimental set-up. **B.** Side-view sketch of the sonication of the SHS placed at the acoustic focus (AF). **C.** Top-view of plain PDMS and wetting states. **D.** Exemplary cases of SHS under high-speed Schlieren imaging with different wetting states: (i) plain PDMS without microstructures and SHS with microstructures in (ii) W state and (iii) in CB state. The CB state shows capability to reflect US waves, whereas W state facilitates transmission and absorption of US in PDMS. W state results in the SHS heating, evidenced by brighter or darker contrast on top or bottom of the SHS, respectively, identified with the changes in the optical refractive index gradient detected with Schlieren imaging.

Methodology

The experimental setup displayed in Figure 1A is as follows. A polydimethylsiloxane (PDMS) fluoro-coated SHS (manufactured by soft lithography), consisting of an homogenously dispersed array of cylindrical pillars (50 μm high, 20 μm wide and 25 μm apart), is submerged in a pure water-filled acrylic tank and placed at the focus of a HIFU transducer (Sonic Concepts, Model: H-147; f = 2.5 MHz; focus width at -6dB: 0.51 mm; focus length at -6dB: 3.28 mm). Its side-view stroboscopic visualization, while being actuated by an US burst (pulse repetition frequency = 65 kHz and pulse-average acoustic intensity = 11.5 W/cm²), as schematically shown in Figure 1B, is done via a high-speed camera (64250 fps, Vision research, Phantom v1612) incorporated in a Schlieren imaging system. A top-view visualization of the optically transparent SHS is also provided with a second camera (100 fps, Vision research, Phantom v1612) to assess its wetting state, as shown in Figure 1C.

The investigation focuses on the acoustic transmission, reflection, and absorption by three different configurations of SHS and wetting states, (i) a plain (not microstructured) sample (control), (ii) a microstructured SHS in Wenzel state and (iii) a microstructured SHS in Cassie-Baxter state.

Results and Discussion

As the PDMS is matching rather well the acoustic impedance of water, and the microstructures are too small to impede the travelling 600 μm long waves, the results are very similar in both the cases of the plain sample (control) and the W state, as Figure 1D shows. Most of the energy of the incident wave is transmitted through the SHS with comparable energy in both cases. Also, a thermal increase of the SHS is observed, visible on both sides of the sample. It is evidenced by growing regions of brightening (top) or darkening (bottom), reaching a maximum after 6 seconds of US actuation. A few seconds after US exposure, the sample recovers its initial (room) temperature and does not show any signs of irreversible damage.

The opposite scenario happens in the case of the CB state, sonicated with similar acoustic parameters. The air plastron located between the solid and the liquid phases creates a mismatch of acoustic impedance, reflecting most of the incident wave. From the optical information, this corresponds to 97% of the incident wave being reflected. As a result, this CB prevents the SHS from heating, which is also confirmed from the Schlieren imaging information, thus acting as a shield against the thermal effect of focused ultrasound.

An analogy can be drawn between this CB state configuration and well-known soundproof double-glazing, but here applied to micro scale and higher frequencies (> MHz).

Conclusion

In conclusion, our findings show how an acoustofluidics approach, employing thin films, effectively shields surfaces from the acoustic thermal effects associated with ultrasound exposure. This study has broad implications for applications in biomedical (e.g. shock-wave lithotripsy and immunotherapy) and surface engineering (e.g. amorphous polymer-based materials) applications, highlighting the importance of preserving surface integrity in diverse fields.

Acknowledgements

References

[1] V. S. Bachu et al. *Ann Biomed Eng* **49** 1975 (2021) https://doi.org/10.1007/s10439-021-02833-9
[2] R. Illing et al. *Br J Cancer* **93** 890 (2005) https://doi.org/10.1038/sj.bjc.6602803
[3] E. S. Ebbini et al. *Int. J. Hyperth.* **31**(2) 77 (2015) https://doi.org/10.3109/02656736.2014.995238
[4] J.-Y. Lu et al. *IEEE International Ultrasonics Symposium*, Rome, Italy, 2009, pp. 1195-1198 https://doi.org/10.1109/ULTSYM.2009.5441719
[5] P. Wrede et al. *ACS Applied Materials & Interfaces* **15**(45) 52224 (2023) https://doi.org/10.1021/acsami.3c11656
[6] Z. Izadifar et al. *Journal of Clinical Medicine* **9**(2) 460 (2020) https://doi.org/10.3390/jcm9020460
[7] B. Liu et al *Macromol. Chem. Phys.* **214** 2519 (2013) https://doi.org/10.1002/macp.201300320
[8] S. S. Latthe et al. *Prog. Org. Coat.* 128 52 (2019) https://doi.org/10.1016/j.porgcoat.2018.12.008
[9] M. Liravi et al. *Prog. Org. Coat.* 140 105537 (2020) https://doi.org/10.1016/j.porgcoat.2019.105537
[10] G. B. Hwang et al. *ACS Nano*, **12**(6) (2018) 6050 https://doi.org/10.1021/acsnano.8b02293

Acoustic microstreaming around asymmetric bubbles

<u>Claude Inserra</u>[1,2,*], Cyril Mauger[2], Philippe Blanc-Benon[2] and Alexander A. Doinikov[2]

[1]LabTAU INSERM U1032, Université Claude Bernard Lyon 1, Lyon, France
[2]LMFA UMR 5509, Ecole Centrale Lyon, Ecully, France
[*]E-mail: claude.inserra@inserm.fr

Introduction

Oscillating bubbles are known to generate a slow mean flow, called acoustic microstreaming, in their surroundings. These bubble-induced flows have important applications in fluid mixing and surface cleaning. The mathematical investigation of this problem has been treated so far by considering radial and/or translational oscillations of the bubble [1], as well as axisymmetric bubble oscillations [2,3]. Here, the theoretical analysis of acoustic microstreaming in the case of a bubble experiencing asymmetric oscillations is proposed for the first time. The three-dimensional signature of the flow surrounding the bubble is presented for different asymmetric oscillation modes decomposed over the set of spherical harmonics. It is shown that a reversal of the flow direction at the zenith of the bubble is obtained when the oscillation properties of the interface switch from a zonal to a sectoral mode, when keeping the bubble equilibrium radius constant.

Theory

We assume that the surface of the bubble is undergoing asymmetric oscillations, represented by

$$r_s(\theta, \phi, t) = R_0 + e^{-i\omega t} s^{(n,m)} Y_n^m(\theta, \phi) + e^{-i\omega t} s^{(n,-m)} Y_n^{-m}(\theta, \phi), \qquad (1)$$

where R_0 is the bubble radius at rest, ω is the angular frequency of the bubble oscillations, $s^{(n,m)}$ and $s^{(n,-m)}$ are the complex amplitudes of modes (n,m) and $(n,-m)$, respectively, and $Y_n^m(\theta, \phi)$ are spherical harmonics, which are defined by

$$Y_n^m(\theta, \phi) = \sqrt{\frac{(2n+1)(n-m)!}{4\pi(n+m)!}} e^{im\phi} P_n^m(\cos \theta), \ \ 0 \le m \le n, \qquad (2)$$

where $P_n^m(\cos \theta)$ is the associated Legendre polynomial of order m and degree n and (r, θ, ϕ) are the spherical coordinates whose origin is at the equilibrium center of the bubble. The values of $s^{(n,\pm m)}$ and ω are considered as known quantities. They are assumed to be measured experimentally and serve as input data in our study. We assume that $s^{(n,\pm m)}/R_0 \ll 1$, which allows us to linearize the equations of liquid motion when calculating first-order solutions. Eq.(1) indicates that the bubble interface is represented by two spherical harmonics with the same degree n and opposite orders $\pm m$. When the values of $s^{(n,\pm m)}$ are equal, the shape oscillation is stationary along the bubble interface, and hence a standing wave is oscillating at the bubble interface.

In the process of calculating the Lagrangian streaming induced by modes (n,m) and $(n,-m)$, it is first required to derive the first-order liquid velocity field before calculating the acoustic streaming given by the time-averaged Navier-Stokes equation at the second order. This task has been solved exactly, without restrictions on the bubble equilibrium radius and the liquid viscosity, following the approach of Prosperetti [4] and transforming all the equations in terms of the velocity to those in terms of the vorticity $\boldsymbol{\omega}^{(n,m)} = \nabla \times \boldsymbol{v}^{(n,m)}$ of the velocity field and applying the poloidal-toroidal decomposition of the vorticity [5]

$$\boldsymbol{\omega}^{(n,m)} = \boldsymbol{P}^{(n,m)} + \boldsymbol{T}^{(n,m)}. \qquad (3)$$

Results and discussion

In order to illustrate the findings of the present theory, we consider the case of a bubble experiencing radial oscillations and a parametrically-excited sectoral oscillation. Amongst the set of orthonormal spherical harmonics $Y_n^m(\theta, \phi)$ of degree n and order m, sectoral harmonics correspond to the particular case $n = m > 0$. If only a sectoral shape oscillation is parametrically triggered at the bubble interface, then the radial and sectoral oscillations do not oscillate at the same frequency and therefore their interaction provides no contribution to the acoustic microstreaming. It means that the only source of microstreaming results from the self-interacting sectoral mode. Sectoral modes have as many azimuthal deformation lobes as the modal degree n to which they belong. Because the number of nodal parallels of any spherical harmonics equals $n - m$, sectoral modes are devoid of nodal parallels and have only their longitudinal displacement anti-node at the equator, as shown in Fig. 1a, where they exhibit an azimuthal shape that corresponds to $\cos(m\phi)$. Here for $n = m = 3$, the azimuthal shape is easily recognizable from the top view.
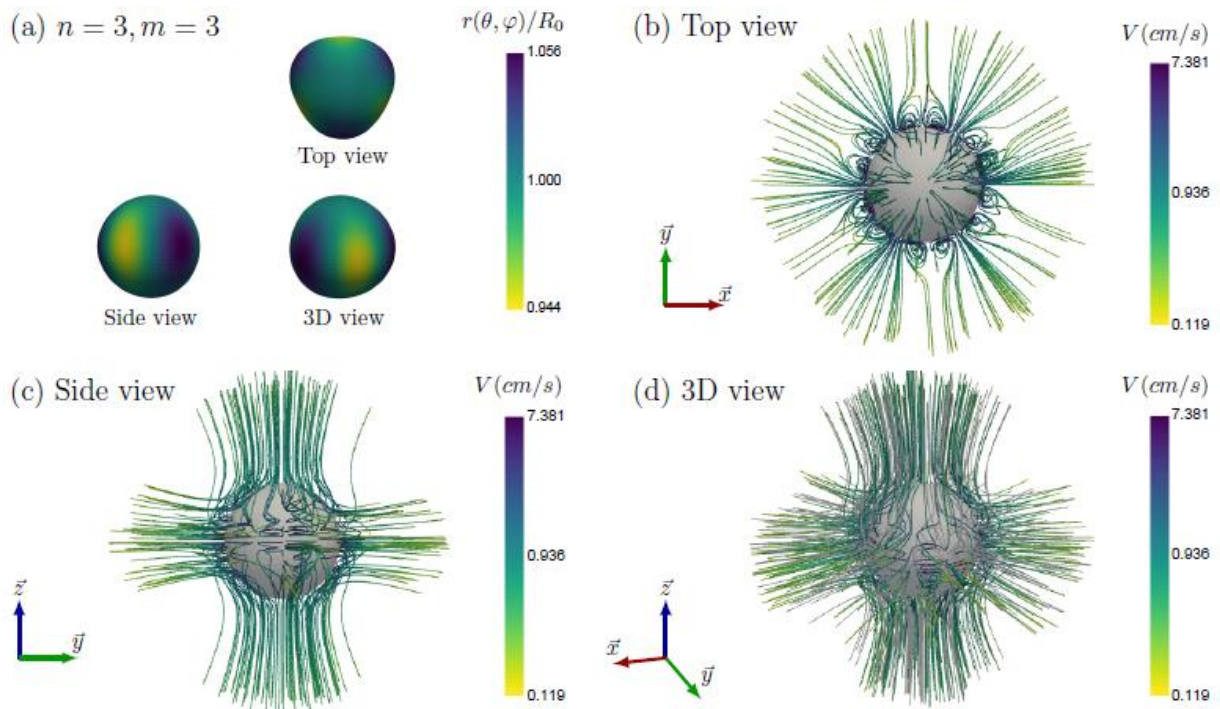
Figure 1: Characterization of the acoustic microstreaming induced by a bubble experiencing radial oscillation and parametrically-excited sectoral oscillation with $n = m = 3$. (a) 3D, top and side views of the bubble shape deformation. (b, c, d) Top, side and 3D views of the streamlines of the Lagrangian velocity field.

The resulting streaming pattern possesses $4n = 12$ lobes assembled by pairs when observed from the top view. The rotational direction of the flow is such that the particles are propelled away from the anti-nodes and attracted to the nodes of displacement of the bubble interface. Each pair of recirculation loops is thus surrounded by areas of particles propelled with a positive radial velocity. From a side view, the streaming pattern resembles a dipole mode, characterized by four lobes of recirculation around the bubble. Above the bubble (at the north pole), the particles follow an anti-fountain-like motion, meaning that the particles are attracted from infinity to the bubble interface. This signature clearly differs from the commonly-observed fountain behaviour when bubbles are oscillating on a substrate, where only axisymmetric oscillations (the zonal harmonics) are triggered.

Conclusion

Analytical equations have been derived that describe acoustic microstreaming induced by a bubble experiencing asymmetric oscillations. The developed theory imposes no restriction on the bubble size and the liquid viscosity. Signatures of the asymmetric flows are highlighted for different oscillations modes of the bubble interface. The sign reversal of the flow direction above the bubble is predicted, which suggests new applications in the control of micro-objects in acoustofluidics.

References

[1] M.S. Longuet-Higgins, *Proc. R Soc. London Ser. A,* **454** 725-742 (1970)
[2] T. Spelman and E. Lauga, *J. Eng. Math,* **105** 31-65 (2017)
[3] A.A. Doinikov et al., *Phys. Rev. E,* **100** 033104 (2019)
[4] A. Prosperetti, *Quart. Appl. Math.,* **34** 339-352 (1977)
[5] G. Backus, *Rev. Geophys.,* **24** 75-109 (1986)

Vesicle-based Drug Loading and Intracellular Delivery by Gigahertz Acoustic Streaming

Haopu Wang[1,2], Shuailong Zhang[1,2,3], Huikai Xie[1,2,3], Yao Lu[1,2,3*]

[1] School of Integrated Circuit and Electronics, Beijing Institute of Technology, Beijing, 100081, China.
[2] Engineering Research Center of Integrated Acousto-opto-electronic Microsystems, Ministry of Education of China, Beijing 100081, China
[3] BIT Chongqing Center for Microelectronics and Microsystems, Chongqing 400030, China
[*]E-mail: y.lu@bit.edu.cn

Introduction

The efficient intracellular delivery of drug carriers is crucial for effective cancer therapy and diverse treatment protocols. In a conventional delivery process, the internalization of drug-loaded carriers into cells depends on endocytosis, which impedes the subsequential drug release to nucleus due to entrapment by endosomes[1]. To address this limitation, different membrane-disruption approaches have been proposed to increase the cell membrane permeability, including sonoporation by ultrasound[2], electroporation with micro-/nano-scale electrodes[3], and thermal membrane disruption methods[4]. In this work, an acoustofluidics-based method with gigahertz (GHz) acoustic streaming is proposed to change the permeability of both small unilamellar vesicles (SUVs, 100 nm) and cancer cells (HeLa cells, 15-20 μm) by disrupt their membranes in an irreversible way, aiming to assemble drug-loaded carriers by controlled doxorubicin (Dox) encapsulation into SUVs, as well as enhanced drug delivery with Dox-SUVs via the GHz acoustic streaming. The method may provide a potential platform for further intracellular delivery system in biomedical applications.

Working principle of the intracellular delivery system

In this work, the GHz acoustic streaming was generated by a bulk acoustic wave (BAW) resonator of 1.5 GHz frequency. In the intracellular delivery system, the GHz acoustic streaming was first used to load Dox molecules into synthesized SUVs to obtain nanoscale drug-loaded carriers (Figure 1a), then, the vesicle-based carriers were delivered into HeLa cells under the stimulation of GHz acoustic streaming (Figure 1b). In this process, the delivery efficiency of drug carriers would be increased by changing the cell membrane permeability via GHz acoustic streaming.
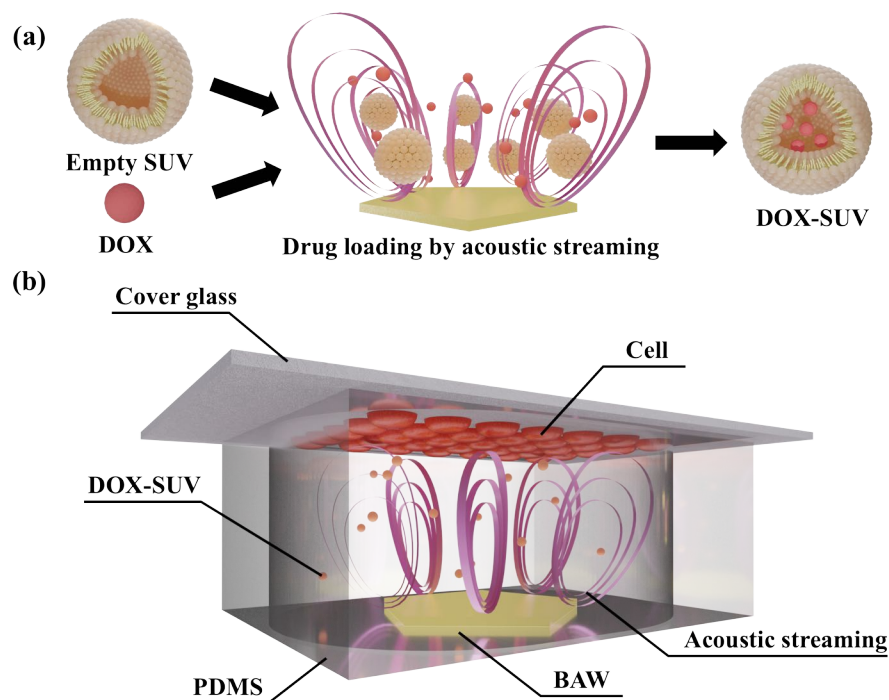
Figure 1: Schematic of the acoustofluidics-based intracellular delivery system. (a) Controlled loading of Dox into SUVs by the GHz acoustic streaming. (b) Enhanced intracellular delivery of Dox-SUVs via GHz acoustic streaming.

Enhanced drug loading and drug carrier delivery via acoustic streaming

To realize vesicle loading with drug molecules, SUVs of DOPC (100 nm) were first synthesized with the extrusion method. Dox molecules were then dissolved in pure water at a concentration of 40 μg/mL. To improve the encapsulation efficiency, the GHz acoustic streaming (input power: 300 mW) was applied to the mixer of Dox and SUVs solution for 15 min, following which, a dialysis membrane was used to separate the Dox-loaded SUVs from the remaining suspended Dox molecules by continuously stirring for 24 h. Figure 2a shows the dynamic light scattering (DLS) results of SUVs before and after the acoustic stimulations, which demonstrates that the SUVs stay intact under the acoustic streaming. The absorbance value in Figure 2b verifies that certain amounts of Dox molecules were successfully loaded into SUVs after the acoustic stimulation with a significant increased value of absorbance at 490 nm.

Furthermore, the Dox-loaded SUVs were delivered to HeLa cells under the GHz acoustic streaming with different stimulation time. To make a comparison, the HeLa cells that were incubated with the same amount of Dox-SUVs but without the acoustic treatment are defined as the control group. As Figure 2c shows, the red fluorescence emitted by Dox-SUVs is almost negligible in the control group, but for the cells that are stimulated with the GHz acoustic streaming at 300 mW, increased red fluorescence occur in the cytoplasm of HeLa cell. Moreover, as the duration of acoustic streaming was extended to 15 min, there is red fluorescence in the nuclear region, which overlaps with the DAPI-stained nuclei in the merged images. The results indicate that more Dox-SUVs were delivered into HeLa cells with the assistance of acoustic streaming, and the total amount can be controlled by adjusting the stimulation time of the GHz acoustic streaming.
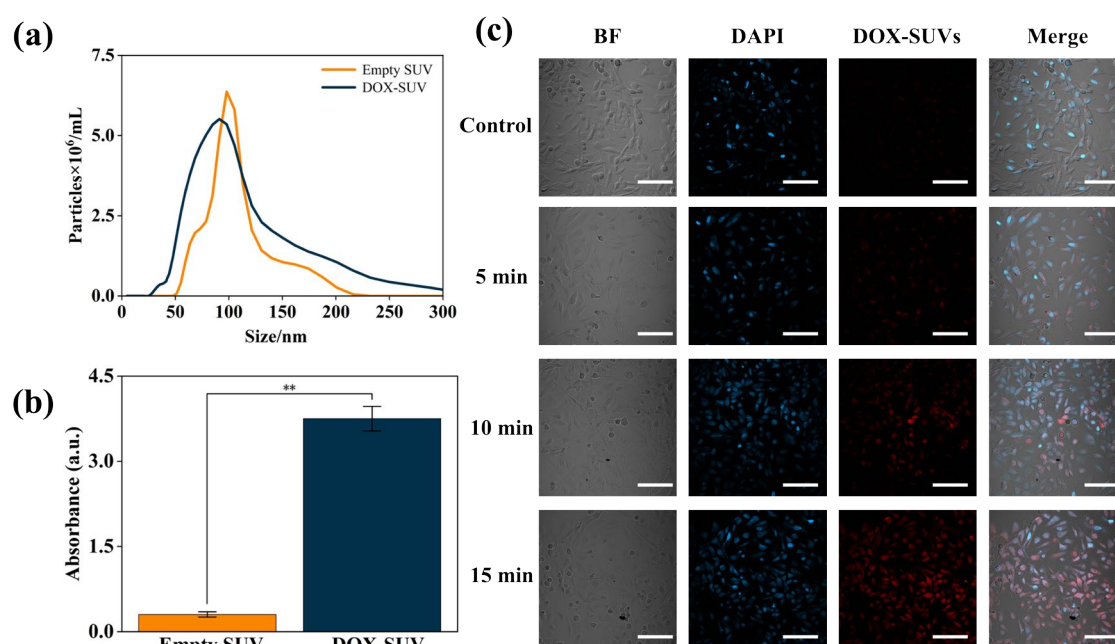
Figure 2: (a) Size distribution of empty SUVs and Dox-SUVs. (b) The absorbance of empty SUVs and Dox-SUVs at 490 nm. **P<0.01. (c) Confocal microscopy images of Dox-SUVs distributed in HeLa cells without (Control group) and with (different durations from 5 to 15 min) the stimulation of acoustic streaming. The input power of the BAW resonator was 300 mW. Scale bars indicate 100 nm.

Conclusion

In our work, the GHz acoustic streaming generated by the BAW resonator was applied to load Dox molecules into SUVs as drug carriers, following which the intracellular delivery of these vesicle-based drug carriers was also enhanced by applying acoustic streaming of different durations. This acoustofluidics-based disruption method significantly improves the delivery efficiency by changing the membrane permeability, which can be used as a potential candidate in controlled drug delivery for further biomedical applications.

Reference

[1] S. Ma, L. Song, Y. Bai, S. Wang, J. Wang, H. Zhang, F. Wang, Y. He, C. Tian and G. Qin, *RSC Adv.*, **13**, 11269, (2023).
[2] E. Thomas, J.U. Menon, J. Owen, I. Skaripa-Koukelli, S. Wallington, M. Gray, C. Mannaris, V. Kersemans, D. Allen, P. Kinchesh, S. Smart, R. Carlisle, and K.A. Vallis, *Theranostics*, **9**, 5595, (2019).
[3] J. Pan, X. Wang, C. Chiang, Y. Ma, J. Cheng, P. Bertani, W. Lu, and L. James Lee, *Lab on a Chip*, **24**, 819, (2024).
[4] Y. Qu, Y. Zhang, Q. Yu, and H. Chen, *ACS Appl. Mater. Interfaces*, **12**, 31054, (2020).

Advancing Size-Selective Particle Separation: Ultrasonic Microbubble Streaming for Automated Depletion

Amirabas Bakhtiari[1,*], and Christian J. Kähler[1]

[1]Institute for Fluid Mechanics and Aerodynamics, Bundeswehr University Munich,
85577 Neubiberg, Germany
[*]E-mail: amirabas.bakhtiari@unibw.de

Introduction
The application of ultrasonic-actuated microbubble streaming, powered by piezo transducers in microfluidic systems, is increasingly gaining interest [1]. In the quest for more efficient lab-on-a-chip applications, our study addresses an automated approach for size-selective particle depletion within microfluidic channels, leveraging the dynamics of microbubble streaming. This method underscores a label-free, sheath-free, and cost-effective strategy for particle separation. The essence of this technique lies in trapping larger particles within counter-rotating vortices near the microbubble, enabling their rapid ejection for subsequent collection or analysis. This experimental investigation encompasses a comprehensive analysis through various dimensions: a detailed statistical examination, flow characterization via volumetric and high-frequency micro Particle Tracking Velocimetry (µPTV), evaluation of particle trapping efficiency across different sizes, and the z-axis distribution assessment of particles. Our findings reveal significant advancements in utilizing acoustic waves for microbubble streaming, achieving unparalleled efficiency in particle separation for diverse lab-on-a-chip applications.

Theory and Experimental procedure
This study explores how microbubble streaming segregates particles by size: small particles flow unimpeded, while larger ones are trapped near the microbubble. Leveraging Poiseuille flow and piezoelectrically-driven microbubble streaming, this method isolates larger particles in a microchannel, allowing smaller ones to proceed. Once larger particles accumulate or space is constrained, they are discharged into a collection chamber through a briefly opened side channel. We experimented with polystyrene microspheres of varying sizes (2, 5, 10, and 15 µm) suspended in a glycerol-water solution. The experimental setup includes a PDMS microchannel, detailed in **Fig. 1**, measuring 100 µm in height, 500 µm in width, and 20 mm in length, with an 80 µm by 200 µm side pit close to a 60 µm discharge channel leading to a microvalve-controlled collection chamber. It features an optical system integrated into a custom LabVIEW control system for real-time imaging and particle detection. This system also controls a function generator, amplifier, oscilloscope, and data acquisition system to precisely manage piezoelectric transducer and microvalve activities.
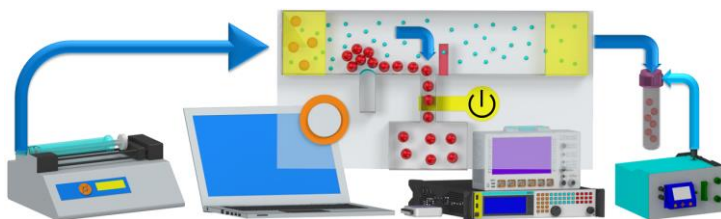
Figure 1: The schematic of test setup. Yellow areas represent regions of interest (ROIs) for counting particles, and the red ROI functions as a sensor to identify particle leaks, initiating valve activation.

Results and Discussion
To optimize system performance, understanding fluid flow in varied conditions is crucial. We studied this by tracking 15-µm particles in fluid flows combining Poiseuille flow and microbubble streaming from a piezoelectric transducer oscillating at 33 kHz with voltages of 70, 35, and 20 V_{pp}. We observed that the flow splits into distinct zones due to the interaction between the microbubble streaming and Poiseuille flow. Particles above the red separatrix line bypass the microbubble's vortices, while those below are trapped close to the microbubble (**Fig.2**). As the Poiseuille flow rate reduces or bubble's excitation amplitude increases, the separatrix and vortex behaviors adjust, impacting particle migration towards the bubble. Through experimentation, we observed that at an average flow rate of 200 µm/s and using a piezo transducer set to an amplitude of 66 V_{pp}, the induced microstreaming efficiently congregates particles of 5, 10, and 15 µm sizes close to the microbubble. These particles are then effectively captured within the inner flow regions, facilitating their subsequent collection.

To evaluate the particle trapping efficiency, experiments were carried out with particles of different sizes (5, 10, and 15 µm) under uniform conditions (microbubble excitation at 33 kHz and 66 V_{pp}, and flow velocity at
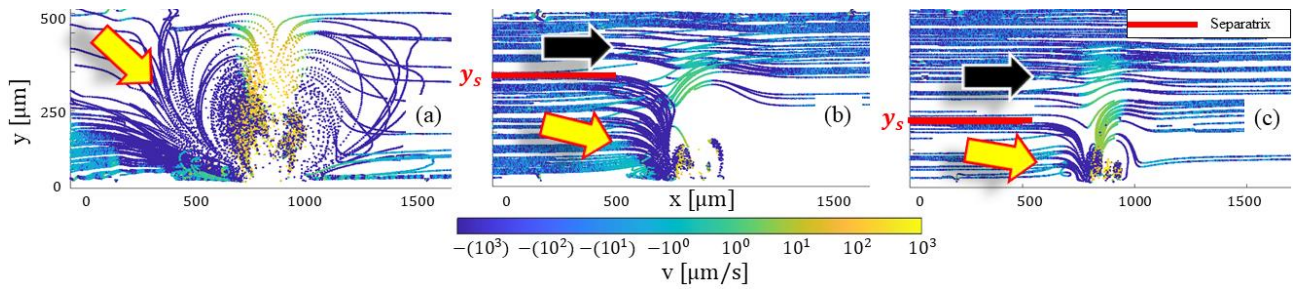
Figure 2: Tracking 15-µm particles in combined flow at different excitation levels: 70 v_{pp}(a) effectively drag particles near the microbubble; at 35 v_{pp} (b) and 20 v_{pp} (c), attraction diminishes, enabling particles to bypass the vortices.

200 µm/s). The efficiency was assessed by comparing the number of particles entering and leaving the microchannel. The most successful trapping occurred with 10-µm particles, where 100 particles were perfectly captured with minimal escape. However, as the influx of particles increased, so did the escape rate, until a balance was achieved between the number of particles entering and exiting. The study also determined the maximum number of particles that could be trapped efficiently without any escaping: 70 particles for 5-µm and 60 for 15-µm particles.

To understand particle leakage relation with the particle size, we used volumetric µPTV with defocus imaging, tracking particle positions along the z-axis as they left vortices and moved through the microchannel. Our findings revealed particles with diameters of 10 and 15 µm clustering near the wall, while 5-µm particles spread throughout the channel depth. This indicates that larger particles (15 and 10 µm) are more affected by shear-induced lift forces, positioning them closer to the channel walls and exiting the channel at a common point along the z-axis. Additionally, the exit process for 15-µm particles is faster than for 10-µm ones, due to quicker space-filling and faster particle interactions.

For scenarios where target particles are scarce, continuous system operation may be unnecessary. Instead, the system can activate automatically upon detecting a particle within the initial ROI. Accurate ROI positioning within the camera's view and understanding the response time for activating the piezoelectric element to redirect particles are essential to ensure effective detection without missing any particles. We used high-frequency µPTV, to analyze flow changes from pure Poiseuille to combined flow with microbubble streaming upon piezoelectric toggling. Our findings (**Fig.3**), illustrated over sequences before and after piezoelectric activation, show immediate particle displacement changes upon bubble excitation, with no temporal delay regardless of particle proximity to the vortex core or the transition back to pure Poiseuille flow.
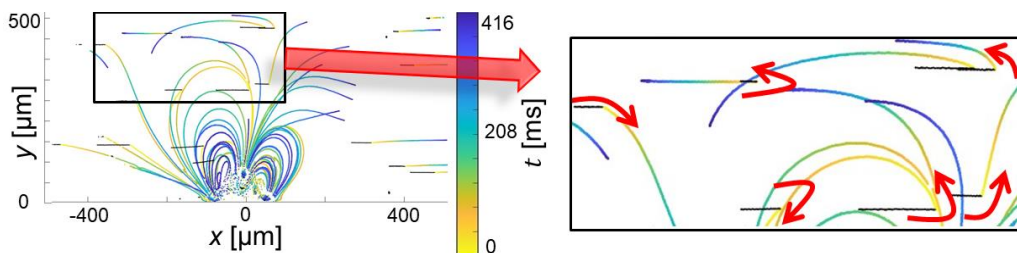
Figure 3: Particle trajectories before (125ms, black) and after (416ms, color) bubble excitation (left). Close-up view of particles far from the bubble, showing synchronized trajectory changes (right).

Conclusion

This study introduces and validates an automated technique for size-selective particle depletion in continuous flow in microchannel. Utilizing PDMS microchannels and piezoelectric technology, this method offers an efficient and inexpensive alternative to more costly devices like flow cytometers. It efficiently retains larger particles for easy removal while allowing the main fluid to flow uninterrupted, reducing fluid wastage and ensuring efficient separation. The research included comprehensive statistical analyses, flow characterization, and evaluation of particle trapping efficiency, using advanced techniques to optimize system performance for various particle sizes, flow rates, and densities. The system's adaptability to different conditions highlights its potential for broad application in microfluidics and particle manipulation, promising significant advancements in the field.

References
[1] A. Bakhtiari , C.J. Kähler, *Microfluidics and Nanofluidics*, **27** 37(2023)

Numerical simulation of bulk acoustic waves induced droplet generation in an immiscible coflow system

Sazid Zamal Hoque[1,2*], and Ashis Kumar Sen[1]

[1]Department of Mechanical Engineering, Indian Institute of Technology, Chennai-600036, India
[2] Department of Physics, Technical University of Denmark, Kongens Lyngby, Denmark
*E-mail: shoque@dtu.dk

Introduction

Since the pioneering work of Rayleigh, it has been well-known that sound exerts radiation force on an object due to the exchange of linear momentum transfer from its surface. The acoustic radiation force is utilized in various acoustofluidics applications, e.g., on-demand droplet splitting, fusion, separation, etc. Hertz and Mende, in 1939, experimentally observed the deformation of fluid interfaces due to acoustics beam, which led to the concept of acoustic radiation pressure that acts on fluid interface [1]. A theoretical description of the acoustic radiation force has been presented for a density interface where the interface is perpendicular to the wave propagation direction. Similarly, for the case where the density interface is parallel to wave propagation, an expression for the acoustic radiation pressure acting on the interface is derived [2]. Recently, the stream-to-drop transition of coflow fluids via exposure to bulk acoustic waves has been shown experimentally [3].

In the present work, we have developed a numerical framework to explain the bulk sound waves induced stream-to-droplet transition in a microchannel. An expression for acoustic radiation pressure acting on the immiscible fluid-fluid interface is developed. Further, the break-up of the coflow stream into droplets is explained via the competition of acoustic radiation pressure and interfacial tension that acts on the interface. The effects of the flow rates and the viscosity of the two fluid phases on the droplet's size and inter-distance are discussed in detail. The droplet formation from a microfluidics coflow stream of fluids via exposure to bulk acoustic waves is a novel technique that is beneficial and usable for many applications dealing with microfluidics.

Theory and Numerical simulation

A schematic of a coflow system before and after sound waves are on is shown in Figure 1. The side-by-side coflow configuration is established between fluid 1 and fluid 2, having an impedance z_1 and z_2 respectively. When the acoustic is on, the fluid 1 flowing with a flow rate Q_1, deforms due to interfacial instability and breaks up into droplets, and further, the droplets are convected downstream with the flow rate Q_2, which is higher than Q_1. The resulting acoustic radiation pressure that acts on the interface due to exposure of bulk acoustic standing wave deforms the interface, leading to the break-up of the continuous stream into uniform droplets diameter d. The acoustic radiation pressure across the interface is obtained as [4],

$$\langle \Delta P^L \rangle = -\langle E_{ac} \rangle \left[\left(e^{+i2k_1 x} + \Delta Z^2 e^{-i2k_1 (x - 2w_1)} \right) - \rho_2/\rho_1 (1 - \Delta Z)^2 \, e^{+i2k_1 w_1} e^{-i2k_2 (w_1 - x)} \right] \tag{1}$$

The eqn. (1) is modeled as a body force term in the Navier-Stokes equation to incorporate the bulk acoustic wave's effect in immiscible fluids. Further, the interface between the two fluids is captured using the phase field method. A sufficiently fine uniform mesh is created to capture the interface deformation throughout the fluid domain.
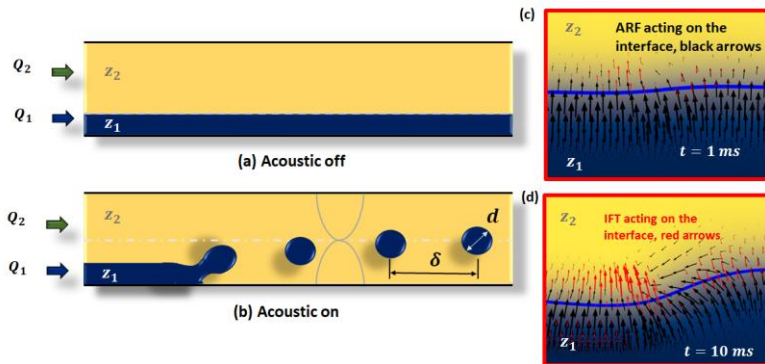
Figure 1: (a) Schematic of the coflow system with fluid 1 and fluid 2 without the acoustic field, (b) Break up of fluid 1 into droplets is shown when the acoustic is on. Simulation images showing the droplet break-up mechanism, (c) the black arrows show the direction of the acoustic radiation force (ARF), (d) interface deflection at t = 10 ms, and the red arrows depict interfacial tension force (IFT).

Results and Discussion

The transient behavior of stream-to-droplet relocation is illustrated in Figure 2(a) when the acoustic fields are turned on at t = 0 s. When the field is turned on, the acoustic radiation pressure is developed at the interface

between the liquids. The acoustic radiation force (ARF) is directed from the higher-impedance fluid to the lower-impedance fluid, as shown in Figure 1(c) at t = 1 ms. The acoustic radiation force acting on the fluid interface deforms the interface, as shown in Figure 1(d). Subsequently, the interfacial tension force is developed at the deformed interface, augmenting the process. Therefore, the interfacial instability grows, and the continuous fluid flow eventually breaks into droplets. The capillary number for fluid 1 and fluid 2 is considered to be 0.062 and 0.083, respectively. The average acoustic energy density E_{ac} in Eqn. (1) is taken to be 50 J/m^3 so that the ARF dominates over interfacial tension force (i.e., the acoustocapillary number, $Ca_{ac} > 1$)[3]. The density and viscosity of the fluid 1 is taken as 1207 kg/m^3 and 47.3 mPa × s respectively. The density and viscosity of the fluid 2 is considered as 857 kg/m^3 and 26.5 mPa × s, respectively.

The flow rates of the two coflowing fluids have a key influence on controlling the size and inter-distance between the droplets. By keeping the flow rate of fluid 1 constant, the effects of the flow rate ratio on the size and inter-distance between droplets are studied by varying the flow rate of fluid 2. As the flow rate of fluid 2 increases, the droplet size decreases, $d/W \propto (Q_2/Q_1)^{-0.42}$ as shown in Figure 2(e). As the flow rate of the fluid 1 increases, the shear rate of fluid 2 also increases, and consequently, the time required for the break-up of the interface decreases. Variation of droplet's inter-distance with the flow rate ratio is of the order, $\delta/W \propto (Q_2/Q_1)^{0.4}$.

The effect of the viscosity of fluid 1 on the size and inter-distance between the droplets is presented in Figure 2(f). As the viscosity ratio increases, i.e., $\mu_1/\mu_2 > 3.0$, a constant value of droplet size ($d/W \sim 0.5$) and interdistance ($\delta/W \sim 2.2$) is reached. As the viscosity of fluid 1 increases, the viscous effects become more significant, which slows down the droplet's break-up process and increases the inter-distance between the droplets. Further, due to the viscous effects, the time required to split the droplets from the neck region increases; hence, the droplet diameter increases.
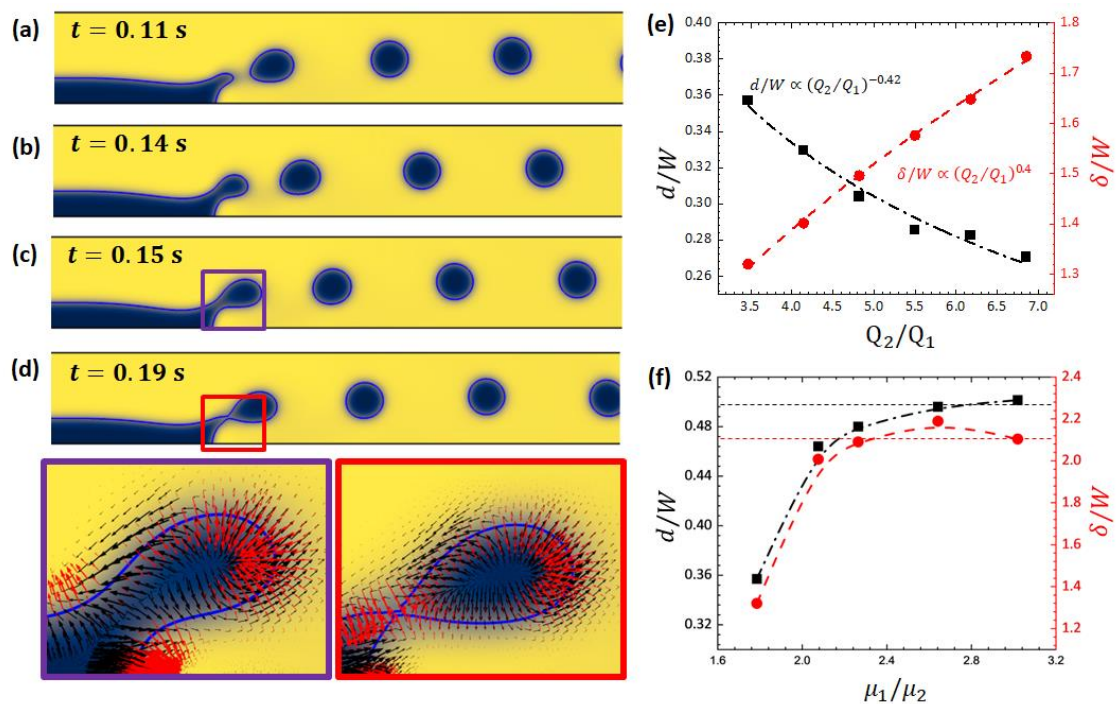
Figure 2: Transient images of the droplet break-up due to ARF obtained from the numerical simulations, (a) t = 0.11 s, (b) t = 0.14 s, (v) t = 0.15 s, (d) 0.19 s, inset images show the competition of the ARF(black arrows) and IFT(red arrows) forces at the fluid interface (e) Effects of flow rate ratio on the droplet size and inter distance between he droplet, (f) Variation of droplet diameter and inter-distance with the viscosity ratio of the two fluids.

Conclusion
Using bulk acoustic waves, we demonstrated an on-demand droplet generation from the co-flowing streams. The acoustic instability due to ARF induces the deformability of the interface, overcoming the interfacial tension force and producing droplets from the co-flowing streams.

References
[1] G. Hertz and H. Mende, Z. Phys. 114, 354 (1939).
[2] C. P. Lee and T. G. Wang, J. Acoust. Soc. Am. 94, 1099 (1993).
[3] E. Hemachandran, S. Z. Hoque, T. Laurell, A. K. Sen, Phys. Rev. Lett. 127(13), 134501 (2021).
[4] S. Z. Hoque and A. K. Sen, J. Acoust. Soc. Am. 155, 1655–1666 (2024).

Numerical study of acoustic streaming in spherical droplets suspended in unconfined media

Pradipta Kr. Das[1,*], Carl D. Meinhart[2], and Maria Tenje[1]

[1]Division of Biomedical Engineering, Department of Materials Science and Engineering, Science for Life Laboratory, Uppsala University, Uppsala, Sweden
[2]Department of Mechanical Engineering, University of California, Santa Barbara, California, United States
*E-mail: pradipta.das@angstrom.uu.se

Introduction

In droplet acoustofluidics, ultrasound is used in microfluidic systems to produce, load, process, or manipulate micron-sized tiny droplets, offering unparalleled precision in focusing cells or particles [1]. Such systems have emerged as a powerful tool for various biomedical applications, starting from drug delivery to single-cell analysis. It is already known that the interaction of acoustics and fluids causes oscillatory acoustic pressure and velocity fields, and in addition to that, steady acoustic streaming evolves slowly due to the nonlinear viscous effect of the fluids [2]. To understand the acoustic-fluid interactions and calculate the acoustic forces acting on tiny droplets, theoretical studies are required. However, only a few analytical studies [3-5] are available on the acoustic streaming inside and around fluid droplets, where viscous liquid droplets in the gaseous medium are considered. Baasch et al. [6] extended the study and presented results for various fluid droplets immersed in both liquid and gases such as air, water, silicone oil and fluorinated (HFE) oil.

While these analytical studies provide a very good understanding of acoustic streaming, numerical models are still needed as they have the flexibility to study complex two-phase systems for which analytical solutions are not available. In this work, we have presented a numerical model of droplet acoustofluidics and validated some of the results with analytical studies from the literature.
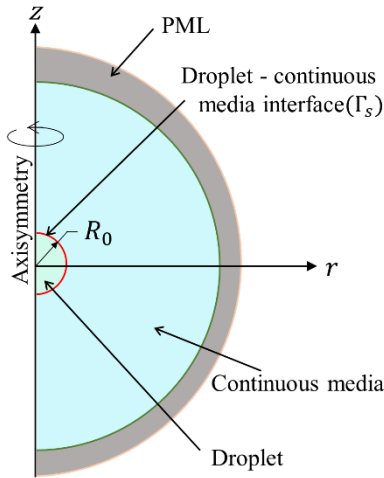
Figure 1: Computational domain comprising a fluid droplet of radius R_0, suspended in an immiscible fluid. PML is used to mimic unconfined domain.

Problem description and Mathematical formulations

We considered a fluid droplet of radius R_0, suspended in an immiscible fluid of infinite extent, subjected to an ultrasonic standing wave of frequency f_0 (angular frequency $\omega = 2\pi f_0$). We considered the droplet to be placed at the pressure node. Both droplet and the outside fluid are assumed to be compressible Newtonian fluids and their motion is governed by continuity and Navier Stokes equations,

$$\partial_t \rho_i + \nabla.(\rho_i \boldsymbol{v}_i) = 0 \qquad (1)$$
$$\rho_i[\partial_t \boldsymbol{v}_i + (\boldsymbol{v}_i.\nabla)\boldsymbol{v}_i] = -\nabla p_i + \mu_i \nabla^2 \boldsymbol{v}_i + (\mu_{bi} + \mu_i/3)\nabla(\nabla.\boldsymbol{v}_i) \qquad (2)$$

Here ρ, μ, and μ_b denote the density, dynamic viscosity, and bulk viscosity of the fluid, p and $\boldsymbol{v}$ are fluid pressure, and flow velocity respectively, subscripts $i = d, m$ denote droplet and continuous medium, respectively. We also denote the droplet-continuous medium interface as $\boldsymbol{\Gamma}_s$. The fluid pressure and fluid density can be correlated as $p_i - p_{i0} = c_i^2(\rho_i - \rho_{i0})$ where p_{i0} and ρ_{i0} are equilibrium fluid pressure and density, c_i is the sonic speed of ith phase, respectively. Due to the presence of inherent fast and slow timescales, we used the regular perturbation technique as $g = g_0 + g_1 + g_2$ where g represents ρ, $\boldsymbol{v}$, or p, and obtain the first-order equations governing the acoustic fields and the second-order equations describing the acoustic streaming.

Utilizing the perturbation expansions, the governing equations for first-order fields are

$$\partial_t \rho_{i1} + \rho_{i0}\nabla.\boldsymbol{v}_{i1} = 0 \qquad (3)$$
$$\rho_{i0}\partial_t \boldsymbol{v}_{i1} = -\nabla p_{i1} + \mu_i \nabla^2 \boldsymbol{v}_{i1} + (\mu_{bi} + \mu_i/3)\nabla(\nabla.\boldsymbol{v}_{i1}) \qquad (4)$$

The associated boundary conditions at the droplet-outside medium interface (on $\boldsymbol{\Gamma}_s$) are given by:
(i) $\boldsymbol{v}_{d1} = \boldsymbol{v}_{m1}$, and (ii) $\boldsymbol{\sigma}_{d1}.\boldsymbol{n} = \boldsymbol{\sigma}_{m1}.\boldsymbol{n}$. Here $\boldsymbol{n}$ is the unit vector along the normal of surface $\boldsymbol{\Gamma}_s$, and $\boldsymbol{\sigma}_{i1} = \mu_i(\nabla \boldsymbol{v}_i + \nabla \boldsymbol{v}_i^T) + (\mu_{bi} - 2\mu_i/3)(\nabla.\boldsymbol{v}_i)\boldsymbol{I}$ is the first-order stress tensor. The governing equations for second-order flow fields are expressed in a time-averaged form where time-averaging has been performed similarly as reported previously [7]. We seek steady second-order fields and set time dependence to zero, leading to

$$\nabla.\langle\rho_{i1}\boldsymbol{v}_{i1}\rangle + \rho_{i0}\nabla.\boldsymbol{v}_{i2} = 0 \qquad (5)$$
$$\langle\rho_{i1}\partial_t \boldsymbol{v}_{i1}\rangle + \rho_{i0}\langle(\boldsymbol{v}_{i1}.\nabla)\boldsymbol{v}_{i1}\rangle = -\nabla p_{i2} + \mu_i \nabla^2 \boldsymbol{v}_{i2} + (\mu_{bi} + \mu_i/3)\nabla(\nabla.\boldsymbol{v}_{i2}) \qquad (6)$$

For the second-order pressure, and flow fields, we consider the following boundary conditions at the interface $\boldsymbol{\Gamma}_s$: (i) $\boldsymbol{v}_{d2} + \boldsymbol{v}_{d2s} = \boldsymbol{v}_{m2} + \boldsymbol{v}_{m2s}$ (ii) $(\boldsymbol{v}_{d2} + \boldsymbol{v}_{d2s}).\boldsymbol{n} = (\boldsymbol{v}_{m2} + \boldsymbol{v}_{m2s}).\boldsymbol{n} = \boldsymbol{0}$ (iii) $\boldsymbol{t}.(\boldsymbol{\sigma}_{d2} + \boldsymbol{\sigma}_{d2s}).\boldsymbol{n} = \boldsymbol{t}.(\boldsymbol{\sigma}_{m2} +$

$\sigma_{m2s}).\boldsymbol{n}.$ Here, we assume the droplet shape remains spherical, and only balanced by the tangential stress components. $\boldsymbol{v}_{i2s}$ and $\boldsymbol{\sigma}_{i2s}$ are Stokes drift velocity and shear stresses, respectively, and $\boldsymbol{t}$ is the unit vector along the surface tangent.

Numerical setup and Model validations

In this work, the problem described above has been solved numerically using finite element-based software COMSOL Multiphysics 6.1. The problem is axisymmetric and therefore, only a 2D-axisymmetric domain has been considered for our numerical study as shown in Figure 1. We used a perfectly matched layer (PML) to absorb all the outgoing waves mimicking the computational domain equivalent to an unconfined domain. The ultrasonic standing wave actuated in the continuous fluid medium can be described by the associated background pressure and velocity fields as $p_b = p_0 sin(k_m z)e^{i\omega t}$ and $v_b = (i\,p_0/\rho_{m0}c_m)cos(k_m z)e^{i\omega t}$ where p_0 is the background pressure amplitude and k_m id the wave number in continuous medium ($k_m = \omega/c_m$). Before we proceed with our study results, we first validated our model to the analytical results from Baasch et al. [4] for a water droplet in air and a HFE oil droplet in air for $R_0 = 20\mu m$, $f_0 = 1MHz$, $p_0 = 1\,Pa$, considering monopole and dipole oscillations of a standing wave. The properties of the fluids have been taken from reference [4]. Our numerical results agree quite well (within $\pm10\%$) with the analytical predictions.

Results and Discussions

Figure 2 shows the acoustic fields along with the acoustic streaming for an olive oil droplet in air. The droplet size is 40 μm and the standing wave pressure amplitude is $p_0 = 100\,Pa$. The properties of olive oil have been taken from reference [8]. We observed significant acoustic velocity gradient in the air near the droplet/oil interface whereas the variation of the acoustic velocity inside the droplet is negligibly small compared to the that at the outside. Due to that, we observed strong microstreaming vortices in the air adjacent to the droplet surface. This type of vortices is absent on the inner side of the interface.
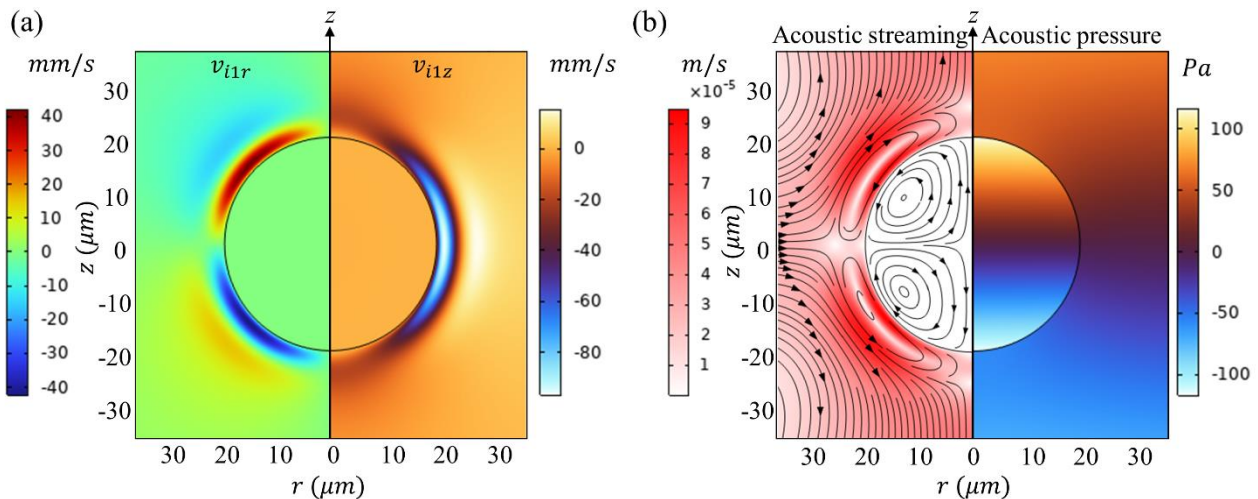
Figure 2: (a) Acoustic velocity components (left: radial and right: axial) in and around an olive oil droplet suspended in air. The droplet is of 40 μm diameter and subjected to 1 MHz standing wave with pressure amplitude p_0 =100 Pa. (b) Acoustic streaming with streamlines (left) and acoustic pressure (right) for the same scenario.

Conclusion

We have developed a numerical model for the acoustic streaming around fluid droplets suspended in an unbounded immiscible fluid. We adopted the perturbation technique and obtained the acoustic fields and streaming velocity by solving the first-order equations in the frequency domain, and the second-order equations in the stationary domain. The model has been validated successfully by comparing its results with available analytical solutions from the literature. We show acoustic streaming for olive oil droplets in air and observed strong microstreaming around the droplet. The model can be extended further for complex geometries, and fluid properties, providing thorough insights relevant to practical droplet-based acoustofluidic systems.

References

[1] J. Rufo, F. Cai, J. Friend, M. Wiklund, T. J. Huang, *Nat Rev Methods Primers* **2**, 30 (2022).
[2] S. J. Lighthill, *J. Sound Vib*. **61**, 391 (1978).
[3] J. Wu, G. Du, *J. Acoust. Soc. Am*. **101**, 1899 (1997).
[4] H. Zhao, S. S. Sadhal, E. H. Trinh, *J. Acoust. Soc. Am*. **106**, 3289 (1999).
[5] A. Y. Rednikov, H. Zhao, S. S. Sadhal, *Q. J. Mech. Appl. Math*. **59**, 377 (2006).
[6] T. Baasch, A. A. Doinikov, J. Dual, *Phys. Rev. E* **101**, 013108 (2020).
[7] P. K. Das, A. D. Snider, V. R. Bhethanabotla, *Phys of Fluids*, **31**, 106106 (2019).
[8] A. Fornell, F. Garofalo, J. Nilsson, H. Bruus, M. Tenje, *Microfluid Nanofluidics* **22**, 75 (2018).

Droplet Dynamics Beyond the Rayleigh Limit under acoustic-gravity forces: A Route to Extract Specific Droplet Sizes from a Broad Range.

Jeyapradhap Thirisangu[1] and Karthick Subramani[1,*]

[1]Department of Mechanical Engineering, Indian Institute of Information Technology Design and Manufacturing, Kancheepuram, India
*E-mail: karthick@iiitdm.ac.in

Introduction

In this paper, we study the droplet dynamics beyond the Rayleigh limit under acoustic fields using numerical and theoretical analysis. We demonstrate that the suspension behavior of the droplet is determined by the interplay between the acoustic and gravity forces. Remarkably, we show that at specific frequencies of the wavefield and E_{ac}, the acoustic force exerted on the smaller droplet is capable of counteracting gravity ($F_{ac} = F_g$), resulting in suspension, whereas in larger droplet, gravity dominates acoustic force ($F_{ac} < F_g$) leading the droplet to settle. Interestingly, by controlling frequency, an inverse scenario is observed, where smaller droplet settles while larger droplet undergoes suspension. Unlike the conventional sorting, using this technique the specific droplet sizes can be extracted from the broad range.

Governing Physics

The dynamics of the droplets subjected to acoustic fields are governed by the following equations,

$$\nabla . v = 0 \tag{1}$$

$$\rho \, {Dv}/{Dt} = -\nabla p + \eta \nabla^2 v + \beta \eta \nabla (\nabla . v) + f_g + f_{ac} + f_\sigma \tag{2}$$

$$\partial_t \emptyset + v . \nabla \emptyset = \nabla . \frac{\gamma \tau}{\varepsilon^2} \nabla (-\nabla . \varepsilon^2 \nabla \emptyset + (\emptyset^2 - 1)\emptyset) \tag{3}$$

where ρ is the density, v is the velocity, p is the pressure, η is the dynamic viscosity of the fluid, ξ is the bulk viscosity, $\beta = (\xi/n) + (1/3)$, $\emptyset$ is volume fraction, γ is mobility tuning parameter, τ is the mixing energy density, f_{ac} is the acoustic force, f_g is the gravity force, and f_σ is the interfacial tension force. In our previous experimental work [1], we show that the minimum acoustic power (P_{min}), minimum acoustic energy density (E_{min}) required to suspend the droplets are a function of the droplet size up to $d/\lambda = 0.5$. Now, we proceed to numerically investigate the behavior of droplets beyond the Rayleigh limit under the acoustic fields and gravity. For the numerical analysis, a channel of $12 \, mm$ width (w) and $6 \, mm$ height (h) is considered with water ($\rho = 1000 \, kg/m^3$, $c = 1500 \, m/s$) as the dispersed medium and mineral oil ($\rho = 857.5 \, kg/m^3$, $c = 1440 \, m/s$) as the continuous medium. The analysis is carried out using COMSOL Multiphysics 6.0.

Results and Discussion

Interestingly, for the given two droplet sizes beyond the Rayleigh limit, our findings indicate that at a certain frequency of the wavefield and E_{ac}, the net acoustic force acting on the smaller droplet can suspend it against gravity ($F_{ac} = F_g$),whereas for larger droplets gravity dominates the net acoustic force ($F_{ac} < F_g$) results in settling as shown in the Fig. 1a. By changing the frequency, the opposite of the above is also observed where smaller droplet settles and larger droplet suspends as illustrated in the Fig. 1b. Additionally, droplets of any specific size can be suspended within a given broad range of sizes, as depicted in Fig. 1c by controlling frequency. Let us proceed to understand, how this phenomenon is achieved.

When an acoustic field is not present, a higher-density droplet (water) settles in a lower-density continuous medium (mineral oil) due to the balance between gravity and drag forces. Whereas, in the presence of both gravity and an acoustic field, the behavior of the droplets is governed by the interplay between these forces, resulting in either the suspension or settling of the droplets within the medium. Unlike the gravity force which is uniform and always acts downward along the y direction as shown in the Fig. 2a, the acoustic force is non-uniform and its direction either upward or downward along the y direction depends on the position of the portion of the droplet with respect to node (Fig. 2a). If the applied acoustic energy (E_{ac}) is strong enough to overcome gravity (F_g), the droplet suspends in the medium. When the applied acoustic energy (E_{ac}) is insufficient to counteract gravity, the droplet settles. Unlike the case of droplets of size $d < \lambda/4$ which is completely accommodated in the positive acoustic force region, some portion of the droplets of size $d > \lambda/4$ is always present in the negative acoustic force region as shown in the Fig 2a. Thus to suspend the droplets of size $d > \lambda/4$, the positive acoustic force acting on a portion(s) of the droplet not only opposes the gravity force but also counteracts the negative acoustic force acting on the other portion(s) of the same droplet as shown in Fig. 2a. Because of this reason, the net volume available for the positive acoustic force (V_{net}) is significantly less than the total volume of the droplet.
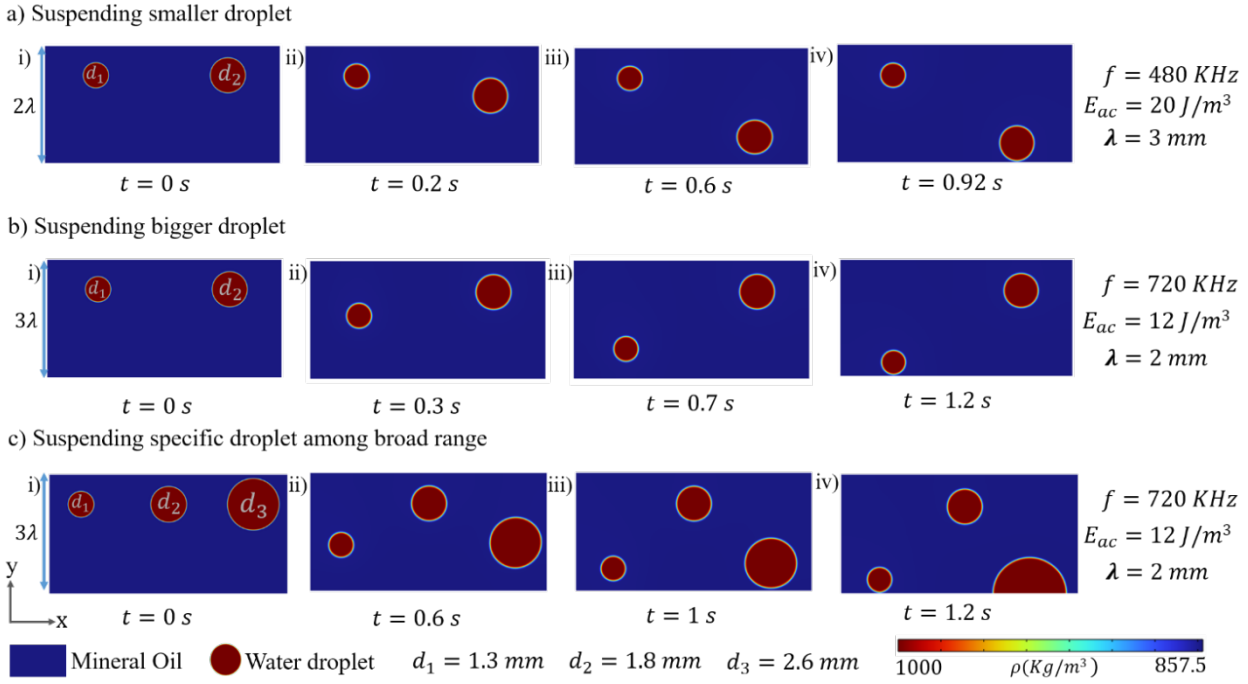
Figure 1: Sorting of the droplet among a given broad range of droplets a) suspending the smaller droplet b) suspending larger droplet c) suspending specific droplet.

For a given frequency, when the net volume available for the positive acoustic force (V_{net}) acting on the droplet is less, the minimum acoustic energy density (E_{min}) required to suspend the droplet is more, and vice versa. The variation in the net volume available for the positive acoustic force (V_{net}) with respect to the d/λ is non-monotonous as shown in the Fig. 2b. Surprisingly, for a given frequency, V_{net} for the smaller droplet can be more than the V_{net} of the larger droplet and vice versa as shown in the Fig. 2b. From this, it is evident that the E_{min} required to suspend the smaller droplet can be greater than the larger droplet and vice versa. This interesting phenomenon gives the pathway to manipulate the suspension of the droplets among any given broad range.
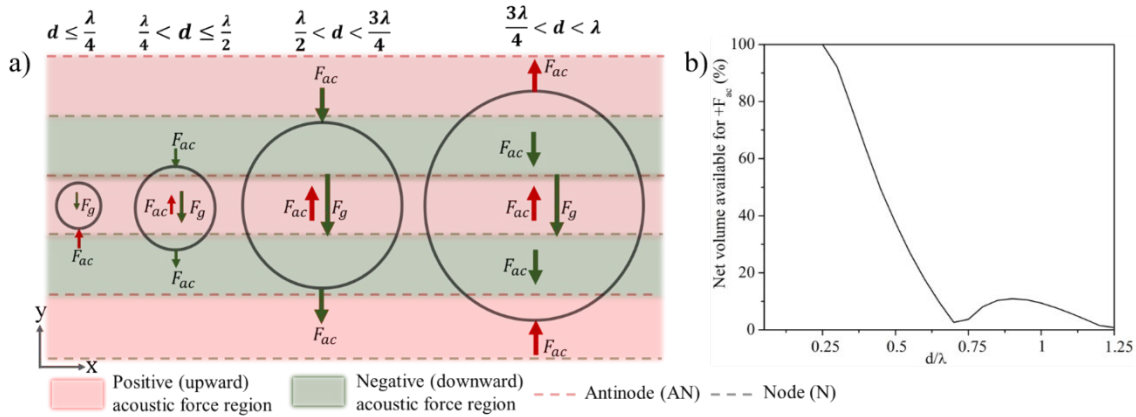
Figure 2: a) Schematic representation of the interplay between the acoustic and gravity forces of different droplet sizes. b) Available net volume (V_{net}) for the positive acoustic force acting on droplets with respect to the d/λ.

Conclusion

We demonstrated the interplay between the acoustic force and gravity to suspend the droplet beyond the Rayleigh limit. Since variation in the net volume available for the positive acoustic force (V_{net}) with respect to the d/λ is non-monotonous, surprisingly for a given frequency, V_{net} for the smaller droplet can be more than the V_{net} of the larger droplet and vice versa. Consequently, the E_{min} required to suspend the smaller droplet can be greater than the larger droplet and vice versa. This interesting phenomenon gives a route to extract specific droplet sizes from a broad range.

References
[1] Jeyapradhap Thirisangu, E. Hemachandran, and Karthick Subramani. Suspending droplets beyond the Rayleigh limit: The interplay of acoustic and gravity forces. Phys. Fluids, 35(12), AIP Publication, December 2023.

Acoustic-Driven Liquid Atomization for Nanosatellite Maneuvering

Amihai Horesh[1,*], William Connacher[2], and James Friend[2]

[1]Department of Agriculture Engineering, Agriculture Research Organizing, Rishon LeZion, Israel
[2]Depratment of Mechanical and Aerospace Engineering, University of California San Diego, USA
[*]E-mail: amihaih@volcani.agri.gov.il

Introduction

The increasing deployment of miniature "CubeSat" satellites for diverse space missions, ranging from telecommunications, to interplanetary exploration, and burgeoning space tourism, highlights the growing demand for small-scale thrusters to facilitate their maneuverability. Yet, achieving efficient thrust generation, particularly in satellites weighing around 100 kg or less, remains a persistent challenge. Existing technological solutions have often fallen short of meeting the required specifications [1].

In this study, we propose a novel method for generating microNewton-scale thrust using 60 MHz acoustic waves to create a directed atomized spray [2]. This approach not only addresses the challenge of efficient thrust production, but also mitigates the risk of freezing of the working fluid, a common issue in liquid-thrust systems exposed to the extreme thermal conditions of space. By harnessing acoustic energy for both heating and atomization, we demonstrate its effectiveness in supporting solid/liquid phase transition and producing controlled thrust.

Our experimental results corroborate the viability of this approach [3]. We observe that the specific impulse and thrust of this thruster, though modest at 0.1–0.4 s and 0.7–12.3 μN respectively, represent a promising alternative to current microthruster technologies. Furthermore, our findings are supported by a simple energy conservation model, underscoring the potential of acoustofluidic systems for microthruster applications in space exploration.

Theory and Experimental procedure

Experimental Procedure:
The experimental setup utilizes a focused 60 MHz surface acoustic wave (fSAW) device constructed with lithium niobate (LN) specifically engineered to induce thrust through the atomization of water supplied via a 100 μm nozzle. The fSAW device was carefully positioned atop a Peltier thermoelectric control (TEC) module to facilitate precise control over the freezing conditions of the working fluid placed on the device as shown in Fig. 1. Initially, we introduced a 1 μl droplet of dyed de-ionized (DI) water onto the fSAW device and allowed it to undergo freezing under the influence of the TEC. Upon activation of the fSAW, we monitored the solid/liquid phase transition of the working fluid, followed by atomization induced by the acoustic excitation.

Theory:
We characterized the melting process induced by the acoustic excitation as a function of the response time required for a CubeSat to orient its trajectory within its orbit. To predict this response time, we developed a simple mathematical model derived from the first law of thermodynamics. This model comprehensively incorporates the work performed and the heat transferred via conductivity from the oscillating acoustic device to the droplet, as well as the radiation exchanged between the droplet and its surroundings.
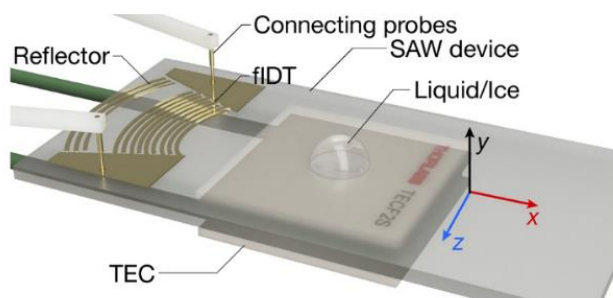
Figure 1: Acoustic device positioned on a thermoelectric unit enables freezing of a liquid droplet. 60 MHz surface acoustic waves induce solid/liquid phase transition within the droplet, facilitating subsequent atomization and generation of microscale thrust [3].

Results and Discussion

The melting process, depicted in Fig. 2, demonstrates complete melting within seconds, in line with our mathematical model's predictions. At low input power, melting was only achieved at the highest initial temperature, consistent with model projections. Melting time increased with lower temperatures and reduced

input power, but at high power levels, minimal differences were observed across starting temperatures, suggesting greater influence of conduction and radiation at lower power levels. The energy introduced by the acoustic device predominates at high power levels. Furthermore, latent heat emerges as the principal component driving phase changes.
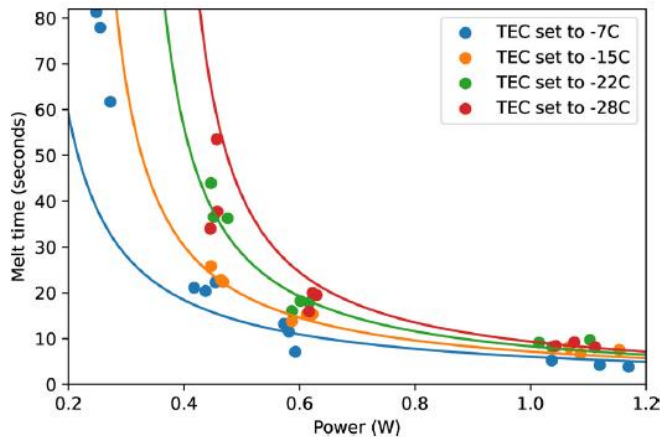
Figure 2: Experimental data and model predictions illustrating the time required to melt a 1 µl frozen water droplet from various equilibrium temperatures. No experimental data points appear below a certain power threshold where droplets did not melt when the thermoelectric control (TEC) was set below -10°C. Droplets consistently melted within 10 seconds or less when employing 1W or more for the focused surface acoustic wave (fSAW) excitation [3].

Atomization was side view captured at 6400 frames per second (fps) to determine the exit velocity of atomized droplets for various fSAW power inputs, as detailed in Table 1. The exit velocity of the working fluid and the mass flow rate were utilized to calculate the equivalent thrust. Notably, each atomized droplet is ejected in the direction of the net acoustic wave propagation within the parent droplet, making our estimated thrust reasonable. The uniform surface tension surrounding each atomized droplet is maintained due to the parent droplet's larger size, minimizing curvature issues during ejection. Additionally, the subsequent dispersion of droplets is primarily influenced by drag from the surrounding quiescent air. This contrasts with droplet ejection from an orifice, where drag by the orifice alters the trajectory of ejected droplets, potentially causing significant momentum away from the main atomization axis.

Table 1: Thrust and Specific Impulse Data from Experimental Results

Input power (Watts)	Thrust (µN)	Specific impulse (sec)
1.0	0.71	0.17
2.0	4.65	0.29
3.0	12.30	0.38

Conclusion

The device showcased in this study achieves melting and atomization of a 1 µl drop with an input power of approximately 1W, producing thrust ranging from 1–10 µN. While this thrust capability is notably lower than that of conventional thrusters, which typically range from 1mN to 10N, it presents an intriguing approach. Additionally, the specific impulse ranges from 0.1 to 0.4 seconds, indicating a significant decrease compared to cold gas thrusters (50 seconds) and electric thrusters (three orders of magnitude) [3]. Despite these differences, the compact size of the thruster, measuring 12 x 20 x 0.5 mm³ and weighing 0.6 grams, offers potential scalability. It's crucial to consider the mass of the working fluid, piping, and other components in comprehensive application design. Notably, a significant advantage of this method is the ability to finely adjust thrust direction and magnitude by simply modifying the drive signals input into the fIDTs, without requiring any moving parts.

Acknowledgements

References

[1] Information, N. center for A. State - of - the - Art Small Spacecraft Technology. NASA Tech. Rep. NASA/TP-2020 5008734 (2021).
[2] Connacher, W., Orosco, J. & Friend, J. Droplet Ejection at Controlled Angles via Acoustofluidic Jetting. Phys. Rev. Lett. 125, 184504 (2020).
[3] Horesh, A., Connacher, W. & Friend, J. Acoustothermal phase change and acoustically driven atomization for cold liquid microthrusters. Appl. Phys. Lett. 122, 014104 (2023).
[4] Krejci, D. & Lozano, P. Space Propulsion Technology for Small Spacecraft. Proc. IEEE 106, 362–378 (2018).

Acoustically Levitated Droplets for Chemical Reactions and Bioassays

Ruchi Gupta, School of Chemistry, University of Birmingham, UK
r.gupta.3@bham.ac.uk

Chemical reactions and bioassays can be performed in droplet microfluidic devices to increase automation and reduce sample and reagent volumes. In current microfluidic devices, however, (1) droplets are in contact with either solid walls or immiscible liquids [1], and (2) operations on droplets are conducted on two-dimensional surfaces [2] (see Figures 1 (a)). While the former can result in loss of sample/reagents and cross-contamination, the latter can limit throughput per unit footprint of devices. These issues can be addressed by performing reactions in levitated droplets as shown in Figure 1 (b). Furthermore, acoustic forces are beneficial because droplets of up to 100 µL of all types of materials can potentially be levitated stably [3].

In this presentation, I will describe our studies on an oscillatory chemical reaction (Belousov–Zhabotinsky (BZ) reaction) [4] and a bioassay (fluorescein diacetate (FDA) and esterase enzyme assay) in acoustically levitated droplets. For the BZ reaction, our studies showed that the oscillation period in acoustically levitated droplets are consistent with previous work carried out in cuvettes, test tubes, vials, and beakers. We have also shown that it is possible to perform multiple simultaneous reactions with good reproducibility and repeatability, thus opening the possibility of using acoustic levitation for high-throughput experimentation. Similarly, for the FDA esterase enzyme assay, the enzyme kinetics in acoustically levitated droplets are consistent with previous work carried out in cuvettes. In addition, the solution volume used in the levitator was 4 µL compared to 3 mL in vials, a reduction by a factor of 750, making this method well suited for experimentation with high-cost materials.

Future work will focus on increasing the number of levitated droplets and automating the initial loading of our acoustic levitators and subsequent addition of droplets to minimise user interventions and errors.
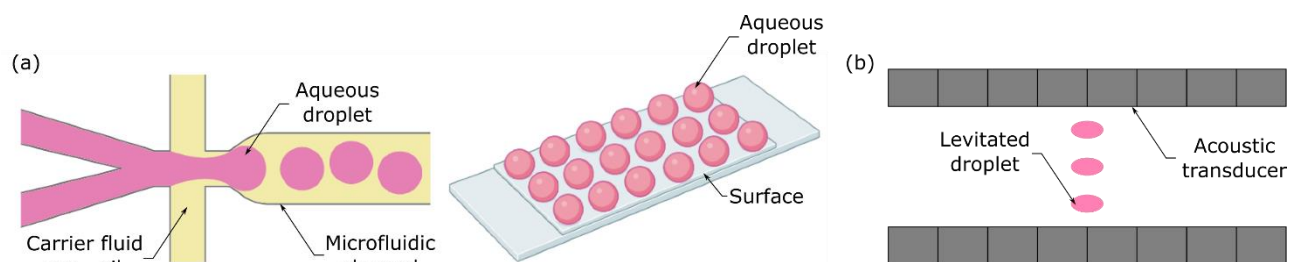
Figure 1: Droplets in (a) current microfluidic devices and (b) acoustic levitators

References

[1] G. Etienne, A. Vian, M. Biočanin, B. Deplancke, E. Amstad, Cross-Talk Between Emulsion Drops: How Are Hydrophilic Reagents Transported Across Oil Phases?, Lab on a Chip, **2018**, 3903.
[2] M.J. Jebrail, M.S. Bartsch, K.D. Patel, Digital Microfluidics: A Versatile Tool for Applications in Chemistry, Biology and Medicine, Lab on a Chip, **2012**, 12, 2452.
[3] M.A.B. Andrade, T.S.A. Camargo, A. Marzo, Automatic Contactless Injection, Transportation, Merging, and Ejection of Droplets with a Multifocal Point Acoustic Levitator, Review of Scientific Instruments, **2018**, 89, 125105.
[4] R. Songsaeng, N.J. Goddard, R. Gupta, An Investigative Study into an Oscillatory Reaction in Acoustically Levitated Droplets, RSC Advances, **2023**, 13, 30002.

Acoustofluidic Sorting of Red Blood Cells using Real-time Machine Vision

Raj Kumar Rajaram Baskaran[1,*], Andreas Link[1] and Thomas Franke[1]

[1]Department of Biomedical Engineering, University of Glasgow, Scotland, United Kingdom

[*]E-mail: RajKumar.RajaramBaskaran@glasgow.ac.uk

Introduction

This work presents an integrated system for real-time sorting of red blood cells (RBCs) in a microfluidic device using machine vision, machine learning, and acoustofluidic actuated sorting. Background subtraction extracts RBCs images from microscopy videos [1], and a deep convolutional neural network (CNN) classifies detected cells as "native" or "modified" based on optical features [2]. The classified cells are then sorted into separate outlets using an interdigital transducer (IDT) that generates acoustic streaming in the channel to deflect cells into one of two outlet channels. The machine learning classification [3] model has been implemented on a standard computer for real-time classification into two classes of RBCs. The two types of cells are then directed in two separate outlet channels. The low-latency pipeline enables accurate, label-free sorting at throughputs suitable for biomedical applications.

Theory and Experimental procedure

The core of the acoustofluidic sorting system is a microfluidic channel with an integrated IDT at the end. The IDT consists of parallel electrodes patterned on a piezoelectric substrate (lithium niobate) that generates a surface acoustic wave. The wave is triggered by a TTL signal from the AI based classifier if the classifier identifies the cell as a target or non-target. The cell is then deflected into a collect channel or a waste channel. The setup is mounted on an inverted microscope equipped with a high-speed camera. The video frames are processed in real-time using a background subtraction algorithm (Gaussian Mixture Model) to isolate the image of the RBC from any background and noise. The extracted RBC images are then fed into a pre-trained CNN classifier, which predicts whether each cell is native or modified based on its features as shown in Fig.1.
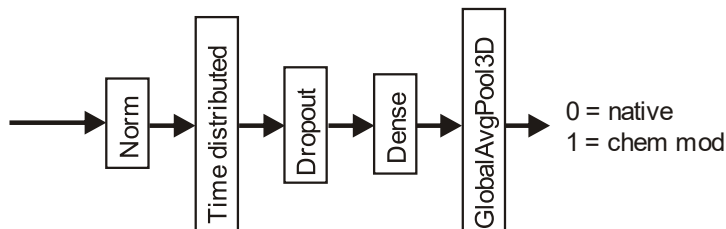
Figure 1: TensorFlow pipeline: Norm (0-1 rescaling), TimeDistributed (EfficientNetB0 per video frame), Dropout (prevents overfitting), dense (standard layer), GlobalAvgPool3D (pooling). Two outputs: native & modified RBC detection. [3]

Upon classification, a control signal is sent to the IDT, modulating the acoustic field to deflect the classified modified cells into a separate output channel, while native cells continue along the main flow path. This system, implemented on a Linux computer (Ubuntu kernel) with TensorFlow and OpenCV, enables high-throughput, label-free RBC sorting based on optical properties via real-time video processing and CNN inference [4].

Results and Discussion

The integrated acoustofluidic sorting system demonstrates the ability to perform real-time, label-free sorting of red blood cells. The Gaussian Mixture Model (MOG) background subtraction algorithm achieves a low latency of approximately 3ms per video frame, enabling efficient extraction of RBC regions from the microscopy videos. It takes 7ms for the classification after the background subtraction and sends a TTL signal to IDT to sort the RBC.

The deep convolutional neural network (CNN) classifier, trained on a dataset of native and chemically modified RBCs, showed high accuracy in distinguishing between the two cell types based on their optical features. Specifically, the CNN achieved an accuracy of 100% for classifying native cells but a slightly lower accuracy of around 80% for modified cells. This discrepancy in performance could be attributed to factors such as data imbalance in the training set or limitations in the CNN model architecture.

The IDT played a crucial role in deflecting the classified modified RBCs into a separate output channel. Through numerical simulations, the IDT design and operating frequency were optimized to generate acoustic streaming that efficiently deflected modified cells while minimizing the deflection of native cells. Acoustic streaming patterns were analyzed to ensure stable and consistent cell trajectories in the microfluidic channel.
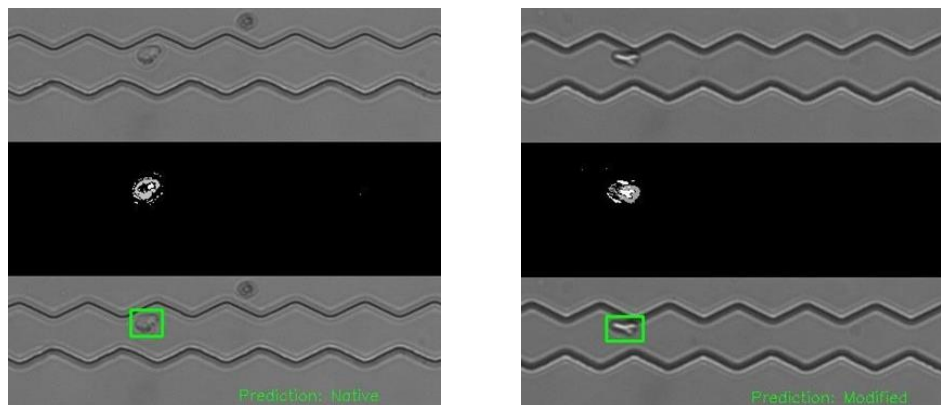
Figure 2: Background Subtraction and Red Blood Cell Type Inference: Native (left) vs Modified (right)

Conclusion

This work demonstrated the successful integration of machine learning, and acoustofluidics for real-time low latency sorting of red blood cells in a microfluidic device that operates label-free.

The system's performance highlights the potential of machine learning techniques for AI enhanced sorting for diagnostics and in biomedical applications. Additionally, integrating feedback control of the IDT based on the sorting results could further improve the system's high throughput performance and adaptability.

Acknowledgements

References

[1] A. Cioppa et al, *IEEE International Conference on Image Processing (ICIP),* 2020, pp. 3214–3218.
[2] M. Xu et al., *PLoS Comput. Biol.,* vol. 13, no. 10, p. e1005746, 2017.
[3]R. K. Rajaram Baskaran, et al., *Soft Matter*, 2024, 20, 952-958.
[4] M. R. Islam et al., *18th Biennial Baltic Electronics Conference (BEC),* 2022.

Acoustofluidic Characterization of the Effect of Staining on Cell properties

Qing Wang[1], Andreas Lenshof[1], Alexander Edthofer[1], Thierry Baasch[1], Thomas Laurell[1], and Wei Qiu[1]

[1]Department of Biomedical Engineering, Lund University, Lund, Sweden
E-mail: qing.wang@bme.lth.se

Acoustofluidics 2024
14-16 August 2024
Uppsala University, SWEDEN

Introduction

Cell staining techniques are essential tools in biology, pathology, and clinical diagnostics to enhance the optical contrast of cells and their components for observation and bioanalysis. Despite its important applications in various fields, the effects of staining processes (dye penetration, adsorption, or hydrogen bonding) on the physical properties of cells have not been well investigated. It has been demonstrated that the physical properties of cells, such as the effective acoustic impedance of single cells [1] and the averaged compressibility of a population of cells [2], can be measured using acoustofluidics. In this work, we study the migration of cells subject to a half-wavelength standing-wave field to characterize the effects of four different staining protocols on the physical properties of the breast cancer cell line MCF-7. Both the acoustic mobility ratio of the stained and unstained cells with respect to 5 μm green polystyrene particles and the cell effective acoustic impedance are measured.

Materials and methods

A standard glass-silicon-glass chip with a straight channel of 45 mm in length, 375 μm in width, and 150 μm in height is used for all the measurements. A 1-mm-thick PZT transducer is mounted to the side of the chip, which excites a half-wavelength standing-wave field along the channel width direction at 2 MHz. A half-wavelength standing-wave field can also be excited along the channel height direction at 5 MHz by a 0.4-mm-thick PZT transducer mounted to the device bottom, as shown in Figure 1(a). Four different dyes, i.e., DAPI, EpCAM, E-cadherin, and calcein AM, are selected to stain MCF-7 cells following their respective protocols.

To measure the acoustic mobility ratio between cells and 5 μm green polystyrene particles as well as the stained and unstained cells immersed in PBS solutions are infused to the channel one species at a time. The suspended particles or cells are first levitated to channel mid-height by the 5 MHz mode, then focused to the channel center by the 2 MHz mode when the 5 MHz PZT transducer is off, as shown in Figure 1(b). More than 30 repetitions are performed, resulting in more than 150 trajectories collected for each species. The individual trajectories of particles and cells are tracked using DefocusTracker [3]. The mean amplitude of focusing velocity v is obtained by fitting all the trajectories with the sinusoidal function, and the mobility ratio is calculated as $v_{cell}\xi_{cell}/v_{ref}\xi_{ref}$, where ξ_{cell} and ξ_{ref} are the wall correction factors for cells and particles [4]. Cell sizes are measured using the Coulter counter before the focusing experiments are performed.

For measuring the cell acoustic impedance, iodixanol solutions with different concentrations ranging from 4% to 31% are prepared. The iodixanol concentration has a direct impact on the acoustic contrast factor of the cells. Qualitatively we observe a transition from positive to negative acoustic contrast factor when increasing the iodixanol concentration from low to high, see Figure 1(c). By counting the number of cells migrating to node and anti-node, the cell effective acoustic impedance can be obtained from the cumulative distribution function (CDF) fitting of a normal distribution [5]. Only the tracking of polystyrene particles for mobility ratio measurements and the counting of calcein-stained cells for acoustic impedance measurements are performed using fluorescence imaging, while all the other experiments are conducted using phase-contrast imaging.
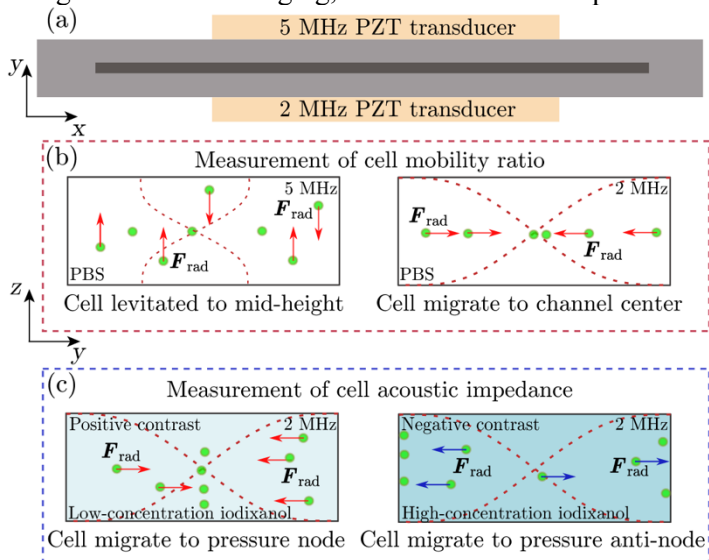
Figure 1: (a) Schematics of the acoustofluidic device used in this study. Two PZT transducers are mounted to the side and the bottom of the device to excite half-wavelength standing-wave fields in the channel width and height directions, respectively. (b) To measure the cell acoustic mobility ratio, the particles or the cells in PBS solutions experience the acoustic radiation force $\boldsymbol{F}_{rad}$ and are first levitated to channel mid-height using the 5 MHz mode, followed by focusing to the channel center using the 2 MHz mode. (c) The cell acoustic impedance is measured by immersing the cells in solutions of different iodixanol concentrations. By exciting the 2 MHz mode, the cells migrate to the pressure node in low-concentration iodixanol solutions due to the positive acoustic contrast factor, while they migrate to the pressure anti-node in high-concentration iodixanol solutions when the acoustic contrast factor becomes negative. The acoustic impedance of the cells and the iodixanol solution at the transition level is approximately equal.
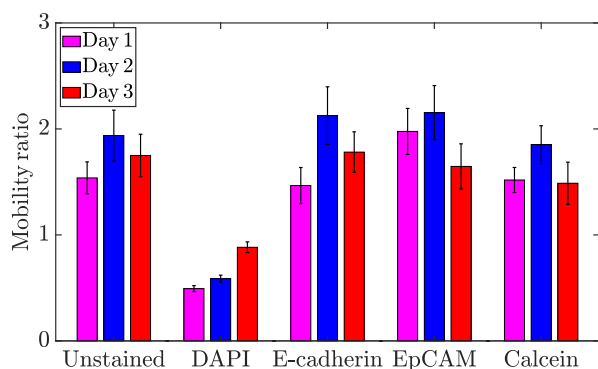
Figure 2: The measured acoustic mobility ratio of MCF-7 cells with respect to 5 μm green polystyrene particles. Experiments are performed on three different days, and on each day the measurements are carried out for unstained and stained (using four different dyes) cells. The error bars represent the 95% confidence interval.
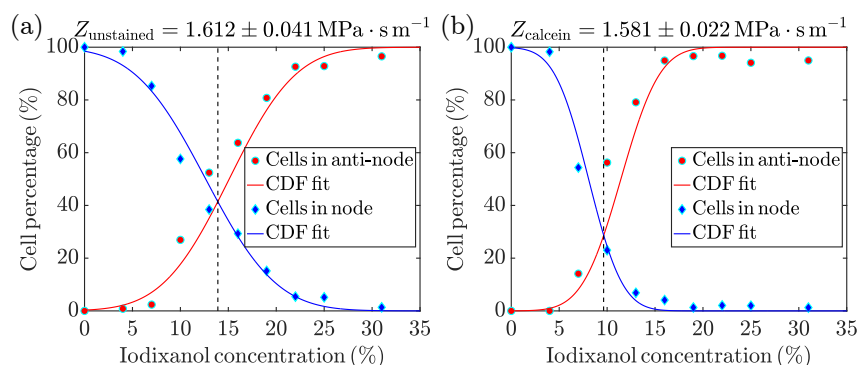
Figure 3: The measured effective acoustic impedance of unstained (a) and calcein-stained (b) cells obtained by fitting the cell percentage using the cumulative distribution function (CDF) of a normal distribution. The cell counts collected on three different days are combined, resulting in 240 to 600 total cell counts in each iodixanol concentration. The total number of counted cells also includes the cells following the acoustic streaming.

Results and discussion

We found the acoustic mobility ratio between MCF-7 cells and 5 μm green polystyrene particles to be much lower for DAPI-stained cells than that of the unstained cells, as shown in Figure 2. The decrease of the mobility ratio is in line with the decrease of the cell size from 21.3 ± 8.3 μm for unstained cells to 15.1 ± 7.6 μm after DAPI staining. The reason for the reduction of the cell size after DAPI staining is mainly due to the exposure of the cells to saponin, a required step in the DAPI staining protocol, which makes the cell membrane permeable in order for the DNA-stain to reach the cell nucleus. Day-to-day variations have been observed for each category of cells, but a significant change in cell acoustic mobility ratio is not detected for the cells stained using E-cadherin, EpCAM, and calcein.

In contrast to mobility ratio measurements, clear difference in effective acoustic impedance can be found when the cells migrate in iodixanol solutions with different concentrations. The majority of the unstained cells start to have a negative acoustic contrast factor, hence migrate to pressure anti-node, when the iodixanol concentration is higher than 14.4%, see Figure 3(a). However, the sign inversion of acoustic contrast factor occurs at an iodixanol concentration of 9.6% for calcein-stained cells, as illustrated in Figure 3(b). The intersection between the two CDF fitting curves for the cell percentage migrating to pressure node and anti-node represents the iodixanol concentration at which the cell acoustic contrast factor is zero, hence the cell effective acoustic impedance can be approximated to the acoustic impedance of the medium at this point [1]. The acoustic impedance of the MCF-7 cells displayed a reduction of 1.9% after calcein staining as compared to the unstained cells. Compared to the mobility ratio measurements, this method demonstrates a higher resolution for detecting the difference in cell properties. The same experiments were carried out for the MCF-7 cells stained with two types of membrane staining, but no change in cell acoustic impedance was found with 1.613 ± 0.045 MPa $\cdot$ s m^{-1} after E-cadherin staining and 1.609 ± 0.041 MPa $\cdot$ s m^{-1} after EpCAM staining.

Conclusion

In this work, we demonstrate the acoustofluidic characterization of the effect of staining on cell properties. A clear reduction in acoustic mobility is observed for the MCF-7 cells undergoing DAPI staining. A decrease as small as 1.9% in acoustic impedance is detected for calcein-stained MCF-7 cells by migrating them in different iodixanol concentrations, while no change in the cell acoustic impedance is found after membrane staining. The corresponding experiments will also be performed for other types of cancer cell lines and will be reported in the conference.

References

[1] P. Augustsson, J. T. Karlsen, H.-W. Su, H. Bruus and J. Voldman, *Nat. Commun.* **7** 11556 (2016)

[2] D. Hartono, Y. Liu, P. L. Tan, X. Y. S. Then, L.-Y. L. Yuan, and K.-M. Lim, *Lab Chip* **11** 4072 (2011)

[3] R. Barnkob and M. Rossi, *Exp. Fluids* **61** 110 (2020)

[4] A. Edthofer, J. Novotny, A. Lenshof, T. Laurell, and T. Baasch, *Anal. Chem.* **95** 10346 (2023)

[5] K. Olofsson, B. Hammarström, and M. Wiklund, *Lab Chip* **20** 1981 (2020)

Analytical solution of source term for bulk acoustic streaming with nonlinear propagation

Shiyu Li[1], Weiwei Cui[2], Thierry Baasch[3], Bin Wang[1,4], and Zhixiong Gong[1,4,*]

[1]State Key Laboratory of Ocean Engineering, School of Ocean and Civil Engineering, Shanghai Jiao Tong University, Shanghai, China
[2]State Key Laboratory of Precision Measuring Technology and Instruments, Tianjin University, Tianjin, China
[3]Department of Biomedical Engineering, Lund University, Lund, Sweden
[4]Key Laboratory of Marine Intelligent Equipment and System, Ministry of Education, Beijing, China
[*]E-mail: zhixiong.gong@sjtu.edu.cn

Introduction

The bulk (Eckart) acoustic streaming [1] comes from the acoustic absorption in the fluid volume when acoustic waves propagate inside. Recent developments with the frequency up to GHz have been made for nano-sized biosensors [2], nanoliter microreactors [3], and microfluid jet producer [4]. As is known that the computational cost is extremely large to solve a three-dimensional (3D) streaming problems based on the direct numerical simulations. A recent work proposes a method to solve this issue into two parts: the computation of acoustic propagation and the solution to the Stokes equation for a steady fluid motion with a source term [5]. Another work also obtains the same formulas of source term by using the conception of acoustic radiation force driving the motion of the absorbed fluid [6]. However, these formulas are not direct to solve the bulk streaming with nonlinear propagation, e.g., the case for high-power ultrasound. In this work, we revisit the source term as obtained in [5] based on the perturbation method and derive the explicit expression of the source term for the bulk streaming when high-order harmonics occur. The main results of this work are given in [7].

Conclusion

When using a high-power ultrasound field as the input to drive the bulk streaming, it is possible to induce a nonlinear acoustic propagation. For example, the second-order harmonic cannot be ignored for the bulk streaming at 1.5 GHz with the pressure amplitude of 10 MPa when the traditional Goldberg number is 1.8. In this work, we derive the explicit expression of source term of bulk acoustic streaming with the consideration of high-order harmonics. Numerical results show that the contribution of higher-order harmonics increases the maximum velocity of the streaming flow by more than 20% compared with the case of only linear acoustic propagation. The detailed derivation is given in [7] with some theoretical and numerical results at the regime of GHz. In addition, both theoretical and numerical examples are given to illustrate that the source term in Nyborg's work [8] involves the contribution for acoustic radiation which should be avoided in the following simulations for the bulk acoustic streaming [5,7].

Acknowledgements

References

[1] C. Eckart, *Phys. Rev.,* **73** 68 (1948)
[2] W. Cui, *et al.*, *Nanoscale,* **11** 14625 (2019)
[3] R. J. Shilton, *et al.*, *Adv. Mat.,* **26** 4941 (2014)
[4] M. B. Dentry, *et al.*, *Phys. Rev. E,* **89** 013203 (2014)
[5] A. Riaud, *et al.*, *J. Fluid Mech.* **821** 384 (2017)
[6] F. Prieur, and O. A. Sapozhnikov, *J. Acous. Soc. Am.* **142** 947 (2017)
[7] S. Li, *et al.*, *arXiv preprint arXiv:2403.00350* (2024)
[8] W. L. Nyborg, *J. Acous. Soc. Am.* **25** 68 (1953)

Computational optimization of acoustofluidic devices

<u>Kirill Kolesnik</u>[1], Vijay Rajagopal[1,2], and David J. Collins[1,2,*]

[1]Department of Biomedical Engineering, University of Melbourne, Melbourne, Australia
[2]Graeme Clark Institute, University of Melbourne, Melbourne, Australia
[*]E-mail: david.collins@unimelb.edu.au

Introduction

Acoustofluidic devices hold promise for versatile applications offering a non-invasive, precise, rapid, and label-free approach for manipulating biological samples [1]. These devices find applications in various biomedical studies, including single-cell analysis, point-of-care testing, lab-on-a-chip devices, and tissue engineering [2,3]. The device performance modeling is the key to optimizing their performance prior to the experimental work [4,5]. Whereas analytical equations can be used to describe acoustofluidic phenomena and scaling in a general sense, accurately predicting interactions and effects in actual physical geometries often benefits from computational analysis. COMSOL Multiphysics is a widely used Finite Element Method (FEM) software, extensively used to simulate and analyze acoustofluidic problems, allowing the optimization of designs based on modeling results [6–8]. The rapid and reliable analysis can minimize the number of experimental iterations and, as a result, reduce the cost and time of the study.

In this work, we discuss the key aspects of modeling and optimization using COMSOL Multiphysics software in the context of innovative acoustofluidic devices. First, we revisit the fundamental equations and boundary conditions at the device interfaces. Second, we discuss the approaches for the model parametrization. Third, we outline objective functions that can be used to evaluate device performance. Finally, we evaluate various optimization algorithm available in the software and their impact on accuracy and computational time. The modeling pipeline is exemplified by the following acoustofluidic devices: traveling surface acoustic wave (TSAW) device, planar resonator, acoustofluidic superstrates, microresonators, and sharp-edged structures (Fig. 1).
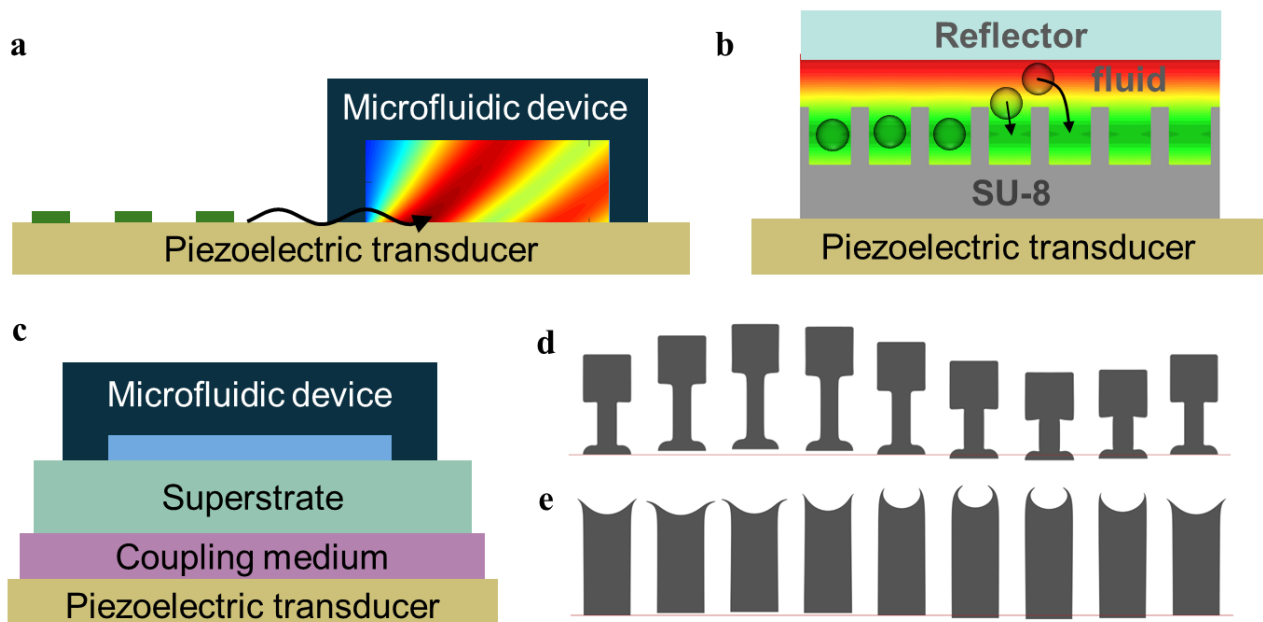
Figure 1: Acoustofluidic devices: (a) traveling surface acoustic wave (TSAW) device, (b) microwell-based planar resonator, (c) attachable superstrate, (d) mass on spring microresonators, (e) sharp-edged microstructures.

Device configurations
In first example we conducted a numerical analysis to evaluate the impact of channel size on the device performance actuated by the TSAW (Fig. 1a). A parametric study is followed by an analysis of acoustic fields and induced acoustic streaming phenomenon in each case. The study categorizes particle micromanipulation modes depending on particle size and channel configurations, enabling a higher degree of control of the streaming and pressure patterns, which is essential for controllable micromanipulation.

A microwell-based device was also computationally optimized to enhance patterning capabilities (Fig. 1b). The device employs a structured layer integrated into a planar acoustic resonator. This configuration brings injected micro-objects into wells or valleys of the microstructured layer to form a desired pattern. Numerical optimization is used to simulate and optimize the device layout to enhance the patterning efficiency. Compared to traditional acoustofluidic resonators, this stencil-based approach enables multiplexed, complex, and sub-wavelength resolution patterning while keeping the fabrication approach simple.

Acoustic superstrates are acoustofluidic devices that are temporarily attached to a piezoelectric actuator rather than bonded permanently (Fig. 1c). This layout allows the ability to reuse the actuator with multiple devices, although in many implementations the acoustic actuation in the attachable device can be insufficient because of poor acoustic signal coupling. Computational analysis was employed to study the impact of materials and their thickness on wave propagation. A parametric study is performed to evaluate optimal configurations, providing guidelines to design attachable acoustic chips with bulk-wave actuation. This study demonstrated the complex interreference of the design parameters on the resulting performance. It underlines the importance of comprehensive analyses and optimization, showing the potential to achieve higher response in such a system compared to non-optimized set-ups.

We also explored the role computational optimization for 3D-printed microstructures. Such structures leverage their intricate shapes to create novel acoustic effects, not possible with conventional microfabricated features. For example, proposed structures use resonance effect to produce localized actuation suitable for particle patterning (Fig. 1d). Modeling and optimization were used to enhance the patterning performance of the structures by optimizing their shape. This creates a pathway for designed particle patterning and manipulation in a microfluidic environment based on the structure configurations.

Another type of microstructure in this work employs a sharp-edge interface (Fig. 1e). This allows generating a strong recirculation flow due to acoustic streaming effects. The computational analysis is completed to access multiple configurations and define an optimal configuration. More specifically, the impact of the angle at the sharp interface was evaluated to amplify acoustic streaming. These structures hold the potential for targeted microparticle micromanipulation in a microfluidic environment.

Conclusion
In this work, we report computational analysis and optimization techniques applied to study and optimize various acoustofluidic devices. System configurations were optimized by performing a parametric sweep study or by using an optimization algorithm, which is based on iteratively constructed quadratic approximation. A parametric sweep was found useful to analyze the systems where the number of variables is relatively low (1-3). Optimization with an iterative algorithm was employed for studies in which the systems have a higher degree of freedom of the variable space (4-10). By leveraging computational modeling and optimization, we unlocked the full potential of acoustofluidic devices, paving the way for advancements in micromanipulation.

References
[1]   K. Kolesnik, M. Xu, P.V.S. Lee, V. Rajagopal, D.J. Collins, *Lab Chip* 21 (2021)
[2]   Y. Xie, Z. Mao, H. Bachman, P. Li, P. Zhang, L. Ren, M. Wu, T.J. Huang, *J Biomech Eng* 142 (2020)
[3]   Z. Liu, Y. Lei, Z. Yu, Z. Meng, S. Jin, X. Qu, Z. Jiang, F. Zhang, X. Wei, *Sens Actuators B Chem* 322 (2020)
[4]   P. Hahn, O. Schwab, J. Dual, *Lab Chip* 14 (2014)
[5]   J.S. Bach, H. Bruus, *Phys Rev Lett* 124 (2020)
[6]   A. Aghakhani, H. Cetin, P. Erkoc, G.I. Tombak, M. Sitti, *Lab Chip* 21 (2021)
[7]   Z. Ni, C. Yin, G. Xu, L. Xie, J. Huang, S. Liu, J. Tu, X. Guo, D. Zhang, *Lab Chip* 19 (2019)
[8]   R. Barnkob, N. Nama, L. Ren, T.J. Huang, F. Costanzo, C.J. Kähler, *Phys Rev Appl* 9 (2018)

Concept of Acoustic Buoyancy

Andreas Fuchsluger [1,*], Annalisa De Pastina [2], Tina Mitteramskogler [1], Bernhard Jakoby [1]

[1]Institute for Microelectronics and Microsensors, Johannes Kepler University Linz, Linz, Austria
[2]Microsystems, Silicon Austria Labs, Villach, Austria
*E-mail: andreas.fuchsluger@jku.at

Introduction

The well-established derivation of the acoustic radiation force based on time-averaged second-order scattering theory [1, 2, 3] is difficult to understand for undergraduates as well as for scientists from other areas or research. Therefore, we tried to devise an intuitive explanation of the acoustic radiation force for the case of a small compressible particle in a plane standing acoustic wave. Based on the work of Leighton [4] concerning air bubbles dispersed in a fluid, and extending it by introducing an "acoustic buoyancy", which is analog to the static buoyancy following Archimedes' principle in fluid mechanics, we obtained a straightforward derivation of the compressibility-component which is exactly matching the $(1 - \kappa_p/\kappa_{fl})$ expression in the literature, e.g., in [3] (arising from monopole coefficient f_1), with κ_p and κ_{fl} being the compressibility of the particle and the fluid, respectively.

Similarly, in Crum's work [5] the compressibility of a liquid drop ins incorporated into the Nyborg's approach [6] for rigid spheres to correctly achieve the formula of [1] and [2]. But here we miss some argumentation how forces are caused by differences in compressibility of the fluid and droplet, particularly the "1" in $(1 - \kappa_p/\kappa_{fl})$ which is a result from scattering theory and not explained in Crum's paper.

Results

Concerning only the compressibility κ_p of a small particle (or droplet or bubble) of volume V suspended in a (for now incompressible) fluid, a non-zero mean force $\boldsymbol{F}_p = - \langle V \operatorname{grad}(p) \rangle$ on the particle arises in presence of a standing acoustic plane wave, because of a change of the particle's volume during a cycle of the wave due to the pressure change at position x (Fig. 1). With the pressure $p(x,t) = \hat{p} \cos(k\,x) \sin(\omega\,t)$ the force on the particle in x-direction calculates to

$$F_p(x,t) = - \kappa_p \times V_0\, \hat{p}^2\, k \times \sin(2kx) / 4 \qquad (1)$$

where $\hat{p}$ is the pressure amplitude, k is the wavenumber, and ω the angular frequency of the acoustic wave.
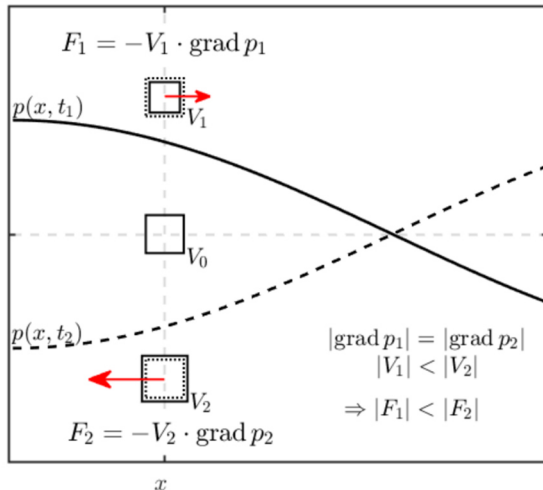
Figure 1: Taking into account only the compressibility of the particle, a non-zero mean force arises in an acoustic standing wave, which in general points towards the pressure slopes of the wave. Due the particles volume being compressed and expanded during a cycle in the oscillating pressure field, the force in the lower cycle (t_1) pointing towards the pressure node is larger than the force in the higher cycle (t_2), which is pointing towards the pressure slope.

However, in this simplified picture the force is *always* pointing towards the slopes of the pressure wave irrespective of dealing with particles, droplets or bubbles, which is strongly contradicting the experimental experience, where hard particles always, and bubbles sometimes, travel towards the pressure nodes of the standing acoustic wave. The solution for suspended bubbles is using their resonance frequency, which can be approximated by $f_{Air} = 3/a$ [6] for air bubbles in water, where a is denoting the radius of the air bubble. When the frequency of the standing wave is located above the resonance frequency of the air bubble, a 180° phase shift in the volume oscillation arises compared to above, changing the sign in (1), and leading to a force in opposite direction, now pointing towards the pressure nodes. For 20 μm sized bubbles, this frequency would

be about 150 kHz, and in our experiments with actuation frequency of ca. 500 kHz – 2 MHz [7] they would travel towards the pressure nodes. Unfortunately, this tactic does not work out for the 20 μm PS beads used in our experiments, because the resonance frequency of this particles is located around 120 MHz (estimated by $f = c_{PS}/(2a)$, using $c_{PS} = 2400$ m/s [8]), and thus by far exceeding the frequency range of our acoustofluidic device.

Taking into account the compressibility of the fluid, we come to the conclusion that the acoustic field is also exerting a force on the fluid itself or, more precisely, on every arbitrary (small) fluid volume. Again, the force is pointing towards the pressure slopes and regarding a volume V_0, a non-zero time-averaged force on this volume arises analog to a particle mentioned above, calculating to $F_{fl}(x,t) = -\kappa_{fl} \times V_0\, \hat{p}^2\, k \times \sin(2kx)\,/\,4$. Considering now the situation, where we have the particle suspended in the fluid and a force acting on both of them with different strength (F_p on the particle of volume V_0 and F_{fl} on a fluid volume V_0), it is inevitable to think of Archimedes' principle, where the situation is in principle the same. Analog to the buoyancy arising from gravity on a body submerged in the fluid being equal to the weight of the displaced fluid volume, we now introduce an *acoustic buoyancy* where the particle experiences an additional force which is equal to the "acoustic weight" F_{fl} of the displaced volume and pointing away from the slope towards the pressure node. Now, if the particle's compressibility is much lower than that of the fluid (which is the case for PS particles, where $\kappa_{ps}/\kappa_{fl} \approx 0.53$ [8]), the acoustic buoyancy $-F_{fl}$ of the particle is higher than its acoustic weight F_p and the particle is acoustically floating up towards a pressure node (Fig. 2) with the total force

$$F(x,t) = F_p - F_{fl} = (\kappa_{fl} - \kappa_p) \times V_0\, \hat{p}^2\, k \times \sin(2kx)\,/\,4, \qquad (2)$$

which is, after multiplication by $1 = \kappa_{fl}/\kappa_{fl}$ and some slight rearrangement, exactly the compressibility component in [3].
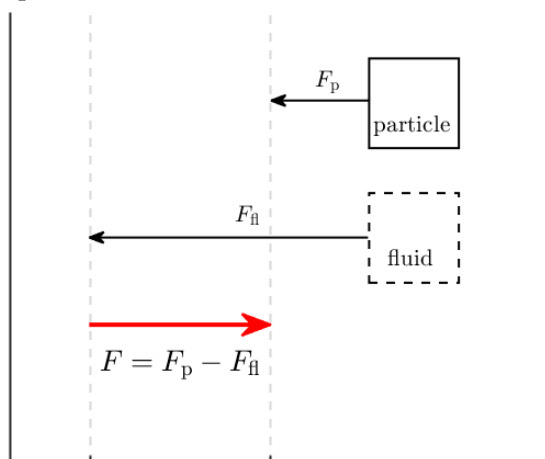
Figure 2: The concept of acoustic buoyancy. The situation of an acoustic force acting on both, the particle and the fluid, is equivalent to a particle surrounded by a fluid and gravity acting on both. In latter, Archimedes' principle is valid, where the particle experiences a hydrostatical buoyancy leading to an uplift which is equal to the weight of the displaced fluid volume. The same principle applied in acoustofluidics gives the exact formulation for the compressibility component of the acoustic radiation force and leads to a net force on the particle, which can be directed towards the pressure nodes, if the compressibility of the fluid is higher than that of the particle.

Conclusion
We introduced the concept of *acoustic buoyancy* for deriving the compressibility component of the acoustic radiation force. Our derivation gives a simple explanation and understanding of the compressibility component suited for undergraduates and also for many graduate scientists.

References
[1] K. Yosioka and Y. Kawasima, Acta Acust. united with Acust., **5** 167 (1955)
[2] L. P. Gor'kov, Sov. Phys. - Dokl., **6** 773 (1962)
[3] H. Bruus, Lab Chip, **12**, 1014 (2012)
[4] T. G. Leighton, A. J. Walton and M. J. W. Pickworth, Eur. J. Phys., **11** 47 (1990)
[5] L. A. Crum, J. Acoust. Soc. Am., **47** 82 (1971)
[5] W. L. Nyborg, Journalof Acoust. Americ, **42** 947 (1967)
[6] M. Minnaert, Dublin Philos. Mag. J. Sci., **16** 235 (1933)
[7] A. Fuchsluger, et al., 2023 IEEE Sensors (2023)
[8] J. T. Karlsen and H. Bruus, Phys. Rev. E - Stat. Nonlinear, Soft Matter Phys., vol. 92, 2015.

Design optimization of acoustic cavity traps for effective microparticle trapping

Pradipta Kr. Das[1,*], Gabriel Werr[1], and Maria Tenje[1]

[1]Division of Biomedical Engineering, Department of Materials
Science and Engineering, Science for Life Laboratory, Uppsala University, Uppsala, Sweden
*E-mail: pradipta.das@angstrom.uu.se

Introduction

Trapping of microparticles or cells has an immense role in various biomedical applications such as cell culturing, targeted drug delivery, or diagnostics [1]. However, immobilizing small cells/particles in a tiny volume against a flow in micro-confinements is extremely challenging. Microparticles are observed to be trapped experimentally using hydrodynamic, electrical, optical, magnetic, or acoustic forces [2]. Among these, acoustic systems have shown significant potential as they are biocompatible and can be regulated effectively in small systems. To trap microparticles, we consider an acoustic trap as shown in Figure 1, with a so-called "cavity design". This type of design ensures the standing half-wave acoustic resonance is confined inside the cavity, leading to particle focusing within that cavity region only.

In acoustofluidic systems, the suspended particles experience two kinds of forces: (i) drag force induced by the acoustic mean flow, known as acoustic streaming, and (ii) the acoustic radiation force caused by the scattering of the acoustic waves on the particles. For small particles (less than a micron-sized particles in 1 MHz acoustic fields), the motion of the particle is dominated by acoustic streaming only [3] whereas the acoustic radiation force dominates for larger particles, meaning that the particle can be effectively manipulated using acoustic fields [4]. In this work, we consider the situation where the particle is sufficiently large to be dominated by acoustic radiation force and our objective is to optimize the trap design based on the optimization of the acoustic radiation force field.
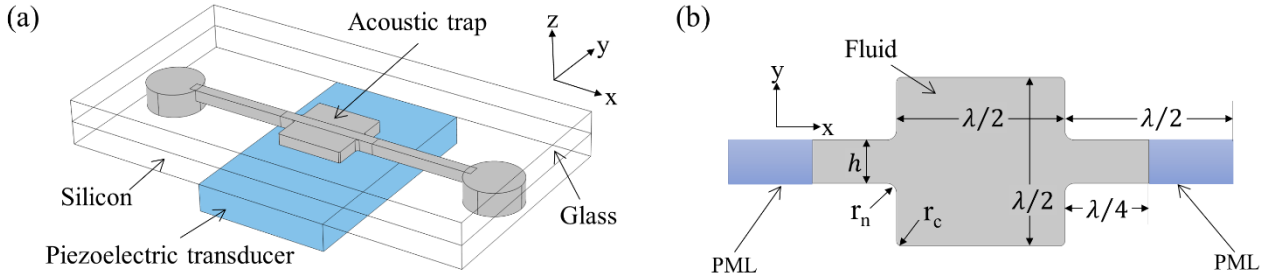
Figure 1: Schematic of the silicon-glass acoustic cavity trap system excited by a piezoelectric transducer from a 3D perspective (a) and the computational domain in 2D (b).

Problem description and Mathematical formulations

Figure 1a shows the schematic of the acoustic trap where the trapping is performed in the cavity region. To avoid singularity, the neck and corner are tapered with curvature radii r_n and r_c, respectively. The trap size is kept as $\lambda/2 \times \lambda/2$ where λ is the acoustic wavelength. The width of the narrow inlet and outlet is denoted as h. The depth of the acoustofluidic system is taken as $\lambda/4$. We calculated the acoustic radiation force field for the system numerically using a 2D computational domain as shown in Figure 1b. To truncate the computational domain and focus on the cavity region, we use perfectly matched layers (PMLs) on both ends of the trap. The trap is filled with a Newtonian fluid of density ρ, viscosity μ, and bulk viscosity μ_b. The governing equations for the acoustic fields can be obtained by employing the regular perturbation technique used in theoretical acoustofluidics [5]

$$\partial_t \rho_1 + \rho_0 \nabla . \boldsymbol{v}_1 = 0 \tag{1}$$
$$\rho_0 \partial_t \boldsymbol{v}_1 = -\nabla p_1 + \mu \nabla^2 \boldsymbol{v}_1 + (\mu_b + \mu/3)\nabla(\nabla . \boldsymbol{v}_1) \tag{2}$$

where ρ_1, p_1, and $\boldsymbol{v}_1$, denote acoustic density, pressure and velocity fields, respectively. ρ_0 indicates the fluid density at rest. Acoustic radiation force acting on the small spherical particles of radius a ($\ll \lambda$) suspended in the fluid can be expressed in terms of the gradient of the Gorkov potential [6] as $F_{rad} = -\nabla U_{rad}$ where

$$U_{rad} = 4\pi a^3/3 \left(f_1 \kappa_0 |p_1|^2/4 - 3f_2 \rho_0 |\boldsymbol{v}_1|^2/8 \right) \tag{3}$$

In the above, κ_0 is the compressibility of the fluid; f_1 and f_2 are monopole and dipole scattering coefficients, respectively, and they are given by

$$f_1 = 1 - \kappa_p/\kappa_0, \quad f_2 = 2(\rho_p - \rho_0)/(2\rho_p + \rho_0) \tag{4a, b}$$

where ρ_p and κ_p are density and the compressibility of the particle, respectively. In this study, we consider particles with a positive contrast factor. These particles experienced force towards the low Gorkov potential zone. Given that, to optimize the acoustic trap, we define an objective function,

$$\text{F} = \frac{1}{\mho_\Omega E_{ac,total}} \int_\Omega U_{rad} d\mho \qquad (5)$$

where Ω denotes the fluid domain and $\mho_\Omega = \int_\Omega d\mho$ is the total volume of that domain. $E_{ac,total}$ is the total acoustic energy, calculated as $E_{ac,total} = \int_\Omega E_{ac} d\mho$ where acoustic energy density is given by $E_{ac} = \kappa_0 |p_1|^2/4 + \rho_0 |v_1|^2/4$.

(a)

F = 1.385×10^{-6}

(b)

F = 1.385×10^{-6}

$r_n = 93.75\ \mu m$ $r_c = 18.44\ \mu m$
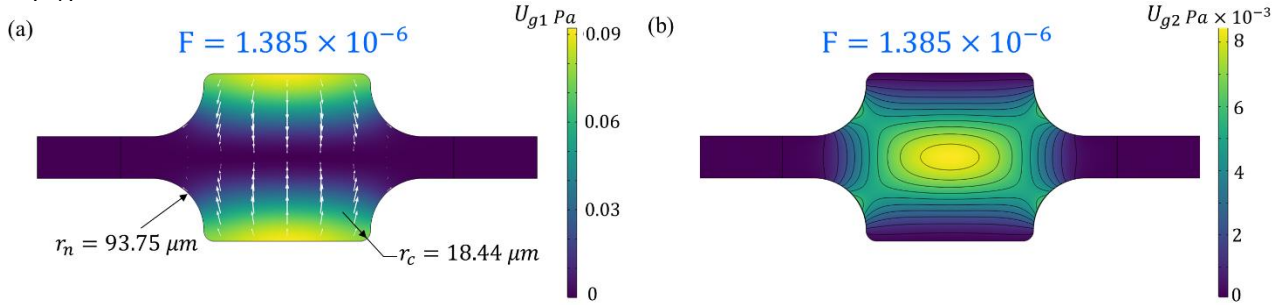
Figure 2: Surface plot of U_{g1} (a) and U_{g2} (b) for optimized acoustic trap. Arrows in (a) show acoustic radiation force vectors and lines in (b) show contours of U_{g2}.

Results and Discussions

We have carried out numerical simulations using finite element-based software COMSOL Multiphysics 6.1 to calculate the objective function for a $300\ \mu m \times 300\ \mu m$ trap filled with water. The actuation frequency is set as $f_0 = 2.5\ MHz$ and the walls of the trap are actuated vertically (along y-direction) with displacement field $d = d_0 e^{i\omega t}$ where $d_0 = 0.1\ nm$, and $\omega = 2\pi f_0$. The inlet and outlet channel width, h is kept at $h = \lambda/8$ and considering the practical fabrication issues, the minimum value of r_c and r_n is taken as $10\ \mu m$. The optimization has been performed for polystyrene particles of diameter $5\ \mu m$ with $\rho_p = 1050\ kg/m^3$ and $\kappa_p = 2.38\ TPa^{-1}$. Figure 2a-b show the acoustic trap with the optimized design having the neck radius, $r_n = 93.75\ \mu m$ and the corner radius $r_c = 18.44\ \mu m$. We have shown surface plots of Gorkov potential factors U_{g1} ($=f_1 \kappa_0 |p_1|^2/4$) and U_{g2} ($=3f_2 \rho_0 |v_1|^2/8$) associated with monopole and dipole scattering coefficients to illustrate the relative contributions of the acoustic pressure and velocity fields, respectively.

F = 1.572×10^{-6}

$r_n = 10\ \mu m$ $r_c = 10\ \mu m$
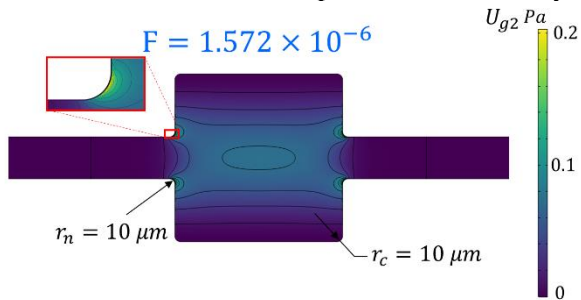
Figure 3: Surface plot and contours of U_{g2} for acoustic trap with $r_n = r_c = 10\ \mu m$.

Figure 2a shows the surface plot of U_{g1} with arrows indicating the acoustic radiation force vectors whereas Figure 2b illustrates the surface and contour plot of U_{g2}. The zone with lower U_{g1} and higher U_{g2} occurs at the central elliptical region and hence the trapping is most favorable in that region. On the contrary, we have also calculated the base case scenario with $r_n = r_c = 10\ \mu m$ and Figure 3 shows the plots of U_{g2} for such devices. Instead, here the neck region is having larger U_{g2} and we can see that the trapping is not favorable at the trap center, rather the particles will be attracted towards the neck region.

Conclusion

Numerical studies have been conducted to optimize the corner radius of acoustic cavity traps for trapping positive contrast factor microparticles. Our study shows that the optimized traps have the most favorable trapping at the central region of the trap. On the other hand, in non-optimized devices, the central zone of the trap is not so favorable for trapping, rather, particles seem to be attracted towards the trap-neck, indicating inferior performances.

References

[1] K. Cheng, J. Guo, Y. Fu, J. Guo, *Sens. Actuator A: Phys* **322**, 112616 (2021).
[2] J. Nilsson, M. Evander, B. Hammarström, T. Laurell, *Anal. Chim Acta* **649**, 141-157, (2009).
[3] R. Barnkob, P. Augustsson, T. Laurell, H. Bruus, *Phys. Rev E* **86**, 056307 (2012).
[4] P. B. Muller, R. Barnkob, M. J. H. Jensen, H. Bruus, : Lab Chip, **12**, 4617–4627 (2012).
[5] H. Bruus, *Lab Chip* **12**, 20 (2012).
[6] L. P. Gorkov, *Soviet Physics – Doklady*, **6**, 773–775 (1962).

Electrokinetic interactions between Surface Acoustic Waves and Electrolyte Solutions

Oles Dubrovsky[1], Sudeepthi Aremanda[2], and Ofer Manor[1,2,*]

[1]Applied Mathematics, Technion – IIT, Haifa
[2]Chemical Engineering, Technion – IIT, Haifa
*E-mail: manoro@technion.ac.il

Introduction

This study commenced several years ago when we asked ourselves how MHz- to GHz-frequency surface acoustic waves (SAWs) that travel in a solid substrate influence the dynamics of ions in neighboring electrolyte solutions. While it is known that electrolyte solutions affect SAWs in piezoelectric materials through the conductivity of the electrolyte, our question followed an observation in the opposite direction: Acousto-capillary flows in micron thick films of water, excited by SAWs, did not show the nice agreement to fluid mechanics theory that silicon oils showed. The difference between oil and water dynamics suggests contributions of ion pressure, also known as electrical double layer (EDL) pressure, to water film dynamics. Moreover, EDLs and boundary layer flow induced by MHz-frequency SAWs exist at similar time and length scales, so that one expects an interaction. [1]

EDLs of ions are a surface phenomenon. These are nanometer thick clouds of ions that appear at the charged interface between a substrate and an electrolyte solution and give rise to the complexity of biology and to countless industrial processes and products from water desalination to shampoo and super-capacitors. Ions diffuse through the EDL nanometer thickness in microseconds to nanoseconds: These are ion-specific times for charging or discharging the EDL and are known as the EDL relaxation times. When the EDL relaxation times are similar to the periodic times of SAWs and of the periodic leading order flow field that the SAW generates near the solid surface, one expects direct interactions between the SAW and ions near the solid.

Experiment and Results

Under SAW excitations, ions in the EDL vibrate and undergo electro-mechanical resonance at the SAW frequency; the ion vibration results in the leakage of same frequency electrical fields off the EDL; see figure 1. By measuring these electrical fields, we identify the interaction between the SAW and the ions, and further obtain the ion-specific relaxation times in the EDL and hence the intrinsic rate of EDL charge and discharge.

Conclusion

We show that MHz-frequency SAWs directly interact with ions near the solid surface through the boundary layer flow, which the SAW generates near the solid. We use the interactions between SAWs and ions to show a new type of spectroscopy in the MHz frequency spectrum that gives ion fingerprints and their dynamics in EDLs and observe that a dynamic EDL under such an excitation is much more than a capacitor. [2]

Figure 1: (right) Illustration of a surface acoustic wave (SAW) that travels in a solid substrate and dynamically perturbs ion positions in an electrical double layer (EDL) by generating an evanescent wave in the neighboring electrolyte solution, where red and blue indicate fast and slow ion motions [3]; this results in the leakage of an electrical field, $\vec{E}$, that we measure using our experimental system (left).
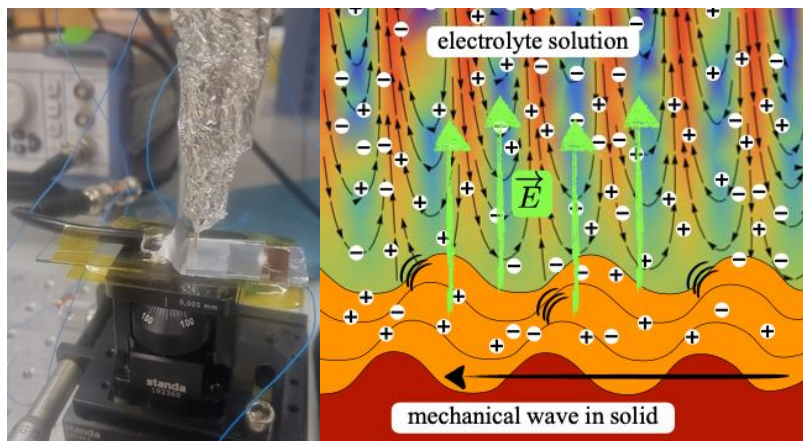
References
[1] O. Dubrovski and O. Manor, *Langmuir*, **37**, 14679–-14687 (2021)
[2] S. Aremanda and O. Manor, *J. Phys. Chem. C*, **127**, 20911–20918 (2023)
[3] O. Manor, L.Y. Yeo, and J.R. Friend, *J. Fluid Mech.*, **707**, 482–495 (2012)

Electronics for Acoustofluidic actuators, versatile vs specific

Raimund Brünig[1,*], Melanie Colditz[2], Andreas Winkler[2]

[1]BelektroniG GmbH, Freital, Germany
[2]IFW Dresden, Dresden, Germany
*E-mail: r.bruenig@belektronig.de

Introduction

BelektroniG, a former spinoff from the IFW Dresden / SAW Lab Saxony, has been working in the field of electronics for 15 years now and manufactures electronics for acoustofluidics since. We present our redesigned driving unit for acoustofluidics, our SAW Generator, show the concept of the electronics as well as a new concept for a much more compact unit for integration into future custom applications.

We think that besides the research work which often aims at miniaturization of test setups or PoC-diagnostics the engineering of the electronics for the analysis is also worth being recognized.

Re-designed SAW Generator

A driving unit for SAW actuators is mainly a frequency generator, generating an alternating sine-shape voltage with an adjustable frequency and amplitude. But to make it a versatile device for acoustofluidics, certain additional requirements arise. We have examined a large number of such requirements, based on our own experiences as well as feedback from researchers working in this field. Each requirement, e.g. frequency range, amplitude range etc. results in different demands for the electronics but may also result in benefits in additional possible features. The following table gives an overview of requirements, demands and benefits:

Requirement for device	Demand for electronics	Solution / Benefit
Large frequency range	Broadband frequency generator	Usage of a Direct Digital Synthesis (DDS) Generator,
Large amplitude range	Adjustable high power amplifier stage	Usage of DDS plus VGA allows large dynamic range and high amplitude resolution
Feedback about condition of SAW-device	Power and S-Parameter measurement	Allows automatic device detection, resonant frequency tracking, network analyzer functionality
Generation of standing waves on SAW -device	2-channel output	2-channel device allows adjustable phases, shifting of pressure nodes
Generation of pulsed SAW	Pulse generator	DDS allows modulation of AM, FM, PM

The above mentioned requirements could mostly be matched by a combination of classical laboratory and measurement devices like network analyzer, frequency generator and power amplifier. However, such many devices will stack up a lot, with costs increasing up to 100k€ and therefore contradicting the idea of Lab-on-Chip and PoC.
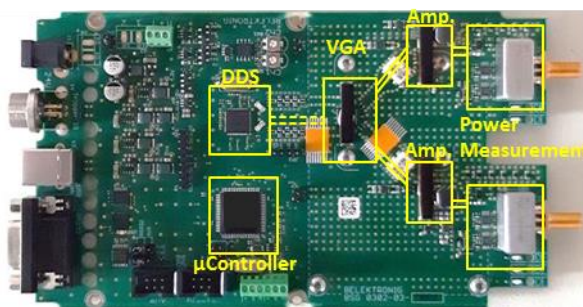
Figure 1 Foto of the newly developed electronics consisting of µController, DDS-generator, Power amplifier and power measurement with 2-channel output.
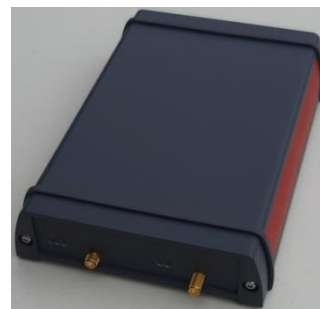
Figure 2 Electronics mounted in a compact housing with optimized heat removal.

Our solution is a compact electronic module consisting of a 2-channel DDS-device as frequency generator, a power stage and a power measurement part for each of the channels. The device is controlled by a microcontroller and can output 2 independent sine-signals between 1-215MHz and up to 5W of output power. The internal sampling rate reaches up to 12kHz with 4 power waves measured in parallel and used to calculate the S-parameter. This allows a fast SAW-device and resonance detection as well as frequency tracking and pulsed outputs. Several challenges had to be met in order to achieve a compact design. For example a high power output require a large amplification, which results in a strong risk of crosstalk between the channels, or feedback into its own input, which in turn will create unwanted oscillations. That means the

shielding between an amplifiers output and its input must be larger than its gain, which is difficult to achieve at small sizes. Furthermore broadband amplifiers require class-A amplifiers with a low efficiency, resulting in larger waste heat which needs to be dissipated from a small space.

All features of the new electronics have been tested in close collaboration with the IFW Dresden / SAWLab Saxony. The following pictures show examples of the capabilities of the new electronics.
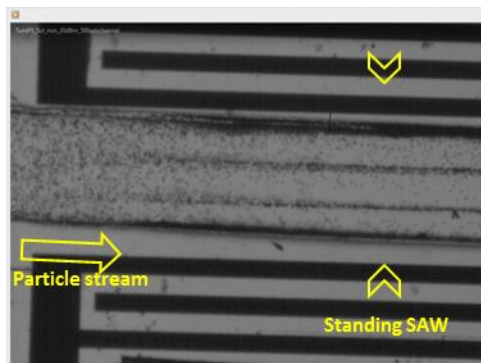
Figure 3 Concentration of 7µm PS-particles in a 500µm channel using 12,8MHz sSAW at 20dBm (Foto: IFW)
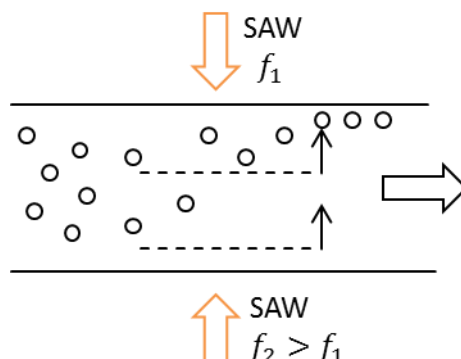
Figure 4 Interference of slightly different SAW frequencies creates moving pressure nodes and allow to "comb out" particles to one channel side. (Video shown)

Concept of compact and specific electronics for acoustofluidics

The above shown versatile electronics for acoustofluidics is very suitable for research purposes but it still requires expensive RF-components making the device still kind of expensive. Affordable electronics for real PoC analysis require even more cost reduction. This can be achieved by much further specialization e.g. to a lower frequency and power range and removing all functionality which are not needed in the specific application. BelektroniG plans to create a low cost electronic consisting of a clock generator, followed by a switched power stage and a low pass filter to create a sine shaped output signal. Information of the SAW-device condition will be correlated by measuring the overall input power. E.g. a disconnected SAW-device will result in a drop of needed power.
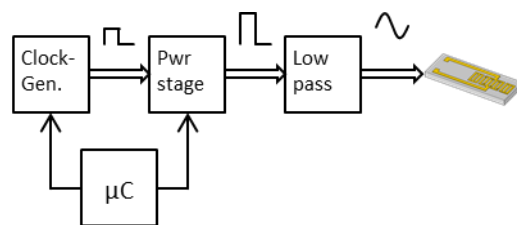
Figure 5 Proposed specialized low cost solution to drive acoustofluidic applications

Results and Discussion

BelektroniG has developed a versatile driving unit for acoustofluidic setups which can reduce costs for measurement and signal generator devices from the range of 100k€ down to 10k€ and also reduced setup size and improved usability a lot. Further specializing for specific applications will allow costs reduction for electronics down into the ranges of 100-200€.

Conclusion

To achieve real Lab-on-Chip and PoC applications, the electronics required for recording the actual measurement should be taken into account. While as long as physical effects like acoustofluidic are in the field of research, versatile measurement setups are required. But even here it is already of advantage to think about more specialized electronics than combinations of standard devices. When it comes to a specific application, the electronics should be specialized too, allowing much less costs and real compact setups.

References

[1] Mehrzad Roudini et al, Ultrasonics Sonochemistry, 98, p106530 (2023)
[2] A. Fakhfouri et al., ACS Appl. Mater. Interfaces, 15, 20, pp. 24023–24033 (2023)

Elucidating fluid mixing in an acoustic bioreactor with application to yeast growth

Gabriel Dumy[1,*] Thomas Chomette[2], Marin Virey[1], Siriny Laumier[1] and

[1]KOLIBRI, Paris, France
[2]ESPCI, Paris, France
*E-mail: gabriel@kolibrilab.com

Introduction

Ultrasonic standing waves can be used to effectively trap passive particles, but also live ones. It has been several years now that several research groups have demonstrated not only acoustophoresis of live bacteria, yeast or mammalian cells, but the potential patterning and growth of these under the influence of said acoustic waves [1,2,3].

We have developed a bioreactor relying on the principle of acoustic levitation culture. The cells, whether prokaryotic or eukaryotic, are grown without substrate, within the pressure nodes of a standing acoustic wave. Shaping the acoustic wave to yield a collection of cell layers stacked upon each other and providing a low enough trapping force to keep the cells alive make for a very interesting bioproduction tool.

However, as with any bioproduction method, one need to ensure nutrients and dissolved gases are transported efficiently to and from the culture layers. In this experimental study, we present the investigation of the convection mechanisms underlying transport in an acoustic bioreactor, with application in the case of the culture of *Saccharomyces Cerevisiae*, a yeast that is helpful into investigating the dynamics of our system. We show that while the acoustic field populating the cavity is paramount for cell culture, it is not the root of fluid motion in this case, and that thermal control of the cavity is, and that for an efficient yeast amplification an additional convection source might be needed.

Experimental setup and method

We use an acoustic trapping system made from a transducer attached to a regulated liquid container made of biocompatible materials, comprising an acoustic reflector facing the transducer. The distance between the two acoustic elements and the frequency of the field can be finely matched to ensure resonance of the cavity, paramount to our culture system. To accommodate the needs of microorganisms, the container is regulated in temperature. A camera allows for real time imaging of the whole liquid region, and a lateral illumination was provided by a laser beam split into a sheet by a half-cylindrical lens.

Using PIV (Particle Image Velocimetry, [4]) technique to map out the fluid flows inside the cavity, we investigated the effects of either the amplitude of the acoustic field, the potential heating induced by the piezoelectric transducer, and the heating of the temperature regulation system. Care was given to the choice of tracers, that must not be sensible to the acoustophoresis phenomenon to effectively follow the fluid motion, hence have as low an acoustic contrast as possible.
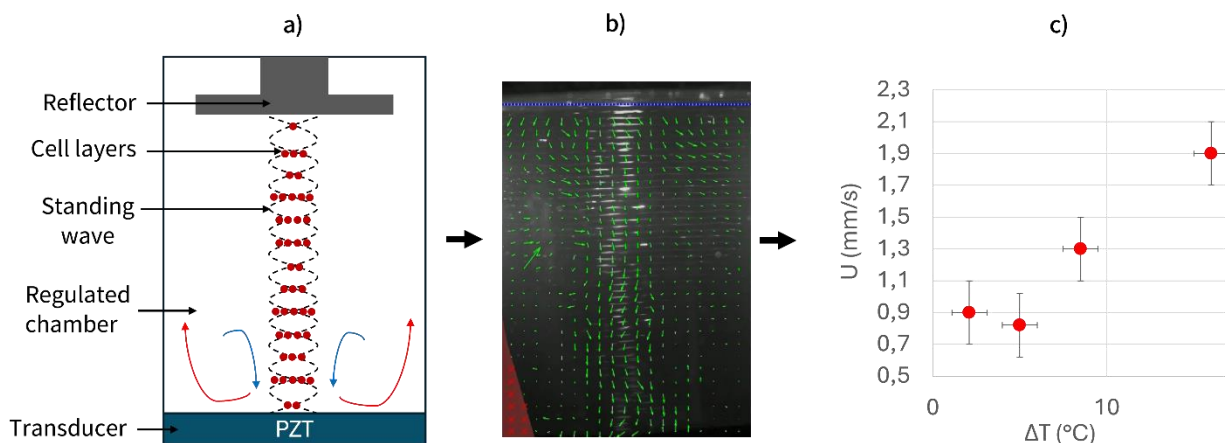
Figure 1: We studied the convection mechanisms within our regulated acoustic cavity (a), using standard PIV techniques, yielding a total mean velocity field for various parameters (b), such as the dependence on temperature gradients over the cavity (c)

Results and Discussion

The PIV measurements conducted show that in our system comprising a large number of standing pressure nodes, acoustic streaming has very little influence over the whole volume, as does the transducer induced heating when properly cooled: the flows measured in these cases were not differentiable from the ambient non-acoustic ambient temperature control. However, the temperature regulation system, heating from the sides, induces a much larger convection (Figure 1. c)), that scales linearly with the temperature gradient once the Rayleigh number threshold is crossed. This leads to a control in our current system of the mixing of gases and nutrients through the temperature input of the regulation system, which offers a bit of latitude but is limited to what the manipulated microorganisms can sustain.

Biological application

Initially developed for mammalian cells (slow growth, a division about every 24h), it was time-consuming to evaluate the dynamic limits of this mixing mechanism. We have thus exploited a much faster growing yeast strain, *Saccharomyces Cerevisiae* [5], to evaluate it. Having determined the right acoustic parameters to allow their growth, these microorganisms demonstrate that while the initial exponential growth phase is on par with the control, the current thermal mixing is not performing as well as the usual stirring of conventional bioreactors, since a lower final biomass is reached in our system versus the control.
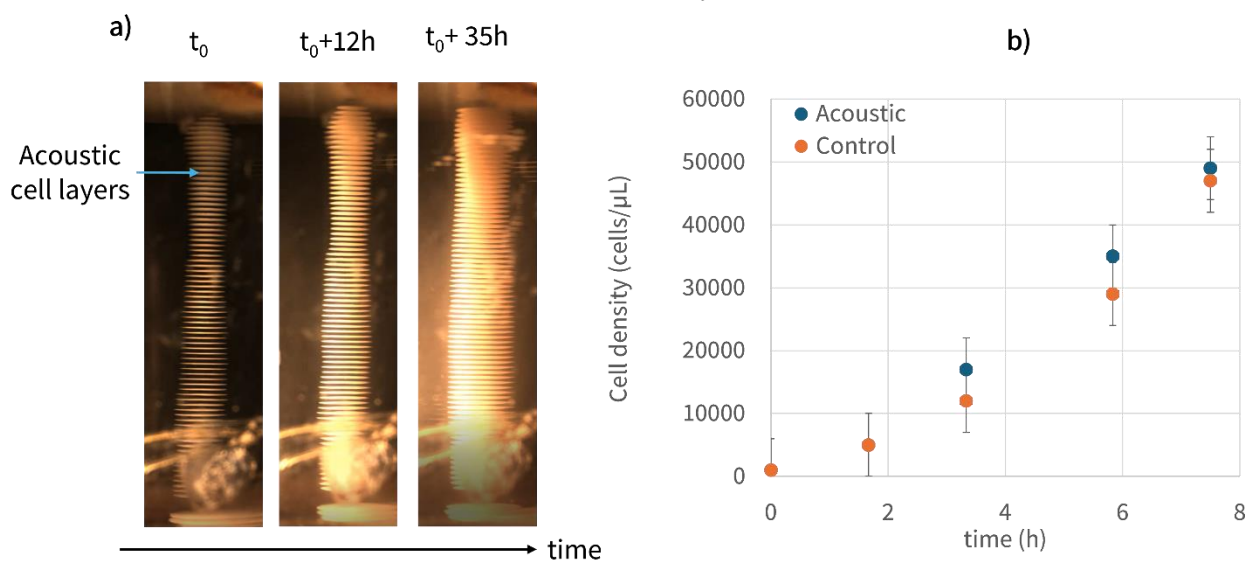
Figure 2: Illustration of the culture of yeast over two days in our acoustic bioreactor system (a), and the quantification of the cell density versus regular stirred control during the exponential phase (b)

Conclusion

We demonstrate in this study that for large multi-nodes resonant cavities such as the one we use for acoustic cell culture, the fluid convection is dominated by thermal convection, mostly coming from the temperature regulation system. Having this dependance means that one cannot force a higher convection using higher amplitude acoustic waves so far and is bounded by the thermal tolerances of the microorganisms grown. Further research will explore whether acoustic streaming can be induced in controlled anchor points in space, to enhance the mixing of the culture medium and allow for a better bioproduction.

Acknowledgements

References (Times New Roman 10 pt)

[1] M. Wiklund, in Microscale Acoustofluidics, ed. T. Laurell and A. Lenshof, The Royal Society of Chemistry, 2014, ch. 21, pp. 545-565.
[2] Wiklund, Martin. "Acoustofluidics 12: Biocompatibility and cell viability in microfluidic acoustic resonators." *Lab on a Chip* 12.11 (2012): 2018-2028.
[3] Jeger-Madiot, Nathan, et al. "Self-organization and culture of Mesenchymal Stem Cell spheroids in acoustic levitation." *Scientific reports* 11.1 (2021): 8355.
[4] Thielicke, W. and Stamhuis, E.J. (2014): PIVlab – Towards User-friendly, Affordable and Accurate Digital Particle Image Velocimetry in MATLAB. Journal of Open Research Software 2(1):e30
[5] Radel, S., et al. "Viability of yeast cells in well controlled propagating and standing ultrasonic plane waves." *Ultrasonics* 38.1-8 (2000): 633-637.

Enrichment of protein crystals in serial crystallography using flow control

Varun Kumar Rajendran[*], Björn Hammarström, Martin Viklund, and Jonas Sellberg [1]

[1]Department of Applied Physics, KTH Royal Institute of Technology, Stockholm, Sweden
[*]E-mail: vkraj@kth.se

Introduction

X-ray crystallography is one of the most widely employed techniques to study the atomic structure of proteins. Despite numerous approaches developed over the years for efficient sample handling, the challenge of reliably focusing particles inside the nozzles for crystallography persists [1], particularly at elevated concentrations and flow rates. In a novel attempt to address this challenge, Hammarström *et al.* [2] introduced the use of acoustic forces to focus protein crystals for Serial Femtosecond Crystallography (SFX), termed Acoustofluidic Crystallography (AFX). While the developed AFX showed promise in overcoming clogging issues, practical limitations stemming from misalignment between the acoustic focusing capillary and the crystallography injection nozzle have restricted its effectiveness in enriching crystals beyond certain thresholds of size and flow rate. In this study, we report an acoustofluidic flow control system designed to overcome the limitations of misalignment in AFX setups and enhance protein crystal enrichment. The effectiveness of the proposed system is demonstrated using numerical analysis under various misalignment conditions that may arise in practical AFX setups.

AFX setup

The AFX setup consists of two major sections, an acoustic focusing section in a square glass capillary of $400 \, \mu m$, where the protein crystals are focused using a standing acoustic wave generated by a piezoelectric transducer attached to its bottom, and the crystallography section is a circular glass nozzle of OD 375 µm and ID 100 µm, where the focused crystals from upstream are delivered to high-intensity X-ray beams as shown in Fig.1. As shown in the figure, the centerline of acoustic focusing (A) does not coincide with that of the centerline of the circular nozzle (B), which creates a misalignment of 12.5 µm due to geometrical constraints. Moreover, during experiments, it was found that the axis of acoustic focusing was slightly above the geometric centerline thereby further increasing the offset between A and B. As a result the crystals could not be enriched beyond an inlet flow rate of 108 µl/min as significant amounts of crystals deflected to waste.
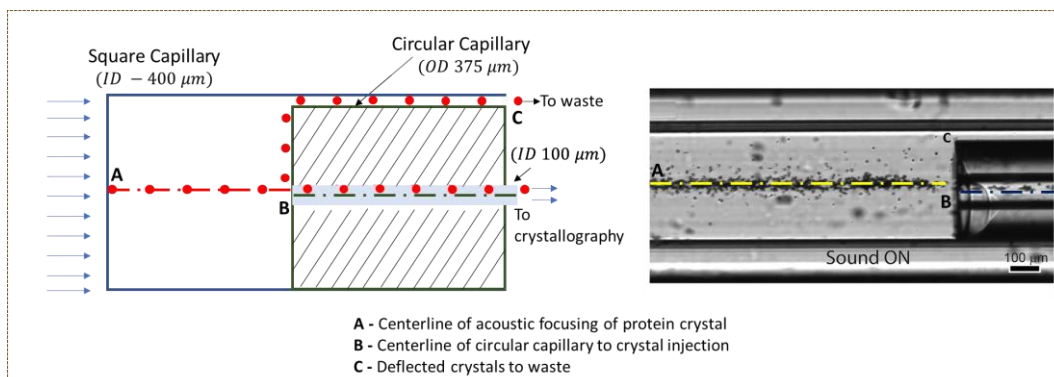
Figure 1: Schematic of AFX setup [2]. A square capillary of 400 µm is coupled with a circular capillary of OD 375 µm, ID 100 µm. The centerline axis of focusing (A), does not coincide with the centerline of the circular capillary (B), hence causing the misalignment of 12.5 µm. At higher flow rates the crystals get deflected to waste (C).

Enrichment using the flow control system

Fig. 2.a) shows the design of the flow control system to enrich protein crystals to mitigate the effect of misalignment. The proposed system has one inlet (Q_{in}) and three outlets (Q_{out-1}, Q_{out-2} and to crystallography). By adjusting the outlet flow rate (Q_{out-1}, Q_{out-2}), the acoustically focused protein crystals A, can be aligned with the axis of the circular capillary B, which can then be directed to crystal injection. In the AFX setup, if the focused crystals are offset with the circular capillary in the positive Y direction, then by adjusting the flow rate $Q_{out-2} > Q_{out-1}$, the crystals can be aligned with the axis of the circular capillary as shown in Fig.2.b and in a similar way if the focused crystals are offset with the circular nozzle on the negative Y direction, then by

setting $Q_{out-1} > Q_{out-2}$, the offset can be negated as shown in Fig.2.c), thereby achieving maximum enrichment. The working of the proposed system is illustrated using COMSOL Multiphysics 6.0 for two different conditions.
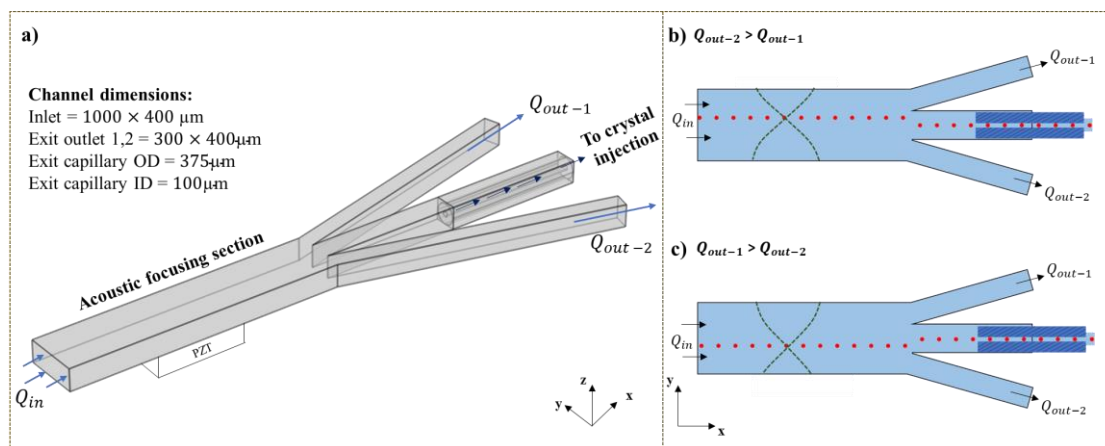
Figure 2: Schematic of flow control enrichment system. a) Design and geometrical model of the system. Alignment of acoustically focused crystals with the centerline of circular capillary could be achieved b) by setting up $Q_{out-2} > Q_{out-1}$ if the offset is in the positive Y direction, and c) by setting up $Q_{out-1} > Q_{out-2}$ if the offset is in the negative Y direction.

Case i): Offset between A and B is 37.5 µm in the positive Y direction, $Q_{out-2} = 103$ µl/min, $Q_{out-1} = 66$ µl/min and Case ii): Offset between A and B is 37.5 µm in the negative Y direction, $Q_{out-2} = 66$ µl/min, $Q_{out-1} = 103$ µl/min. In both cases, the inlet flow rate is set to 300 µl/min. These results suggest that the flow control method could overcome the limitations of misalignment in AFX setups and enhance protein crystal enrichment. The system holds good for offset pronounced in other directions.
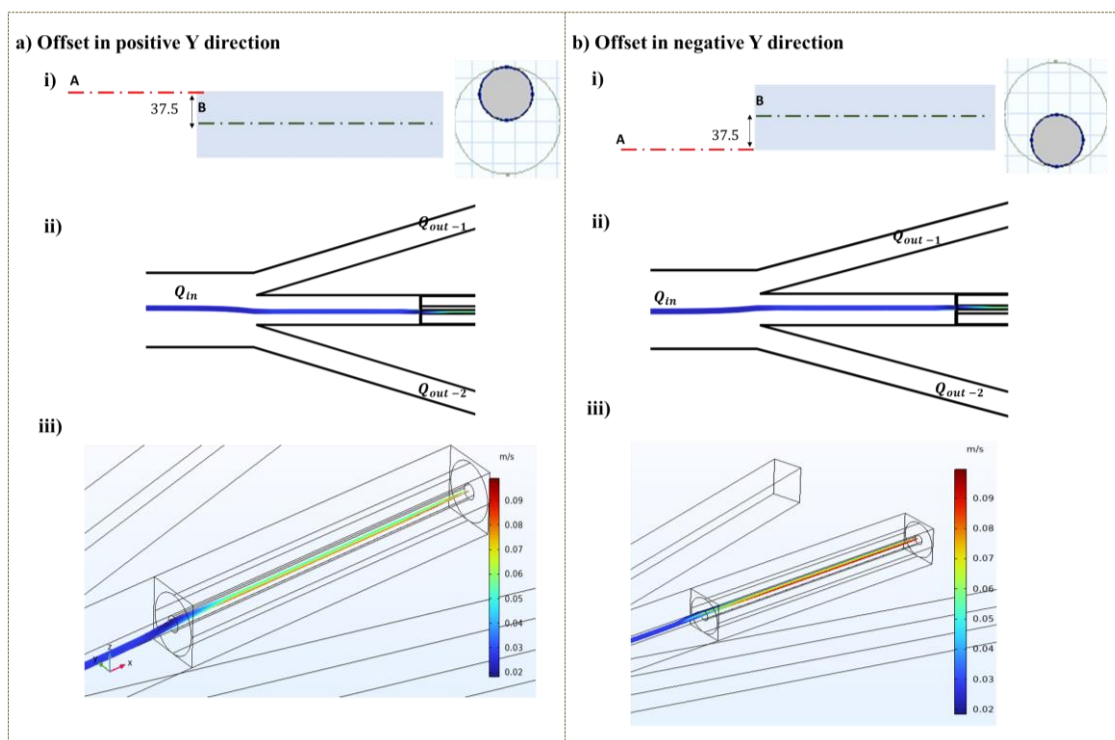
Figure 3: Enrichment using flow control for an offset of 37.5 µm between A and B in a) positive Y direction and b) negative Y direction. i) schematic of the offset, ii) streamlines of particle adjusting due to the flow rate control, and iii) velocity at the circular capillary.

References

[1] Knoška, J. et al. Ultracompact 3D Microfluidics for Time-Resolved Structural Biology. *Nat. Commun.* **11** (1) pp 657 (2020)

[2] Hammarström et al. Acoustic Focusing of Protein Crystals for In-Line Monitoring and Up-Concentration during Serial Crystallography. *Anal. Chem.* 94 (37), 12645-12656 (2022)

Equilibrium position stabilization of multimodal particle manipulation with reinforced learning

Alexander Edthofer,[*], Thomas Laurell[1], and Thierry Baasch[1]

[1]Department of Biomedical Engineering, Lund University, Lund, Sweden
[*]E-mail: alexander.edthofer@bme.lth.se

Introduction

Controlling the motion of one or multiple particles is the backbone of acoustophoresis. Typically, only a single actuation mode is utilized, which pushes the particle to its equilibrium position within that mode. Notably, it is also possible to move particles to intermediate positions between the equilibrium positions of two modes by modulating them. Thus, it becomes possible to achieve higher degrees of control over the particle trajectories, such as moving them along a predetermined line [1] or separating two different particle types [2].

However, the additional complexity of such systems may mean that the modulated equilibrium positions are not sufficiently stable, and finding the optimal interplay between the actuation modes is not trivial. Control algorithms can be applied to control the motion of particles. Here, we apply a reinforced learning approach to control the position of the particles between two modes.

Initial Study

In this initial study, a simple reinforcement learning algorithm moves particles to a predetermined target position by selecting two modes in an acoustofluidic particle manipulator. The force profiles of the modes are shown in **Fig.1**. The study is inspired by the work of Glynne-Jones et al. [3], who used quarter- and half-wave modes in their device, which are equivalent to the force profiles obtained from modes 1 and used in this study (**Fig.1**). Glynne Jones et al. [3] tuned the equilibrium position of the particles by altering the modulation ratio, analogous to the results shown in **Fig. 2**.

For an equilibrium to be stable, the slope of the force profile at equilibrium needs to be negative, such that a small perturbation of a particle's position away from the equilibrium gets automatically corrected. As shown in **Fig.2**, the slope becomes flatter as the modulated equilibrium position approaches the equilibrium position of the pure quarter-width mode, which indicates a decrease in stability.
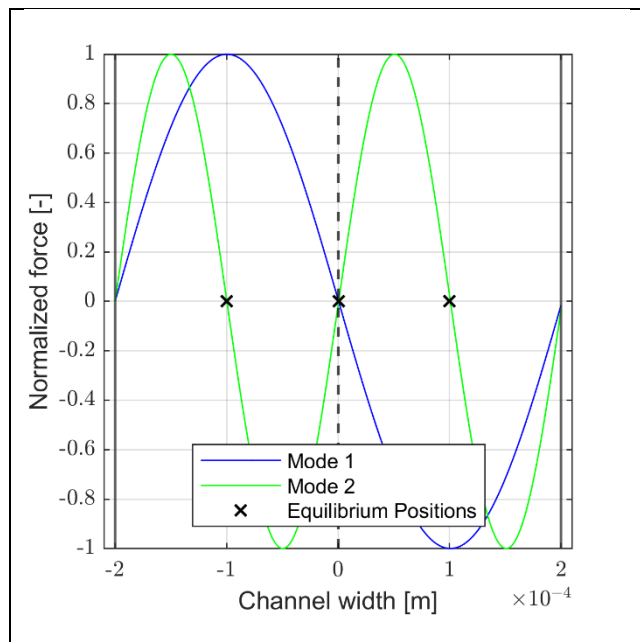
Fig.1 The time averaged force profiles of the two actuation modes used in the study.
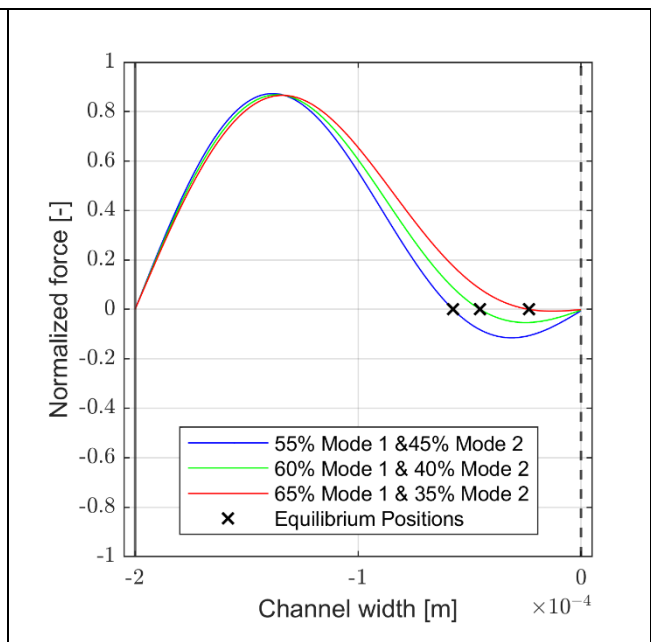
Fig.2 The time-averaged force profile of three different modulation ratios, using the method proposed by Glynne-Jones et al. [3] The amplitude of both modes is equal and normalized.

Equilibrium position stabilization by reinforced learning

The weakly stable equilibrium positions show that there are limitations to the periodic modulation of equilibrium positions. A real system has noise, imperfections, and Brownian motion, which would make it difficult to stabilize particles in such positions. Therefore, to achieve an increased control over particle position, it is necessary to implement active feedback.

Reinforced learning is a first step towards training a control system to give accurate and precise active feedback. In the initial phase of this research project, a custom environment was defined for MATLAB's' built-in Deep Q-network (DQN) algorithm, with the objective to move particles towards a predetermined target position between the stable equilibrium positions of the two modes shown in **Fig. 1**.

First the algorithm was trained by seeding a particle at random within the defined region. Then, it was allowed to activate either of the two modes for a short amount of time and adjust the amplitude of the generated force profile, with the goal of moving the particle towards the predetermined target position. During training, the algorithm was punished when moving the particle further away from the target position and rewarded for moving the particle closer to the target position. After training was finished the algorithm was deployed and its performance was evaluated. **Fig. 3** shows the trajectories of 15 randomly seeded individual particles under the action of the control algorithm after training. First, the target position was chosen in a region with a strong stable equilibrium according to the periodic modulation model by Glynne-Jones, see **Fig. 3a**. Second, the target position was chosen in the region of the channel that has a weak stable equilibrium according to the model by Glynne Jones, **Fig. 3b**. To further challenge the algorithm and test its robustness, a small random contribution was added to the particle's position after each time-step.
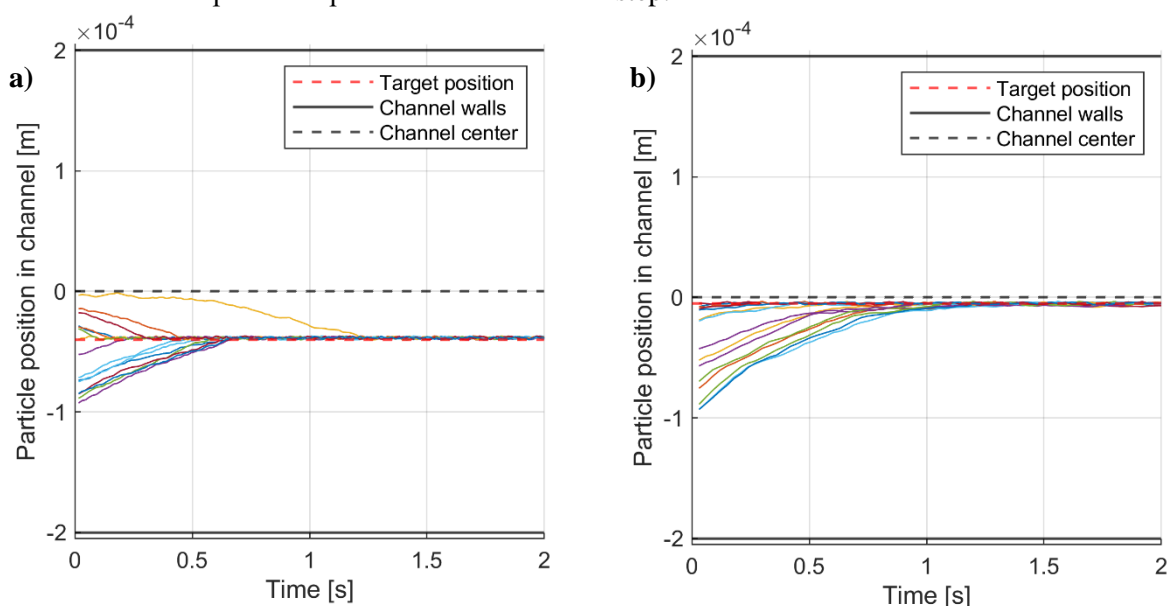
Figure 3: Particle trajectories of 15 randomly seeded particles being controlled towards the target position and stabilized. **a)** The target position is in a region with strong stable equilibrium positions for the modulated modes. **b)** The target position is in a region with weak stable equilibrium positions for the modulated modes.

Discussion, Conclusion and Outlook

We presented an initial study that aims to utilize machine learning for active control of particle trajectories within acoustofluidic devices. Although good progress has been made in the literature [1] the area remains largely unexplored and has the potential to significantly boost the control over particle manipulation. In this initial study a standard reinforcement algorithm solved a simple toy problem: the movement and stabilization of a single particle by modulating two actuation modes. As it was able to easily meet this first challenge and showcase that, even in its early stages, the reinforced leaning algorithm is powerful enough to improve upon existing techniques, the project will focus on more complicated problems in the coming months, starting with the separation of two different particles and moving a single particle along a predetermined path.

References
[1] K. Yiannacou, and V. Sariola, *Advanced Intelligent Systems,* **5.9** 2300058 (2023)
[2] C. Siversson, F. Petersson, A. Nilsson, and T. Laurell, *MicroTas 2004: Volume 2,* 329 (2007)
[3] P. Glynne-Jones, R. Boltryk, N. Harris, A. Cranny, and M. Hill, *Ultrasonics,* **50.1** 68-75 (2010)

Experimental Demonstration of long-Range Acoustic Pulling using Mode Conversion in Waveguide

Yanlong Guo[1,2], Feiyan Cai[2], and Degang Zhao[1], Hairong Zheng[2]

[1]Department of Physics, Huazhong University of Science and Technology, Wuhan 430074, China
[2]Paul C Lauterbur Research Center for Biomedical Imaging, Shenzhen Institutes of Advanced Technology, Chinese Academy of Sciences, Shenzhen 518055, China
E-mail: fy.cai@siat.ac.cn,   dgzhao@hust.edu.cn

Introduction

Acoustic waves have proven to be a valuable tool for contactless and noninvasive manipulation of objects in various fields, including physics, chemistry, and biology. This manipulation is achieved through the interaction between acoustic waves and objects, involving processes such as absorption, scattering, and reflection. These interactions result in the exchange of momentum and energy between the waves and objects, ultimately generating an acoustic radiation force on the objects. While it is intuitively expected that a plane wave would push a particle in the direction of wave propagation, there has been growing interest in the counterintuitive phenomenon of acoustic pulling, where particles are pulled toward the acoustic source.

The concept of acoustic pulling was initially proposed by Marston, who theorized that it could be achieved using Bessel Beams [1]. The underlying physical mechanism for this pulling force involves either suppressing backward scattering or maximizing forward scattering, leading to an enhanced net linear momentum propagation in the direction of wave propagation and causing objects to be pulled toward the acoustic source [2]. Then, scientists have explored various methods to realize acoustic pulling forces, including tailoring the incident beam (e.g., using two plane waves) [3], engineering unconventional objects (e.g., metamaterials with anomalous acoustic scattering) [4], and designing structured material backgrounds (e.g., phononic crystal waveguides) [5]. However, experimental realizations of acoustic pulling forces have been limited, with only a few cases reported, such as using a two-dimensional source array to pull a large triangular object [6].

In this study, we present an experimental demonstration of acoustic pulling over long distances in a waveguide based on mode conversion. Specifically, we show that an elliptic object can be successfully pulled toward the acoustic source using this technique. This achievement further advances the understanding of acoustic pulling and opens up new possibilities for its practical applications.

Materials and methods

We selected an air rectangular waveguide surrounded by polystyrene for our experiment. The dimensions of the inner area are as follows: the width (lx) is 8.89 mm, the height (ly) is 2.2 mm, and the length (lz) is 150 mm. Inside the waveguide, we placed an elliptic foam particle with parameters width $rx = 1.5$ mm and height $ry = 7.5$ mm. At the entrance of the waveguide, we positioned a loudspeaker with a radius of 3.5 mm and a central frequency of $f = 40$ kHz. To capture the particle movement, we positioned a camera directly above the waveguide. To analyze the dispersion curves and field distribution of the waveguide, we used the COMSOL Multiphysics software. The acoustic radiation force was calculated by integrating the stress tensor over a closed surface that covers the object.

Results and discussions
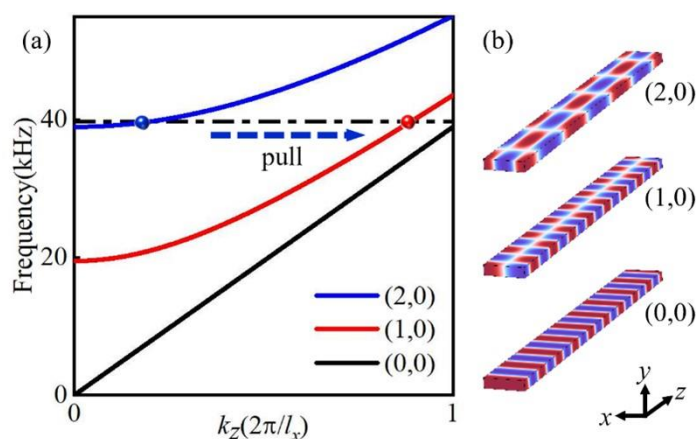
Figure 1: Theoretical analysis of the waveguide. (a) Dispersion curve of the rectangular waveguide. (b) Eigen field distribution inside the waveguide of mode (2,0), (1,0) and (0,0).

Fig.1 (a) shows the dispersion curve of the air rectangular waveguide, while Fig. 1(b) illustrates the eigenfield distribution of three modes at 40 kHz. At this frequency, there are three modes present in the width direction: the second order, the first order, and the zero order. The height direction is so small that there exists a plane wave mode (zero mode). It is important to note that as the order increases, the momentum (k) decreases.

When an object is placed in the waveguide, it can scatter acoustic waves within the waveguide, converting incident phonons in one mode into scattered phonons in another mode. If an incident phonon is in the low momentum mode and scatters into a high-momentum mode, the object experiences a pulling force. This intuitive picture provides insights into the origin of acoustic pulling force.

Experimental results, as shown in Fig. 2(a), support this intuitive understanding. When an acoustic wave with a frequency of 40 kHz is generated by the loudspeaker, this is also near the cut-off frequency of the second mode, an elliptic foam particle placed in the waveguide moves towards the source. Conversely, in Fig. 2(b), we present a case where a microsphere object with a diameter of $r = 1mm$ experiences a pushing force and moves away from the source.

To further analyze the phenomena observed in the experiment, we conducted a theoretical analysis of the acoustic radiation force on the particle. Fig. 2(c) demonstrates that for the elliptic foam particle, the acoustic radiation force in the z direction is negative above the second-order cut-off frequency of 39 kHz. However, for the spherical foam particle, the acoustic radiation force in the z direction is always positive, as shown in Fig. 2(d). The size of the particle influences wave scattering and in the case of the elliptic particle present in the waveguide, it scatters the second-order mode to the first order and zero-order modes with a larger wave vector, resulting in the achievement of acoustic pulling through mode conversion of the acoustic field.
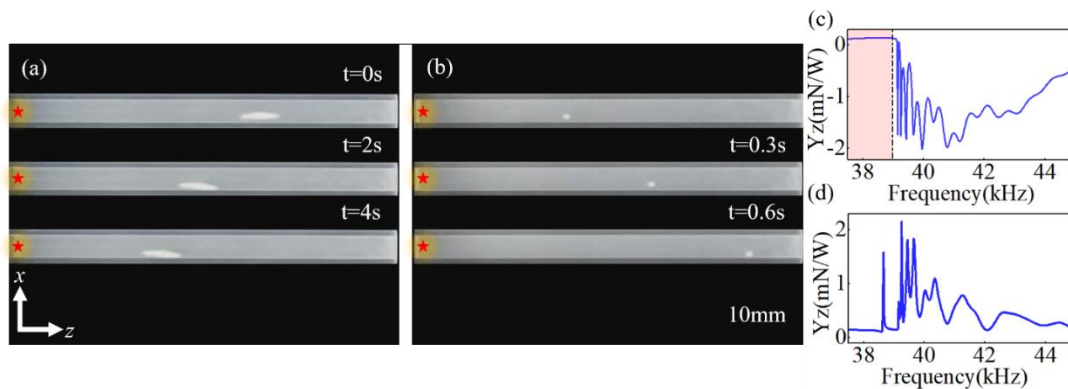
Figure 2: Experimental observation and numerical analysis of acoustic pulling and pushing inside the rectangular waveguide. (a) Sequential images illustrate the pulling motion of an elliptic object over time. The elliptic particle is observed moving irregularly toward the source (marked by the red star) (b) Comparative experiment using a microsphere as the object, which was exerted by a push force and moving away from the source. (c) Calculation of the non-dimensional acoustic radiation force (Yz) versus frequency on the elliptic particle. (d) the same as (c) but for spherical particle.

Conclusion

Our experimental study successfully demonstrated the occurrence of stable and long-range acoustic pulling inside an air waveguide using an elliptic object. The observed pulling force arises from mode conversion within the waveguide. These findings present a novel, straightforward, and robust method for achieving stable long-range acoustic pulling, while also enhancing our understanding of the interaction between acoustic waves and matter.

Acknowledgments

References
[1]   P. L. Marston, *JASA,* **120**, 3518-3524, (2006).
[2]   L. Zhang and P. L. Marston, *JASA,* **140**, EL178-EL183, (2016).
[3]   S. Xu, C. Qiu, and Z. Liu, *EPL,* **99**, 44003, (2012).
[4]   M. Stein, S. Keller, Y. Luo, and O. Ilic, *Nature Communications,* **13**, 6533 (2022).
[5]   Y. Gao *et al.*, *Photonics,* **10**, 1325, (2023).
[6]   C. E. M. Démoré, *PRL*, **112**, 174302 (2014).

Focused ultrasound induced fluid flow in a silicon capillary determined via micro-PIV treatment

Elisa Ghiringhelli[1,*], Carine Guivier-Curien[1], Philippe Lasaygues[2], Cécile Baron[1]

[1]Aix Marseille Univ, CNRS, Centrale Méditerranée, IRPHE UMR 7342, Marseille, France
[2]Aix Marseille Univ, CNRS, Centrale Méditerranée, LMA UMR 7031, Marseille, France
[*]E-mail: elisa.ghiringhelli@univ-amu.fr

Introduction

Bone tissue is known to be a regenerative tissue that adapts to mechanical forces, optimizing its structure through a process known as bone remodeling. Nonetheless, under pathological conditions, this process must be assisted. Several clinical studies proposed low-intensity ultrasound (LIUS) to enhance bone regeneration [1], however, the detailed mechanism of how LIUS affects bone cells, remain an open question [2]. Identifying and quantifying the mechanical stresses LIUS exerts on bone cells is essential to develop more effective and nuanced therapeutic methods and to provide clarity in this complex field of study. Our work hypothesis relies on the interaction between LIUS and the osteocyte microenvironment, the lacuno canalicular system, that, being saturated with interstitial fluid, potentially causes a hydrodynamic phenomenon, the acoustic streaming, generating shear stresses at the osteocyte dendrite wall that may trigger a biological response [3].

Materials and Methods

A micro-PIV set-up has been developed to visualize the fluid flow in microchannels, representing the canaliculi, under the stimulus of three dimensional ultrasounds pressure waves. The velocity field can be reconstructed thanks to the presence of 1µm diameter fluorescent microparticles used as trackers [4]. Images are taken via an inverted microscope with a green laser, see Figure 1 for the schematics of the experimental set up. Experiments are carried out in a straight channel with a squared cross section of 200µm, nevertheless, later on, the geometry will be manufactured to better reproduce the micro-environment of the osteocyte. Acoustic pressure waves are generated by a focused transducer, to reproduce the therapeutical conditions.
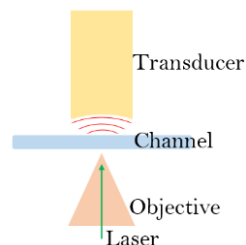
Figure 1: Schematics of the microfluidic chip and the experimental setup used at IRPHE in Marseille.

Results and Discussion

The flow velocity induced by focused ultrasound, was obtained thanks to a PIV treatment. Different flow patterns and velocities (under 5µm/s) are obtained for different modal frequencies. The highest velocities, up to 20µm/s, are obtained at the resonance frequency (3.75MHz, for a squared cross-section channel of 200µm). For this particular case, the fluid moves towards the focal point in the channel's bottom region, the focal plane further away from the transducer, whereas the opposite behavior is observed on the top, see Figure 2.
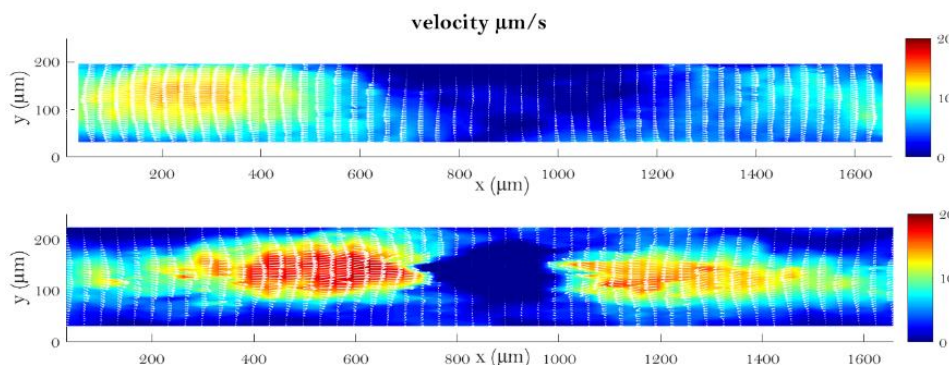
Figure 2: Velocity field of the fluid under ultrasound stimulation at the bottom of the channel (a) and at the top (b). Treatment is done at t = 17s.

Conclusion

An experimental set-up for the visualization of the fluid flow induced by ultrasound waves was developed. Results show highly three dimensional flows depending on the frequencies of the pressure waves, along with the possibility of improving the comprehension of the ultrasound stimulation of bone regeneration. To verify the phenomenon, the experimental set up is to be reproduced in Comsol Multiphysics, allowing the validation of the numerical model. Consequently, the computational model can be complexified to better match the reality of the fluid cell micro-environment

References (Times New Roman 10 pt)
[1] Schandelmaier & al., BMJ (2017).
[2] Aspenberg & al., Acta Orthop. (2017).
[3] Weinbaum & al., J. of Biomechanics (1994).
[4] Barknob & al. Physical Review (2012).

Gentle blood plasma separation with surface acoustic wave-based microfluidics

Melanie Colditz[1,*], Armaghan Fakhfouri[1], Romy Kronstein-Wiedemann[2], Kateryna Ivanova[1], Torsten Tonn[2] and Andreas Winkler[1]

[1]Leibniz-IFW Dresden, Helmholtzstr. 20, 01069 Dresden, Germany
[2]TU Dresden/ DRK-Blutspendedienst Nord-Ost gGmbH, Blasewitzerstr. 68/70, 01370 Dresden, Germany
[*]E-mail: m.colditz@ifw-dresden.de

Introduction

Liquid biopsy has become an important tool for the diagnosis and monitoring of various diseases as it provides minimally invasive access to biomarkers for disease detection and treatment evaluation. However, one of the major bottlenecks in liquid biopsy is sample preparation. Blood, the most important fluid for liquid biopsy, contains a large number of biomarkers in the nanometer and sub-micron range in its plasma fraction. However, the large cell content presents a challenge in the search for innovative biomarkers in blood plasma. Conventional methods of cell separation, such as centrifugation, often involve strong forces that risk rupturing the cells and releasing unwanted cell cargo and thereby contaminating the plasma sample for further analysis. To meet this challenge, there is a growing interest in alternative methods for gentle blood plasma separation. With surface acoustic wave (SAW)-based microfluidics the sorting of blood cells as well as focusing of these and influencing of nanoparticles was already demonstrated [1,2]. The following experimental study prioritizes the reproducible and gentle separation of blood cells and plasma.

Experimental methods

Human blood from healthy donors was obtained and processed using two different methods for blood plasma separation: SAW-based microfluidics and conventional centrifugation for comparison. For SAW-based microfluidics, blood was diluted 1:5 with PBS and introduced directly into the microfluidic channel, where two separation stages were used to displace blood cells towards the channel walls within the acoustic field, resulting in purified plasma in the channel center (see Figure 1). Each separation stage consists of a pair of interdigital transducers which were operated at a frequency of 12.82 MHz and an input power of 1200 mW each. In parallel, blood samples were processed by centrifugation following the International Society on Thrombosis and Haemostasis guidelines, which recommend two centrifugation steps at 2500 x g for 15 minutes.

For analysis the initial cell concentration was determined using a hematology analyzer directly after blood draw. For the low concentration of remaining red blood cells (RBCs) in separated plasma samples, Neubauer-Improved hemocytometer was used with a 3 x 3 mm² cell counting area. Platelet (PLT) concentrations were determined indirectly using the RBC/PLT ratio obtained by flow cytometry using fluorescence staining with anti-CD41a-PerCP-Cy5.5 for PLTs and anti-CD235a-FITC for RBCs.
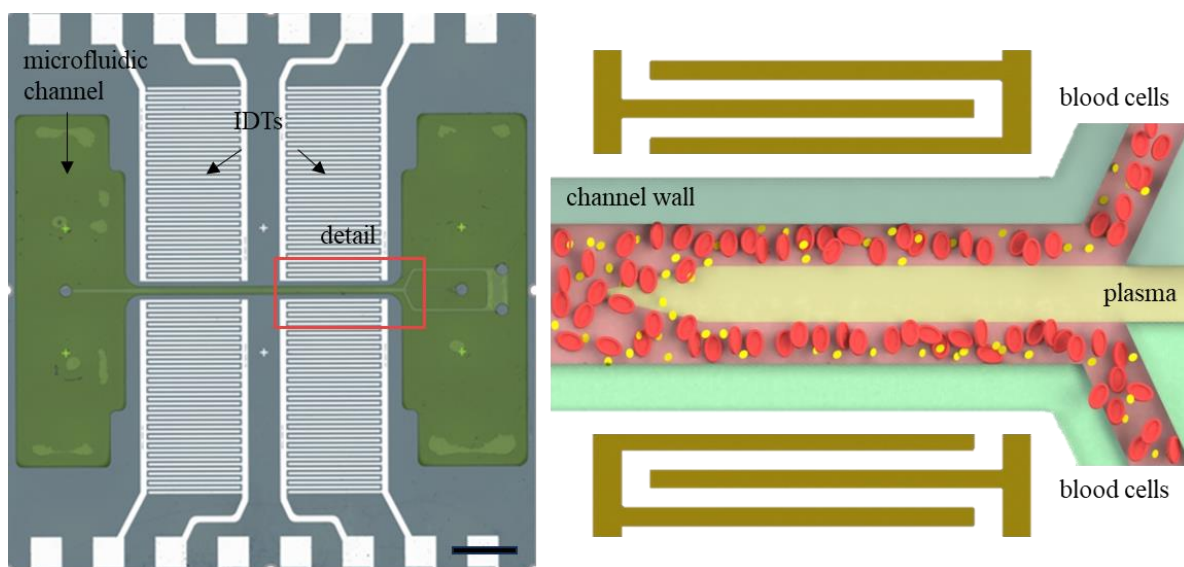
Figure 1: SAW chip with two metal interdigital transducer (IDT) pairs and on-chip microfluidic channel, scale bar 2 mm (left), Detail of blood cell separation in the acoustic flied (right)

Results and Discussion

With our continuous SAW sorting approach (see Figure 2A), we achieved an RBC separation purity of 99.96 % and a PLT separation purity of 58.41 %. The former is in the same range as centrifugation, while the PLT concentration has been considerably reduced but still needs to be optimized. However, analysis using flow cytometry, hematology analyzer and hemocytometer showed that, as expected, centrifuged samples contain a high proportion of destroyed cells, cell debris and agglomerates. In contrast, for the SAW-based microfluidics, the hemocytometer images show no difference in size of the RBCs and no agglomerates (see Figure 2 B, C). This is also confirmed by the measurements of the RBC and PLT indices with the hematology analyzer, which correspond in volume, size distribution, etc. to those of the freshly drawn blood. By measuring free hemoglobin in the plasma, it was also found that the separation of blood plasma by SAW does not damage the RBCs. Furthermore, the measurements of the SAW-purified plasma indicate a higher reproducibility than the plasma samples by centrifugation, although all were processed together, on the same day and with blood from the same donor.
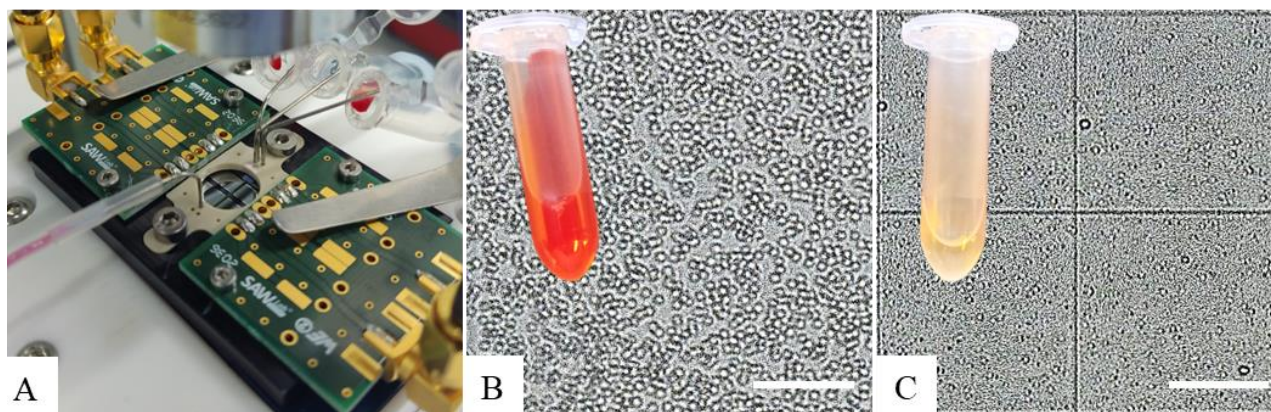
Figure 2: (A) Setup during blood plasma separation with SAW chip connected to printed circuit boards for electrical connection and fluid connector to flow through blood. Samples were collected in tubes at the outlets. (B) Hemocytometer image of initial blood 1:500 diluted with PBS, scale bar 100 µm (C) Hemocytometer image of SAW-purified plasma sample, scale bar 100 µm

Conclusion

Overall, the analysis shows that centrifugation generally shows a higher separation purity than our SAW-based microfluidic approach. However, in contrast to centrifugation, where optimization is already established, SAW-based microfluidics still offers room for improvement. Furthermore, it showed a gentler and more reproducible cell separation from plasma than centrifugation, which has a positive impact on subsequent liquid biopsy analyses, especially for optical methods. The release of hemoglobin and red coloring caused by centrifugation is a challenge for many methods. In addition, the destruction of cells can distort the isolation and quantification of biomarkers. This study presents an innovative method for separation of plasma from human blood as well as an extensive analysis of its residual cells and cell condition. The approach shows potential for future use in a biomedical application.

Acknowledgements

References

[1] C. Richard et al., *Lab Chip*, **19**, 24, pp. 4043-4051 (2019)
[2] A. Fakhfouri et al., *ACS Appl. Mater. Interfaces,* **15**, 20, pp. 24023–24033 (2023)

High throughput acoustic cell washing and concentration for CAR T cell therapy

Anke Urbansky[a], Karl Westerlund[a], Raghuraman Srinivasan, Erik Karlsson, Cecilia Magnusson, Erling Nielsen, Julia Alsved, Jessica Congiu, Magnus Hivert, <u>Pelle Ohlsson</u>*

AcouSort AB, Lund, Sweden www.acousort.com
*E-mail: pelle.ohlsson@acousort.com
[a]Equal contribution

Introduction

Chimeric antigen receptor (CAR) T cell therapy is a promising treatment mainly for blood cancers, with around 364 ongoing clinical trials (March 2019) [1]. When the therapy is done autologously using the patient's own cells, T cells are harvested from the patient's blood, genetically modified to target the patient's own cancer and infused back into the patient. The genetical modification is typically done manually using advanced equipment in a cleanroom. The manual processing, however, causes variability, contamination, and prohibitively high costs, limiting access to the therapy. To alleviate these problems there are initiatives to automate the sample processing into closed systems. Here, acoustofluidics has turned out to be promising for many of the steps to be automated including cell separation, washing and concentration (fig. 1). Since the volumes to be processed are often on the order of hundreds of milliliters per hour, we have pushed our acoustic separation technology to throughputs of 3-6 mL/min per channel. In this study we have investigated the performance of our cell concentration and washing modules, showing cell recoveries of 93-99%, 97% retained viability and 99% contamination removal.
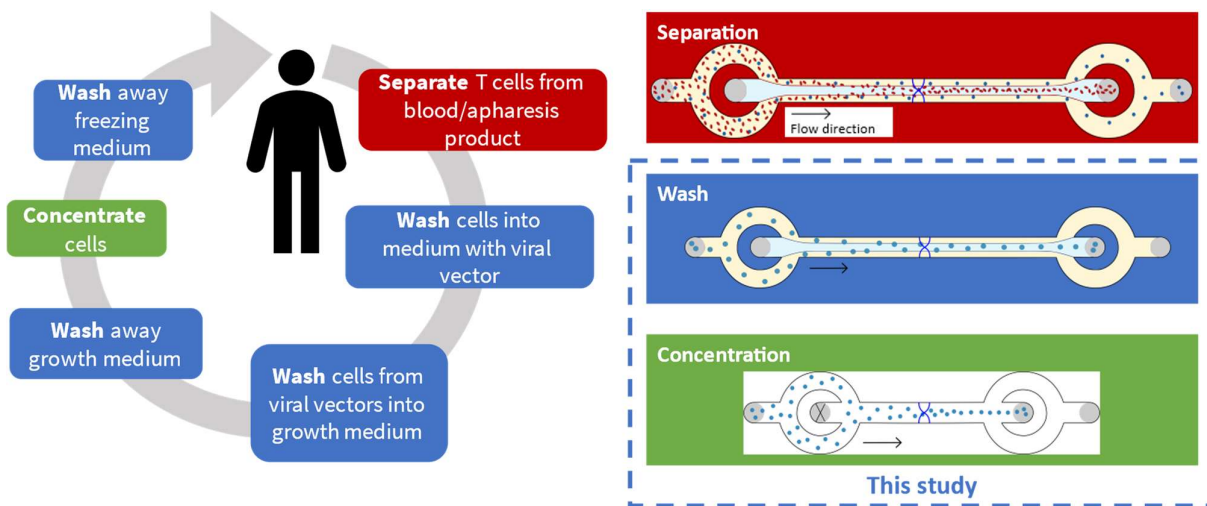
Figure 1: Steps in autologous CAR T cell therapy sample preparation where acoustofluidics may be helpful.

Methods

Our acoustofluidic module consists of a glass chip actuated by a piezoelectric transducer. This generates an acoustic standing wave in the channel, pushing cells towards the centerline. In this study, we used the chip for concentration, where the focused cells are separated from the depleted liquid by a flow splitter, and for washing where cells are laminated on the sides of a center medium that they are focused into (fig. 1).

Syringe pumps were used to control all flows. Flow cytometry (Luminex Guava EasyCyte) was used to analyze the input and output samples to calculate the focusing efficiency, here defined as the number of cells in the target outlet divided by the number of cells in both outlets combined.

Concentration was tested using white blood cells (WBCs) that were isolated from whole blood by selective lysis and suspended in a sample medium consisting of 1x PBS, 0.5% BSA, 1 mM EDTA at a concentration of 100 000 cells/mL. To evaluate the performance at higher particle concentrations, samples of either cultured Jurkat cells at 50 million cells/mL or 5 µm polystyrene beads at concentrations of up to 500 million/mL were used.

Cell washing was tested using samples of either white blood cells (WBCs), isolated as previously described and resuspended at a concentration of 500 000 cells/mL, or 5 µm polystyrene beads at concentrations of up to 500 million/mL. Washing efficiency was evaluated by spiking the input sample with 100 ng/mL fluorescein and measuring the fluorescence in the input and output samples using a Tecan Infinite 200 Pro F Nano plate reader.

Results

Our acoustofluidic module was able to concentrate both WBCs (100 000 cells/mL), cultured Jurkat cells (50 million/mL) and 5 µm polystyrene beads (up to 500 million/mL) with a factor of 5 with a sample throughput of 4-6 mL/min and a recovery of >98%, 93% and >94% of the target cells or particles recovered in the target outlet respectively (fig. 2). Cell viability was maintained to 97% through the process.
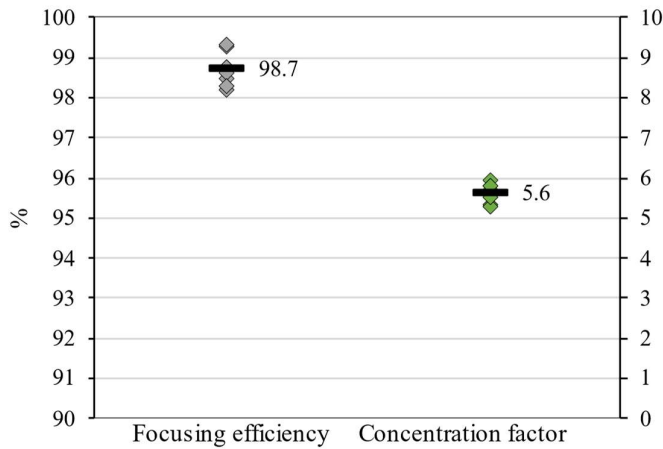
Figure 2: Focusing efficiency and concentration factor for the cell concentration.

For cell washing, >98.5% of spiked fluorescein was removed from the cell sample while recovering >97% of the cells in the central outlet and maintaining the viability to 97%. For polystyrene bead samples at concentrations of up to 500 million/mL, 99% of the beads were recovered in the central outlet while removing >98.8% of fluorescein from the originally suspending solution.
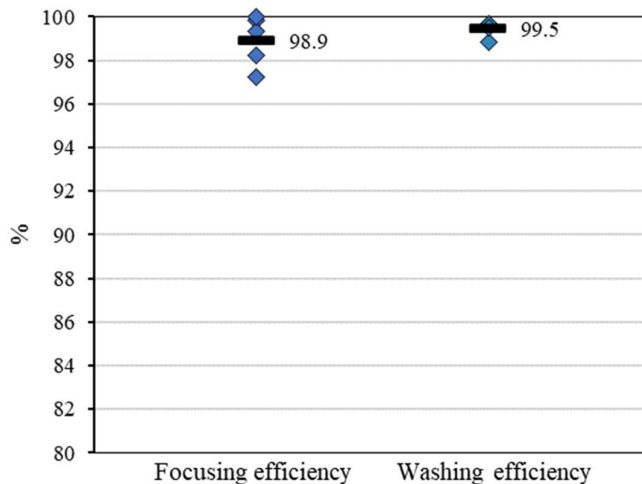
Figure 3: Focusing and washing efficiency for cell washing.

Conclusion

This study shows that high focusing efficiency, washing efficiency and viability can be maintained at high sample throughputs of 3-6 mL/min per channel, which is promising for use in autologous CAR T cell therapy sample preparation.

References

[1] Xin Yu J, Hubbard-Lucey VM, Tang J, Nature Reviews. Drug Discovery. **18,** 11, 821–822 (2019)

Identifying temperature gradients inside acoustofluidic channels

Gabriel Werr[1], Pradipta Kr Das[1], Zahra Khaji[1], and Maria Tenje[1, *]

[1] Department of Materials Science and Engineering, Science for Life Laboratory, Uppsala University, 721 29 Uppsala, Sweden
*E-Mail: maria.tenje@angstrom.uu.se

Introduction

Acoustophoretic devices have a wide variety of applications for particle manipulation, from sorting and trapping to mixing and washing [1, 2]. For stable operation of such systems, constant behaviour of the microfluidic chip is required, such as laminar flow with predictable mixing via diffusion. As recently shown by Joergensen *et al.* [3] the non-linear effect of thermoacoustic heating arises as a critical factor at high acoustic energies (>100 J/m^3) leading to changes in the acoustic streaming profile. It therefore becomes critical to monitor the temperature inside acoustophoretic channels for controlled operation. Here, we present a silicon-glass acoustophoretic channel with integrated thin film resistive sensors (RTDs) distributed across the width of the microfluidic channel, positioned at the silicon-glass interface. These sensors allow for *in situ* measurements of the temperature inside the channel during acoustophoresis at different energy levels to enable reliable prediction of the system performance.

Theory and Experimental procedure

The microfluidic channel was etched in a 512 µm thick silicon wafer with a channel depth of 150 µm and a channel width of 600 µm via DRIE (Deep Reactive-Ion Etching), resulting in a half wave resonance frequency of ≈ 1.4 MHz. The channel was closed with a glass wafer that had eight 4-wire RTDs 150 nm thick recessed into the surface to allow the two wafers to be anodically bonded together, a modified fabrication technique for sensor integration developed by our group [4, 5]. The sensor placement can be seen in Figure 1. Care was taken to position the sensors appropriately in relation to the pressure node of the acoustophoretic channel to investigate the effect of the acoustic force field on the temperature. After dicing the bonded wafers, capillaries were glued for fluidic connections and the RTDs were connected to a PCB using silver-epoxy.
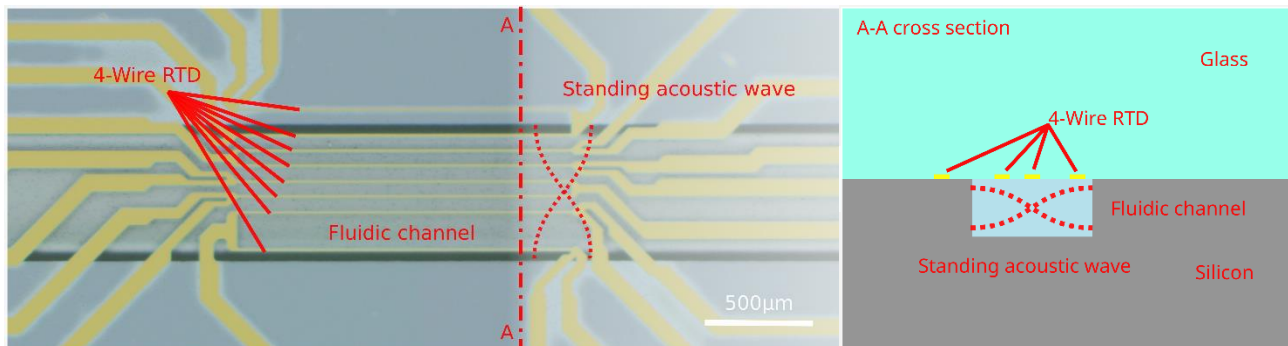
Figure 1: Top view of the microfluidic channel and RTD placement in both top view and simplified sketched cross section view.

To characterize the temperature inside the channel, we have measured the RTD resistance change during acoustic resonance inside the channel where the piezoelectric transducer (PZT) was cycled on and off in 20 min intervals. All measurements were then pooled together and normalized to a sensor placed outside the fluidic channel.

Results

RTD resistance outside the fluidic channel was measured around 450 Ω. After actuating the PZT for 20 min the resistance of the RTDs inside the channel increases and Figure 2 shows the change in RTD resistance along the channel width. The resistance can be correlated to the temperature with equation 1.

$$R_{RTD} = R_0(1 + A * T + B * T^2) \qquad (1)$$

where R_0 is the RTD resistance at T=0 °C and R_{RTD} is the RTD resistance at T °C. The shift in RTD resistance observed at the glass-silicon interface of the microfluidic channel varied from 9.06 Ω to 9.12 Ω when measured across the acoustophoretic channel. It shall be noted that this device did not include any electrical insulation between the Si wafer and the RTDs, which has affected the measurements, resulting in an interaction of neighbouring sensors possibly distorting the expected symmetrical temperature gradient.
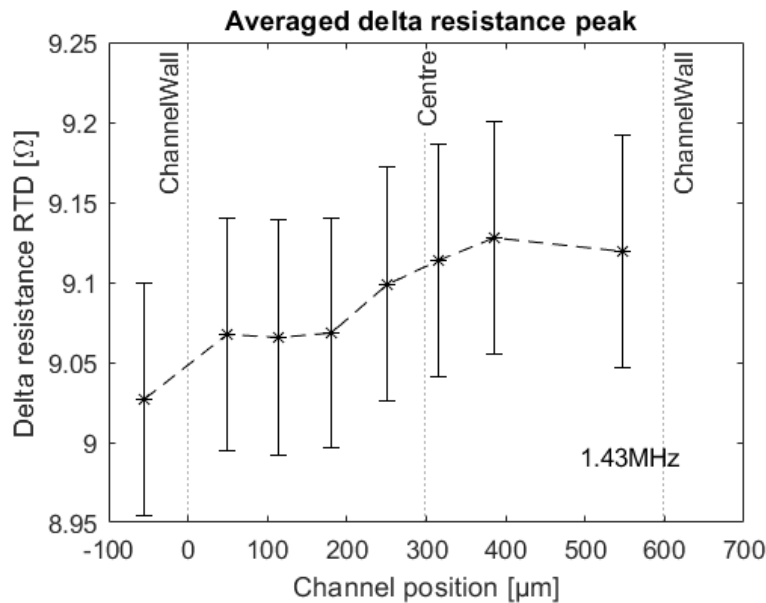
Figure 2: Averaged peak resistance from 25 on/off cycles, plotted with a 95% confidence interval. The resistances are shown relative to the RTD outside the fluidic channel at room temperature resistance.

Conclusion

Temperature measurements inside an acoustophoretic channel have been reported, indicating a gradient across the channel width. Temperature gradient was evaluated by measuring the change in the RTD resistance. We have observed a significant shift in RTD resistance (from 9.06 Ω to 9.12 Ω) across the channel width. The resistance data was expected to be symmetrical around the centre. However, the interaction of neighbouring sensors may affect the measurements, leading to distortion of the profile. To have a detailed understanding, an improved design will be fabricated and tested in a future study. This setup has the potential to also observe the cause of the change in acoustic streaming, *i.e.* the internal heating at the viscous boundary layer.

Acknowledgements

References

[1] M. Evander, J. Nilsson, *Lab on a Chip* **12**, 4667 (2012).

[2] A. Lenshof, C. Magnusson, T. Laurell, *Lab on a Chip* **12**, 1210 (2012).

[3] J.H. Joergensen, W. Qiu, H. Bruus, *Phys. Rev. Lett.* **130** (2023).

[4] M. Andersson, J. Ek, L. Hedman, F. Johansson, V. Sehlstedt, J. Stocklassa, P. Snögren, V. Pettersson, J. Larsson, O. Vizuete, K. Hjort, L. Klintberg, *Journal of Micromechanics and Microengineering* **27**, 15018 (2017).

[5] K. Svensson, S. Södergren, K. Hjort, *Scientific Reports* **12**, 569 (2022).

Increased throughput and capacity of nm-particle trapping using an ultrasound activated packed bed

Michael Gerlt[1,*], Ted Bondesson[1] and Thomas Laurell[1]

[1]Biomedical Engineering, Lund University, Lund, Sweden
*E-Mail: michael.gerlt@bme.lth.se

ABSTRACT
We present an acoustofluidic device capable of efficient nm-particle trapping at a sample throughput of 50 µL/min. By filling a capillary with 100 µm PS beads and actuating the system with a piezoceramic actuator glued to the capillary we trap 270 nm polystyrene particles with efficiencies exceeding 60%. We prove that trapping can be achieved across a wide actuation frequency and can be performed in a corresponding polymer 3D-printed device, demonstrating the versatility of the approach.

Introduction
Research on extracellular vesicles (EVs) is gaining increased attention given their potential to serve as a possible biomarker and thus novel diagnostic tool for cancer or time critical diseases such as sepsis. The state-of-the-art method to isolate EVs from their host liquid is ultracentrifugation. However, this method demands large sample volumes, significant manual labor and long processing times, not amenable for diagnostics. An alternative for efficient isolation of EVs is acoustic particle trapping using levitated seed particles in a λ/2 resonator as demonstrated by Evander et al. [1]. The major drawback is the modest capacity of this system. Here we propose to use a capillary filled with seed particles (packed bed) which enables an arbitrary increase in throughput, capacity, and recovery. Our approach enables a wide frequency actuation range and neither does rely on tuning the actuation frequency to resonate the trapping beads as in the case of Neild et.al [2], nor does it depend on tuning the system to the capillary cavity resonance [3].

Experimental Setup
We filled a glass capillary (4 mm width, 0.4 mm height, 0.28 mm wall thickness, 2540 Rectangle VitroTubes™, Vitrocom, USA) with 100 µm diameter polystyrene (PS) particles and sintered a small portion near the outlet to retain the packed bed against flow. A piezoelectric element (Pz26, 10 mm length, 4 mm width, 0.5 mm height) was glued to the bottom of the capillary (Fig.1).
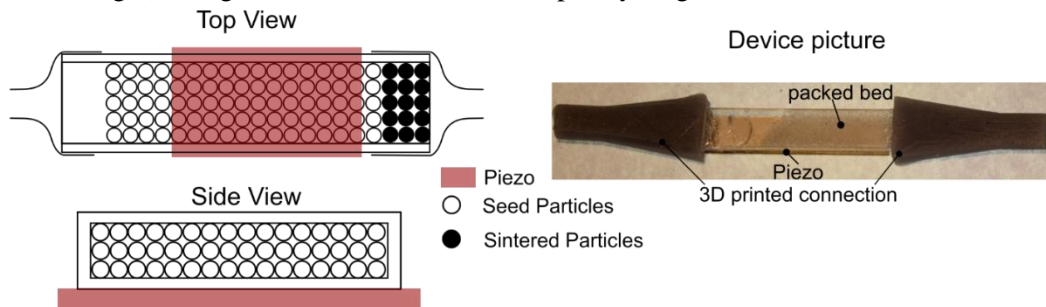
Figure 1: Sketch and picture of the packed bed device used for nm-particle trapping.

The setup consisted of two syringe pumps connected to a valve, the traping device and a fluorescnce microscope for trapping efficiency analysis (Fig. 2). One of the syringe pumps was filled with particles dissolved in PBS and the other with pure PBS for washing. The fluorescnent microscope was equipped with a CoolLED, FITC filter set (excitation: 475±17.5 nm, emission 530±21.5 nm) and monochrome camera (U3-3880CP, IDS, Germany). We utilized blue fluorescent PS particles of 2 µm and 0.27 µm diameter (Fluoro-Max™, Thermofischer, USA). Further, we developed a protocol to determine trapping efficiency and capacity of our devices: 1. Flush with buffer to attain background signal, 2. Inject particles to the trap, 3. Wash with PBS, 4. Turn ultrasound off. Trapping efficiency was determined by integrating the area of the fluorescent signal for step 4 and divide it by the combined area of step 2, 3, and 4 (Fig 3(a)).
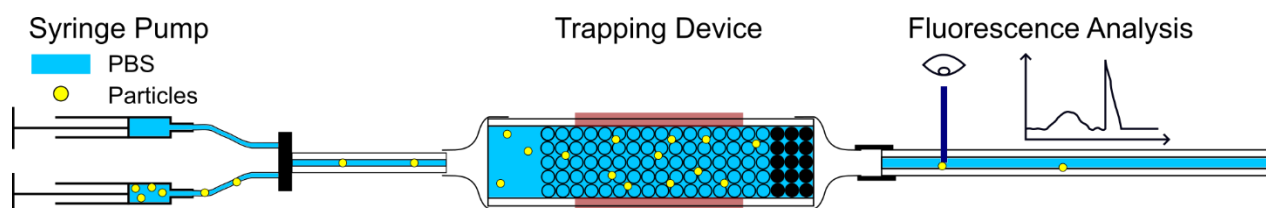
Figure 2: Setup for in flow analysis of trapping efficiency.

Results and Discussion

As an initial experiment, we injected ~3×10^6 of 2 µm PS particles at a flow rate of 50 µL/min, washed with 200 µL of PBS. While injecting particles, we excited the ultrasound transducer at a frequency of 460 kHz at an input power of 440 mW, leading to a temperature of 30.5 °C at the glass capillary. When turning off the ultrasound, we recorded a trapping efficiency of 48% (Fig 3 (a)). In further experiments, we varied the excitation frequency of the piezoelectric element. We were able to capture particles at a very wide frequency range (0.4-5 MHz). It is noted that the best trapping efficiencies were achieved close to the width mode of the piezoelectric transducer. The thickness mode (4.7 MHz) lead to a comparatively low trapping efficiency but could be used with much less input voltage (Fig 3 (b)).
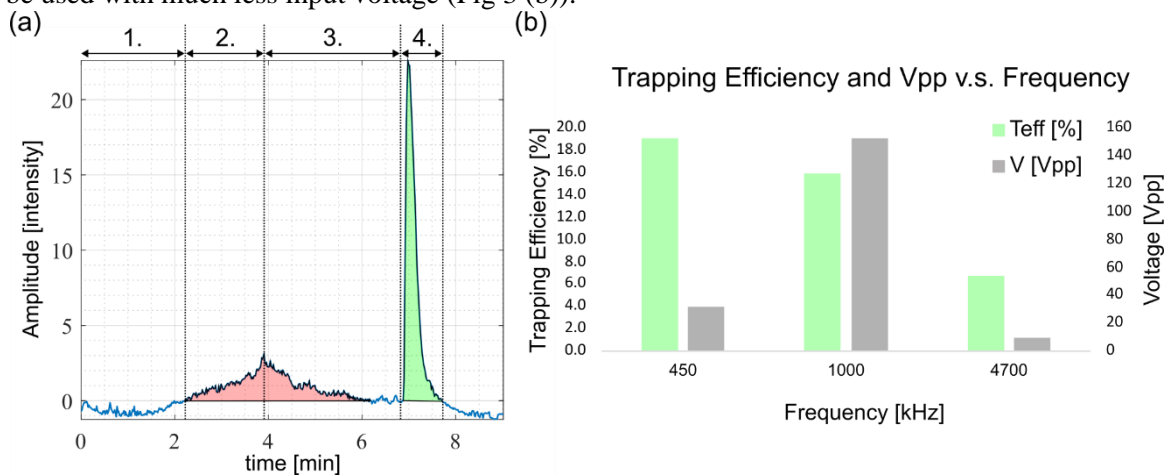
Figure 3: (a) Trapping of 2 µm PS particles with the described protocol. (b) Trapping efficiency for various excitation frequencies. Nm-particle trapping is possible at a wide frequency range.

Additional to the different frequencies we tested a capillary with 5x more capacity for trapping particles. Our initial experiments showed satisfying trapping performance (data not shown), demonstrating the scalability of the packed bed system.

Further, we tested the applicability of our method to nm-particle trapping. We inserted 4.8×10^4, 270 nm PS particles at a flow rate of 20 µL/min followed by washing with 200 µL of PBS. With similar settings as before, we recorded a trapping efficiency of 63% (Fig 4 (a)). Finally, we fabricated a polymer version of our device via 3D-printing. At similar operating conditions we achieved a trapping efficiency of 16% (Fig 4(b)).
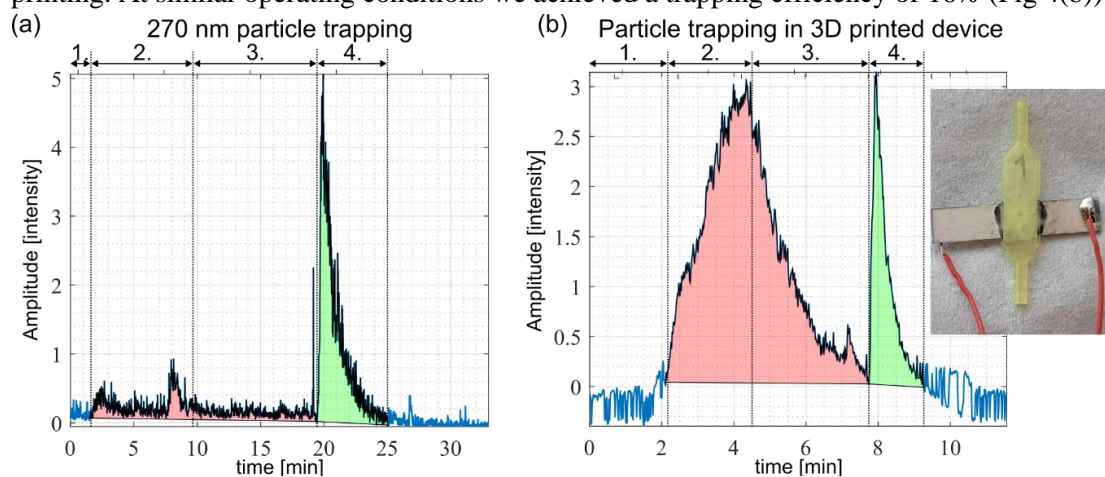
Figure 4: (a) Trapping of 270 nm particles in the glass capillary using the described protocol. (b) Trapping of 2 µm particles in a polymer mimic of the glass device, produced by 3D printing (picture shown in insert).

Conclusion

In this abstract, we presented nm-particle trapping in a packed bed which is scalable, enables actuation across a wide frequency range and can be manufactured in polymer offering opportunities for low-cost device manufacturing and high throughput EV isolation.

References

[1] Evander et al., Lab Chip, 2015, 15, 2588-2596.
[2] Habibi et al., Lab Chip, 2019, 19, 3032-3044.
[3] Gupta et al., Ultrasonics, 1997, 35, 131-139.

Investigation of acoustic wave attenuation in polydimethylsiloxane for acoustofluidic applications

Jeongeun Park[1], Beomseok Cha[1], Furkan Ginaz Almus[2], Mehmet Akif Sahin[2], Ghulam Destgeer[2,‡], and Jinsoo Park[1,*]

[1] Department of Mechanical Engineering, Chonnam National University, South Korea
[2] Control and Manipulation of Microscale Living objects, Center for Translational Cancer Research (TranslaTUM), Department of Electrical Engineering, Technical University of Munich, Germany
[*]E-mail: jinsoopark@jnu.ac.kr and [‡]E-mail: ghulam.destgeer@tum.de

Introduction

Acoustical effects are implemented in diverse fields, i.e., microfluidics, 3D printing, and imaging, in a way that coupling the acoustic sources to the applied medium is always a design consideration. For instance, strong coupling between the piezoelectric substrate and microfluidic channel requires an irreversible bonding that limits the components to being single-use and fragile to any assembly error. To address this issue, reversible assembly is achieved by confining the microchannel with a thin polydimethylsiloxane (PDMS) film, which allows the microchannel and expensive piezoelectric substrate to be reused (Figure 1a) [1]. However, using PDMS leads to acoustic wave attenuation, resulting in heat generation and energy loss. This also increases the risk of thermal damage to biological samples [2]. Despite these challenges, there are no guidelines for the optimal design of acoustofluidic systems that use the PDMS film to confine microchannels. Here, we investigate the thickness of the PDMS membrane and propose a design rule for reconfigurable acoustofluidic systems by quantitatively analyzing the wave attenuation in PDMS thin film. Our finding suggests that the PDMS membrane thickness ratio to acoustic wavelength determines the wave attenuation in PDMS and influences the acousto-thermal heating, acoustic radiation force, and acoustic streaming flow (Figure 1b).
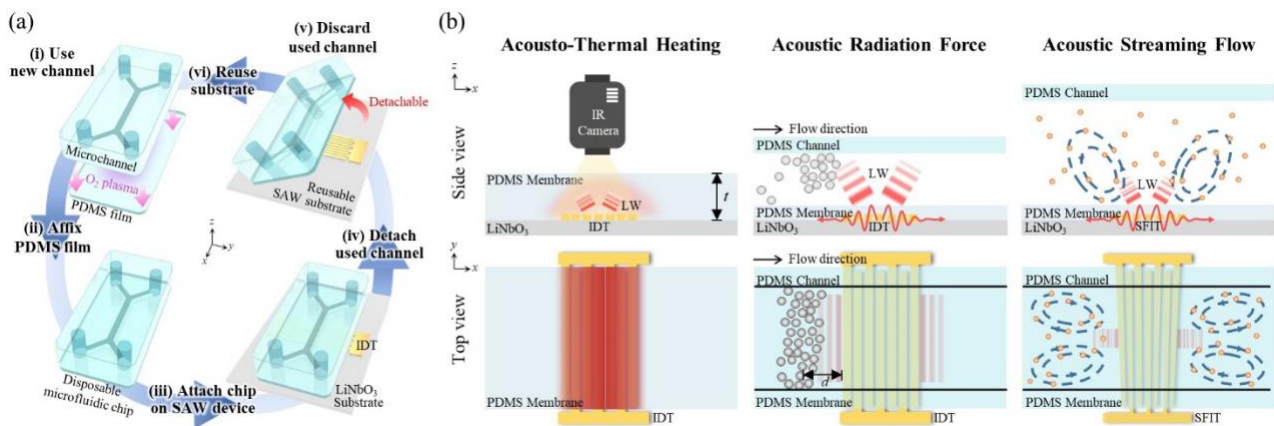
Figure 1. (a) Fabrication process of reconfigurable acoustofluidic systems with an added PDMS film starting from PDMS film bonding by oxygen plasma (i) and attaching to the interdigital transducer (IDT) device (iii) to discarding the microchannel (v) and reusing the substrate(vi). (b) Experimental schematic diagram of wave attenuation visualization using acousto-thermal heating (ATH), particle trapping utilizing acoustic radiation force (ARF), and microflow induction through acoustic streaming flow (ASF).

Experimental procedure

We analyzed the acoustic wave attenuation phenomenon in PDMS through three experiments utilizing acousto-thermal heating (ATH), acoustic radiation force (ARF), and acoustic streaming flow (ASF) (Figure 1b). Assuming that the acoustic wave attenuation would depend on the PDMS thickness (t) and acoustic wavelength (λ_{PDMS}), each experiment was conducted by varying the t and λ_{PDMS}. The PDMS used in each experiment was prepared with a ratio of 10:1 between the base and curing agent. In the ATH experiment, an infrared camera was used to measure the heat generation, and the piezoelectric substrate was placed on a Peltier cooling system set at 20°C (TRT) to prevent unwanted heating from the substrate. In the ARF experiment, a solution comprising microparticles and water was injected into the microchannel at a flow rate of 3 µl/min, and the particle size was selected to be close to a Helmholtz number of 1.5 [3]. For the ASF experiment, slanted finger interdigital transducer (SFIT) and particle image velocimetry were used for quantitative analysis.

Results and discussion
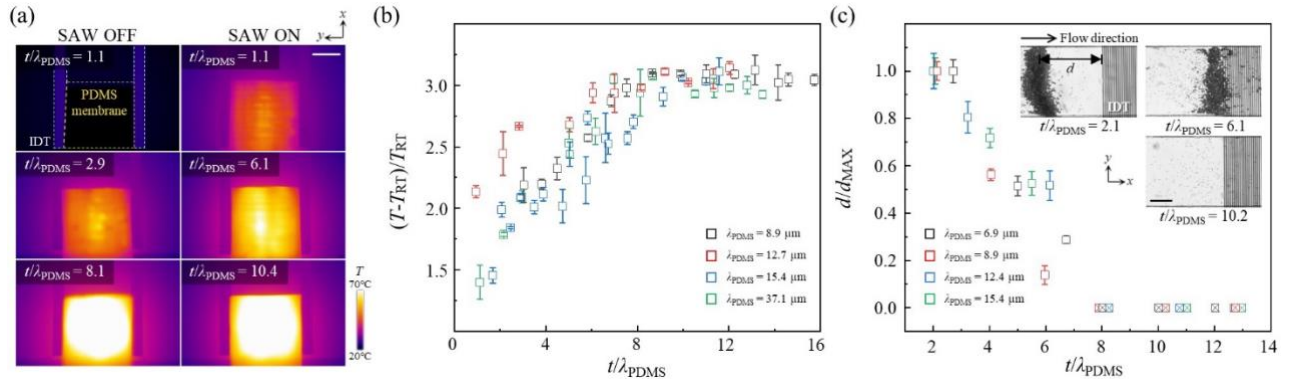
Figure 2. (a) Thermal camera footage of the surface temperature change of varying PDMS membrane thickness, t, due to viscoelastic attenuation when $\lambda_{PDMS} = 37.1$ µm. The scale bar is 1mm. (b) The normalized temperature change of PDMS according to ratio of t/λ_{PDMS}. (c) The normalized trapped particle distance from IDT due to ARF according to λ_{PDMS} and t, along with a inset image of the particles trapping when $\lambda_{PDMS} = 8.9$ µm. The scale bar is 100 µm.

In the ATH experiment, an increase in the t corresponded to an elevation in the surface temperature (T) of the PDMS film (Figure 2a). By introducing the dimensionless variable t/λ_{PDMS}, it was observed that T increased due to wave attenuation until t/λ_{PDMS} approached approximately 8. Beyond this point, most of the wave dissipated, and T stabilized (Figure 2b). In the ARF experiment, an increase in t/λ_{PDMS} led to a reduction in the acoustic energy transmitted into the channel, resulting in a decrease in the trapping distance (d) of micro-particles. Beyond $t/\lambda_{PDMS} \approx 8$, particle trapping was no longer observed (Figure 2c). Similarly, in the ASF experiment, as t/λ_{PDMS} increased, we observed a decrease in the maximum vorticity (ω_{MAX}), and after $t/\lambda_{PDMS} \approx 8$, vorticity was virtually absent (Figure 3a, b). Through three acoustical phenomena, we quantitatively analyzed that most acoustic energy is dissipated after approximately eight attenuations of the acoustic wave within PDMS. Our findings suggest that the ratio of PDMS thickness to acoustic wavelength determines the wave attenuation in the PDMS membrane, thereby influencing the acoustofluidic phenomena.
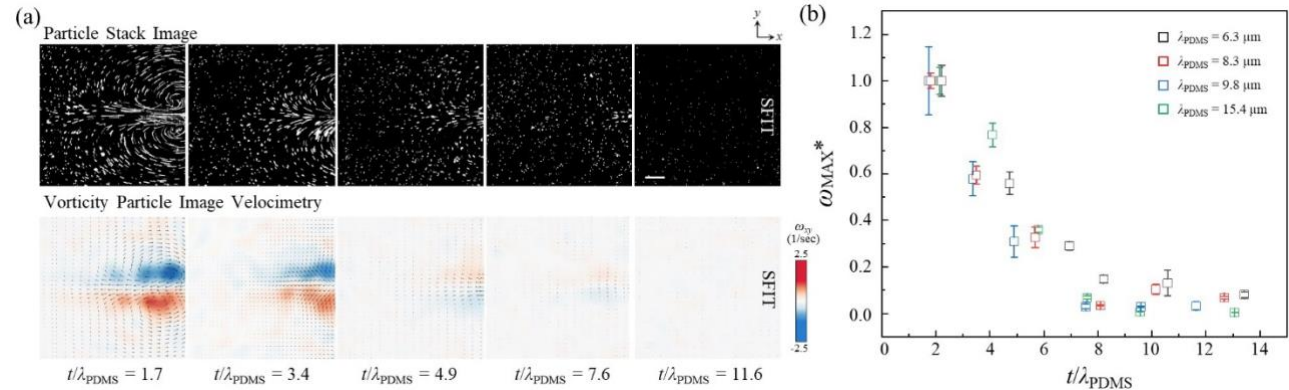
Figure 3. (a) Variation of acoustic streaming flow according to through visualization of particle trajectories and vorticity field when $\lambda_{PDMS} = 9.8$ µm. (b) The maximum value of the generated vorticity, ω_{MAX}, with respect to the membrane thickness ratio to acoustic wavelength in PDMS. The scale bar is 100 µm.

Conclusions
We investigated the effects of PDMS thickness on acoustofluidic phenomena and proposed a design rule for reconfigurable acoustofluidic systems. The thickness ratio to wavelength effect was quantitatively analyzed and validated through acousto-thermal heating, acoustic radiation, and acoustic streaming experiments. The guidelines suggested in this study are expected to be beneficial to the researchers to design and produce a reconfigurable acoustofluidic platform in an energy-efficient and cost-effective manner.

Acknowledgements

References
[1]   Park J., Jung J. H., Park K., Destgeer G., Ahmed H., Ahmad R., Sung H. J., Lab on a Chip 18.3: 422-432, 2018.
[2]   Mulvana H., Cochran S., Hill M., Advanced drug delivery reviews 65.11-12: 1600-1610, 2013.
[3]   Destgeer G., Sung H. J., Lab on a Chip 15.13: 2722-2738, 2015.

Modes that form seven types of node

Jeremy J Hawkes[1,*], Sadaf Maramizonouz[2] and Richard Yongqing Fu[3]

[1]Acoustic Machines, Liverpool, UK
[2]Newcastle University, Newcastle upon Tyne, UK
[3]Northumbria University, Newcastle upon Tyne, UK,
[*]E-mail: JeremyJHawkes@gmail.com

Introduction

Since modes are difficult to identify in many systems we have simplified some systems to find the modes. For our planar systems fluid is held in a capillary bridge to avoid interference from side walls. Our tubular systems are filled with air to avoid interference from liquid-wall coupling. We identified seven different types of node and their associated modes. Solutions for the node to node separation at fixed frequency show that, while a $c_f/2f$ separation is common in acoustofluidic systems it may indicate a resonance in the fluid or an added mass effect. With very thin planar geometry, the thickness of the substrate (drive plate), fluid or Top changes the node to node separation due to the added mass effect[1]. In tubular systems we find, streaming is governed by the mode and the node position.

Glossary: f =frequency, c_f = Bulk longitudinal velocity in fluid, c_{shear} = Bulk shear velocity, Vph = Phase velocity, Vph_{Top} = Phase velocity of the Top material, ρ = density, ν = Poisson's ratio, E=Young's modulus.

Node type 1	Chladni Plate model:	Node to node separation = $Vph/2f$

Node to node distance depends on the mode used. The asymmetric A0 mode is the typical mode for Chladni plates. The A0 phase velocity Vph increases with plate thickness from 0 to the Rayleigh velocity, RV $c_{shear}(0.87 + 1.12\nu/1 + \nu)$ as shown in Fig.1a. For most solid plates separation reaches 1/e (~37 %) of the Rayleigh velocity/2f at less than 0.5 mm thickness at 1 MHz and 10 mm at 40 kHz. The symmetric S0 mode is present in some plates, its velocity decreases from Young's velocity, YV $\sqrt{E/\rho(1-\nu^2)}$ to RV with increasing plate thickness.
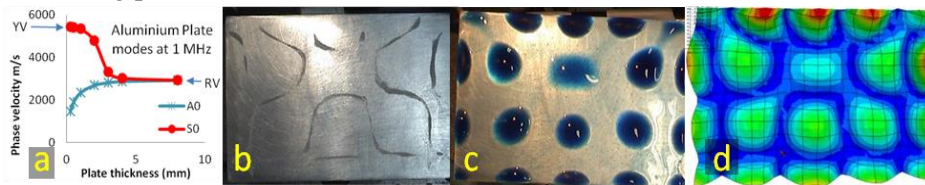
Figure1: a) Model[2] of A0 and S0 modes at 1 MHz. (b-d) Patterns on a 40 kHz Chladni plate produced by b) Glass beads c) Blue liquid and d) Displacement, blue = 0. From Abaqus FEA software.

Chladni plates move solid particles to the displacement nodes whereas liquids stream to the antinodes to form liquid heaps (Fig. 1b, 1c and 1d). Here glass particles are not shown in water, they were carried by the streaming and collect at the center of the water heaps.
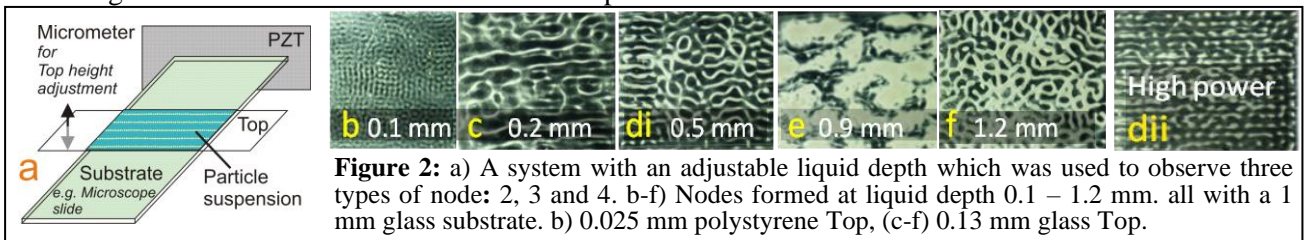
Figure 2: a) A system with an adjustable liquid depth which was used to observe three types of node: 2, 3 and 4. b-f) Nodes formed at liquid depth 0.1 – 1.2 mm. all with a 1 mm glass substrate. b) 0.025 mm polystyrene Top, (c-f) 0.13 mm glass Top.

Node type 2	Fluid resonance	Node to node separation = $c_f/2f$

Nodes of this type are produced by a resonance in the fluid (Fig 3a) and are used in some single node chambers and larger volume multi-wave chambers. In the adjustable depth system (Fig 2a) they form when sound is reflected by the Top. They produce the large irregular clumps seen in Fig. 2e. This view is from above and at multi-node depths there is a column of separate clumps below the top visible clump. The plot of the number of these irregular clumps (Fig. 3b) shows these clumps only occur at narrow ranges of depths. The depths depend on the type of Top used: Hard Tops, such as glass or polystyrene film act as reflectors.

Resonances formed near the water depths ½, 1 and 1 ½ wavelengths as indicated by red vertical lines. Whereas soft Tops, such as a free water surface, polyethylene or cling film act as pressure release surfaces. Resonances formed near the water depths ¼, ¾, and 1 ¼ wavelength as indicated by blue vertical lines.

Figure 3: a) The wave pattern and nodes formed by fluid resonances. b) Number of clumps formed by fluid resonances. The system in Fig 2a was used for depth adjustment with four different Top layers. Vertical lines: red = ½, 1, 1 ½ wave depth. Blue = ¼, ¾, 1 ¼ wavelength water depths.
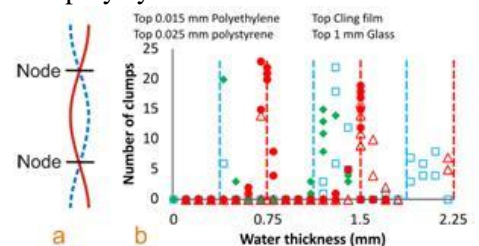
Node type 3 Interference from parallel sources 180º out of phase   Node to node separation is varied
If Substrate $Vph >$ fluid c_f then increasing fluid depth decreases separation due to added mass (also known as mass loading)[1]. At zero added mass the separation is $Vph / 2f$ (Variation1). The separation decreases towards $c_f/2f$ (V2). This decrease in separation is almost complete when fluid + Top (mass per meter) >the (mass per meter) of a 0.5 wavelength depth of fluid.
If Substrate $Vph <$ fluid c_f the separation is $Vph / 2f$ (V3) and the nodes are evanescent (short).

Figure 4: a) The whole system driven by the substrate moves together as a "substrate-fluid-Top" unit. b) Diagram of (a), identifying the wave components. Adjacent wave fronts emerge from the substrate with 180º phase difference. c) Node to node spacing with 1 mm thick glass and polystyrene substrates (Sub) at 1 MHz. Solid lines are from Disperse[2].
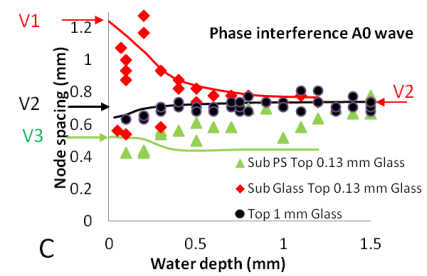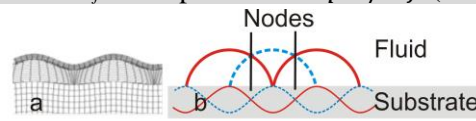
This node type is commonly found in single node systems. In Fig. 4a the upper and lower surfaces are just wave boundaries while the ends are reflectors. The diagram is visually meaningful however, to locate the nodes it is helpful to consider the waves fronts emitted into the fluid as somewhat isolated from the substrate (Fig 4b). In the example experiment of a thin Top with a high *Vph* substrate Fig. 2c, 2d and 2f node to node separation decreases with fluid depth (V1 to V2,). It is plotted (red data) in Fig. 4c together with two examples where separation is not affected by fluid depth: a thick 1 mm glass top (V2) and a low *Vph* polystyrene substrate (V3).

At high power, streaming moves particles arranged along the node lines into discrete clumps between the nodes. As shown in Fig. 2dii.

Node type 4   Induced evanescence   Node to node separation = $Vph_{Top} / 2f$ of the Top plate
Sound is transferred through the fluid to the Top in Fig. 2b where a 25µm polystyrene film is used. The thin polystyrene Top governs the wavelength producing very short node to node spacing, as in the Fig1a A0 mode. The low sound speed produces and evanescent wave where many particles are in contact with the Top.

Node type 5   Bessel based separation in a tubular system vibrating in the breathing mode Node to node separation follows a Bessel function. Central node (1st) = 1.56 $c_f / 2f$, 1st to 2nd node separation = 0.98 $c_f / 2f$, 2nd to 3rd node separation = 0.97 $c_f /2f$.
In the example shown in figure 5, aerosols are viewed as they emerge from resonating tubes. Liquid droplets move to the pressure nodes (Fig. 5a), whereas, solid particles (smoke) move to the pressure antinodes (Fig. 5b). Solid particles are separated from liquid droplets (Fig. 5c). A possible explanation for the difference between solid particle and droplet movement is: The acoustic radiation force reverses from positive to negative for small solid particles, allowing streaming to influence their position In contrast the viscous penetration depth keeps the force positive on droplets[3] so they are less influenced by streaming.
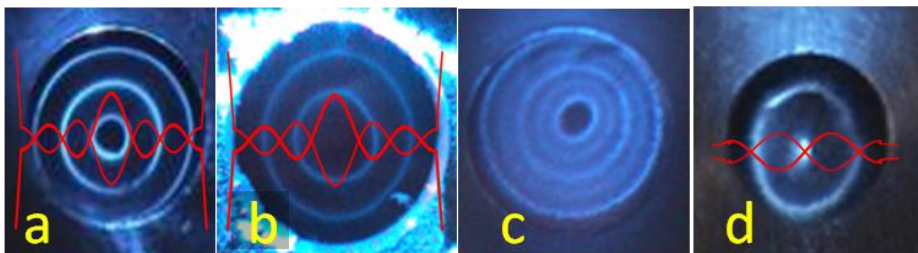

Figure 5: Tubes vibrating at 200 kHz (a-c) the intersection of the tube Longitudinal (0,1) and cavity L(0,3) modes. (a) 5 µm liquid aerosol droplets (water) at the pressure nodes. (b) 1 µm diameter solid particles (smoke) at the pressure antinodes (the pressure profile created by Disperse is overlaid as red lines). (c) separation of a mixed aerosol of liquid droplets and solid particles (10 µm polystyrene). d) Water aerosol moved to central pressure node wall mode L(0,1), with flexural cavity mode F(1,2).

Node type 6   Zero centre   In Fig. 5a-5c droplets travel to the nodes and solids to the antinodes but all particles move away from the centre. It is possible the travel direction of solid particles is away from the axis because there is: (1) Weaker central streaming since the displacement antinode (not shown) is ~20% closer to the axis than the pressure node; or (2) A greater radiation force due to the higher central pressure antinode,

Node type 7 Central pressure node Flexural modes rotate around the axis create the axial node in Fig. 5d.

Conclusion A mode based approach to system design could lead to more node functions and more precision.

References
[1] J.J. Hawkes, S. Maramizonouz, C. Jia, M. Rahmati, T. Zheng, M.B. McDonnell, Y.-Q. Fu, Node formation mechanisms in acoustofluidic capillary bridges, Ultrasonics, 121 (2022) 106690.
[2] B. Pavlakovic, M. Lowe, Disperse, Software Package for generating Dispersion curves, Disperse, Software for generating dispersion curves, Mechanical Engineering, Imperial College, London, 2.0.16i (2011).
[3] A.A. Doinikov, Acoustic radiation force on a spherical particle in a viscous heat-conducting fluid. I-III, J. Acoust. Soc. Am., 101 (1997) 722-740.

Multi-frequency ultrasonic atomization driven by bending mode using a parabolic reflector

Weiquan Wang[1,*], Chikahiro Imashiro[2], Hiroshi Hasegawa[3], Kohsuke Hirano[3], and Takeshi Morita[1,2]

[1] Graduate School of Frontier Sciences, the University of Tokyo, Chiba, Japan
[2] Graduate School of Engineering, the University of Tokyo, Tokyo, Japan
[3] Kaijo Corporation, Tokyo, Japan
[*]E-mail: hyrtong501@g.ecc.u-tokyo.ac.jp

Introduction

Ultrasonic atomization can be performed from tens of kHz to tens of MHz with different devices, producing droplets with diameters from a dozen micrometers to several micrometers. This technology has been well established and widely applied in drug delivery, micro synthesis, and environmental humidification [1-3]. However, less research has been conducted on transducers. Researchers typically used Langevin transducers at frequencies of tens of kilohertz while disc-type transducers were applied in the megahertz range. Most of these transducers own only one operating frequency, which is unable to control the size of the particles. In a previous research, we reported a novel ultrasonic transducer using the bending mode of a circular plate and a parabolic reflector, which can be driven at several different resonance modes from several hundred kHz to approximately 2 MHz [4]. In this study, four different operating frequencies were chosen to conduct atomization experiments using this transducer. Atomization videos were captured, and the distribution of particle diameters was counted at each selected frequency. Results showed that the diameter distribution of particles followed log-normal distribution and the transducer had an excellent performance for generating micro-sized droplets with different mean diameter at different frequencies.

Theory and Experimental Procedure

The cross-section view and principle of the transducer are illustrated in Fig. 1a. It consists of a Lead Zirconate Titanate (PZT) ring and a metal waveguide. Plane longitudinal waves can be irradiated by exciting the PZT ring's thickness mode. The parabolic reflector can focus the reflected longitudinal waves to the lateral surface of the circular bending plate at the center of the waveguide and excite the bending mode. The parabolic reflector focuses the energy and transforms it to the center through bending mode, causing a large vibration velocity. The dimensional configuration of the transducer is given in Fig. 1b. The metal waveguide was fabricated by stainless steel (SUS304), which has a larger yield strength to afford the large stress at the focal point. A hard-type PZT (MT-18K, Niterra Co., Ltd.) was selected to generate strong incident waves at thickness mode. Driven by 10 V_{pp} voltage, the frequency response in terms of admittance and central vibration velocity of the transducer is shown in Fig. 1c-1 and 1c-2. Compared with traditional Langevin or single-disc type atomizer, the proposed transducer owns multiple resonance modes, which correspond to the modes of PZT ring, parabolic reflector, circular plate, and their combination. Such property indicates the potential for multi-frequency driving. Therefore, in this study, we selected 734 kHz, 949 kHz, 1530 kHz, and 2063 kHz as the operating frequency for ultrasonic atomization.
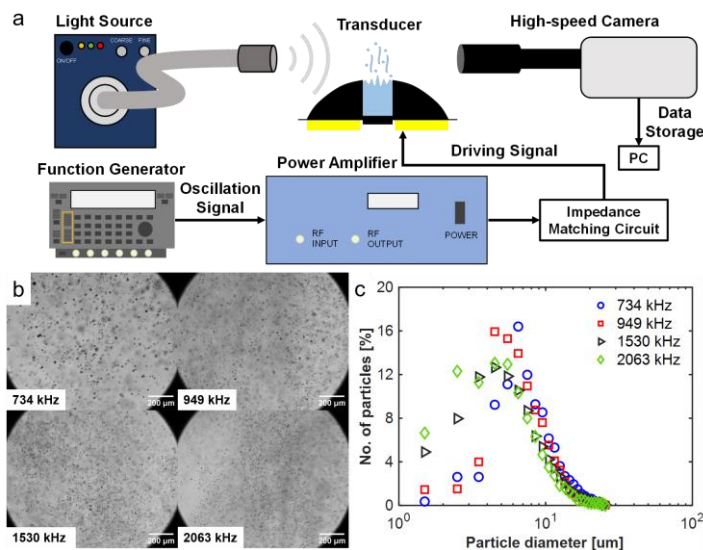

Figure 1: a Scheme of the applied transducer [4]. **b** Dimensional configuration of the transducer. **c** Frequency response in terms of admittance and velocity from (**1**) 0.5 MHz to 1.5 MHz and (**2**) 1.5 MHz to 2.5 MHz.

The experimental setup is illustrated in Fig. 2a, a high-speed camera (HAS-D73, DITECT Co. Ltd.) was utilized to capture videos, the frame rate and shutter speed were set to 2,000 fps and 1/200,000 s respectively. Pure water saturated with air was selected as the target liquid. Images were analyzed using ImageJ (ver. 1.54i,

National Institutes of Health). A function generator (WF 1966, NF Corporation) was utilized to excite continuous sinusoidal signal. For all operating frequencies, the electric power was amplified to 30 W by a RF power amplifier (A150, Electronics & Innovation Ltd.) to drive the transducer. Between the transducer and power amplifier, a transformer with a ratio of 3:1 was introduced to match the terminal impedance.

Figure 2 a Experimental setup for ultrasonic atomization videos capture. **b** Example images of atomized water particles at different frequencies. **c** Relationship between the percentage of particles and the particle diameter at different frequencies.

Results and Discussion

Atomization images at different frequencies are shown in Fig. 2b. The figures show that the particle diameter tended to get smaller while the amount became larger as the frequency increased. Then, setting 1 um as a range, the percentage of atomized particles with different diameters was counted, as shown in Fig. 2c. The figure shows that the diameter distribution of the particles follows a log-normal distribution. As the frequency increased, the center diameter of the particles became smaller, which is consistent with Fig. 2b. Meanwhile, the distribution became more dispersed. Using MATLAB's distribution fitter toolbox (R2022a, MathWorks), the data was fitted with log-normal distribution, as shown in Fig. 3a-d. The probability distribution function (PDF) is given by:

$$f(x) = \frac{1}{x\sigma\sqrt{2\pi}} \exp\left(-\frac{(\ln x - \mu)^2}{2\sigma^2}\right) \tag{1}$$

where x is the particle diameter, μ and σ are mean and standard deviation of the diameter's natural logarithm, respectively. Choosing the confidence level to be 95% in the fitting, the calculated μ and σ are shown in Fig. 3. The expected value (E_x) and variance (var_x) of the diameter are thus culculated by the followng equations:

$$E_x = \exp\left(\mu + \frac{\sigma^2}{2}\right), \qquad var_x = [\exp(\sigma^2) - 1]\exp(2\mu + \sigma^2) \tag{2}$$

which are 8.60 of E_x and 16.61 of var_x for 734 kHz; 7.68 and 13.31 for 949 kHz; 7.15 and 23.29 for 1530 kHz; 6.38 and 18.78 for 2063 kHz.
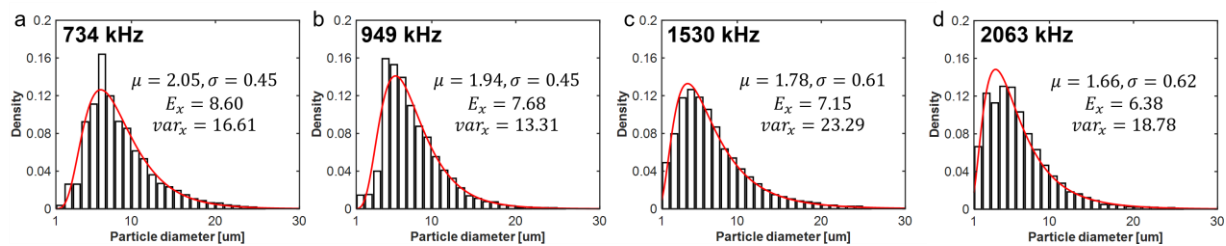
Figure 3 The distribution density of particle diameters and the fitted Probability Density Function (PDF) at **a** 734 kHz, **b** 949 kHz, **c** 1530 kHz, and **d** 2063 kHz.

Conclusion and Prospects

In this study, we utilized a novel multi-modal ultrasonic transducer realizing atomization at four different frequencies. The atomization videos were captured by a high-speed camera and the diameter distribution was analyzed. Results showed that the transducer could generate fine water particles with different mean diameters at different frequencies, which could be a promising tool for atomization applications such as medical therapy or material fabrication. In future studies, we will further evaluate the output properties of the device, such as acoustic pressure and ultrasonic intensity. These properties in relation to the size and amount of the atomized particles will also be investigated.

References

[1] L. Y. Yeo, J. R. Friend, M. P. McIntosh, E. N. Meeusen, and D. A. Morton, *Expert Opin. Drug Deliv.*, **7**(6), 663 (2010)
[2] S. C. Tsai, Y. L. Song, C. S. Tsai, C. C. Yang, W. Y. Chiu, and H. M. Lin, *J. Mater. Sci.*, **39**, 3647 (2004)
[3] Z. Feng, X. Zhou, S. Xu, J. Ding, and S. J. Cao, *Build. Environ.*, **133**, 62 (2018)
[4] W. Wang, K. Yamada, H. Hasegawa, K. Hirano, and T. Morita, *Jpn. J. Appl. Phys.*, **63**(4), 04SP27 (2024)

Multichannel acoustofluidic separator for high-throughput multiplexed biomolecule detection on biofunctional elastomeric particles

Cooper P. Thome[1,*], Creighton T. Tisdale[1], and C. Wyatt Shields IV[1]

[1]Department of Chemical and Biological Engineering, University of Colorado Boulder, Boulder, USA
[*]E-mail: cooper.thome@colorado.edu

Introduction

Detection of biomarkers, including antibodies, antigens, and other physiologically relevant molecules, is essential for patient diagnosis and disease management. Multiplexed assays, which simultaneously detect multiple biomarkers in a single assay, can significantly enhance diagnostic confidence. However, conventional detection assays, such as enzyme-linked immunosorbent assays (ELISA), are generally not suitable for rapid multiplexed detection, especially for biomarkers of disparate physical morphology (e.g., proteins, small molecules). Moreover, traditional biosensing techniques often require complex processing steps that introduce potential points of error and make detecting multiple biomarkers tedious. To address these challenges, we report a novel biospecific particle-based, acoustofluidics-enabled system for the simultaneous purification, preparation, and detection of multiple proteins and small molecules from complex biofluids. The central innovations of this technology are i) a class of fluorescently barcoded, functional negative acoustic contrast particles (fNACPs) that are modularly modified with antifouling polymers terminated in biorecognition motifs for the specific capture of biomarkers and ii) a 3D printed, high-throughput multichannel acoustofluidic separator that interfaces with 12-channel pipettes for the purification of fNACPs from whole blood. Here, we show the rapid, sensitive, and simultaneous capture, purification, and detection of an antibody (Ab), antigen (Ag), and small molecule using the fNACP-based, acoustofluidic separator system.

Theory and Experimental Procedure

When subjected to a half-wavelength standing wave within a microfluidic channel, positive acoustic contrast particles (PACPs) with diameters much smaller than the wavelength are forced to the pressure node, located along the middle of the channel, by primary radiation force [1]. Conversely, NACPs are forced to the antinodes along the walls of the channel. Beyond this, particles and cells in the channel also experience a secondary radiation force, which is attractive between particles at close distances [2,3]. Therefore, after acoustophoresis to the walls of the channel, NACPs subsequently aggregate. Finally, particles in an acoustofluidic channel experience a lateral acoustic radiation force that originates from gradients in the local acoustic potential along the channel and acts parallel to the channel, toward regions of local acoustic minima or maxima. At high acoustic radiation forces, this can result in acoustic trapping, which we define as the immobilization of NACPs along the walls of a straight channel in the presence of an applied flow, due to both the lateral component of the primary acoustic radiation force and the secondary acoustic radiation force exceeding the force on NACPs from Stokes' drag [3,4]. In this work, we synthesized NACPs via homogenization and polymerization of a Sylgard 184 and triethoxyvinylsilane polymer precursor. Following polymerization, we isolated a low-polydispersity fraction of the NACPs by sequential vortexed filtration through 40, 30, and 20 μm filters, collecting the NACPs retained by the 20 μm filter. The surfaces of NACPs were functionalized by conjugating the particles with biotin-polyethylene glycol (PEG)-silane linkers and streptavidin, in that order. Because of its four biotin-binding sites, addition of streptavidin to the fNACPs enables subsequent conjugation of a variety of biotinylated recognition elements to allow detection of disparate biomarker types (Fig. 1a). Here, to create fNCAPs specific to a model Ab, Ag, and small molecule, we functionalized fluorescently barcoded fNACPs with biotinylated ovalbumin Ag (OVA), anti-prostate specific antigen Ab (anti-PSA), and pyrabactin resistance 1 (PYR1) protein for the detection of anti-OVA Ab, PSA Ag, and the small molecule abscisic acid (ABA), respectively. The second enabling feature of this assay is the use of a 3D printed, high-throughput acoustofluidic separator that interfaces with 12-channel multichannel pipettes to rapidly purify captured biomolecules on the fNACPs from biofluids (Fig. 1b) The separator was designed using Fusion CAD software and printed on a Prusa SL1S 3D printer. The device houses a 12-channel trapping array, fabricated by bonding 12 square glass capillaries to a piezoelectric transducer in parallel. The transducer is actuated by an applied AC signal at 750 kHz, which generates a pressure node along the center of each channel and antinodes along the walls of each channel. To assess trapping performance, 5×10^4 NACPs were mixed with 1000 μL buffer, and the mixture was passed through each of the trapping channels with acoustics engaged, yielding waste and enriched samples. These samples were analyzed via flow cytometry to quantify NACP retention. To evaluate the fNACP assay performance and limit of detection (LOD), anti-OVA Ab, PSA Ag, and ABA were spiked into 100 μL buffer or porcine blood containing 10^4 fNACPs of each type (i.e., Anti-OVA, PSA, and ABA-specific) and 10^4 nonfunctionalized NACPs as an internal control. After target capture, the fNACPs and

NACPs were purified using the multichannel acoustofluidic separator and incubated with fluorescently tagged secondary labels. After this incubation, the fNACPs were purified once more and analyzed via flow cytometry.
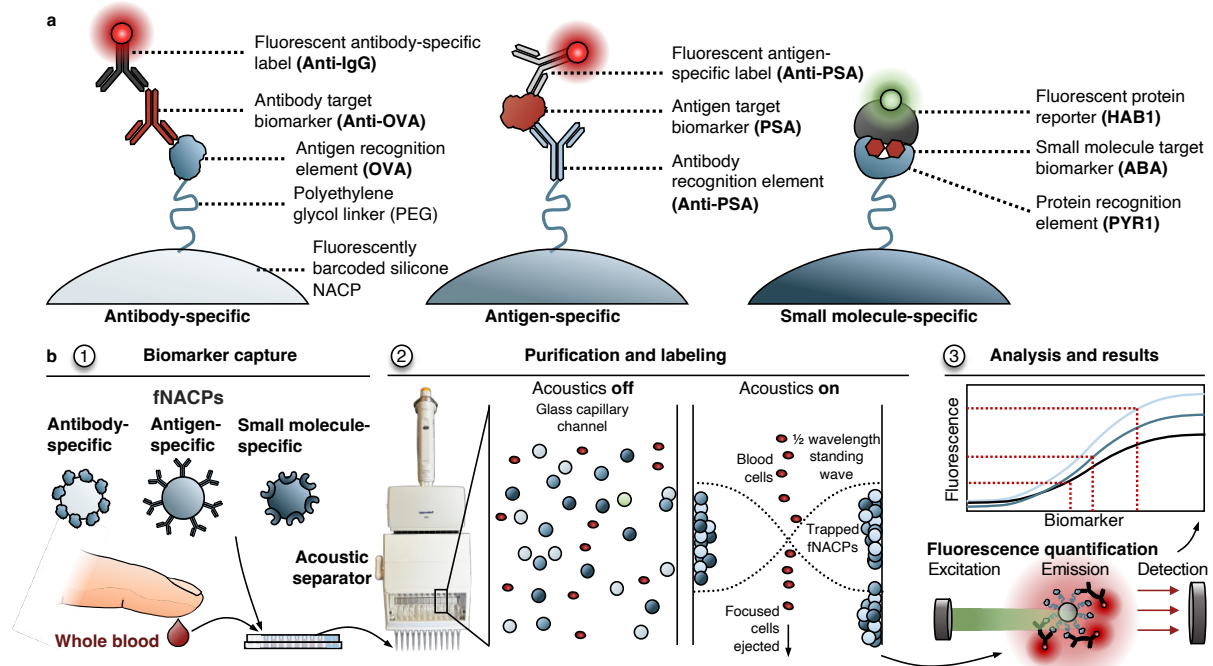

Figure 1: Schematic overview of the particle-based, multichannel acoustofluidic separator-enabled assay. a. Schematic overview of the fluorescence barcoding and functionalization approach employed to create antibody, antigen, and small-molecule-specific NACPs. **b.** 1) fNACPs of varied biomarker specificity are mixed with whole blood spiked with various biomarkers in a 96-well plate. 2) After incubation, the fNACPs are purified from blood using the multichannel acoustofluidic separator. 3) After fluorescent labelling and subsequent purification in the separator, the fNACPs are collected for fluorescence analysis.

Results and Discussion

Using the described NACP synthesis and filtration approach, we isolated a low polydispersity fraction of NACPs with a mean size of ~25 μm. While the use of smaller particles in assays may offer the potential for faster particle-biomarker binding interactions due to increased diffusivity, we expected that larger particle sizes facilitate faster, more robust trapping of particles under flow, as the magnitude of acoustic radiation forces scales proportionally with the volume of particles (cubically with the radius) [2]. The discriminant forces acting on fNACPs and blood cells enabled their efficient (over 95% retention) separation in short timescales (<60 sec) using the 3D printed, multichannel acoustofluidic separator. By functionalizing fluorescently barcoded fNACPs with a biotinylated OVA, we demonstrate the detection of anti-OVA antibodies at picomolar levels (60 pM), a sensitivity competitive with commercial ELISAs. We then show the sensitive detection of PSA by anti-PSA-functionalized fNACPs at physiological levels. Finally, we report the detection of small molecules by functionalizing fNACPs with a plant hormone receptor-inspired biorecognition motif. This third type of fNACP addresses an important limitation of traditional biosensing assays. While many immunoassays detect protein biomarkers, small molecules (i.e., molecules < 1000 Da) also serve as important indicators of disease, metabolic function, and toxin exposure. However, detecting small molecules is challenging due to their miniscule size and similarities in structure. We addressed this issue by functionalizing fNACPs with PYR1, which changes conformation when bound to the small molecule ABA, allowing complex formation with a secondary fluorescent protein, HAB1, and resultantly providing a means to quantify ABA concentration [5].

Conclusion

We demonstrate an fNACP-based, acoustofluidics-enabled assay that offers a simple and versatile approach for the rapid, sensitive, specific, and simultaneous detection of a range of target biomolecules, including proteins and small molecules. Through barcoding the three types of fNACPs, we show simultaneous detection of three disparate biomarkers from whole blood. By using a novel multichannel acoustofluidic separator capable of interfacing with multichannel pipettes, the fNACP-based assay can be carried out with minimal user engagement in under 70 minutes, significantly enhancing assay throughput in laboratory settings.

References

[1] Gao, L. *et al. Biomicrofluidics* **9**, 014105 (2015).
[2] Laurell, T., Petersson, F. & Nilsson, A. *Chem. Soc. Rev.* **36**, 492–506 (2007).
[3] Evander, M. & Nilsson, J. *Lab. Chip* **12**, 4667–4676 (2012).
[4] Hammarström, B., Laurell, T. & Nilsson, J. *Lab. Chip* **12**, 4296–4304 (2012).
[5] Beltrán, J. *et al. Nat. Biotechnol.* **40**, 1855–1861 (2022).

On the Evolution of a Neutral Configuration of Inhomogeneous Fluids under Acoustic Fields

Sujith Jayakumar[1], <u>Videsh VK</u>[1], Jeyapradhap T[1], Hemachandran E[2], and Karthick Subramani[1,*]

[1]Indian Institute of Information Technology, Design and Manufacturing, Kancheepuram
[2]National Institute of Advanced Manufacturing Technology, Ranchi
[*]E-mail: karthick@iiitdm.ac.in

Introduction

We investigate the behaviour of miscible inhomogeneous two-inlet fluid flow in microchannel subjected to standing acoustic waves. Particularly, we delve into the evolution of fluid flow which is initially at neutral equilibrium configuration (i.e. fluid interface is positioned initially at the pressure node of the wave). Intriguingly, acoustic forces result in a spatial bifurcation, stabilizing the neutral configuration in one half of the domain (suppressing Rayleigh streaming) while destabilizing the other half (leading to fluid relocation) as diffusion between two inhomogeneous fluids progresses. The findings presented in this paper offer an effective technique for sorting particles of both micron and sub-micron sizes in the presence of inhomogeneous fluids.

Physics of the problem

The equations governing the physics of acoustofluidics include the continuity equation ($\delta_t \rho + \nabla \cdot (\rho v) = 0$), the momentum equation ($\rho[\partial_t v + (v \cdot \nabla)v] = -\nabla p + \eta \nabla^2 v + \beta \eta \nabla(\nabla \cdot v) + \rho g$) and the advection diffusion equation ($\partial_t s + v \cdot \nabla s = D \nabla^2 s$). When the microchannel containing the fluids is actuated by acoustic fields of $\sim 1\ MHz$ frequency, the acoustic fields are decomposed by perturbation theory for two separate time scales, i.e., fast scale acoustics ($t_f \sim 0.1\ \mu s$) and slow scale hydrodynamics ($\tau \sim 10\ ms$). The emergence of second-order slow-scale hydrodynamic flows is a consequence of the divergence of time-averaged second-order Reynolds Stress tensor [1] ($f_{ac} = -\nabla \cdot < \rho_0 v_1 v_1 >$). A system of inhomogeneous fluids inside an enclosed domain in the absence of interfacial tension can remain in equilibrium if the body force is entirely accounted by pressure, $f_{rl} = \nabla p$. The equilibrium configurations can be obtained by taking curl of the above equation ($\nabla \times f_{rl} = 0$). Through the stability analysis, the eigenvalue n that determines the nature of the stability of the system initially in equilibrium is found to be [2],

$$n = \sqrt{\frac{k_y}{\rho_A + \rho_B} \Phi E_{ac}(Z_B - Z_A) \sin(2k_w x_s)}$$

where ρ_A and ρ_B indicate the densities of fluids A and B respectively, $\Phi = 2k_w/Z_{avg}$, k_w is the wavenumber, k_y is the wavenumber considered along the y-direction, E_{ac} describes the acoustic energy and x_s corresponds to the location of the fluid interface from the node. The configuration is described to be in stable equilibrium if the eigenvalue is imaginary and unstable if the value is real. When the eigenvalue $n = 0$, it describes a neutral equilibrium configuration. The equilibrium nature of various inhomogeneous fluid configurations is depicted in Fig.2 in Rajendran.et.al,2022[2].

The resultant 2-inlet 3D miscible inhomogeneous fluid flow problem is modelled and studied as a 2D problem where all the physics can be captured with minimal computational time and requirements. The first-order and second-order Navier-Stokes equations are bidirectionally coupled and solved numerically at all slow-time steps in COMSOL Multiphysics 6.0. The walls of the microchannel ($380\mu m \times 190\mu m$) are actuated with a velocity of $(2\Pi f_0)d_0 \approx 10^{-3}\ m/s$, resulting in a half standing acoustic wave being produced horizontally in the microchannel. The properties of the fluids used correspond to Ficoll PM70 and DI (de-ionized) water [3].
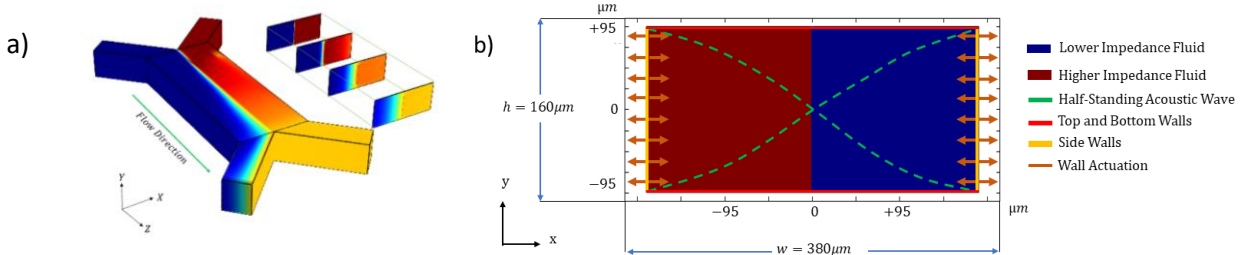

Figure 1: (a) Evolution of neutral configuration fluid flow profile under acoustic actuation of the microchannel. (b) A 2D cross section of the acoustofluidic microchannel subjected to acoustic standing half-wave (in the x-y plane), is employed to study the dynamics of inhomogeneous fluids whose density, speed of sound, and solute concentration are functions of space and time. The side walls (yellow) are actuated with a constant wall amplitude ($d = 0.261\ nm$).
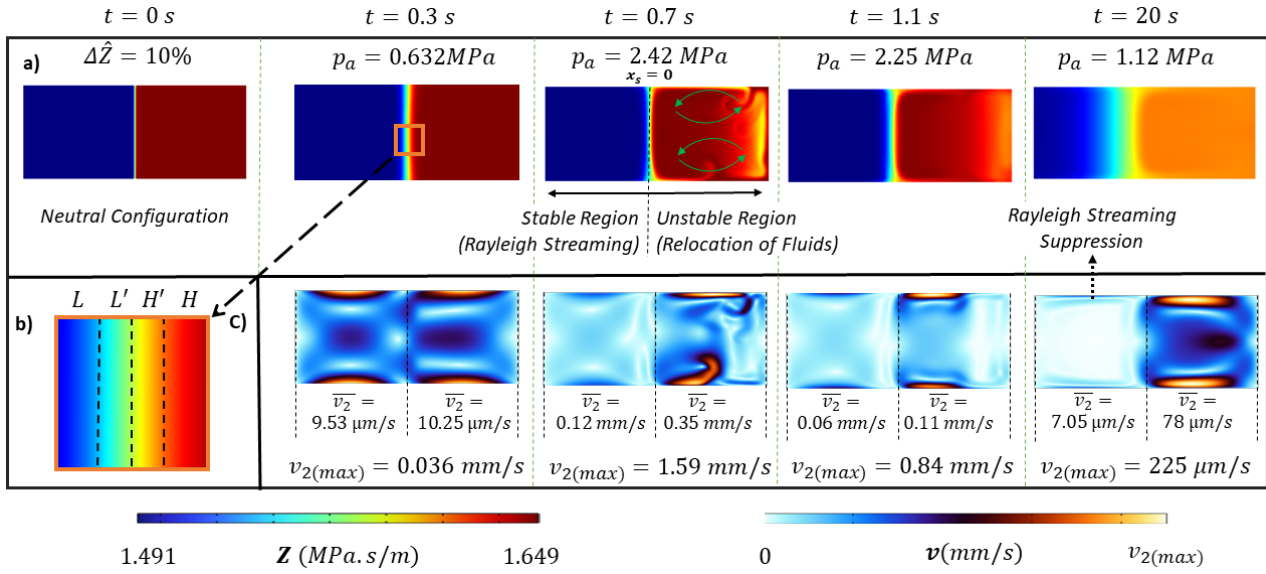
Results and Discussion

Figure 2: Simulation snapshots illustrating the evolution of an acoustofluidic microchannel with a neutral configuration of two miscible, homogeneous fluids (Impedance difference $\Delta Z = 10\%$) initially with the fluid-fluid interface at the node, at different time instances. Fig.2.(a) in the first row presents impedance plots, Fig.2.(b) provides a magnified depiction of the diffusion at the fluid interface and Fig.2.(c) in the second row displays velocity distributions. The change in concentration (ρ and c) profile over time leads to a change in first order fields (p_1, v_1) which in turn results in significant change in the second order velocity magnitude (v_2).

Acoustic forces acting in the microchannel drive the inhomogeneous fluids to a stable configuration where the higher impedance fluid relocates to the pressure node and the lower impedance fluid to the antinode. When the miscible inhomogeneous fluids in a neutral configuration were subjected to acoustic waves as shown in Fig.1.(b), diffusion at the interface separating the fluids led to increased impedance ($L' > L$) at the left side of the interface/node and decreased impedance ($H' < H$) at the right side as in depicted in Fig.2.(b). Remarkably, this resulted in an interesting spatial bifurcation with i) a stable configuration at the left half of the domain, featuring the lowest impedance fluid (L) at a pressure anti-node and a higher impedance fluid (L') occupying pressure nodal area and ii) conversely, an unstable configuration at the left half of the domain with the highest impedance fluid at the pressure anti-node (H) and the lower impedance fluid (H') near the node. Acoustic forces due to inhomogeneity effectively suppress Rayleigh streaming ($\sim O(10)$) in the stable domain (L and L') as shown in Fig.2.(c) ($t = 20\ s$). Whereas, in the unstable domain (H and H'), the acoustic forces relocate the low impedance fluid from the node to the antinode and high impedance fluid to the node with a much higher relocation velocity than streaming. Eventually, the configuration evolves towards homogeneity due to the combined effects of acoustic relocation, streaming, and diffusion. This results in increased fluid flow in the right of the domain while the left side experiences nearly still or minimal flow. The above results indicate that when employing a two-inlet acoustofluidics microchannel for particle sorting applications, it is crucial to have the cells or particles suspended within a low impedance fluid medium while ensuring that a high impedance fluid serves as the sheath. Furthermore, it's essential that the width of the channel occupied by the high impedance fluid is equal to or greater than that occupied by the low impedance fluid.

Conclusion

The discovery was made that upon actuation at the appropriate frequency, the neutral configuration bifurcates into a Rayleigh Streaming suppressing stable domain and an unstable domain resulting in the relocation of fluids with a velocity magnitude one order higher than Rayleigh streaming velocity. The findings and knowledge gained from this research will be helpful for particle sorting and fluid manipulation applications in acoustofluidic devices.

References

[1] V. K. Rajendran, S. Jayakumar, M. Azharudeen, and K. Subramani, *Theory of nonlinear acoustic forces acting on inhomogeneous fluids*, J. Fluid Mech. 940 (2022), 10.1017/jfm.2022.257

[2] V. K. Rajendran, S. P. A. Ram, and K. Subramani, *On the stability of inhomogeneous fluids under acoustic fields*, J. Fluid Mech. 964, A23 (2023)

[3] S. Jayakumar and K. Subramani, *An investigation of acoustic relocation phenomenon in a microchannel under acoustic fields*, Phys. Fluids 34 (2022), 10.1063/5.0100386.

On the fabrication of a SAW-based microfluidic device with raised acoustic energy density and tailored acoustic pressure field using dry film resist

Sebastian Sachs[*], David Schreier, Jörg König, and Christian Cierpka

Institute of Thermodynamics and Fluid Mechanics, Technische Universität Ilmenau, Ilmenau, Germany
[*]E-mail: sebastian.sachs@tu-ilmenau.de

Introduction

Acoustofluidic devices based on standing surface acoustic waves (sSAW) emerged as a flexible and scalable tool to precisely separate micro particles and cells according to their size or acoustic contrast. The continuous separation is typically performed in micro channels made of polydimethylsiloxane (PDMS), which leads to a significant attenuation of the surface acoustic waves (SAW) due to the channel side walls and transmission of radiated bulk acoustic waves (BAW) in the fluid at the channel cover. However, a much higher reflection of up to 89% is achieved by implementing a glass cover, resulting in a much higher acoustic energy density in the fluid [1]. An innovative channel design based on dry film resist (DFR) further enabled a precise and reproducible positioning of the micro channel with lithographic resolution [2]. In this study, the advantages of both approaches are combined by fabricating an acoustofluidic device with a channel cover of high acoustic impedance bonded to channel side walls made of DFR. To account for the anisotropic thermal expansion of the widely used 128° YX LiNbO$_3$ substrate and to improve adhesion of the channel cover, a thin layer of SU-8 photoresist was applied between the DFR and the channel cover. The proposed fabrication process provides easy on-chip integration with a channel side wall thickness down to 50 μm to limit the attenuation of the SAW while maintaining a reliable sealing. Based on numerical calculations, both the achievable acoustic pressure amplitude and the position of pressure nodes of the acoustic wave field can be adapted by adjusting the channel height, applying multiple DFR layers. Using the established fabrication process, acoustofluidic devices with reliable channel geometry and positioning are obtained, which can be employed not only for sSAW-based particle separation but also for a variety of particle or cell manipulations ranging from mixing to patterning.

Methods

The acoustofluidic device is based on two opposing interdigital transducers (IDT, Ti/Al 5/295 nm) deposited on a 128° YX LiNbO$_3$ substrate by electron beam evaporation. To prevent corrosion and mechanical damage, the substrate is coated with a 385 nm layer of SiO$_2$. Following the fabrication process illustrated in Fig. 1a, the DFR Ordyl® SY300 was first laminated onto the substrate surface. To adjust the channel height H, successive lamination of multiple layers is possible. After selective exposure using a photo mask, a post exposure bake was performed at 65°C for 1 min to homogenize the cross-linked DFR. Finally, unexposed DFR was removed during development, while the exposed channel structures were retained permanently. For the channel cover, silicon (Si, <100>) was used in which fluid inlets with a diameter of 1 mm were etched. Afterwards, a thin layer of SU-8 photoresist (~ 2 μm) was spin coated onto the Si substrate. Following a relaxation time of 10 minutes, both substrates were bonded at 65°C with a force of approx. 90 N for 1 hour. Sealing of the micro channel is provided by the SU-8 layer, which was subsequently heat-treated at 65°C for 1 hour. While the previous process steps can be performed at wafer level, bonding is recommended at chip level due to the anisotropic thermal expansion of the 128° YX LiNbO$_3$ substrate. The stacked acoustofluidic device is shown schematically in Fig. 1b.
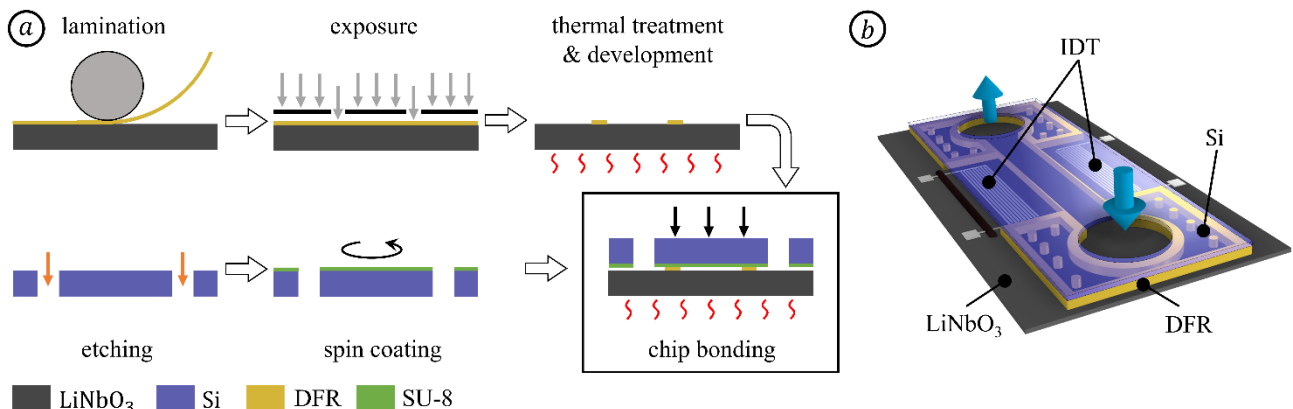

Figure 1: (a) Schematics of the fabrication process and (b) the stacked acoustofluidic device.

A 2D numerical model developed in our previous work [3] was used to resolve the pattern of the acoustic pressure in the fluid domain. The excitation by the sSAW was implemented as boundary condition at the channel bottom, while impedance boundary conditions were set at the channel side walls and cover [2].

Results and discussion
In Fig. 2a, micro channel structures composed of three layers of DFR are depicted in a scanning electron microscopy (SEM) image. To establish a reliable fabrication protocol, the DFR was patterned on a cost-efficient Si substrate in this case. The thickness of the channel side walls was reduced to about 50 µm across the aperture of the IDTs to limit the distance along which the SAWs are attenuated. A bonded chip with two pairs of IDTs in a multi-stage tilted sSAW arrangement is shown as inset, which is intended to be used for particle separation. The impact of a channel cover made of PDMS and Si is illustrated in Fig. 2b based on the normalized time-averaged absolute acoustic pressure $\langle|\tilde{p}_1|\rangle$ at a frequency of 25.72 MHz in the left and right halve of the image, respectively. In contrast to the channel cover made of PDMS, a significantly higher reflection of the BAWs occurs when using Si, which results in a more regular pattern of $\langle|\tilde{p}_1|\rangle$ with maxima at the channel cover and a 5.3-times higher pressure amplitude. With a Si cover, pressure nodes form symmetrically to $z \approx H/2$, which is beneficial for a continuous particle separation since particles with positive acoustic contrast factor being focused to positions of similar hydrodynamic forces caused by the fluid flow. The normalized mean acoustic energy density $\tilde{E}_{ac}$ shows clear peaks with increasing channel height as depicted in Fig. 2c. The distance between the peaks amounts to approx. $\lambda_f/2$ at resonance of the BAW radiated into the fluid (water) with wavelength λ_f. However, an irregular trend is expected due to the complex acoustic pressure and velocity fields for a channel width $W > \lambda_{SAW}/2$, where λ_{SAW} denotes the wavelength of the SAW [4]. Based on the numerical findings, a channel height H corresponding to the peaks in $\tilde{E}_{ac}$ is favorable, e.g. for an sSAW-based particle separation. Considering the proposed fabrication process, the channel height is adaptable by the number of DFR layers.
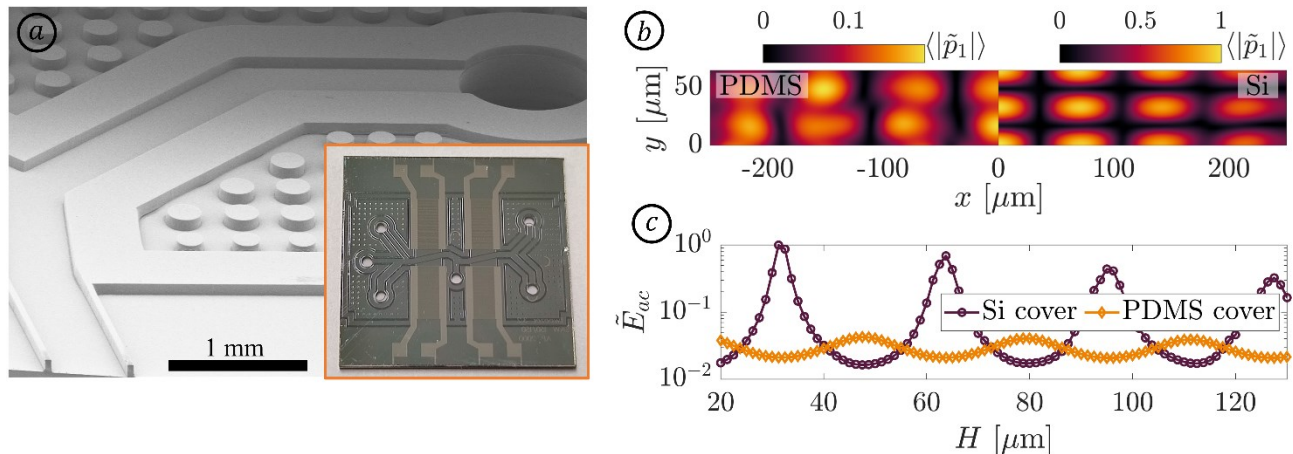
Figure 2: (a) SEM image of micro channel structures fabricated by three layers of DFR on a Si substrate with a photograph of a bonded acoustofluidic device as inset. (b) Numerically calculated acoustic pressure $\langle|\tilde{p}_1|\rangle$ in a micro channel with PDMS (left halve) or Si (right halve) cover. (c) Mean acoustic energy density as a function of the channel height H.

Conclusion
The fabrication process of an acoustofluidic device combining the advantages of precise positioning of the micro channel using a dry film resist (DFR) with a high reflecting channel cover of Si has been demonstrated. Based on numerical simulations, a significantly increased mean acoustic energy density E_{ac} was revealed in comparison to a channel cover made of polydimethylsiloxane (PDMS). In particular, distinct peaks in E_{ac} were found by varying the channel height, which can be considered in the fabrication process by applying multiple layers of DFR. The increased E_{ac} and regular pattern of the acoustic pressure field promise high progress in the particle and cell separation based on standing surface acoustic waves. In addition, the proposed fabrication process allows to use materials with well-known acoustic properties, which paves a way for a precise design of acoustofluidic devices for various applications such as separation, mixing, concentration or patterning.

References
[1] M. Wu, P. Huang, R. Zhang, Z. Mao, C. Chen, G. Kemeny, P. Li, A.V. Lee, R. Gyanchandani, A.J. Armstrong, M. Dao, S. Suresh, T.J. Huang, *Small*, **14** e1801131 (2018)
[2] A. Fakhfouri, M. Colditz, C. Devendran, K. Ivanova, S. Jacob, A. Neild, A. Winkler, *ACS Applied Materials & Interfaces*, **15** 24023-24033 (2023)
[3] S. Sachs, M. Baloochi, C. Cierpka, J. König, *Lab on a Chip*, **22** 2011-2027 (2022)
[4] D.J. Collins, R. O'Rorke, C. Devendran, Z. Ma, J. Han, A. Neild, Y. Ai, *Physical Review Letters*, **120** 074502 (2018)

Optimizing transducer configurations for 2D acoustic focusing

Tuva Eriksson Viklund[1,*], Varun Kumar Rajendran[1], Martin Wiklund[1], Jonas Sellberg[1], Björn Hammarström[1]

[1] Department of Applied Physics, KTH Royal Institute of
Technology, Stockholm, Sweden
*E-mail: tuvav@kth.se

Introduction

X-ray crystallography is a widely employed technique to determine the atomic structure of proteins. Recent advances have enabled Serial Femtosecond Crystallography (SFX) where a flowing stream of crystals is analyzed, and here microfluidics have provided a variety of new nozzles and a more efficient sample handling [1]. However, reliable focusing of particles inside the nozzles for crystallography remains a challenge as they tend to clog or aggregate, especially at elevated concentrations and flow rates. Acoustic forces have emerged as a promising solution for effectively handling protein crystals by Acoustofluidic Crystallography (AFX) [2]. In addition, recent studies have suggested the use two transducer configurations for in-line particle focusing [3]. In state-of-the-art SFX the x-ray focus can be minimized to a few microns while the acoustic contrast of protein crystals may be quite low. To generate sufficient focus on these low contrast particles, we report an optimization study of 2D acoustic focusing of polystyrene beads in a square microchannel. We investigate two distinct approaches to achieve 2D focusing: (i) actuating a single transducer attached to the bottom of the square microchannel and (ii) actuating two transducers, which are attached perpendicularly to each other on the square microchannel. The outcomes of these experiments are compared to arrive at optimum conditions that result in the minimum spot area of acoustic focusing.

Experimental procedure

A square glass capillary of 400×400 µm^2 is considered for the study. Polystyrene (PS) beads (10 % concentration) of 3 µm are suspended in water and are subjected to acoustic fields by actuating a piezoelectric transducer (PZT) having a fundamental resonance of 2 MHz at a constant flow rate of 10µl/min. The fluid-particle mixture is subjected to 2D acoustic focusing in two different ways as shown in Fig.1. The experiments are carried out at an amplitude of 15 V$_{pp}$ on a set frequency ranging from 1.73 MHz to 2.23 MHz , with and without a frequency sweep of 50 kHz around the set frequency.
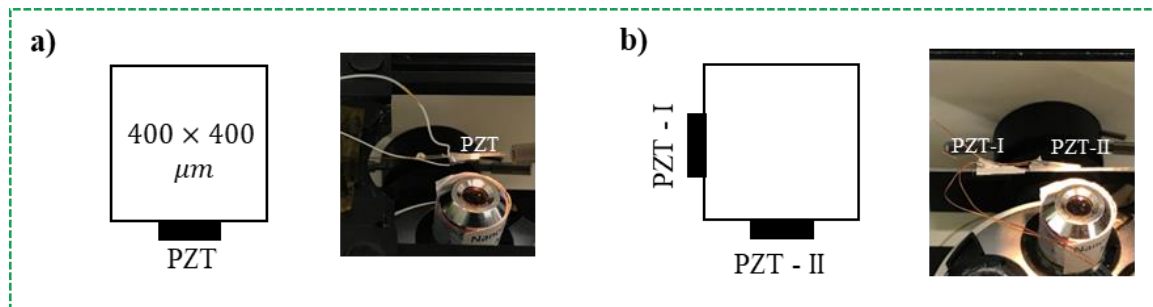
Figure 1: Schematic for 2D focusing of PS beads in a square capillary of 400×400 µm^2 a) actuating a single transducer attached to the bottom of the microchannel and b) actuating two transducers, which are attached on the surface of the channel, perpendicularly to each other.

Results and Discussion

By imaging a section of the capillary with focused PS beads flowing at 10 µL/min and integrating the image intensity over time, the particle distribution along the width and height of the channel at full-width half maximum (FWHM) is determined as shown in Fig. 2 along with the microscopic image of focusing. Figure 3 shows the plot for the area of the focused region for different frequencies at different conditions when single and dual transducers are actuated. It can be seen that for both single and dual piezo cases, the trend of variation of the area of focus is almost similar for without and with frequency sweep. Upon closely examining, for the single piezo actuation 2D acoustic focusing, the minimum concentration of the area of particles is $149~\mu m^2$ when the transducer is actuated at 1.92 MHz and the area is even more concentrated, $117~\mu m^2$ if the transducer is actuated at a linear frequency sweep of 50 kHz around the center frequency of 2.13 MHz. For the case of 2D focusing using two transducers the lowest possible concentration area is 99 µm^2 at 1.84 MHz and 151 µm^2 if both the transducers are actuated at a linear frequency sweep of 50 kHz around the center frequency of 1.87 MHz.
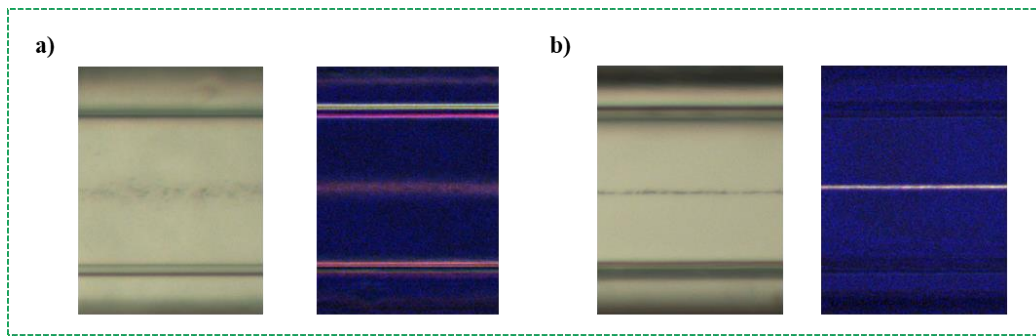
Figure 2: Acoustic focusing of PS particles in a square microchannel. Microscopic images of particles on the left and the corresponding integrated image over time on the right. Acoustic focusing of particles when a) a single transducer attached to the bottom of the channel is actuated at 2.13 MHz b) a transducer attached to the bottom and another attached to the side, both actuated at 1.84 MHz.

These results clearly demonstrate that a stronger focusing can be obtained when the transducer(s) is actuated at a single resonant frequency than sweeping it near the resonant frequency, however, actuating the transducer at this frequency is often not reliable as even the slightest deviation from the resonant frequency will disperse the particle for a wider focus as shown in Fig. 3.
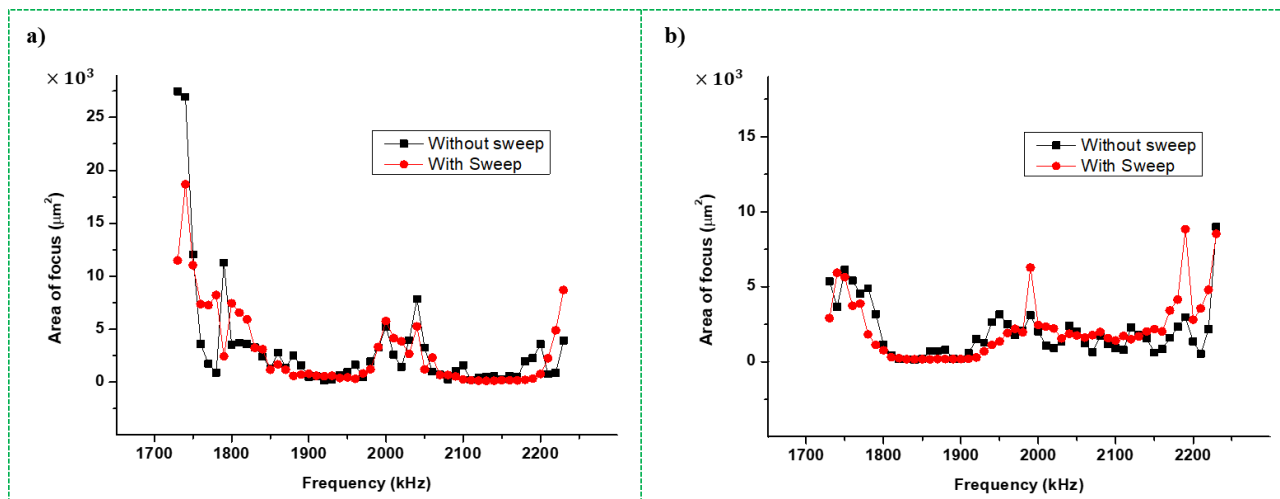
Figure 3: Plots showing the area of the focussed region for different frequencies. a) for a single transducer actuated at a set frequency and for a linear frequency sweep of 50 kHz around the set frequency, and b) for dual transducers both actuated at a set frequency and for a linear frequency sweep of 50 kHz around the set frequency.

Conclusion

We have experimentally investigated 2D focusing of small PS beads in a square microchannel with single and dual transducers. Among all the conditions, the 2D acoustic focusing using dual piezo transducers results in the highest concentration of particle area about 99 μm^2. However, for practical applications, since the method of frequency sweep is preferable over operating at a single resonant frequency, the 2D focusing using a single transducer is preferred and it produces a better concentration area of 117 μm^2. This study also opens up the possibility of investigating 2D focusing using dual transducers with each of the transducers actuated at a different frequency that is resonant with the dimensions, where an even higher concentration of focusing could be achieved.

References
[1]   Knoška, J. et al. Ultracompact 3D Microfluidics for Time-Resolved Structural Biology. *Nat. Commun.* **11** (1) pp 657 (2020)
[2]   Hammarström et al. Acoustic Focusing of Protein Crystals for In-Line Monitoring and Up-Concentration during Serial Crystallography. *Anal. Chem.* 94 (37), 12645-12656 (2022)
[3]   Gerlt, M. S. et al. Focusing of Micrometer-Sized Metal Particles Enabled by Reduced Acoustic Streaming via Acoustic Forces in a Round Glass Capillary. Phys. Rev. Appl. 17, 014043 (2022).

Particle radiation and acoustic mixing in a CNC milled aluminum-based device

Amaury de Hemptinne[1,*], Pierre Gelin[1], V.R. Misko[1], and Wim De Malsche[1].

[1]µFlow group, Chemical Engineering Department, Vrije Universiteit Brussel, Brussel, Belgium
*E-mail: Amaury.de.hemptinne@vub.be

Introduction

Acoustic waves present a compelling solution for multiple microfluidic chip operations. Utilizing layered resonators, acoustic waves enable precise particle control and efficient mixing in microreactors[1]. Acting through device walls, it avoids contamination and requirement of labeling. While silicon chips have historically dominated, the transition to aluminum offers a cost-effective alternative, facilitated by CNC milling for rapid prototyping. Despite challenges like precision issues, ongoing advancements in CNC technology are enhancing aluminum's viability for microdevices. Tapered channel shapes resulting from milling, usually considered as problematic, showed in this field some interesting secondary effects.

In this experimental study, we have made multiple improvements to enhance the financial accessibility of acoustic devices. The cost associated with silicon-based chip production and prototyping have decreased through the shift from silicon to aluminum. Internal volume was extended through channel parallelization and reusability is possible by the development of reversible opening and closing of device.

Experimental procedure

In this study, we initially applied acoustic waves within a single channel in an aluminum-based chip. While aluminum device was sealed with PDMS in former work[2], we sealed the chip with glass cover, material presenting high acoustic impedance. Subsequently, we addressed upscaling by employing parallelization. While this was developed in a former work in a silicon-based chip[3], it was done here in an aluminum device. Two chip production methods, depicted in Fig 1 (a) and (b), were developed: one entailed sealing the chip with UV glue bonding of a glass cover, while the other involved evaluating a reversible system for chip closure using seal and a glass cover press together. This system enabled the implementation of multiple opening and cleaning procedures, thereby facilitating the reuse of the acoustic devices.

The acoustic resonance was characterized through measurement of the focusability of 5 µm fluorescent PS particles and observation of streaming with 450 nm fluorescent PS particles.
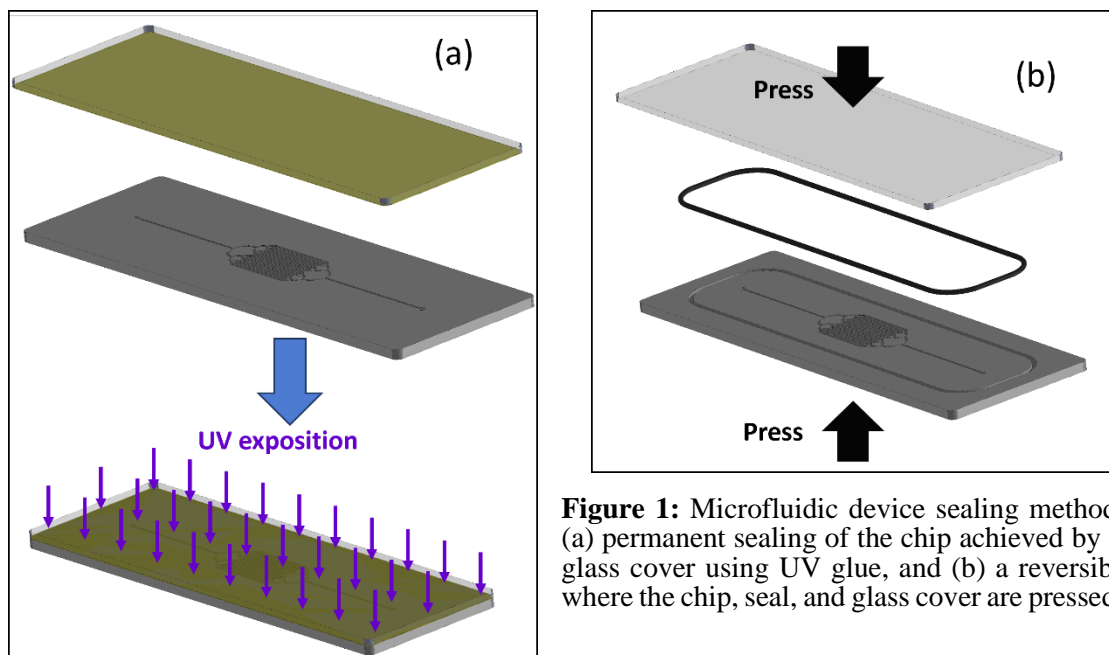
Figure 1: Microfluidic device sealing methods include (a) permanent sealing of the chip achieved by bonding a glass cover using UV glue, and (b) a reversible system where the chip, seal, and glass cover are pressed together.

Results and discussion

The figure depicting a cross-section of a milled channel (Fig. 2 a)) clearly illustrates its tapered shape. The typical angle of the tapered was measured at $101.1 \pm 0.8°$. Consequently, rather than exhibiting resonance at a sharp frequency range, as observed in channels with perfectly vertical walls in silicon-based chips[3], standing acoustic waves are observed across a broader frequency range.

In a parallel configuration, it was noted that each channel corresponds to a specific resonance frequency range. Recent investigations suggest that this phenomenon may stem from slight variations in channel geometries[3] and their positioning relative to the PZT[4]. The average focusability across 16 parallel channels is plotted against frequency in Fig. 2 (b) together with the variance between channels. A high average focusability combined with a low variance indicates a simultaneous high resonance in all channels. The graph illustrates that some specific frequencies yield good acoustic resonance across all channels simultaneously, such as at 2.2 MHz. We hypothesize that this may be attributed to the tapered shape of the channel.

Still, the frequency sweeping method developed for silicon-based chips[3] remains effective for enhancing simultaneous resonance in all channels in aluminum, as corroborated by the graph.
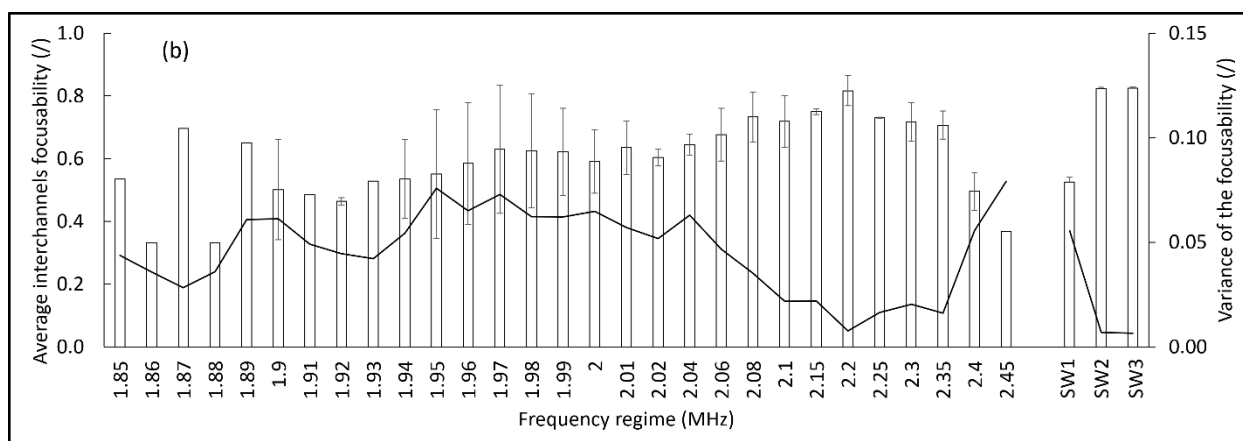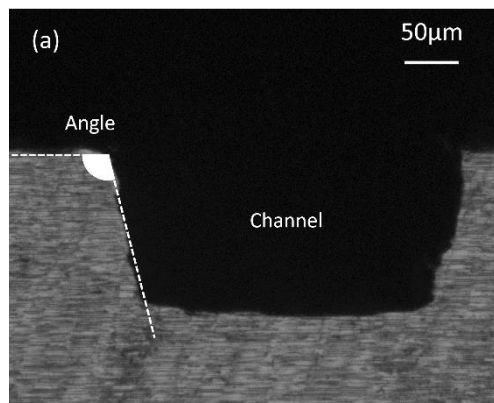
Figure 2: (a) Picture of the section of a channel milled in aluminum. The taper shape is observed. (b) Average inter-channel focusability and variance of the focusability between channels as a function of the frequency. Three sweeping, SW1, 2 and 3, of the frequency are also plotted (1.85–2.00, 1.85–2.30 and 2.00–2.30 MHz).

Conclusion

We have measured the focusability of particles in multiple aluminum-based chips produced with different methods. Streaming in these chips were also observed confirming the potential to use the devices as a particle controller as well as for microreactors technologies. The taper shape resulting from the milling procedure, generally seen as a negative effect, is proposed here as a solution to present parallel channels all resonating at the same time.

Acknowledgements

References
[1]   A. de Hemptinne, P. Gelin, I. Bihi, R. Kinet, B. Thienpont, and W. De Malsche, "Exploring operational boundaries for acoustic concentration of cell suspensions," *Appl. Microbiol. Biotechnol.*, vol. Preprint, 2024.

[2]   W. N. Bodé, L. Jiang, T. Laurell, and H. Bruus, "Microparticle acoustophoresis in aluminum-based acoustofluidic devices with PDMS covers," *Micromachines*, vol. 11, no. 3, pp. 1–15, 2020.

[3]   A. de Hemptinne, V. R. Misko, P. Gelin, and W. De Malsche, "Acoustic standing wave with a frequency sweeping in a microfluidic system of parallel channels," *Chem. Eng. Process. - Process Intensif.*, vol. 194, no. November, p. 109607, 2023.

[4]   A. Tahmasebipour, L. Friedrich, M. Begley, H. Bruus, and C. Meinhart, "Toward optimal acoustophoretic microparticle manipulation by exploiting asymmetry," *J. Acoust. Soc. Am.*, vol. 148, no. 1, pp. 359–373, 2020.

Pressure controlled variable volume ultrasonic bioreactor for bioproduction applications

Gabriel Dumy[1,*], Marin Virey[1], Siriny Laumier[1], Florian Dittman[1], Noémie Cavanna and Mathilde Maestrali[1]
Underline the presenting author

[1]KOLIBRI, Paris, France
[*]E-mail: gabriel@kolibrilab.com

Introduction

Acoustophoresis has been used for almost two decades, in air and liquids, to move various particles ranging from polymer microbeads to microorganisms. While transient and standing waves can be used to do so [1], standing waves are often preferred for their low power properties and the fact that they offer fixed points in space to work with [2]. These trapping site can be used as a surrogate for the culture substrate usually exploited in adherent cell culture (fixed beds, microcarriers or the bottom of a culture plate/well), with a lot of upsides, such as the ease of harvest, release form the substrate influence on cell behavior, real time reconfiguration of the cultured cells microenvironment.

To ensure the resonant aspect of said standing wave, the natural way is to tune the field to the geometry of the cavity, and its has been done in [3]. However, this approach imposes constraints on the generated field itself, geometry of the cavity and repeatability of the generated pressure field if tuning is not well done. Here we introduce the concept of a variable geometry resonant acoustic field for microorganisms trapping and culture, enabling to precisely match the resonant dimension to the transducer emitted wave no matter its frequency. We experimentally characterize the dependance of the pressure field to the volume, match it with finite element simulations and exhibit how it could be use as a variable volume bioreactor.

Experimental setup and results

We developed a device comprising a piezoelectric transducer that attaches to a biocompatible liquid container, with an acoustic reflector facing the transducer. The distance between transducer and reflector can be precisely tuned with a linear actuator. In essence, the principle of our resonant cavity is much like a stacked resonator usually exploited in acoustofluidics applications [4], but with a real time control of its resonant dimension.
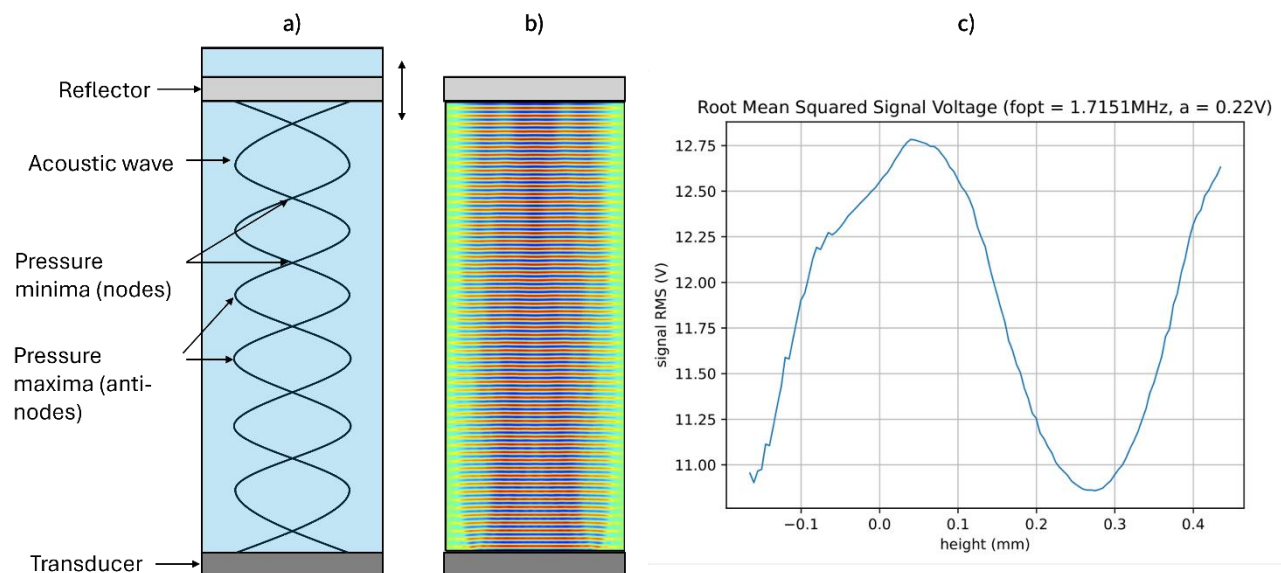
Figure 1: a) Schematic of the variable height acoustic cavity we are characterizing here, either experimentally or b) via a finite element simulation in COMSOL (pressure field represented in the colormap here). c) is the plot of the live piezoelectric transducer voltage as we sweep up the reflector by half a wavelength, exhibiting its sensing capacities.

The transducer is fed a sinusoidal signal through a standard signal generator coupled to an amplifier, and we monitor the voltage at the electrodes of the transducer for the whole experiment, which gives us a measure to tie to our pressure field (Figure 1. C)). Calibrations are performed several times, by sweeping an
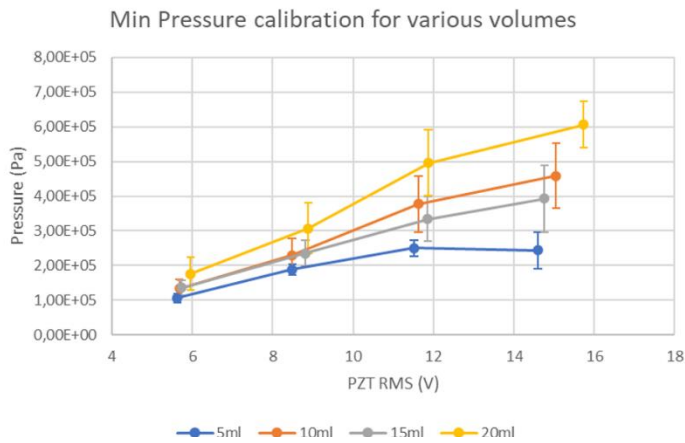
Figure 2: Pressure measured in the pressure nodes of the standing wave at 37°C in culture medium, for various volumes (N=3)

hydrophone across the standing wave in order to measure the maxima and minima in pressure over the whole volume, and associate it to the voltage applied to the transducer. Taking the average and deviation of this pressure measurement yields calibration plots such as Figure 2, which enables the operator to know which constraints the cells will undergo in the pressure nodes.

Once these calibrations are performed, it is easy to exploit them to continuously tune the reflector position not only to the volume inside the bioreactor, but also to any change in resonance properties of the cavity itself, such as a temperature rise, a density of the medium affected by the cells growing in it, and so on.

Biology relevance and application

The main objective to develop this item was to be able to continuously affect the liquid volume where the microorganisms we work with are trapped. Indeed, in bioproduction it is often desirable to have a constant microorganism density, hence with the growth of these the need to increase said volume to keep a constant density, or to perform other tasks such as concentration or dilution of these organism. In addition, considering the variability of these live organisms, it is paramount to reduce the variability of the acoustic constraints added on their culture.
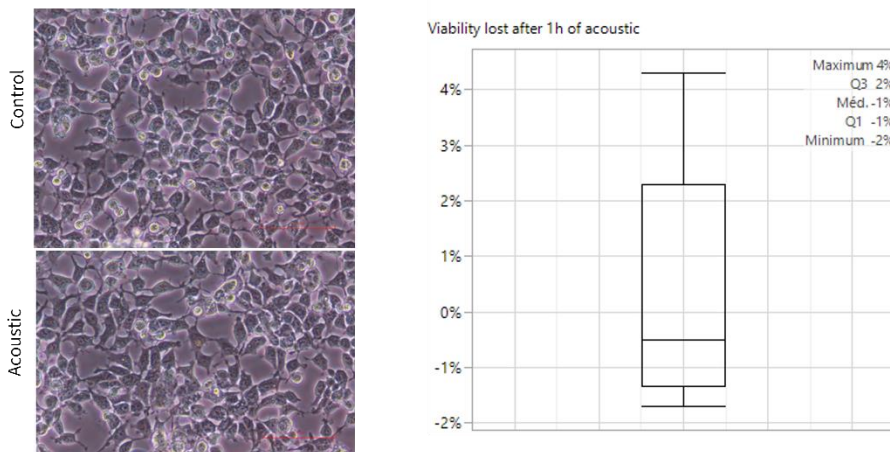
Figure 3: HEK293 mophology is not affected through culture in the acoustic system decribed here (left), and (right) no significant viability loss results from this exposure when compared with control (N=6)

Conclusion

We have described how with a sufficiently low-quality factor a standing wave system can have its resonant dimension changed almost continuously without effectively lowering its acoustic trapping performances. With the right characterization and control algorithm, having a complete control on this resonant dimension can allow to apply exactly the right amount of pressure on the trapped or cultured microorganisms within the acoustic field, accommodating for volume variation needed for their bioproduction or any change that would affect the standing aspect of the acoustic wave (temperature, density of the medium etc). Next development steps will involve exploring the influence of the parallelism between transducer and reflector, and their relative shape on the pressure field that we work with.

Acknowledgements

References (Times New Roman 10 pt)

[1] Baresch, Diego, Jean-Louis Thomas, and Régis Marchiano. "Observation of a single-beam gradient force acoustical trap for elastic particles: acoustical tweezers." *Physical review letters* 116.2 (2016): 024301.

[2] Gesellchen, Frank, et al. "Cell patterning with a heptagon acoustic tweezer–application in neurite guidance." *Lab on a Chip* 14.13 (2014): 2266-2275.

[3] Dual, Jurg, and Dirk Möller. "Acoustofluidics 4: Piezoelectricity and application in the excitation of acoustic fields for ultrasonic particle manipulation." *Lab on a Chip* 12.3 (2012): 506-514.

[4] Lenshof, Andreas, et al. "Acoustofluidics 5: Building microfluidic acoustic resonators." *Lab on a Chip* 12.4 (2012): 684-695.

SMART Microacoustic Setup for Automated Ice Sensing and Deicing Using Surface Acoustic Waves

Kiana Khodakarami[1], Stefan Jacob[3], Atefeh Karimzadeh[1], Uhland Weissker[1], Shilpi Pandey[1], Jaime del Moral[2], Jorge Gil-Rostra[2], Ana Borrás[2], Agustin R. González-Elipe[2], Andreas Winkler[1]

[1]Leibniz IFW-Dresden, SAWLab Saxony, Acoustic Microsystems, Helmholtzstr. 20, 01069 Dresden, Germany.
[2]Nanotechnology on Surfaces and Plasma Lab, Materials Science Institute of Seville, Consejo Superior de Investigaciones Científicas (CSIC), Americo Vespucio 49, 41092 Sevilla, Spain.
[3]Physikalisch-Technische Bundesanstalt (PTB), Bundesallee 100, 38116 Braunschweig, Germany.
*E-mail: k.khodakarami@ifw-dresden.de

Introduction
The high demand for prevention of ice formation and de-icing in a broad range of applications including transport, robotics, photovoltaics, and telecommunications requires new sustainable, cost-efficient, and effective solutions. Whilst active de-icing is key in various industry sectors, the development of de-icing method faces compatibility challenges with existing devices and real-world conditions. The recent employment of acoustic waves (AWs), in particular surface acoustic waves (SAW) for de-icing or anti-icing has proven to be a very promising approach and may open the path for a powerful alternative to the conventional solutions, especially for transparent materials or such with low heat conductivity. This work addresses the de-icing of several mm thick glaze ice layers on square substrates with several centimeter side length using nanoscale activation through surface acoustic waves (SAWs).

Theory and Experimental procedure
Proving the capability of our approach, Rayleigh-SAWs were generated using interdigital transducer (IDT) electrodes to de-ice surfaces of $LiNbO_3$ substrates coated with fused silica in an environmental chamber at -10°C. We utilized thermo-camera measurements to demonstrate that IDT-related Joule effects do not play a significant role in de-icing low-thermal conductive substrates. To understand the acoustic mechanisms underlying the deicing process, we have performed accompanying finite-elements analysis simulations using Comsol Multiphysics of SAW propagation and interaction with ice-and water at reduced temperature.
Furthermore, this study presents a smart technological approach enabling seamless transition between different acoustic modes within a single device, facilitating efficient de-icing without significant changes to the setup or chip layout. By reversing the polarity of the IDT electrodes in conventional sSAW devices, a shear-thickness dominant (SD) bulk acoustic mode in the low MHz frequency range, ideal for surface sensing, can be excited. The switching is achieved using a relay circuit with microcontroller, an RF signal source and the microacoustic chip, requiring no conceptual changes to existing setups and utilizing only the already existing IDT electrodes.

Results and Discussion
Automated ice detection via SH-BAW and ice melting via Rayleigh-SAW was demonstrated successfully on $LiNbO_3$ substrates with several cm side length using a smart setup. Possible Joule effects due to ohmic losses in the IDTs can been excluded based on the chip temperature distribution during activation at and out of SAW resonance conditions. Further, the de-icing mechanism of glaze ice by SAW activation has been revealed, supported by FEM simulation of the SAW propagation on ice-covered surfaces at reduced temperatures and experimental analysis of the ice melting process. The process involves a combination of ice mechanical stress activation and heating through the initially formed water/ice front. The energy density required for SAW-based de-icing was low compared to other methods, while the method is compatible to other passive and active deicing techniques.
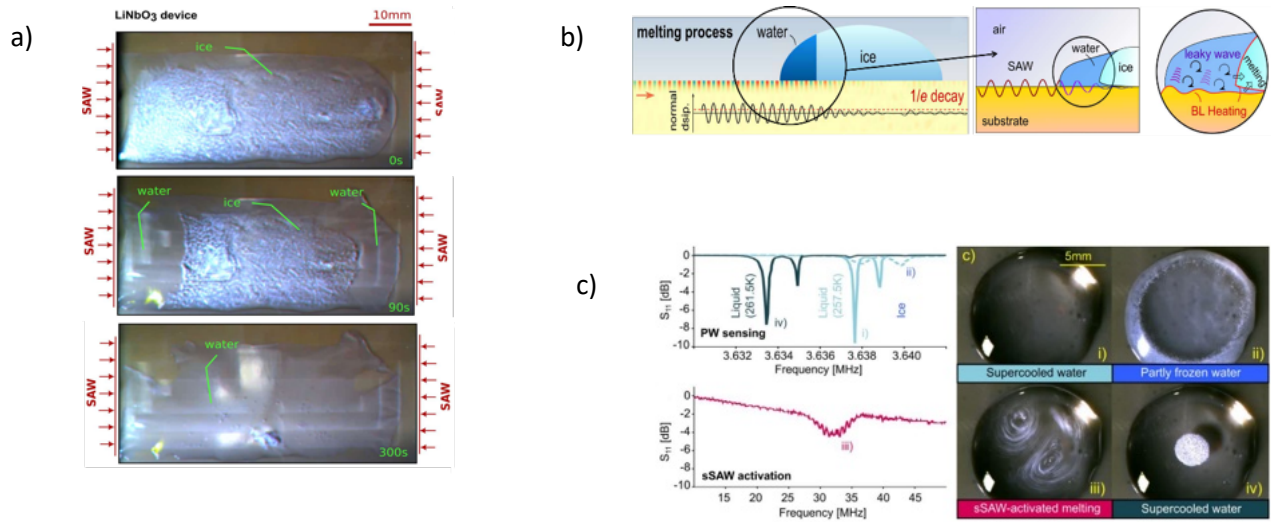
Figure 1: a) SAW-induced de-icing on a 7 x 3 cm² LiNbO3 substrate; b) SAW interaction with water and glaze ice; c) Smart operation of a SAW device for deicing application.
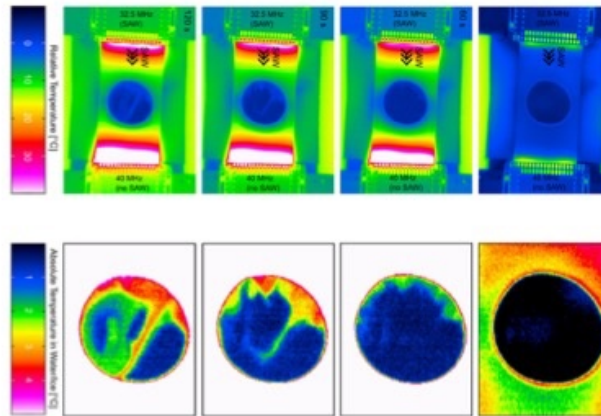

Figure 2: Thermal images of a de-icing process on a LiNbO3 device.

Conclusion

This study demonstrates the development of a smart acoustic de-icing system, addressing ice accretion challenges with low-power consumption, efficient ice-detection using bulk shear waves (SH-BAW), and subsequent reliable ice melting using Rayleigh-type surface acoustic waves (SAW). On one hand, the introduced SH-BAW mode provides a sensor signal highly-sensitive to surface load variations as well as to temperature. On the other hand, Rayleigh-SAW actuation allows centimeter-scale deicing of transparent substrates with low heat conductivity. Combining both modes, a smart deicing setup was realized and applied for studying microacoustic deicing. Further, the deicing mechanism for glace ice excited by Rayleigh SAW was determined experimentally and supported by FEM simulation.

Acknowledgements

References

[1] E. Jacob, S., et al., Advanced Materials Technologies, https://doi.org/10.1002/admt.202300263 (2023)
[2] del Moral, J., et al., Advanced Functional Materials, https://doi.org/10.1002/adfm.202209421 (2022)
[3] Karimzadeh, A., et al., Advanced Materials Technologies, https://doi.org/10.1002/admt.202301749 (2024)

Study of SAW field nonuniformity for optimization of SAW based acoustic streaming micropump

Chen Wu[1,2], Grim Keulemans[2], Benjamin Jones[2], Veronique Rochus[2], Xavier Rottenberg[2], Paul Heremans[1,2]

[1]Department of Electrical Engineering, KU Leuven, B-3001 Leuven, Belgium
Email: chen.wu@student.kuleuven.be
[2]imec, Kapeldreef 75, B-3001 Leuven, Belgium

Introduction

Micropump plays an important role in microfluidic systems and the interdigitated transducer (IDT) surface acoustic wave (SAW) micropump has drawn increasing attention due to its ease of fabrication, miniaturized footprint, high working frequency and precise control of the flow velocity. The IDT, which is composed of multiple comb-like electrode finger pairs, is used to generate the SAW. A PDMS microfluidic chip is bonded adjacent to the IDT. From Fig.1, the generated SAW first propagates along the substrate, penetrates through the channel side wall and subsequently couples with the fluid inside the channel to induce directional acoustic streaming to realize the pumping functionality. However, the amplitude of the SAW is extremely low (in sub nanometer range). What's worse, the SAW experiences a severe acoustic energy attenuation when propagating through the channel side wall under high working frequency. All these drawbacks result in an extremely low pumping velocity (0.99 mm/min) [1]. It is obvious that the PDMS channel side wall should be as thin as possible to minimize the acoustic attenuation. The position of the channel also has a significant impact on the pumping velocity and is worth investigating. In this work,

Figure 1: Schematic of the cross-section view of the IDT-based SAW acoustic streaming micropump.

based on the above-mentioned design of the IDT based SAW micropump, we propose a study of the non-uniformity of the SAW field. We define an optimal position where the maximum displacement amplitude of the SAW is obtained, leading to an increased pumping velocity.

Theory and simulation

The displacement amplitude of the planar SAW on the piezoelectric substrate is simulated according to Zhang et al [2]. The result shown in Fig. 2.a is for a SAW with a wavelength of 120 μm, which is generated by an IDT with 40 electrode finger pairs and an aperture length of 2400 μm.
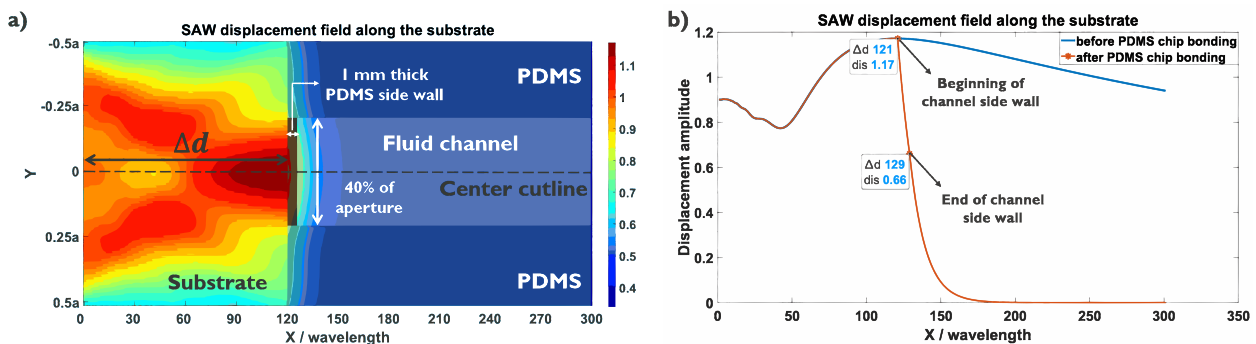
Figure 2: (a) SAW displacement field and the preferred position of the fluidic channel. "a" is the aperture and "Δd" is the distance between the beginning of the channel side wall and the IDT. (b) Comparison of the SAW displacement amplitude at the Y-axis center along the substrate before and after PDMS channel bonding.

As indicated in Fig. 2.a, starting from the outermost electrode finger, the amplitude of the SAW first experiences a diffraction in the near field, then reaches its maximum and subsequently decays gradually along the substrate. The resulting SAW field leads to the determination of the optimal position of the microfluidic channel. Firstly, in the X direction along the substrate, the beginning of the channel side wall should be aligned to the position where the amplitude of the SAW is maximum. Secondly, in the Y direction, the width center of the channel should be aligned to the aperture center of the electrode finger. Further, the width of the microfluidic channel is designed to cover 40% of the aperture length, where the highest acoustic intensity is

obtained. The SAW (wavelength of 120 μm) displacement amplitude decays dramatically through the PDMS channel side wall and further decays inside the fluid channel, with a decay factor of 593.13 m^{-1} and 785.5 m^{-1} respectively, shown in Fig. 2.b. Note that the x-axis is normalized to the wavelength and the y-axis is also the normalized displacement amplitude which is linearly proportional to the amplitude of the applied voltage.

Device and experiment

As shown in Fig. 3, the IDT, which has identical parameters as in simulation, is deposited on the thin film ScAlN (30% Sc doping). A bent PDMS channel (960 μm in width and 50 μm in height) is bonded on the substrate. The thickness of the channel side wall is 1 mm. The distance between the beginning of the channel side wall and the IDT (Δd), which is measured along the center cutline of the channel (shown in Fig. 2.a), is varied, and measured. The channel is filled with fluorescent particle suspension. The particle streaming velocity is measured and compared using three identical IDT micropump devices, driven under the same voltage amplitude (45 V) and the same resonant frequency (41.3 MHz). The particle streaming velocity is measured at the entrance of the straight channel section and compared with the SAW displacement from the analytical results.
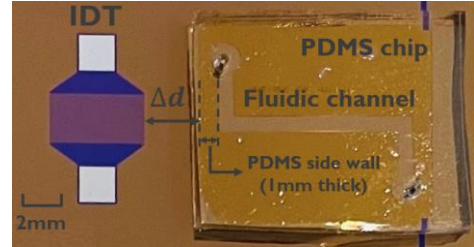
Figure 3: Feature of the IDT based SAW micropump device.

Results

The flow velocity is calculated by taking the average of multiple particles for each device. As shown in Fig. 4.b, the IDT to channel distance (Δd) for three devices (A, B and C) is increased and gradually approach the preferred position (reference $\Delta d = 121\lambda$). In the ideal case, the channel center should be precisely aligned to the middle of the IDT aperture. However, vertical misalignment of the channel during fabrication is inevitable, resulting in a different average SAW amplitude driving the fluid in the channel. Therefore, vertical misalignment is also measured and considered. As indicated in the figure, the amplitude of the SAW increases gradually with the increase of Δd. From Fig. 4.c: as the fluidic channel gradually approaches the optimal position, the measured flow velocity also increases accordingly as expected.
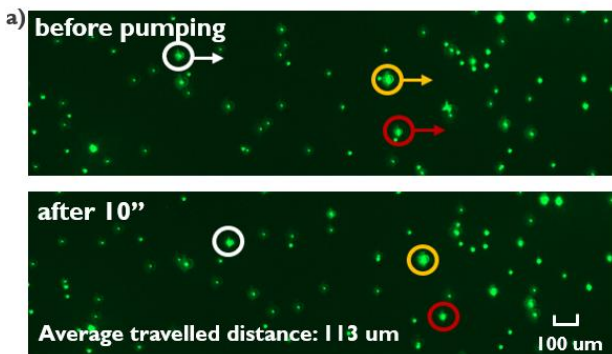
Figure 4: (a) Real time particle tracing for device B. (b) SAW displacement field at the width center of the channel (misalignment is considered). (c) Averaged flow velocity of three devices at different position relative to the IDT.
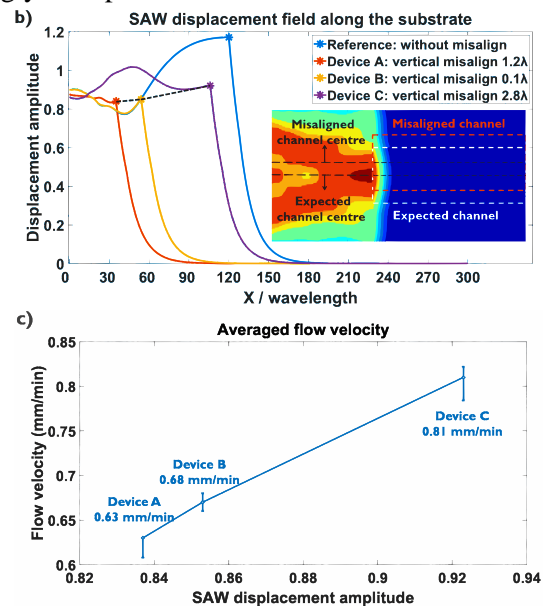
Conclusion

For the IDT based SAW micropump, the position of the fluidic channel has a significant impact on the flow velocity. The proposed study of the planar SAW field non-uniformity is useful to determine the optimal position. For any given IDT, by knowing the wavelength of the SAW, the aperture length and the number of the electrode finger pairs, the position of the fluidic channel leading to the maximum pumping velocity can be predicted. According to our experiments, the closer the channel is to the expected position, the higher the pumping velocity we can obtain. Further efforts are needed to mitigate the vertical misalignment during micro-fabrication and to investigate the impact of different channel geometries and materials.

References

[1] Wang, Tao & Ni, Qi & Crane, Nathan & Guldiken, Rasim. (2017). Surface acoustic wave based pumping in a microchannel. Microsystem Technologies. 23. 1-8. 10.1007/s00542-016-2880-9.
[2] Zhang, Y., Huang, J., and Guo, X., "Field nonuniformity of limited-aperture planar SAWs and its implications for designing SSAW acoustofluidics", Journal of Micromechanics and Microengineering, vol. 31, no. 9, IOP, 2021.

The effect of speed of sound mismatch on acoustophoretic focusing quality within droplets

Qian Shi[1,*], Thierry Baasch[2], Zhenhua Liu[1], Anna Fornell[1], Gabriel Werr[1], Laurent Barbe[1] and Maria Tenje[1]

[1]Department of Materials Science and Engineering, Science for Life Laboratory, Uppsala University, Uppsala, Sweden
[2]Department of Biomedical Engineering, Lund University, Lund, Sweden
[*]E-mail: qian.shi@angstrom.uu.se

Introduction

Droplet-based microfluidics involves the generation of discrete volumes of a dispersed phase (often water) in a continuous and immiscible phase (oil). Bulk acoustic wave acoustophoresis can be combined with droplet microfluidics for droplet handling, or handling of droplet content. Fluorinated oils, e.g. Novec HFE-7500, possess properties such as high permeability for gases and insolubility for most organic compounds, which makes them favorable for droplet-based applications [1]. However, it has been observed that a deterioration in the average magnitude of the primary acoustic radiation force inside water droplets generated in HFE-7500 results in poor acoustophoretic focusing quality [2,3]. As a follow up to these studies, we compared the droplet-internal acoustophoretic focusing performance inside aqueous droplets generated in a selection of oils that have previously been used in two-phase applications [4]. Based on these experiments, we conclude that a match in the speed of sound between the dispersed and continuous phase is paramount to high quality acoustic focusing. Here, we present simulation results of four selected cases, aqueous droplets immersed in linseed oil, light mineral oil, silicone oil 50 cSt and HFE-7500, and offer a theoretical explanation to why it is speed of sound that dominates acoustophoretic focusing performance.

Methods

The COMSOL 2D model consists of three consecutive domains: the droplet, the surrounding fluid and perfectly matched layers (PML) at either ends of the channel, see Figure 1. The droplet has a tip-to-tip length of 1,380 µm and is modeled as a plug confined in a 375-µm-wide channel. The surrounding fluid domain is a representation of the following oil and surfactant combinations: 1) linseed oil with 5% (% v/v) polyglycerol polyricinoleate (PGPR), 2) light mineral oil with 5% (% v/v) PGPR, 3) silicone oil with 5% (% v/v) ABIL EM-90 and 4) HFE-7500 with 2% (% v/v) Krytox FSH-157. The description to how we acquired the speed of sound and density data of all the above samples can be found in [4]. A damping coefficient was introduced to the speed of sound in both the droplet and the surrounding fluid. The PML domains are used to simulate open boundaries at both ends of the channel, where no reflection of acoustic waves occurs. The system is actuated at the top and bottom walls by a harmonic 1 nm displacement with a phase difference of 180°. Linear and inviscid acoustics is assumed when building the model, and the finite element method is used to solve the coupled Helmholtz equation (COMSOL 6.1). The Gorkov potential is computed for a polystyrene particle with a diameter of 10 µm.
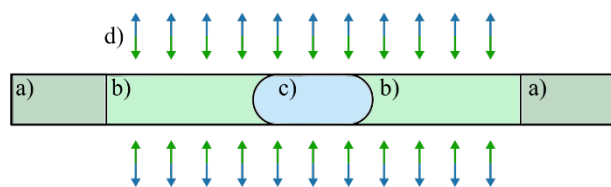

Figure 1: 2D COMSOL model sketch that includes three regions: a) PMLs, b) surrounding fluid, c) water droplet. The actuation of the top and bottom walls has a phase difference of 180° as indicated by the color of the arrows (d).
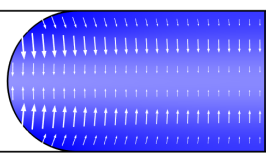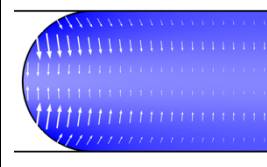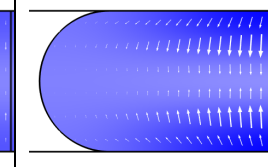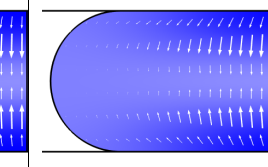
Results and Discussion

The speed of sound and density of DI water at 25°C is 1,496 m/s and 997 kg/m^3, respectively. We observe from figures of the 2D simulation results in Table I that a mismatch in speed of sound between the water droplet and the surrounding fluid results in a diminished Gorkov potential, especially around either ends of the droplet. Therefore, there is also a decay in the acoustic radiation force amplitude in the same regions. This is consistent with previous experimental results [4].

Two boundary conditions need to be fulfilled at the droplet surface: 1. The continuity of the velocity in the surface normal direction and 2. the continuity of pressure. We find that the contribution of the pressure continuity condition dominates the solution, which indicates that matching the speed of sound, and not the density, allows to achieve strong and regular focusing that extends through the droplet caps. This can be shown

by a geometrical analysis of the situation, see Figure 2. In a standing wave the magnitude of the fluid velocity vector is largest at the pressure node. However, as the velocity vector points along the y-axis and is orthogonal to the surface normal at the droplet cap its scalar product will be zero. Consequently, the boundary condition is automatically fulfilled in this region, even for a density mismatch. The same situation occurs close to the walls where we have velocity nodes. This means that the contribution of the velocity field along the side walls to the total solution is also negligible. Therefore, the continuity of pressure contributes primarily to the acoustic fields because the velocity boundary condition's contribution is limited only to the intermediate regions between pressure and velocity node. Considering all contributions, we conclude that the continuity of the pressure field dominates over the continuity of the velocity in the normal direction, and therefore, it is sufficient to match the speed of sound between the water droplet and the surrounding oil to achieve particle focusing along the body of the droplet and inside the droplet caps.

Table I: COMSOL 2D simulation result of the Gorkov potential and velocity field at half-wavelength resonance in half of a water droplet in four different oil-surfactant combinations. For each oil-surfactant combination, the speed of sound, c, and density, ρ, as measured at 25°C is given. The background color in the simulation figures indicates the strength of the Gorkov potential field, the stronger the blue color, the higher the potential. The white arrows represent the direction and strength of the acoustic radiation force.

	Linseed oil	Light mineral oil	Silicone oil	HFE-7500
$c_{25°C}$ (m/s)	1,462	1,428	1,046	710
$\rho_{25°C}$ (kg/m³)	925	845	960	1,618
Frequency (MHz)	1.95	1.91	2.08	2.08
Simulation				
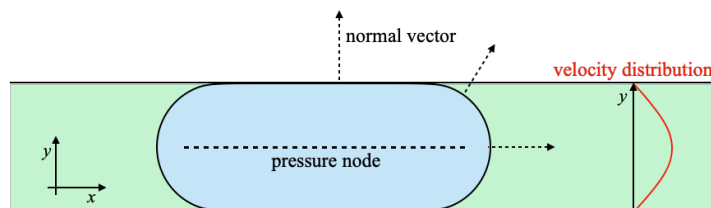
Figure 2: Geometric explanation of the contributions of velocity fields to the boundary condition. The displacement velocity continuity should be at the normal direction to the droplet interface. Based on analysis of velocity distribution along the y-axis (red line) and the direction of the normal vector (dotted arrows) at the interface, the contribution of the velocity fields is negligible as either the velocity field or the contribution of the velocity field in droplet normal direction is small.

Conclusion

We have demonstrated through simulation that speed of sound is the dominating factor on acoustophoretic focusing quality at half-wavelength resonance within channel-confined droplets. Simulations show that particle focusing quality, especially at the cap regions within a water droplet, is greatly affected by the choice of the continuous phase. We prove that a match in the speed of sound between the two fluid phases is sufficient to achieve focusing within the droplets.

Acknowledgements

References

[1] J-C. Baret. *Lab Chip*, **12** 422-433 (2012).
[2] A. Fornell, F. Garofalo, J. Nilsson, H. Bruus and M. Tenje. *Microfluidics and Nanofluidics*, **22** 75 (2018).
[3] M.S. Gerlt, D. Haidas, A. Ratschat, P. Suter, P.S. Dittrich and J. Dual. *Biomicrofluidics*, **14** 6 (2020).
[4] Q. Shi, Z. Liu, A. Fornell, G. Werr, L. Barbe and M. Tenje. *Acoustofluidics Conference*, St. Louis, USA, 2023, pp. 80-81.

The in-flow mobility ratio method enables optimizing acoustophoresis separation quality

Thierry Baasch[*], Alexander Edthofer, Linda Péroux, Olivia Rengbrandt, Lovisa Silversand, Andreas Lenshof, and Thomas Laurell

Department of Biomedical Engineering, Lund University, Lund, Sweden
[*]E-mail: Thierry.Baasch@bme.lth.se

Introduction

Acoustophoretic separation of cell mixtures into their individual constituents, has been used, for example, to isolate circulating tumor cells [1] and separate leukocyte subpopulations [2]. The working principle and the chip used herein [3] is illustrated in Fig. 1a. In the prefocusing channel the particle or cell mixture is focused by ultrasound in two dimensions and enters the separation channel through the side inlet. In the separation channel the half-wave mode in channel width is excited and ultrasound pushes the particles towards the channel center. The acoustically induced migration velocity of the particles depends on their acoustic mobility, a compound parameter based on their size, as well as their and the medium's compressibility and density. If all parameters (flowrate, actuation voltages and flow split ratios) are tuned correctly then the species of high and low acoustic mobility will exit through the center and side outlet, respectively, and be separated from each other. Tuning all parameters correctly is challenging and in practice these parameters are either set by skilled personnel, or determined by trial and error, as well as brute force optimization techniques [4, 5]. Brute-force approaches involve many separations and validation steps based on assessing the separation performance by fluorescence activated cell sorting (FACS), and are impractical, time-consuming, and not scalable. Throughout the years it was stated in literature that measuring the particle or cell properties will allow for optimized separation [6, 7, 8]. Previous research, however, fails to present an optimality criterion, to show a protocol for, or even to perform an optimized separation experiment.

Our protocol based on the in-flow mobility-ratio method [9] and one calibration step provides settings that optimize separation quality. The separation quality, a single parameter introduced herein, denotes the minimum of the separation efficiency collected at each outlet.

Theory and Experimental procedure

Five parameters need to be determined to achieve optimal conditions: the voltage at the transducers driving the prefocusing and acoustic separation, the total flowrate, and the flowrate split ratios at the outlet and inlet flow splitter.

Fortunately, three of the parameters can be determined independently from the other. The actuation voltage at the prefocusing piezoelectrical transducer is chosen to achieve good 2D pre-focusing while limiting the heating. The total flowrate should be low enough to avoid inertia effects and high enough to guarantee reasonable sample throughput. The inlet split ratio is chosen such that the prefocused particle beam is as close as possible to the side walls when entering the separation chamber without inducing significant particle wall interactions. Therefore, the optimization problem reduces to determining the outlet split ratio and the separation channel actuation voltage. Two conditions are used to optimize the separation quality: 1. The gap between the two particle species must be maximal close to the separation channel outlet and 2. the flowrate split ratio at the outlet must be chosen such that the flow separation occurs in the exact middle between the particle species.

The separation channel voltage and outlet flowrate split ratio that fulfill conditions 1 and 2 are determined by a combined modelling approach: An analytical model of the particle trajectories is used in combination with in-flow mobility ratio measurements and one calibration measurement to determine the input voltage that achieves the largest gap distance right in front of the outlet split. The corresponding optimal outlet flowrate split ratio is determined from our finite element method (FEM) model [3].

Validation, Results and Discussion

As the FEM model is already published and validated, this study focuses on validating the model-based predictions of the particle stream positions at the outlet fork. We applied our theoretical model to compute the positions of red-fluorescent 5 μm diameter (R5) and green-fluorescent 8 μm diameter (G8) polystyrene particles (Microparticles GMBH) close to the separation channel outlet, see Fig. 1b. The circles represent experimental measurements obtained by fluorescence microscopy while the solid lines are theoretical predictions. The experimental particle positions deviate less than one particle radius from the theoretical prediction on average.

In a next step, we applied our method to separate R5 from G8. The results are summarized in Fig. 1 c and d. The method predicted an optimal voltage of (4.65 Vpp) and an outlet flowrate split ratio of 61.1% side flow

to 38.9% center flow, which yielded a separation quality of 98.2% as measured by FACS, a snapshot of the channel outlet at the optimal conditions is shown in Fig. 1c.

To check if we achieved the optimal separation conditions, we performed 15 additional separation experiments at actuation voltages close to the optimal voltage, see the gray circles in Fig 1d. Our protocol yielded a separation quality comparable to be optimal separation quality obtained by a brute-force parameter sweep. In fact, the obtained separation quality is close to the values presented in literature for comparable situations, Antfolk et al. [4] achieved a separation quality of 98.8% by manual tuning, while Urbansky et al. [5] achieved a separation quality of 95.4% at high sample flowrates and for three bead types.

We applied the protocol to separate DU145 from Jurkat cancer cell lines and achieved a separation quality of 72.3% at the computed optimal voltage (2.49 Vpp) and flowrate split ratio of 62.8% side and 37.2% center at the outlet. The optimality of our settings was confirmed experimentally: we found the separation quality diminished rapidly for neighboring actuation voltages, i.e. for 2.19 Vpp and 2.79 Vpp separation qualities of 44.9% and 53.5% were obtained, respectively.

Conclusion

We present an easy-to-use protocol to achieve optimal acoustophoresis separation quality. The in-flow mobility ratio method is the core of the technique, and in combination with one calibration measurement (black cross, Fig. 1b) allows to model the particle trajectories to unprecedented precision. Our approach performs similarly to the optimal settings determined by brute force parameter sweeps, which proves its optimality.
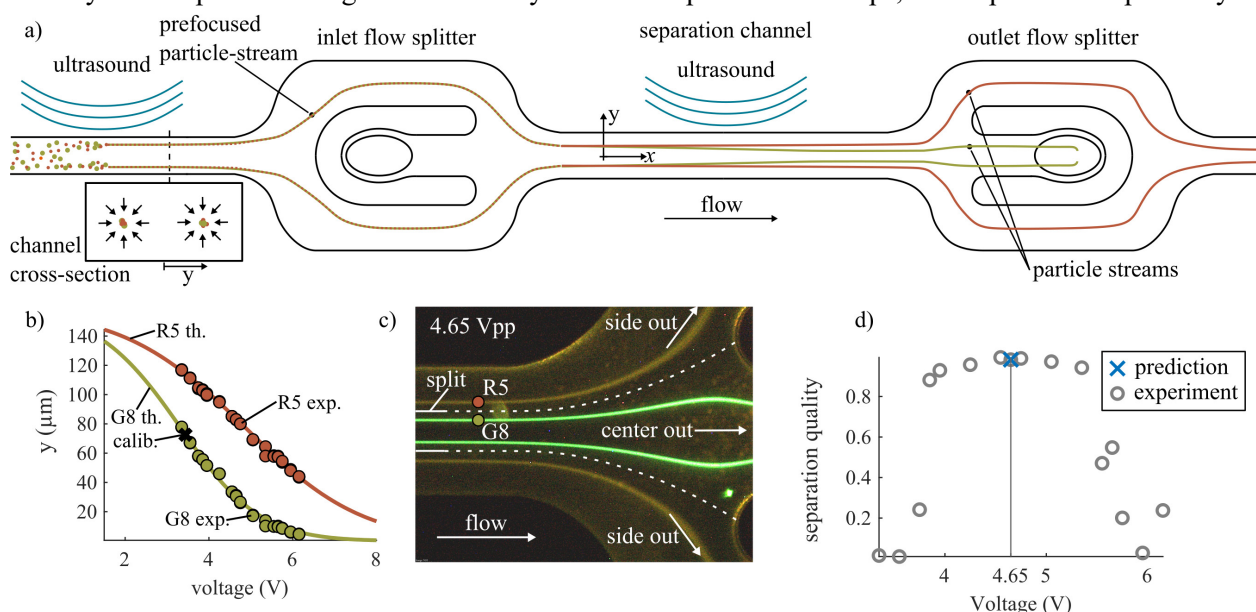
Figure 1: a) Sketch of the microfluidic chip used in this study. Particles or cells are acoustically prefocused and enter the separation channel through the side channel of the inlet flow splitter. In the separation channel ultrasound separates the particles based on their acoustic mobility. Particles of high and low acoustic mobility exit the device through the center and side channel of the outlet flow splitter, respectively. b) Experimental validation of our theoretical model used to predict the positions of the particle beams at the separation channel outlet as a function of the applied voltage. The difference between theoretical prediction (solid line) and experiment (circles) is less than a particle radius on average. c) Snapshot at the channel outlet for the optimal separation conditions. The dotted line sketches the stagnation streamline. d) Validation of the optimal separation. Applied voltages and separation quality are shown on the horizontal and vertical axes, respectively. The separation quality obtained from the predicted optimal settings is shown by a blue cross. The predicted optimal settings show the same performance as a brute-force voltage sweep.

References

[1] E. Undvall, C. Magnusson, A. Lenshof, Y. Ceder, H. Lilja, Thomas Laurell, *Anal. Chem.,* **93** 17076 (2021)

[2] A. Urbansky, F. Olm, S. Scheding, T. Laurell, A. Lenshof, *Lab Chip* **19** 1406 (2019)

[3] E. Undvall, F. Garofalo, G. Procopio, W. Qiu, A. Lenshof, T. Laurell, and T. Baasch, *Phys. Rev. Appl.*, 17, 034014 (2022)

[4] M. Antfolk, C. Antfolk, H. Lilj, T. Laurell, and P. Augustsson, *Lab chip*, **15** 2102 (2015)

[5] A. Urbansky, F. Olm, S. Scheding, T. Laurell, and A. Lenshof, *Lab Chip*, **19** 1406 (2019)

[6] K. Cushing, F. Garofalo, C. Magnusson, L. Ekblad, H. Bruus, and T. Laurell, *Anal. Chem.*, **89** 8917 (2017)

[7] D. Hartono, Y. Liu, P. L. Tan, X. Y. S. Then, L.-Y. L. Yung, and K.-M. Lim, *Lab Chip*, **11** 4072 (2011)

[8] F. Garofalo, A. Lenshof, A. Urbansky, F. Olm, A. C. Bonestroo, L. Ekblad, S. Scheding, and T. Laurell, *Microfluid. Nanofluidics*, **24** 64 (2020)

[9] T. Baasch, L. Péroux, A. Lenshof, and T. Laurell, *Acoustofluidics Conference 2022*, 88 (2022)

Towards Love Wave-based in-situ Measurement of Ice Layer Thickness on Wind Turbine Rotor Blades

Philipp Schulmeyer[1,*] and Hagen Schmidt[1]

[1]Leibniz Institute for Solid State and Materials Research, Dresden, Germany
*E-mail: p.schulmeyer@ifw-dresden.de

Introduction

Cold regions are particularly interesting for the construction of wind farms, as higher wind speeds and wind energy densities can be expected, but there is also a higher risk of atmospheric ice formation. Icing on the rotor blades of wind turbines poses a safety risk to people, nature and infrastructure due to ice throw. It also reduces the performance of the turbines and increases the imbalance of the rotor, which leads to additional wear of the mechanical components. Detecting the icing of rotor blades is crucial to minimise the risk of structural failure and to be able to initiate a de-icing procedure. To date, there is no ice detection system that can be considered an industry standard. Surface acoustic wave (SAW) sensors offer promising features [1] that enable an innovative approach to surface icing detection in harsh industrial environments due to their small and thin design, passive and wireless operation, and retrofittability. While recent investigations focus on the development of ice onset sensors using SAW devices [2-4] the following approach aims towards the development of a wireless SAW reflective delay line sensor making use of Love waves on a 41°-rotated Y-cut lithium niobate crystal with an SiO_2-waveguide layer enabling the measurement of ice layer thicknesses. The ice layer thickness measurement is realised by adapting the principles deployed in wireless interrogated SAW identification tags. Reflector gratings serve as ice thickness indicators. Love waves with their shear-horizontal polarised particle displacement confined to the waveguide, hardly get damped by liquid loads like water drops. They mainly experience damping when water on the sensitive surface freezes increasing the surface load's viscosity and shear coupling. The reflection coefficient characteristics S_{11} in time-domain reveal peaks corresponding to reflector gratings placed in known distances from the interdigital transducer. These peaks can be evaluated when in dry or wet surface condition but will be damped by frozen surface loads enabling statements on the degree of ice-coverage of the device. Furthermore, the shift of S_{11} characteristics in frequency-domain provides additional information about the device temperature helping to even predict icing conditions.
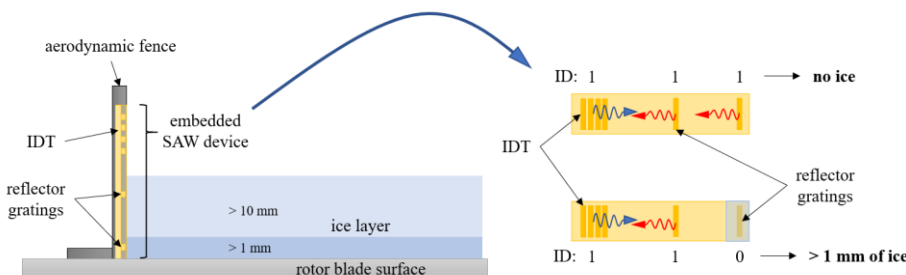

Figure 1: Schematic drawing of ice layer thickness measurement using SAW device on rotor blade surface.

Simulation and experimental results

Finite element analysis performed by using COMSOL Multiphysics 6.2 revealed the existence of Love waves in 41°-rotated Y-cut lithium niobate with a silicon dioxide waveguide layer. The optimal SiO_2 layer height in relation to the SAW wavelength is found to be $h/\lambda = 0.05$. For this waveguide layer height a minimal attenuation coefficient of $\alpha = 0.01$ dB/λ can be expected for both free and shorted substrate surface with a maximum electromechanical coupling coefficient K^2 of 17.5 %.
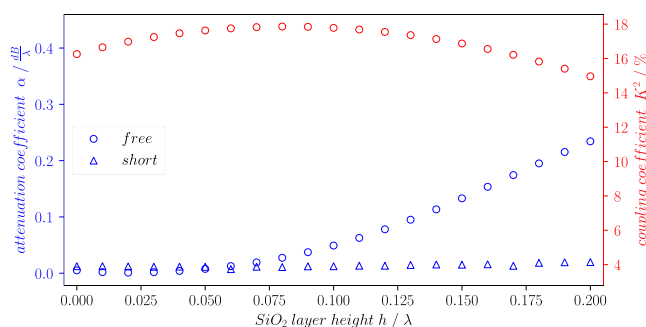

Figure 2: Simulated attenuation coefficient α (blue) for free and shorted substrate surface as well as coupling coefficient K^2 (red) for 41°-rotated Y-cut lithium niobate substrate and SiO_2 waveguide layer.

These simulation results led to the fabrication of a reflective delay line device with an interdigital transducer (IDT) consisting of 31 finger pairs. The solid finger electrode width is 30 µm resulting in an electrode periodicity of 120 µm. The aperture has a width of 2 mm. The single side polished piezoelectric substrate has a thickness of 500 µm and the SiO_2 waveguide layer of 6 µm. The three shorted reflector gratings consist of either three, seven or eleven stripes.

For the experiment the device is mounted onto a chip carrier in a vertical orientation with the IDT and reflector gratings facing downwards. The electrical connection to a vector network analyser (VNA) is realised using gold-plated spring pins soldered to a printed circuit board with conductor-backed coplanar waveguides of 50 Ω characteristic impedance and SMA connectors. This chip carrier is mounted to a height adjustable bracket so that the SAW device can be immersed into a water container underneath. The whole setup is placed inside a temperature chamber to allow the water inside the container to freeze (Figure 3, left).
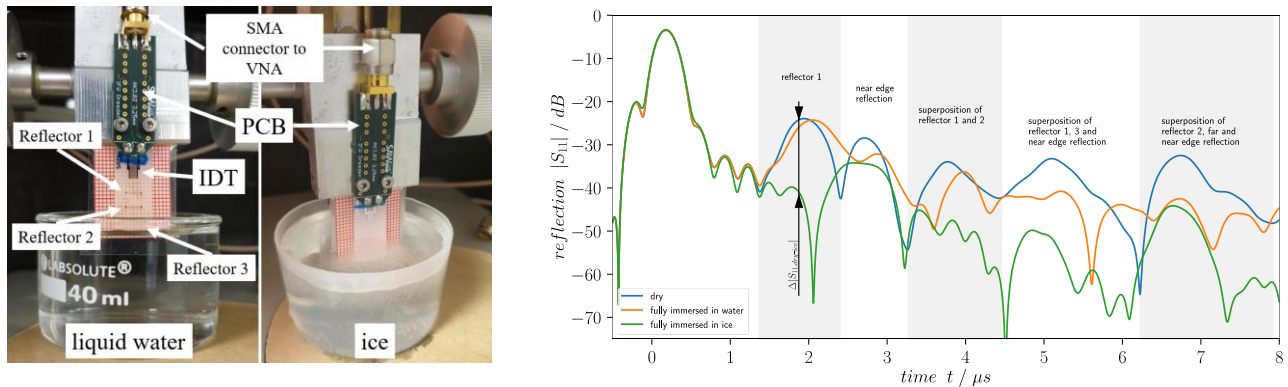
Figure 3: Experimental setup in temperature chamber (left) and reflection characteristics S_{11} in time-domain for device in dry condition, reflector gratings fully immersed in liquid water and in ice (right)

	S_{11} / dB	$\Delta S_{11} = S_{11,dry} - S_{11,ice}$ / dB
Dry	-24.2	
Water	-25.9	-1.7
Ice	-41.1	-16.9

Table 1: Attenuation ΔS_{11} at reflector 1 in dry condition and immersed in water and ice

Discussion

The reflection coefficients S_{11} in time-domain revealed from the experiment enable the determination of reflection peaks corresponding to either reflector gratings, substrate edges or reflections due to superpositions of those. The Love wave propagating from the IDT towards reflector 1 and back to the IDT needs about 1.8 µs. In Figure 3 (right) one can see that the immersion of the device up to reflector 1 in liquid water (fully immersed) leads to a minor attenuation of reflection peaks that only correspond to reflector gratings. Reflection peaks corresponding to substrate edges show a comparatively higher attenuation as the reflection properties of the substrate edges change due to a general surface loading. As soon as the water freezes the Love waves are damped and the peaks corresponding to reflector gratings are strongly attenuated. The attenuation of edge reflections does not change dramatically. Table 1 shows exemplarily for reflector 1 the change of attenuation ΔS_{11} which is -1.7 dB when immersed to liquid water and increases significantly to -16.9 dB when immersed to ice.

Conclusion

The discussed results demonstrate that Love waves propagating on 41°-rotated Y-cut lithium niobate with an SiO_2-waveguide layer enable the distinction between liquid- and ice-covered reflector gratings. This proves the suitability of a reflective delay line device to detect ice layer thicknesses. Ongoing investigations will be presented at the conference to show the device capability for reliable determination of ice layer thickness based on the principles industrially deployed in wireless SAW identification tags.

Acknowledgements

References
[1] M. C. Homola, P. J. Nicklasson, and P. A. Sundsbø, Cold Regions Science and Technology 46, 125 (2006).
[2] Y. Yin, W. Wang, Y. Jia, and Y. Liang, in IEEE International Ultrasonics Symposium, Glasgow, UK (2019) 2553.
[3] V. Anisimkin, V. Kolesov, A. Kuznetsova, E. Shamsutdinova, and I. Kuznetsova, Sensors 21 (2021).
[4] P. Schulmeyer, M. Weihnacht, and H. Schmidt, Sensors 24, 2292 (2024).

Transient buildup and decay of thermo-acoustic streaming

Franziska Martens[1,*], Wei Qiu[1], Ola Jakobsson[1] and Per Augustsson[1,*]

[1]Biomedical Engineering, Lund University (LTH), Sweden
[*]E-mail: franziska.martens@bme.lth.se, per.augustsson@bme.lth.se

Introduction
We recently introduced the concept of thermoacoustic streaming in microchannels wherein a thermal field is generated inside an acoustic cavity. The result is a fast and controllable streaming for which the thermal energy is provided either by an LED light source [1], or a laser [2]. While in previous works we have measured this effect at steady state, we now present measurements of the build-up and decay. We believe that the presented approach can offer the basis for particle sorting or manipulation applications.

Methods
The setup was described directed into a microchannel, that was actuated with ultrasound, and which was filled with dye and 1-µm-sized fluorescent particles. The laser light was absorbed by the dye which heats the fluid locally. The build-up and decay of the thermo-acoustic streaming was recorded at 100 frames per second while turning the laser on and off. The particles were tracked in the imaging plane using a 2D tracking method of DefocusTracker [3] to map the build-up and decay of the thermoacoustic streaming velocity field. The setup, **Fig.1a**, is centered around the acoustofluidic chip with a long channel (375 µm in width, 150 µm in height), which is actuated with a piezoelectric transducer (piezo) near 2 MHz. A half-wavelength standing wave forms across the width. Laser light (785 nm) is guided into the channel and focused near the floor to a spot size of ~50 µm to realize the thermal gradient, **Fig.1b**. To ensure absorption in the liquid, indocyanine-green dye (ICG) was added to MilliQ-filtered water. The concentration of 0.000395 mg/ml led to an absorption of ~30% of the incoming light. The streaming was registered by tracking green, fluorescent particles (1 µm), which were illuminated with an LED. The timing of the camera, laser, and ultrasound was managed using an Analog Discovery (Diligent) with its software WaveForms.
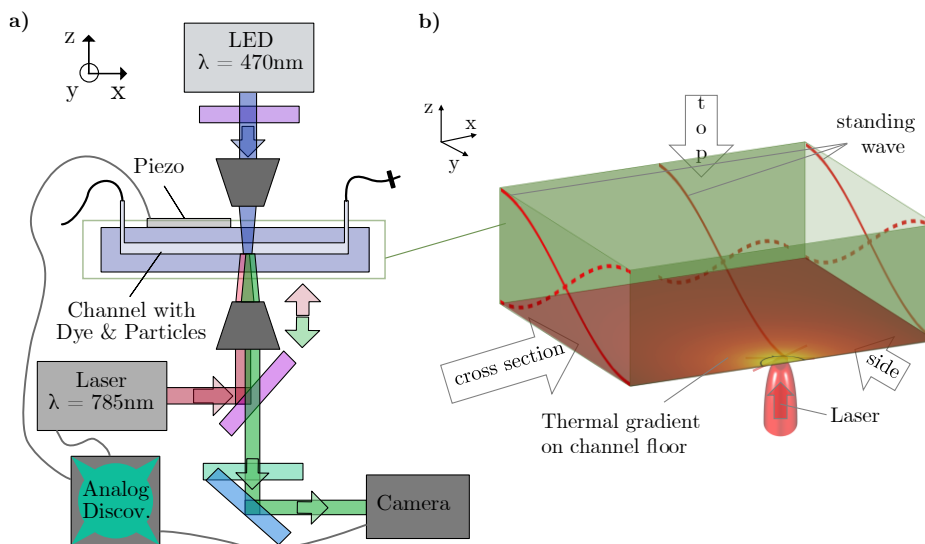

Figure 1: a) Fluorescence microscope imaging of thermoacoustic streaming. Acoustic streaming is induced with the piezo. The thermal gradient is generated by laser light absorption in solute dye molecules in the liquid. Timing of ultrasound onset, camera acquisition, and laser on/off was achieved with an analog discovery 2 (Diligent). b) The laser-induced thermal gradient is indicated on the channel floor. The ultrasound resonates between the channel's silicon and glass walls, generating a standing wave (red curves). Note the view-arrows and coordinate system for orientation.

Results and Discussion
We observed the thermoacoustic build-up and decay upon turning the laser on and off during constant actuation of ultrasound. The laser light, inducing the thermal gradient, was switched on at $\tau = 0$ ms and off at $\tau = 1500$ ms and images were acquired every 10 ms. **Figure 2** shows the resulting streaming patterns at different time points. At time zero, the streaming field is dominated by Rayleigh streaming (manual observation) but the streaming is too slow to be resolved clearly in the registered velocity field, **Fig. 2 (A)**. A thermoacoustic streaming pattern forms within 10 ms, **Fig. 2 (B)**, and the velocity increases rapidly while maintaining the same pattern, **Fig. 2 (C and D)**. After turning the laser off, the velocity decreases rapidly while maintaining essentially the same pattern, **Fig. 2 (E and F)** until reaching the steady-state velocity again, **Fig. 2 (G)**.
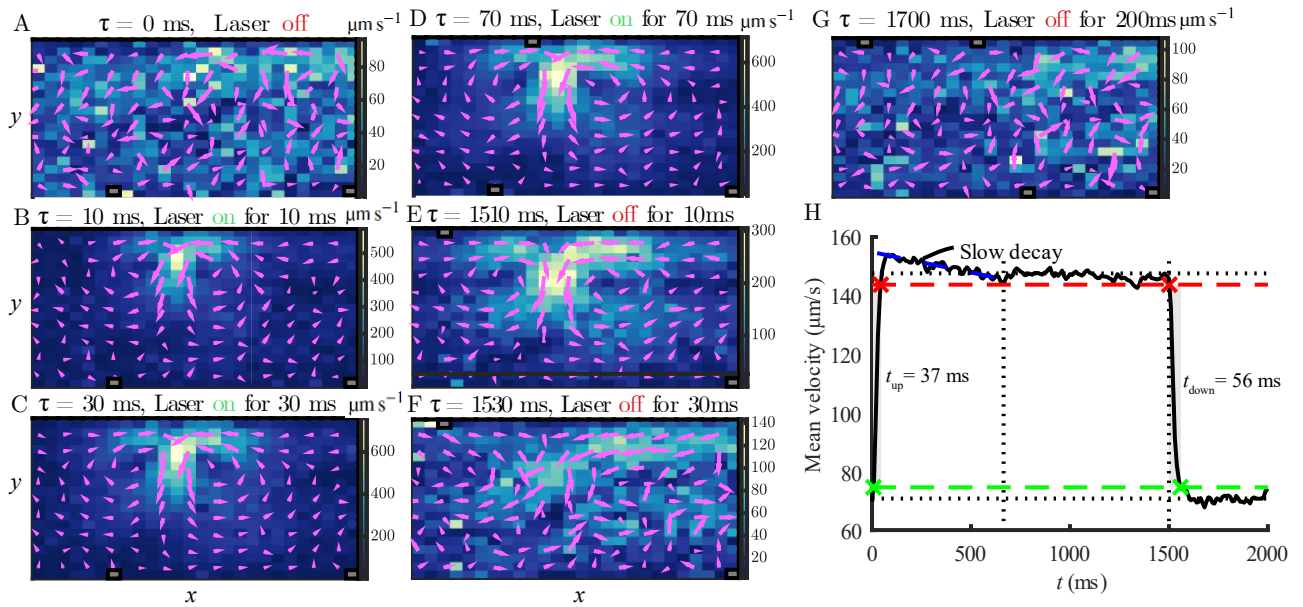
Figure 2: Build-up and decay of laser-induced thermoacoustic streaming showing the (A-D) build-up and (E-G) decay. (H) The velocity magnitude averaged over the field of view with rise time (5% to 95%) and fall time indicated with gray boxes. The blue dashed line emphasizes a slow decay after the laser onset. The red dashed line indicates where 95% of the maximum velocity is reached while the green dashed line indicates the decrease to 5% of the maximum velocity.

To analyze the build-up and decay times, we calculated the averaged velocity magnitude within the field of view and plotted as a function of time, **Fig. 2 (H)**. To estimate the build-up and decay from the averaged velocity magnitude we used the built-in MATLAB functions 'risetime.m' and 'falltime.m', respectively. The build-up time, from 5% to 95% of maximum (green and red dashed line), was 37 ms while the decay time was 56 ms. Notably, the maximum velocity is reached within the first 80 ms and thereafter the velocity decays until reaching a steady state after ~700 ms. The build-up of the streaming for a steady thermal field can be assumed to happen much faster than the build-up of the thermal field. The build-up and decay characteristics are thus primarily related to the establishment of the thermal field. The characteristic thermal diffusion time can be estimated by $t_{diff} = x^2/2\alpha$ with t_{diff}= diffusion time, x^2= diffusion length (here the distance from laser spot to farthest channel wall) and α= thermal diffusivity of water. That leaves: $t_{diff} = (375 \cdot 10^{-6}\text{m})^2/(2 \cdot 0.145 \cdot 10^{-7}\text{m}^2/\text{s}) = 0.48$ s which is close to the above-mentioned point of steady state at 700 ms. Another factor that can influence the build-up and decay is the convective flow which transports heat in the system. At 700 µm/s, this effect cannot be neglected.

Conclusion

The thermoacoustic streaming builds up and decays within ~100 ms, but it takes 700 ms to reach a complete steady state. Comparing the velocity of the two streaming effects, we showed that the velocity amplitude of thermoacoustic streaming is ~10 times higher than that of the Rayleigh streaming. Based on these results we envision a detection-response-based particle guidance mechanism: an approaching particle can quickly be moved away from the channel center to the channel wall, while a particle that is further away from the heat source will remain in its position. In the coming, we will investigate timing the pulsing of the laser light or sound field to actuate the channel for a defined amount of time, to enable this targeted particle motion.

References

1. Qiu, W., et al., *Fast Microscale Acoustic Streaming Driven by a Temperature-Gradient-Induced Nondissipative Acoustic Body Force.* Physical Review Letters, 2021. **127**(6): p. 064501.
2. Martens, F., W. Qiu, and P. Augustsson. *Thermoacoustic streaming induced by asymmetric laser heating.* in *Acoustofluidics 2022*. 2022. Glasgow, United Kingdom.
3. Barnkob, R. and M. Rossi, *DefocusTracker: A Modular Toolbox for Defocusing-based, Single-Camera, 3D Particle Tracking.* Journal of Open Research Software, 2021. **9**(1): p. 22.

Transient model of the opto-acoustophoretic effect using seperation of timescales

Jonas H. Jørgensen[1,*]

[1]Comsol A/S, Kgs. Lyngby, Denmark
*E-mail: jonasj@comsol.com

Introduction

The abstract presents a transient acoustofluidic model using separation of timescales. Separation of timescales is used to model the acoustic fields in the frequency domain and the transient fields in the time domain. Thus, allowing modelling transient behavior on a timescale much longer than the acoustic timescale. The numerical setup is used to model the opto-acoustophoretic effect observed by G. Dumy, M. Hoyos, and J.-L. Aider [1,2]. In their experiment particles are in an acoustic trap and then an LED is turned on. When the LED is turned on the particles are ejected out of the acoustic trap while stating in the nodal plane of the pressure field. The experiment of the opto-acoustophoretic effect is inherently a transient problem since the particles leave the acoustic trap when the LED is turned on. The transient numerical model captures the effects observed experimentally [1,2] of particles leaving the trap in the nodal plane.

The model is used to gain insight into the opto-acoustophoretic effect and demonstrate how a change of fluid from water to an oil or alcohol will revert the acoustic streaming mechanism responsible for the opto-acoustophoretic effect. Thus, in an oil the acoustic streaming will not eject the particles but enhance the strength of the acoustic trap. Where the particles are confined by the acoustic radiation force in the vertical direction and the acoustic streaming in the horizontal plane. Therefore, it might be possible to create an acoustic trap controlled by a spatially localized light source.

Theory and Numerical Model

The model solves two sets of equations; one in the frequency domain (the acoustic fields) and one in the time-domain (the transient fields). When using separation of timescales, it is assumed that the slow transient fields change on a timescale much longer than the fast acoustic fields. This is typically a good assumption for MHz acoustics where the acoustic timescale is t = $1/f_0$ ~ 100 ns while the timescale for the flow and thermal fields are in milliseconds. Thus, the transient fields can be assumed to be steady for the acoustic equations. The acoustic field in the fluid is solved with pressure acoustics and the vibrations in the surrounding solid are represented by a displacement field.

The transient fields are a flow in the fluid (acoustic streaming), a temperature field in both the fluid and the solid, and a concentration field for the particles in the fluid. The fluid flow is dominated by thermoacoustic streaming, which depends on both the acoustic field and the transient temperature field, T. The force term $\boldsymbol{f}_{\text{ac}}$ responsible for the streaming in the fluid domain is given as [3],

$$\boldsymbol{f}_{\text{ac}} = \frac{1}{4}|\boldsymbol{v_1}|^2\boldsymbol{\nabla}\rho_0(T) + \frac{1}{4}|p_1|^2\boldsymbol{\nabla}\kappa_s(T).$$

The force depends on the acoustic pressure p_1 and velocity $\boldsymbol{v}_1$ and the gradients in density ρ_0 and compressibility κ_s. Since the material parameters depend on temperature this corresponds to a dependency on the temperature gradient in the fluid. The temperature field is induced by absorption of light by the particles. The heat source is modelled by the power of the LED and the concentration of particles c. The concentration of particles c is controlled by three terms, convection by acoustic streaming $\boldsymbol{u}$, the acoustic radiation force $\boldsymbol{F}_{\text{arf}}$, and diffusion, with the diffusion constant D,

$$\partial_t c + \boldsymbol{\nabla} \cdot (-D\boldsymbol{\nabla}c + c\mu\boldsymbol{F}_{\text{arf}}) + \boldsymbol{u} \cdot \boldsymbol{\nabla}c = 0.$$

The implementation of the acoustic radiation force follows the implementation by Ley and Bruus [4]. The particles are modelled as a concentration field to make it easier to couple them to the heat source.

The numerical model is made as a 2D axisymmetric simulation representing a thin cylindrical fluid domain in an aluminum chip with a glass lid, see figure 1. The system is actuated from below at the green boundary, representing a piezoelectric transducer. The fluid domain has height H_{fl} = 800 μm and radius R_{fl} = 10 mm. The light source is turned on after 1 second.
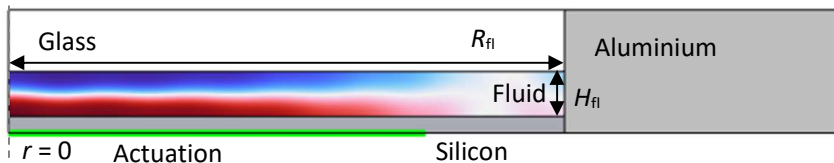

Figure 1: The 2D axisymmetric model geometry. With a fluid on a silicon wafer with a glass lid. The acoustic pressure in the fluid is shown at 942 kHz.

Results and Discussion

In figure 1 the acoustic pressure is shown for the light source turned off. The acoustic field is actuated at the half wavelength resonance which will focus the particles (polystyrene particles with 10μm diameter) in the nodal plane. The light source causes a temperature increase of 0.2 K, so it does not alter the mode of the acoustic pressure, although it can change the acoustic energy density. First, we use water as the fluid as in reference [1,2]. In figure 2 the transient fields (concentration, acoustic streaming, and temperature) are shown at three timesteps showing the effect of turning on the light source. The light source is turned on at t = 1s, after which fast thermoacoustic streaming is induced. The acoustic streaming drags the particles away from the center (r = 0) while staying in the nodal plane. The particles stay in the nodal plane because of the acoustic radiation force. Lastly at t = 10 s the particles have been dragged away from the center which reduces the heat source and thereby the velocity of the acoustic streaming. The magnitude of the thermoacoustic streaming velocity at the given temperature increase and acoustic energy density is consistent with the experiments and modelling results by W. Qiu et al [5], although for a different device.
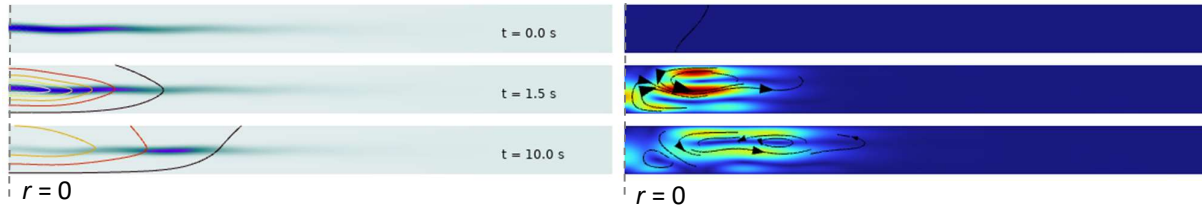
Figure 2: Left: Concentration (from white to blue) and temperature (contour lines from 0 mK to 220 mK) of the simulation with water as the fluid. Right: Velocity magnitude from 0 μm/s (blue) to 320 μm/s (red) and streamlines. The concentration and velocity are shown at three timesteps t = 0, 1.5, and 10 s. The LED light is turned on at t = 1 s.

As the temperature dependency of the material parameters determines the direction of the acoustic streaming, changing the fluid from water to oil will reverse the acoustic streaming. Since the sound speed of oil decrease with increasing temperature. This gives the opportunity to use the opto-acoustophoretic effect to create an acoustic trap. For this purpose, the light is absorbed in the oil instead of by the particles, this corresponds to adding a dye to the oil. Thus, the heat source does not depend on the concentration of the particles. Secondly the size of the acoustic trap is determined by the width of the light source, here a radius of 1.5 mm is used.

For modelling the acoustic trap in oil (rapeseed oil) a transient model is not necessary since the trap is stationary. In figure 3 the concentration, temperature and acoustic streaming is shown for an acoustic energy density of 136 J/m^3 and a maximum temperature increase of 35 mK. The particles are trapped vertically by the acoustic radiation force and horizontally by the drag force from the acoustic streaming. The trap should be able to withstand a flow in the order of the acoustic streaming velocity of 0.2 mm/s. The transient solver can be used to model turning the light source on or off and moving the acoustic trap by moving the light source (this requires a 3D simulation which hopefully can be shown at the conference).
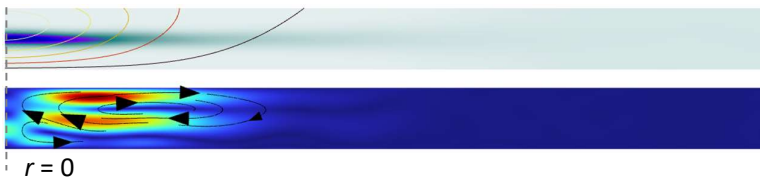

Figure 3: Top: Concentration (from white to blue) and temperature (contour lines from 0 mK to 35 mK) of the simulation with oil as the fluid. Bottom: velocity magnitude from 0 mm/s (blue) to 0.25 mm/s (red) and streamlines.

Conclusion

The separation of timescales allows for numerical modelling of transient acoustofluidic systems without temporally resolving the acoustic timescale. The opto-acoustophoretic effect is investigated and the ejection of particles from the acoustic trap in the nodal plane is observed in agreement with the experiments in [1,2]. The possibility of using the opto-acoustophoretic effect to induce an acoustic trap in an oil that is controlled by a light source is demonstrated. In the acoustic trap the particles are confined vertically by the acoustic radiation force and horizontally by the acoustic streaming.

References

[1] G. Dumy, M. Hoyos, and J.-L. Aider, *Observation of selective optical manipulation of particles in acoustic levitation.* J. Acoust. Soc. Am. 146(6), 4557-4568 (2019)

[2] G. Dumy, M. Hoyos, and J.-L. Aider, *Influence of the temperature on the opto-acoustophoretic effect.* J. Acoust. Soc. Am. 149(1), 556-568 (2021)

[3] J. H. Joergensen and H. Bruus, *Theory of pressure acoustics with thermoviscous boundary layers and streaming in elastic cavities.* J. Acoust. Soc. Am. 149, 3599-3610 (2021).

[4] M.W.H. Ley and H. Bruus, *Continuum modeling of hydrodynamic particle-particle interactions in microfluidic high-concentration suspensions.* Lab Chip 16, 1178-1188 (2016).

[5] W. Qiu, J. H. Joergensen, E. Corato, H. Bruus, and P. Augustsson, *Fast microscale acoustic streaming driven by a temperature-gradient-induced non-dissipative acoustic body force.* Phys. Rev. Lett., 127, 064501 1-6 (2021).

Two-step acoustofluidic cancer cell enrichment

Cecilia Magnusson[1], Mahdi Rezayati Charan[2], and Per Augustsson[2*]

[1]Department of Clinical Chemistry, Lund University, Sweden
[2]Department of Biomedical Engineering, Lund University, Sweden
[*]E-mail: per.augustsson@bme.lth.se

Introduction

We have previously proposed and evaluated acoustophoresis for the enrichment of circulating tumor cells (CTC) and clusters thereof from the blood of patients with prostate cancer [1]. In that protocol, the cells were fixed and preserved in paraformaldehyde before processing and were thus non-viable. To enable future enrichment of also *viable* CTCs from patients, we have in this study investigated the ability to discriminate cancer cell line cells from sub-groups of viable white blood cells (WBC). We found that acoustophoresis alone has poorer performance for viable cells than for fixed cells. Therefore, we added a second step of acoustic gradient separation wherein cells migrate into a medium of increasing acoustic impedance. The resulting separation results in >80% of cancer cells reaching the target outlet while 99.8% of all WBCs are removed.

Background

CTCs are shed into the blood from primary tumors or metastatic lesions. It is well established that high circulating tumor cell counts are associated with poor outcomes and lower survival in metastatic cancers [2]. The FDA-approved CellSearch assay, considered the gold standard to enumerate CTCs, relies on magnetic bead antibody capture. However, it cannot detect cells with low expression of the surface molecule EpCAM. Thus, there's a critical need for alternative approaches to isolate circulating tumor cells. Apart from the enumeration of CTCs to monitor disease progression, there is an interest among cancer biologists to recover viable CTCs from patients to elucidate the underlying mechanisms of metastasis. To achieve this, we have investigated the possibility of using a two-step sequence of acoustic separations.

Experiments

We collected blood from healthy donors, and red blood cells (RBC) were chemically lysed resulting in a population of WBCs. Samples were constructed by mixing cultured cancer cells with WBCs. Cells were either paraformaldehyde-fixed or non-fixed (viable). Two modules for acoustic separation were employed sequentially. **Figure 1(A)** illustrates step 1, which is based on the notion that cancer cells migrate faster than WBCs when exposed to sound [3-5], predominantly due to their larger size. In step 2, the cells from the central outlet, were resuspended in a new medium and subjected to iso-acoustic focusing, wherein cells of low effective acoustic impedance are blocked from entering the central part of the flow, **Fig. 1(B)**.
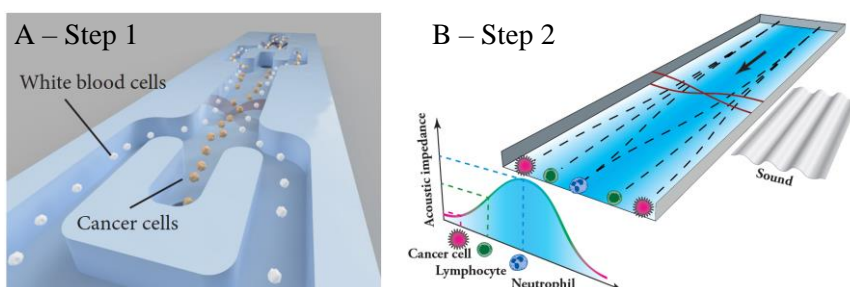

Figure 1: Separation modules. (A) In step 1 cancer cells are separated by their mobility in a saline solution by conventional acoustophoresis. (B) In step 2, contaminating WBCs of high effective acoustic impedance are removed by iso-acoustic focusing.

Results and Discussion

First, we investigated the cancer cell separation efficiency for MCF7 breast cancer cells in step 1 for fixed and viable cells. The central fraction contains ~80% of all recovered cancer cells for both cases, while the contaminating WBCs in the central fraction increase dramatically for non-fixed samples, **Fig 2(A)**. Looking at WBC sub-groups, we found that the main contamination is granulocytes, **Fig. 2(B)**. Granulocytes are in general smaller than MCF7 cells, but their density is considerably higher. Therefore, a large fraction of these cells have acoustic mobilities that overlap with the cancer cells. Flow cytometry analysis (not shown here) indicates that the fixation protocol makes the WBCs smaller and more uniform in size, while MCF7 cells are seemingly unaffected by fixation, and this can explain why separation efficiency is higher for fixed cells.
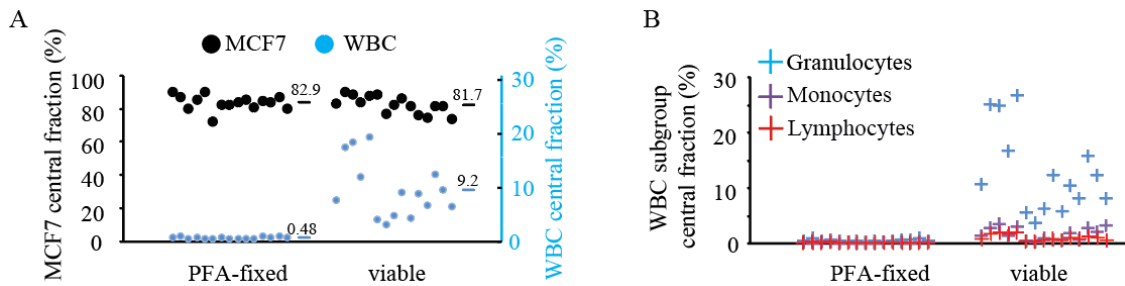
Figure 2: Step 1 acoustophoretic separation of MCF7 cancer cells from WBCs for fixed vs non-fixed (viable) cells. (A) Central fraction of cells comparing MCF7 cells and total WBCs. (B) Contaminating WBC subgroups in central fraction.

To remove the contaminating granulocytes, we ran cells through iso-acoustic focusing with the idea that granulocytes could penetrate further into an acoustic impedance gradient compared to cancer cells [6]. **Figure 3(A)** shows the fraction of MCF7 cancer cells that reach the target side outlet and the corresponding fraction of granulocytes that reach the central outlet when the acoustic impedance of the central flow stream is increased by increasing the concentration of the solute molecule iodixanol. For 16% iodixanol, the barrier blocks nearly all MCF7 cells while ~97% of the granulocytes penetrate the barrier and reach the central outlet.
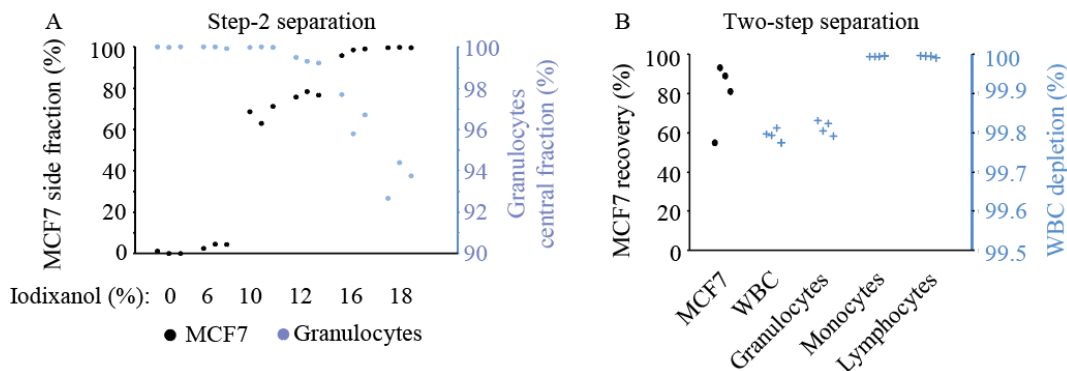
Figure 3: (A) The fraction of MCF7 cells that are blocked by the acoustic impedance barrier and end up in the side outlet and the corresponding fraction of granulocytes that penetrate the barrier and end up in the central outlet, for increasing iodixanol concentration in the central medium. (B) The final recovery (output vs input) of MCF7 cells after the two-step separation and the corresponding depletion of WBCs, by subgroup.

We then constructed samples of 500 µL containing 5×10^5 WBCs and $2 \cdot 10^4$ MCF7 cells and ran them through the two-step separation procedure. When comparing the output to the input, we measured a mean recovery of ~80% and a WBC depletion of 99.8% which is on par with the one-step procedure for fixed cells, **Fig. 3(B)**.

Conclusions
With this work, we demonstrate that multistep acoustic separation of cells presents opportunities to isolate rare cells with high recovery and selectivity based on a panel of biomechanical properties.

References
1. Magnusson, C., et al., *Acoustic enrichment of heterogenous circulating tumor cells and clusters from patients with metastatic prostate cancer.* 2023: [Pre-print] https://shorturl.at/jkt45.
2. Cristofanilli, M., et al., *Circulating tumor cells, disease progression, and survival in metastatic breast cancer.* New England Journal of Medicine, 2004. **351**(8): p. 781-791.
3. Li, P., et al., *Acoustic separation of circulating tumor cells.* Proceedings of the National Academy of Sciences of the United States of America, 2015. **112**(16): p. 4970-4975.
4. Magnusson, C., et al., *Clinical-Scale Cell-Surface-Marker Independent Acoustic Microfluidic Enrichment of Tumor Cells from Blood.* Analytical Chemistry, 2017. **89**(22): p. 11954-11961.
5. Zhang, Y., et al., *Label-Free Separation of Circulating Tumor Cells and Clusters by Alternating Frequency Acoustic Field in a Microfluidic Chip.* International Journal of Molecular Sciences, 2023. **24**(4): p. 3338.
6. Augustsson, P., et al., *Iso-acoustic focusing of cells for size-insensitive acousto-mechanical phenotyping.* Nature Communications, 2016. **7**(1): p. 11556.

Ultrasonic atomization in a superhydrophobic microchannel's plastron.

Maxime Fauconnier[1, *], Bhuvaneshwari Karunakaran[2], Alex Drago-González[1], Laura Fieber[2], William S. Y. Wong[2], Robin H. A. Ras[2] and Heikki J. Nieminen[1]

[1]Department of Neuroscience and Biomedical Engineering, Aalto University, Espoo, Finland
[2]Department of Applied Physics, Aalto University, Espoo, Finland
[*]E-mail: maxime.fauconnier@aalto.fi

Introduction

By minimizing water contact, superhydrophobicity unlocks an underwater world of possibilities, enhancing for instance marine equipment lifespan and operational efficiency. This is made possible by texturing an object's surface with hydrophobic nano- and microstructures. Underwater, this nature-inspired topography prevents liquid entry and impalement, thanks to an air layer forming between the water and the solid phases [1]. In use, this composite layer, commonly called plastron, can be challenged by thermo-hydrodynamic stimuli and, in the absence of prevention means, is likely to collapse. This typically happens via the widely reported mechanisms of sagging and sliding of the plastron interface [2], induced by static pressures. While all theoretical models disregard driving alternating pressures, we report here on a new wetting mechanism induced by acoustofluidics and the formation of intra-plastronic aerosols (*i.e.*, droplets in suspension).

The ultrasound (US) atomization of a gas-liquid interface into aerosols typically results from the capillary instability of the water phase animated by high amplitude ripples oscillating at half the driving frequency f_{ac} [3]. The diameter d of the so-produced droplets can be predicted by Lang's equation [4], as $d = 0.34 \, \lambda_c$, where $\lambda_c = (8\pi\sigma/f_{ac}^2\rho)^{1/3}$ is the capillary wavelength, σ and ρ are the surface tension and the density of the liquid. Simultaneously to the droplets' ejection, the second-order acoustic forces can impose a net displacement of the air-water interface, in a similar fashion to an acoustic fountain [5]. Together, these phenomena can contribute to hasten the wetting of a superhydrophobic surface (SHS), as this work demonstrates, by lowering the well-established critical impalement pressure, *i.e.*, the minimum static pressure required for triggering its wetting.

Experimental procedure

With the means of soft lithography and fluoro-coating, a microchannel with given height h (100 µm), length (1 cm) and width w (25, 50, 75, 100, 125 µm) is manufactured of polydimethylsiloxane (PDMS) and rendered superhydrophobic. Underwater, the side-view imaging (10× optical magnification) of its plastron, while being actuated by a focused 2.5 MHz US pulse (duration 20 µs), turns into picture the generation of intra-plastronic aerosols (*i.e.*, droplets sizing < 10 µm in suspension in air). Their motion and rate of deposition is analyzed by particle tracking velocimetry (PTV) of the bright field images captured at 250 000 frames per second.

Results and Discussion

Figure 1a provides high-speed images of the response of a channel's plastron (w = 75 µm) to an US pulse actuation (time-averaged acoustic intensity = 0.23 kW/m^2). At the same time that the air-water interface of the plastron is pushed down by the acoustic force, droplets are forming and ejected from the interface into the plastron, as shown in Figure 1a. The result of the PTV analysis (not shown) indicates that their ejection speed can reach up to 4 m/s and that the quantity of produced aerosols grows exponentially with the acoustic amplitude.
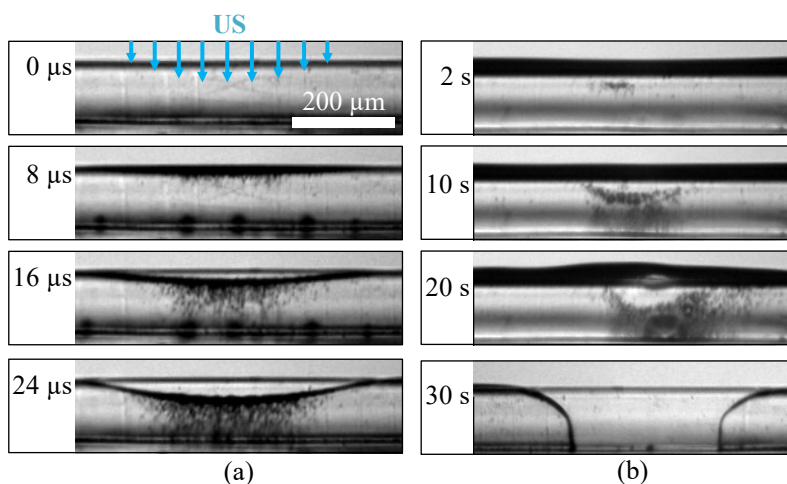

(a)   (b)

Figure 1: Experimental snapshot series showing (a) the generation of aerosols within the plastron of a microchannel, following the actuation of its air-water interface, and (b) the accumulation of droplets attached to the channel's walls, following a similar US actuation repeated with a pulse repetition frequency of 300 Hz. Without changing the acoustic parameters, the collapse eventually occurs after 30 seconds, at a pressure magnitude that was initially not sufficient to trigger the wetting.

Due to the important difference in density between the air and the water aerosols, the Stokes number of these flowing droplets is much greater than 1, meaning that they do not follow the air flow with closeness and fidelity [6]. Instead, they are rather driven by inertia and hence are likely to impact the microchannel walls (*i.e.*, dry deposition). This is confirmed by the presence of many of them, staying still on the walls after the air-water interface has returned to its equilibrium state. Long after US exposure, these drops evaporate into the plastron.

By repeatedly actuating the plastron with a pulse repetition frequency of 300 Hz, the droplets accumulate faster on the channel walls than they evaporate, while allowing the air-water interface to regain its initial state between two actuations. Over time, this favors the droplets coalescence into larger drops, which later move down to the channel bottom, as illustrated in Figure 1b. Eventually, the channel saturates with drops and collapses at a second-order acoustic pressure that was not able to generate the collapse initially, nor was predicted by existing theoretical models [2,7]. In a similar way as reported by Garcia-Gonzalez et al. for the case of condensate droplets [8], the presence of these drops can facilitate impalement, *via* their coalescence with the penetrating air-water interface of the plastron.

By systematically studying this as a function of the channel's width and height, and the acoustic intensity, we evidence the predisposition of certain geometries to undergo that wetting mechanism. An optimal configuration, less prone to this, is eventually proposed, which will hopefully provide insights for the development of ever more robust SHSs.

Conclusion

Describing the dynamics of the wetting transition deepens the fundamental understanding of superhydrophobicity, promoting the development of ever more robust water-repellent materials [9]. This study shows that acoustofluidics can decrease the critical impalement pressure of a SHS and hence weaken its resistance against wetting, *via* the accumulation of US-induced aerosols inside the plastron. It evidences the importance and necessity to consider this wetting mechanism, in addition to the known sagging and sliding regimes, when designing the SHS and the geometry of its microstructures.

Acknowledgements

References

[1] K. Manoharan et al., *J. Micromanufacturing* **2** (1), pp. 59–78 (2019), https://doi.org/10.1177/2516598419836345.
[2] D. Bartolo et al., *Europhys. Lett.* 74 (2), pp. 299–305 (2006), https://doi.org/10.1209/epl/i2005-10522-3.
[3] W. Eisenmenger, *Acustica* **9** (4), pp. 327–340 (1959), no assigned DOI.
[4] R. J. Lang, *J. Acoust. Soc. Am.* 34 (1), pp. 6–8 (1962), https://doi.org/10.1121/1.1909020.
[5] G. Kim et al., *J. Fluid Mech.* **909**, R2 (2021), https://doi.org/10.1017/jfm.2020.1012.
[6] C. Tropea et al., *Springer handbook of Experimental Fluid Mechanics* (Springer Berlin, 2007),
https://doi.org/10.1007/978-3-540-30299-5.
[7] H.-J. Butt et al., Soft Matter 9, pp. 418–428 (2012), https://doi.org/10.1039/C2SM27016A.
[8] D. Garcia-Gonzalez et al., Langmuir 38, pp. 14666–14672 (2022), https://doi.org/10.1021/acs.langmuir.2c02095.
[9] P. Papadopoulos et al., *PNAS* **110** (9), pp. 3254–3258 (2013), https://doi.org/10.1073/pnas.1218673110.

Volumetric temperature measurement in a micro channel subjected by a standing surface acoustic wave

Jörg König[*] and Christian Cierpka

Institute of Thermodynamics and Fluid Mechanics, Technische Universität Ilmenau, Ilmenau, Germany
[*]E-mail: Joerg.Koenig@tu-ilmenau.de

Introduction

The acoustic manipulation of biological samples has gained tremendous interest in biology and medical research, since it provides a precise, contactless and label-free manipulation of particles and cells in a biocompatible manner [1]. However, while systems based on bulk acoustic waves (BAW) with a high quality factor produce very little heat, excessive heating can be induced in acoustofluidic devices with high frequencies and acoustically lossy materials like polymers [1,2]. The latter applies particularly to systems based on surface acoustic waves (SAW), using frequencies above 10 MHz and Polydimethylsiloxane (PDMS) as channel material usually. In this case, the PDMS absorbs most of the acoustic energy [3,4] causing a significant temperature rise of the side walls [5]. Nevertheless, also the temperature of the fluid rises depending on the acoustic power applied [2,4], channel size and material used [2,6]. Temperatures up to 55°C evolving in a stagnant fluid of small volume within a few seconds have been reported in acoustic tweezers using standing surface acoustic waves (sSAW) [2,4]. This may compromise the biocompatibility of those devices. However, regarding the acoustic separation of particles flow through systems are considered mostly [7]. In that case, the constant fluid flow removes the heat and the cells are subjected to the acoustic field only for a short moment. In order to gain experimental insights into the acoustothermal heating in an acoustic tweezer device intended for particle separation, the three-dimensional temperature distribution of the fluid induced by a one-dimensional sSAW was measured. Again, a significant temperature rise to 55°C was observed. In contrast to a stagnant fluid where maximum temperature was found close to the top of the chamber [4,6], the maximum temperature was measured close to the substrate surface indicating that the piezoelectric substrate is an important source of heat.

Experimental methods

Investigations were performed in an acoustic tweezer based on a one-dimensional sSAW excited by two opposing interdigital transducers (IDTs) deposited on a 128° rotated Y-cut lithium niobate substrate (LiNbO$_3$), see figure 1(a). The SAW-wavelength was about 20 µm and the aperture AP of the IDTs was 2 mm. In between both IDTs, a straight micro channel made of PDMS with a cross-section of 500 µm × 500 µm was positioned.
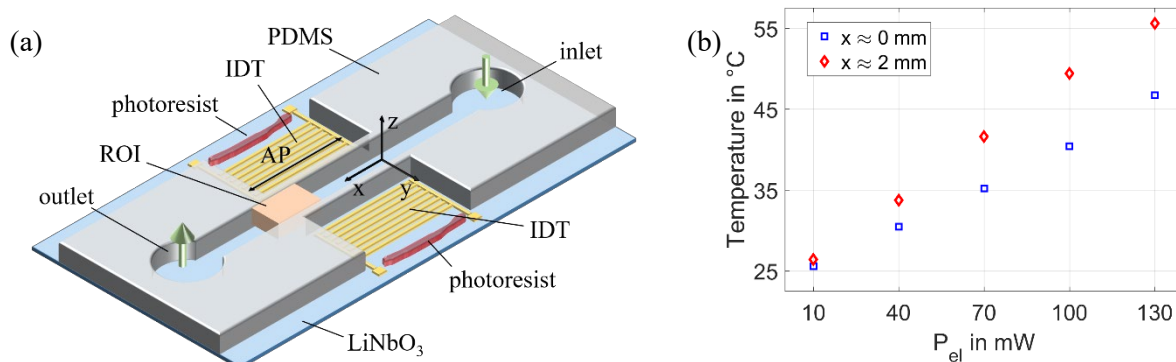

Figure 1: (a) Schematic of the acoustofluidic device used and (b) measured temperature at the beginning of the sSAW (x = 0) and at the end of the sSAW ($x \approx 2$ mm). The latter position coincide with the ROI depicted in (a).

A water-glycerol solution with a density of 1170 kg/m³ was pumped through the micro channel with a constant flow rate of 10 µl/min. To measure the three-dimensional temperature distribution of the fluid inside the micro channel, a combination of astigmatism particle tracking velocimetry (APTV) and luminescence lifetime imaging was utilized [4,8]. This requires the determination of the shape of elliptically distorted particle images according to the principle of APTV, while estimating the decay time of the luminescent light emission from the particles at the same time. As temperature sensors, particles made of polymethylmethacrylate (PMMA) with a diameter of 10 µm were used that contained the temperature sensitive phosphorescent dye europium (III) thenoyltrifluoroacetonate (Eutta, 360/615 nm, Surflay Nanotec GmbH). Details regarding the optical setup of the measurement system can be found in Weser et al. and Deng et al. [4,8]. Since the particle size coincided with the distance between the pressure nodes of the sSAW and density of the fluid was adapted to the density of the temperature sensors (ρ_p = 1118 kg/m³) to avoid strong sedimentation of the PMMA particles, temperature measurements were possible across the entire cross-section of the micro channel. However, the

height of the measurement volume amounted to approx. 110 μm only. Therefore, the measurement volume was traversed through the micro channel with a step size in between of about $\Delta z = 55$ μm, yielding a volumetric ROI of about $700 \times 500 \times 500$ μm³ located at the end of the IDT at $x = 2$ mm. At each height position, 750 double frame images were taken with a frame rate of 10 Hz. During the measurements, the electrical power applied as well as the flow rate were kept constant. In addition, excitation of the sSAW started five minutes before the measurements. Measurements were done for different electric power level applied ranging from $P_{el} = 10$ mW to 130 mW at maximum. In addition to the measurement at the ROI, measurements were done also at the beginning of the sSAW, i.e. at $x = 0$. In this way, the local temperature increase within the aperture of the IDTs dependent on the power applied could be assessed.

Results and Discussion
In figure 1(b), the measured temperature at the beginning of the sSAW at $x = 0$ and at the end of the sSAW at $x = 2$ mm is depicted. As expected, temperature increases linearly with the acoustic power P_{el} applied. While a temperature slightly above room temperature was measured at an electric power of 10 mW, up to 55°C was obtained for an electric power of 130 mW. Therefore, even in a flow through system and at moderate electric power, a temperature level exists that may cause irreversible damage of biological samples. In addition, a significant temperature difference occurred within the short distance of 2 mm given by the aperture of the IDT, which confirms the rapid temperature rise obtained in SAW-based systems [4]. Interestingly, the closer to the substrate surface the higher the temperature, indicating that the piezoelectric substrate may one source of heat due to electromechanical losses. According to the temperature field at $x = 1550$ μm depicted in figure 2(a), maximum temperature occurs close to the center of the micro channel where maximum surface displacement of the sSAW is expected. In addition, warm fluid raise from the bottom to the top of the micro channel, which is in accordance with a strong vortex evolving close to the end of the sSAW at $x = 2$ mm [9]. Beyond the sSAW the fluid temperature drops rapidly.
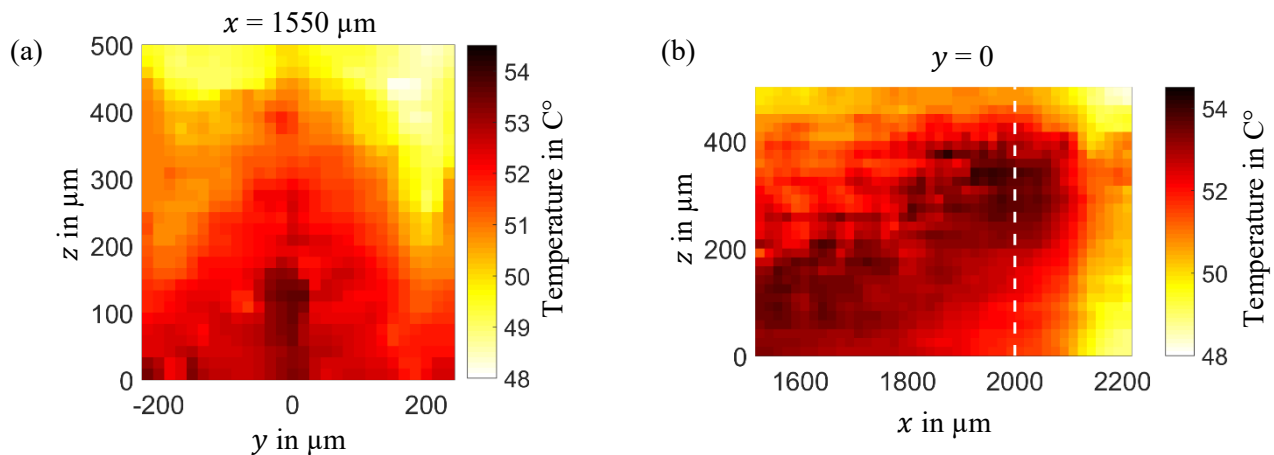

Figure 2: Temperature distribution measured within the ROI close to the end of the sSAW. (a) Temperature field in the cross-section of the micro channel at $x = 1550$ μm and (b) along the micro channel at central position $y = 0$. The white dashed line marks the end of the IDT and, therefore, indicates the end of the sSAW.

Conclusion
The three-dimensional temperature distribution of the fluid in an acoustofluidic device consisting of a straight micro channel and a one-dimensional sSAW was measured. A significant temperature rise was observed, while the temperature distribution inside the channel obviously correlates to the amplitude of the sSAW. During the conference, further results regarding the influence of the SAW-wavelength and the correlation with the fluid flow induced by the acoustic streaming effect will be discussed in detail.

Acknowledgements

References
[1] J. Rufo, F. Cai, J. Friend, M. Wiklund, T.J. Huang, *Nat Rev Methods Primers*, **2**, 30 (2022)
[2] M. Cui, M. Kim, P.B. Weisensee, J.M. Meacham, *Lab Chip*, **21**, 2534-2543 (2021)
[3] F. Kiebert, S. Wege, J. Massing, J. König, C. Cierpka, R. Weser, H. Schmidt, *Lab Chip*, **17**, 2104-2114 (2017)
[4] R. Weser, Z. Deng, V. Kondalkar, A. Darinskii, C. Cierpka, H. Schmidt, J. König, *Lab Chip*, **22**, 2886-2901 (2022)
[5] B. Ha, K. Lee, G. Destgeer, J. Park, J.S. Choung, J.H. Jung, J.H. Shin, H.J.Sung, *Scientific Reports*, **5**, 11851 (2015)
[6] P.K. Das, A.D. Snider, V.R. Bhethanabotla, *Phys. Fluids*, **31**, 106106 (2019)
[7] M. Wu, A. Ozcelik, J. Rufo, Z. Wang, R. Fang, T.J. Huang, *Microsyst Nanoeng*, **5**, 32 (2019)
[8] Z. Deng, J. König, C. Cierpka, *Meas Sci Technol*, **33**, 115301 (2022)
[9] S. Sachs, C. Cierpka, J. König, *Lab Chip*, **22**, 2028-2040 (2022)

Micro-manipulation of miscible fluids with acoustic tweezers

Samir Almohamad[1], Gustav K. Modler[2], Ravinder Chutani[1], Udita U. Ghosh[1], Sarah Cleve[1,*], Henrik Bruus[2], Michael Baudoin[1,3]

[1] Univ. Lille, CNRS, Centrale Lille, Univ. Polytechnique Hauts-de-France, UMR 8520 - IEMN, Lille, France
[2] Department of Physics, Technical University of Denmark, Kongens Lyngby, Denmark
[3] Institut Universitaire de France, Paris, France
[*]E-mail: sarah.cleve@univ-lille.fr

Introduction

The precise control of objects with acoustic fields or forces has been exploited in various works in the past decades due to its great potential for micro-manipulation in *in-vivo* and *in-vitro* applications. Among the different techniques, acoustic tweezers generating acoustic vortices are a particularly promising tool as they allow selective control of individual objects such as particles [1], cells [2] and even kidney-stones [3]. In the past, acoustic fields (not limited to tweezers) have also been used to manipulate immiscible drops [4] and, furthermore, even miscible fluids could be manipulated experimentally in a standing acoustic wave, with the higher-impedance liquid migrating towards the acoustic pressure node [5]. More recently, Karlsen and Bruus [6] have numerically explored the potential of using the radiation force generated by acoustic tweezers to manipulate such miscible fluids. In the present work, we experimentally demonstrate the application of ultrasonic acoustic tweezers to pattern, trap, and displace a higher-impedance liquid (Ficoll) in a lower-impedance liquid (water). Furthermore, we extend the numerical model presented in [5] to take into account the precise physical properties of our experimental system. This allows us to quantify characteristic times of the trapping and patterning process, both experimentally and numerically, and to evaluate the impact of diffusion on the trapping efficiency.

Experimental setup and procedure

The experimental setup, Fig. 1(A), consists of a PDMS microchannel (height 40 µm, width 1500 µm, bonded to a 130 µm thin glass slide) in which we create a band of Ficoll solution (15% Ficoll-PM400 of which 0.75% fluorescent Ficoll in water) between two bands of water by the means of co-flow. We stop the flow just before starting the experiments so that the initial conditions are three parallel liquid bands at rest (as visible in Fig. 2(BI)). The microchannel is placed on an acoustic vortex tweezer of topological charge $l = 1$, which is made of two spiraling electrodes sputtered on a 0.5 mm lithium niobate piezoelectric wafer and covered by a 6.5 mm thick borosilicate glass wafer. For the experiments, the tweezer is excited at its design frequency of 18 MHz, which yields a circular acoustic field in the microchannel, see Fig. 1(B). Once the tweezer is turned on, the higher impedance Ficoll solution is trapped at the pressure minima, in particular at the center of the vortex, thus forming a pattern of concentric rings, see Fig. 2(B). The ensemble of tweezer and microchannel is mounted on an optical microscope (Nikon Ti2E) and the pattering is recorded using a camera (Prime-BSI) at a frame rate of 12.5 fps. During the post-processing the initial gray-scale images are translated into concentration values and the concentration difference between the center of the pattern and the first ring is evaluated, see Fig. 2(A).
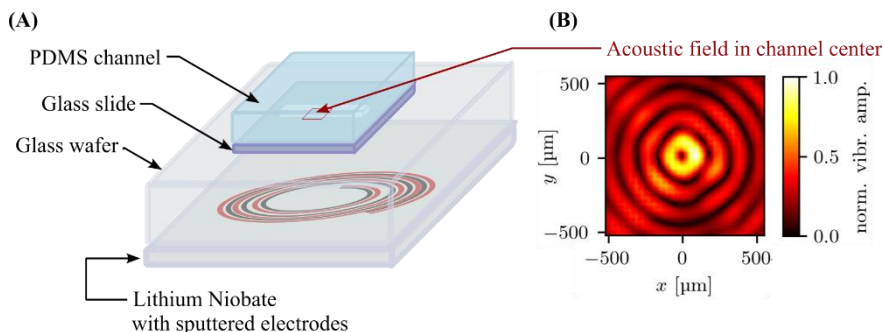

Figure 1: (A) Schematics of the experimental approach: a PDMS channel is bonded to a glass slide and then placed on a tweezer (consisting of a Lithium Niobate wafer with sputtered electrodes to which is glued a glass wafer). The acoustic waves are designed to focus inside the PDMS channel, (B) shows the resulting acoustic field. See Fig. 2 for the liquid distribution inside the channel.

Numerical model and procedure

A numerical model is formulated based on the theory by Karlsen and Bruus [6,7], in which an acoustic field acting on a short time scale gives rise to acoustic body forces acting on a slow time scale. The computational domain consists of a half-circle around the center of the tweezer, thus exploiting axial symmetry and the fact that a 2D model (previously validated by comparison to 3D simulations) can be formulated in terms of average height. Simulations are conducted using a weak-form finite-element scheme in COMSOL Multiphysics 6.1. The initial conditions implemented in the simulations are those of the experiments in terms of initial

concentration profile and physical properties of the two liquid phases. For the purpose of simplicity, the experimental acoustic (vibrational) field is approximated by a Bessel function in the numerical simulations.

Results and discussion

In the present study, we demonstrate the experimental feasibility of trapping the higher-impedance Ficoll solution within the lower-impedance water phase. Selected snapshots of the temporal evolution of the patterning process are shown in Fig. 2(B). Acoustic forces gradually shape the pattern, however, after some time the effect of diffusion becomes obvious. The corresponding simulations, Fig. 2(C), show a nearly perfect agreement with the experiments. To better understand the patterning process, we evaluate the Ficoll concentration in the center and the first ring of the pattern as a function of time. The difference between these two values is plotted in Fig. 2(A) and shows a characteristic maximum at 1.4 s. Repeated experiments and simulations at different vibrational amplitudes show that this characteristic time is inversely proportional to the vibrational amplitude. Furthermore, a more detailed study of the concentration over time curves (and its discrepancy between experiments and simulations), allows us to understand the role of diffusion and some 3D effects on the patterning process, highlighting the limits of trapping miscible liquids. Nevertheless, the acoustic forces are strong enough to efficiently pattern the two liquids and even, once trapped in the center of the tweezer, move the Ficoll solution inside the water phase.
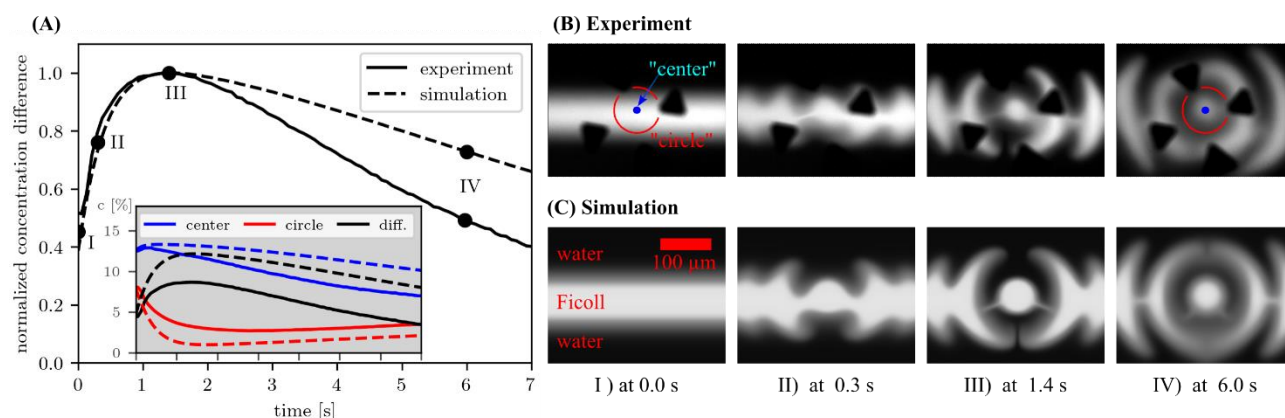

Figure 2: (A) Evolution of the normalized concentration difference between the center of the tweezer and the first ring. The inlet shows the evolution of the absolute concentration values in % over the same time. The discrepancies between experiments and simulations will be discussed in detail at the Acoustofluidics conference. (B) Experimental evolution of the two phases, water (black) and Ficoll solution (white), when turning on the tweezer. (C) The same for the numerical simulations. The snapshots are also referenced in panel (A), the time $t = 1.4s$ (III) corresponds to the moment of maximum concentration difference.

Conclusion

In the present work, we experimentally demonstrate the feasibility of trapping, patterning and moving a high-impedance liquid inside a lower-impedance one. Detailed comparison to numerical simulations allows to confirm a linear dependence between the characteristic patterning time and the vibration amplitude. It furthermore helps to understand the effects of e.g. diffusion on the trapping and patterning processes.

Acknowledgements

References

[1] Baudoin, M., & Thomas, J. L. (2020). Acoustic tweezers for particle and fluid micromanipulation. Annual Review of Fluid Mechanics, 52, 205-234.

[2] Baudoin, M., Thomas, J. L., Sahely, R. A., Gerbedoen, J. C., Gong, Z., Sivery, A., ... & Vlandas, A. (2020). Spatially selective manipulation of cells with single-beam acoustical tweezers. Nature communications, 11(1), 4244.

[3] Ghanem, M. A., Maxwell, A. D., Wang, Y. N., Cunitz, B. W., Khokhlova, V. A., Sapozhnikov, O. A., & Bailey, M. R. (2020). Noninvasive acoustic manipulation of objects in a living body. Proceedings of the National Academy of Sciences, 117(29), 16848-16855

[4] Qin, X., Wei, X., Li, L., Wang, H., Jiang, Z., & Sun, D. (2021). Acoustic valves in microfluidic channels for droplet manipulation. Lab on a Chip, 21(16), 3165-3173.

[5] Deshmukh, S., Brzozka, Z., Laurell, T., & Augustsson, P. (2014). Acoustic radiation forces at liquid interfaces impact the performance of acoustophoresis. Lab on a Chip, 14(17), 3394-3400.

[6] Karlsen, J. T., & Bruus, H. (2017). Acoustic tweezing and patterning of concentration fields in microfluidics. Physical Review Applied, 7(3), 034017.

[7] Augustsson, P., Karlsen, J. T., Su, H. W., Bruus, H., & Voldman, J. (2016). Iso-acoustic focusing of cells for size-insensitive acousto-mechanical phenotyping. Nature communications, 7(1), 11556.

Applications for high-power bulk wave acoustofluidics

Enrico Corato[1]*, Wei Qiu[1], and Per Augustsson[1]

[1]Department of Biomedical Engineering, Lund University, Lund, Sweden
*e-mail: enrico.corato@bme.lth.se

Introduction

Concerning bulk-wave acoustofluidic devices, the potential for improving performance by optimizing the mechanical interface between the piezoelectric elements and microfluidic chips has not been fully investigated yet. Previous research explored the use of wedges to control the angle between the piezoelectric element and the microfluidic chip [1], and the optimal placement of the piezoelectric element when directly glued onto the microfluidic chip [2]. In this experimental work, we investigate the potential applications of our line double-parabolic-reflectors wave-guided high-power ultrasonic transducer (L-DPLUS) that we first presented in Acoustofluidics 2023 [3]. Thanks to the high acoustic energy density this device provides, we demonstrate the focusing of 5-µm polystyrene particles at a high flow rate (8 ml/min) and that of nanoparticles (500 nm in diameter), employing streaming suppression by inhomogeneous media [4].
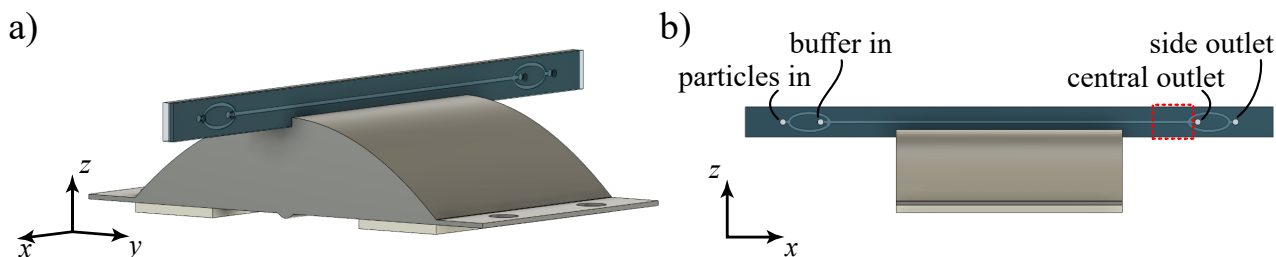
Figure 1: Experimental set-up. a) L-DPLUS system rendering, with a double -inlet, double-outlet chip on top, and two piezoelectric elements (light gray) at the bottom. b) L-DPLUS top view, as mounted on the microscope. The particles enter the system from the side inlet for all experiments, while we inject high-acoustic-impedance medium from the central inlet only in the nanoparticles focusing experiment. The sample is then collected for both the side and central outlets. The imaging region is highlighted by the red dashed rectangle.

Materials and methods

To push the limits of bulk-wave acoustofluidics, we further developed our metallic interface between piezoelectric elements and chip. We used a 30-mm long L-DPLUS fabricated in aluminum via CNC milling (Figure 1). On top of the transducer, we glued a double-inlet, double-outlet glass-silicon-glass chip, with a microchannel (375 µm wide, 150 µm high, and 60 mm long) etched through the silicon layer. Two kerfed piezoelectric elements ($10 \times 30 \times 1$ mm^3) were glued at the L-DPLUS bottom, each of them with a temperature detector to monitor their temperature. The piezoelectric elements were driven by the same sinusoidal signal, with averaged voltage of 25 V$_{pp}$ over the two elements. This system differs from the one we previously presented [3] mainly for the device length (20- vs 30-mm) and the kerfing of the piezoelectric elements. The flow experiments with 5-µm polystyrene (PS) particles flowing at 8 ml/min showcase the capacity of high flow rate. For nanoparticle focusing, a 500-nm PS particles solution flowed in at 20 µl/min as the side stream and a 20% Percoll solution was laminated as the center stream at a flow rate of 30 µl/min. A frequency sweep (1.895 MHz as centre frequency, 50 kHz span, 10 ms duration) was applied as driving signal to avoid center medium deformation under strong sound fields. In both experiments, we acquired images close to the outlet trifurcation, as shown by the red dashed rectangle in Figure 1(b). Moreover, the temperature of the system was stabilized before acquiring the images (± 0.2 °C), thus ensuring no further performance degradation. The measured temperatures were between 26.4 °C and 32.3 °C for all experiments.

Results and discussion

To characterize the system performance, we measured the focusing of 5-µm PS particles flowing at 8 ml/min (average residence time of 12.7 ms in the actuation zone) at different frequencies, with constant averaged voltage of 25 V$_{pp}$ applied to the piezoelectric elements. Examples of good and moderate focusing are shown in Fig.2(a), for 1.890 MHz and for 1.905 MHz actuation, respectively. The corresponding intensity profiles are shown in Fig.2(b), with a green line representing good focusing and a red line representing moderate focusing. The full width at half-maximum is then computed
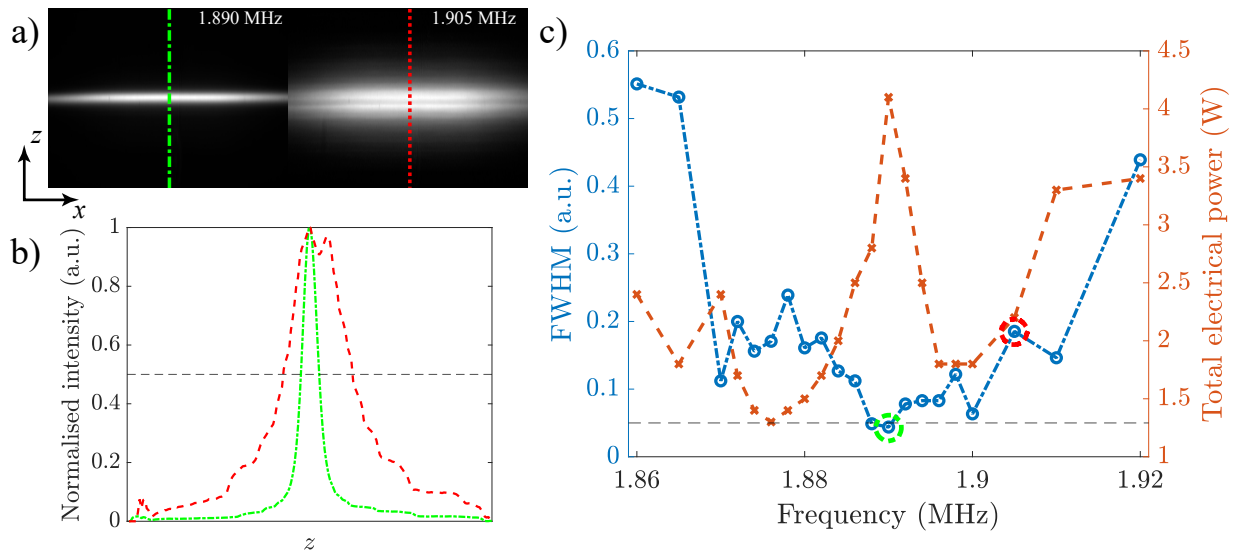
Figure 2: L-DPLUS performance characterization at a high flow rate (8 ml/min). a) Examples of good (1.890 MHz) and moderate (1.905 MHz) focusing. b) Corresponding intensity profiles for the good and moderate focusing in a). The black dashed line shows the level of full width at half-maximum (FWHM) for the normalized intensity. c) Measured normalised FWHM (blue circles) for different frequencies between 1.86 MHz and 1.92 MHz. The orange crosses show the total applied electrical power to both piezoelectric elements. The dashed black line shows 5% of the channel width.

for each frequency and the results are plotted in Fig.2(c) (blue dots), together with the measured total electric power applied to both piezoelectric elements (orange crosses). Compared with our previous work [3], this system has two major advantages. First of all, we applied much lower voltage, decreasing from 50 V_{pp} to 25 V_{pp}, anyway leading to comparable electrical power. Despite this, we can reach even higher flow rates in the current system, clearly showing an increased overall efficiency. Secondly, here we encountered less severe performance degradation due to heat generation, making it possible to stably run the sample through the channel continuously once the temperature plateau is reached.

We then investigated acoustic focusing of 500-nm PS particles. To minimize the disturbance of acoustic streaming on particle focusing, we used a denser medium flowing in the channel centre, while the particle solution was laminated on each side. With a weak sound field, the central medium is stabilized in the centre and the majority of the particles stay at the sides due to the weak acoustic radiation force, Figure 3(a). They will thus exit the channel via the side outlets. When a strong sound field is excited by the experimental conditions described above ($\approx$ 25 V_{pp} applied to the piezoelectric elements with a frequency sweep from 1.87 to 1.92 MHz), the 500-nm particles focus in the channel centre, and the majority of them can be collected through the central outlet, as shown in Figure 3(b).
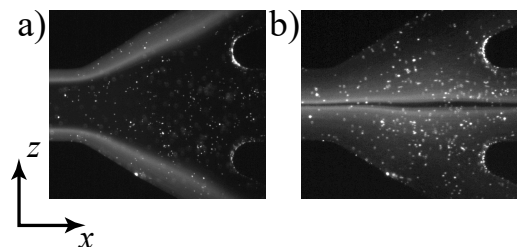

Figure 3: Nanoparticle focusing imaged at the outlet trifurcation. a) With a weak sound field, the denser medium is stabilized in the channel center, and the particles mainly stay at the sides. b) With a strong sound field, the particles are able to enter the denser medium and are focused to the channel centre

Conclusion

In this work, we showed a more efficient L-DPLUS, able to continuously focus 5-μm PS particles at 8 ml/min without heating the microfluidc channel to temperatures harmful to biological samples. Furthermore, we showed focusing of 500-nm PS particles employing streaming suppression by inhomogeneous media. Our further work will include the characterization of the recovery rate of different-sized nanoparticles. Potential applications of this technology encompass focusing of biological nanoparticles, such as bacteria, or high-throughput cell washing or separation.

References

[1] Manneberg, O. et al., J. Micromech. Microeng., **18**(9), (2008).
[2] Qiu, W. et al., Phys. Rev. Appl. **17**, 044043 (2022).
[3] Corato, E. et al., Acoustofluidics Conference (2023)
[4] Van Assche, D., et al., Sci Rep **10**, 3670 (2020).

High-power Bulk-Wave-Acoustophoresis Devices Utilizing an Elliptical Reflector Focusing Transducer

Zhirui Chen[1,*], Chikahiro Imashiro[1], Wei Qiu[2], and Takeshi Morita[1]

[1] Graduate School of Engineering, The University of Tokyo, Tokyo, Japan
[2] Department of Biomedical Engineering, Lund University, Lund, Sweden
*E-mail: chen-zhirui@g.ecc.u-tokyo.ac.

Acoustofluidics 2024
14-16 August 2024
Uppsala University, SWEDEN

Introduction

Acoustophoresis has been proven to be a promising tool in manipulating various biological samples, which may play an important role in contemporary biotechnology. However, the primary drawback of this technique is the relatively low throughput, which limits its clinical applications. To achieve high throughput, a strong sound field is required in the channel to induce large acoustic radiation force on the particles to be handled. Strong sound field in such devices are typically excited by applying large electric power to PZT elements, inevitably resulting in considerable heat generation. In recent studies, efficient driving of the devices has been proposed by optimizing the actuation scheme of the PZT elements [1, 2]. In contrast to driving the device using a single PZT element, in this work, we propose an elliptical reflector focusing transducer which introduces most of the wave energy from the PZT to the chip. Numerical simulations validate the proposed mechanism and demonstrate a high-power output possibility compared to devices driven by the conventional one.
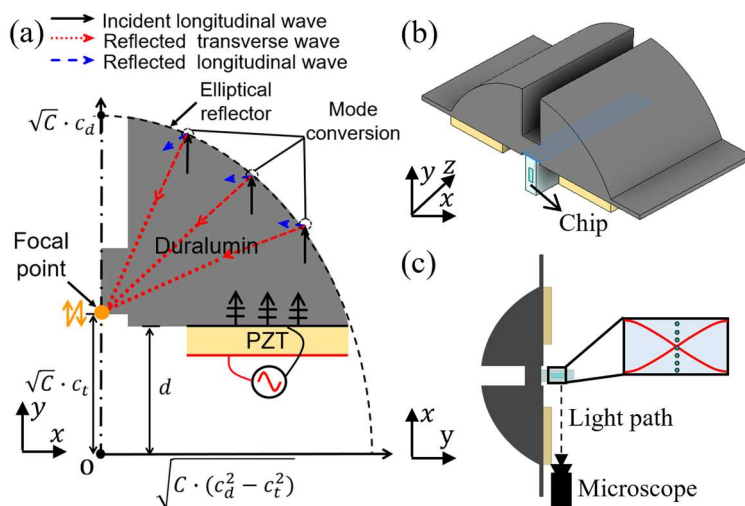
Principle

Figure 1: Scheme of the proposed device: (a) Principle of the proposed elliptical transducer which focuses the transverse waves (red dashed lines) converted from the plane longitudinal waves (black solid lines). (b) 3D sketch of the acoustophoresis device driven by the elliptical transducer. (c) Illustration of the optical access to the channel where a half-wavelength standing-wave field is excited.

The cross section of the proposed transducer structure is depicted in Figure 1(a), which is symmetric with respect to y-axis. The PZT element is operated under its thickness mode, which excites longitudinal planewaves. The incident longitudinal waves undergo mode conversion at the outer surface of the transducer and are partially converted to the transverse waves. To focus the transverse waves to a point, the reflector shape is mathematically calculated to be an ellipse. This transducer design enables the excitation of a strong vertical vibration at the focal point located at $(0, \sqrt{c} \cdot c_t)$, which can be utilized to drive the chip from the side, as shown in Figure 1(b). A half-wavelength standing-wave field can be excited in the channel along y-direction at the right frequencies, as shown in Figure 1(c). It is noted that only part of the ellipse ($y \geq d$) is exploited in the shape design [Figure 1(a)], which reduces the propagation loss by shortening the acoustic path of the incident waves while allowing the optical access to the channel [Figure 1(c)].

Simulation model

Numerical simulations for the acoustophoretic devices are performed in 2D using COMSOL Multiphysics 6.0. The chip used in this study has a glass-silicon-glass sandwiched structure [Figure 2(a)]. To verify the focusing mechanism of the proposed transducer, we first simulate the vibration of the transducer without the chip and compute the y-component of the displacement amplitude d_y averaged along the region where the chip is mounted via its sidewall. The comparison of d_y is conducted for the device driven by a single PZT element [Figure 2 (b)] and the device driven by the designed transducer [Figure 2 (c)] under the same input power. The input power to the elliptical transducer is the total power applied to two PZT elements. Then the model consisting of both the elliptical transducer and the chip was built [Figure 2 (f)], and the device performance was compared to that driven by a single PZT from the bottom (*bap*) [Figure 2 (d)] and from the side (*sap*) [Figure 2 (e)]. Here, a dimensionless efficiency parameter, $\eta = \omega E_{ac} V_I / P_{in}$, is used to quantitatively evaluate the device performance, where ω, E_{ac}, V_I, and P_{in} are the angular frequency, the acoustic energy density, the channel unit volume, and the input power [2]. The efficiency parameter reflects the energy conversion ratio of the electric energy applied to PZT to the acoustic energy induced in the channel. A voltage of 2 V_{pp} is applied to the PZT in all models, and the frequency response is investigated over a range from 1.9 MHz to 2.1 MHz.
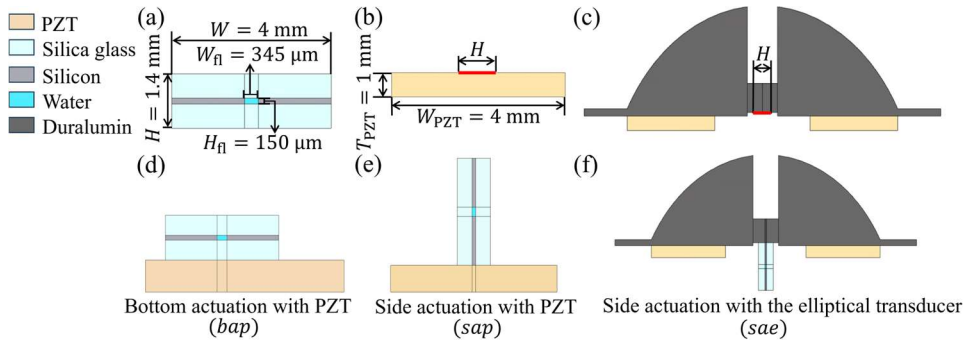
Figure 2: Illustration of the 2D models used in simulations for (a) the chip, (b) the PZT element, (c) the elliptical transducer, (d) bottom actuation with the PZT (*bap*), (e) side actuation with the PZT (*sap*), and (f) side actuation with the elliptical transducer (*sae*).
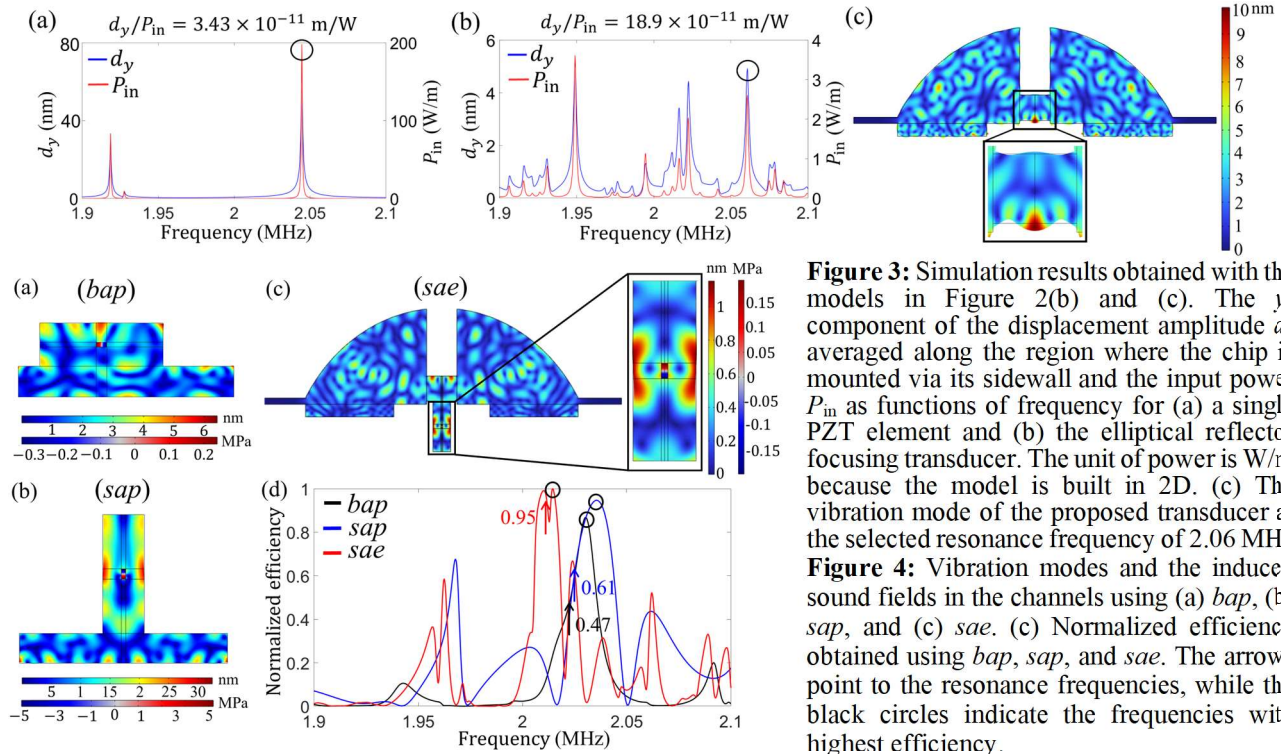
Results and discussion

Figure 3: Simulation results obtained with the models in Figure 2(b) and (c). The y-component of the displacement amplitude d_y averaged along the region where the chip is mounted via its sidewall and the input power P_{in} as functions of frequency for (a) a single PZT element and (b) the elliptical reflector focusing transducer. The unit of power is W/m because the model is built in 2D. (c) The vibration mode of the proposed transducer at the selected resonance frequency of 2.06 MHz.

Figure 4: Vibration modes and the induced sound fields in the channels using (a) *bap*, (b) *sap*, and (c) *sae*. (c) Normalized efficiency obtained using *bap*, *sap*, and *sae*. The arrows point to the resonance frequencies, while the black circles indicate the frequencies with highest efficiency.

In contrast to two clear peaks in the case of a single PZT, multiple peaks in y-component displacement d_y can be found from the frequency response of the elliptical transducer, as shown in Figure 3(a) and (b), which indicates that various resonance modes can be excited within a certain frequency range. The ratio of d_y to the input power P_{in} was calculated at their respective resonance frequencies, and the elliptical transducer produces a d_y 5.5 times higher than that produced by a single PZT under the same P_{in}. The maximum d_y is obtained at the focal point at a frequency of 2.06 MHz, as illustrated in Figure 3(c), further validating the design concept. Vibration modes of the devices driven by different approaches are shown in Figure 4(a)-(c) at their corresponding resonance frequencies. The device driven by the elliptical transducer (*sae*) reveals a clear superiority to the device driven by a single PZT (*bap* and *sap*) in terms of efficiency, as depicted in Figure 4(d). The efficiency at resonance frequency indicated by the arrows is increased by a factor of 2 compared to the bottom actuation and by a factor of 1.6 compared to the side actuation. Additionally, it is found that in all three cases, the frequencies where the efficiency is the highest denoted by the circles do not match the resonance frequencies. Such frequency can be selected as the working frequency, instead of choosing the resonance frequency, to achieve high-efficiency driving. This concept is essential for limiting the heat generation in high-throughput applications by reducing power loss.

Conclusion

In this study, we propose a high-power acoustophoresis device utilizing an elliptical reflector focusing transducer based on mode conversion from longitudinal waves to transverse waves. Numerical simulations confirmed the focusing mechanism, and the induced y-component displacement is 5.5 times larger than that of a single PZT element under the same input power. We further validate that the device driven by the proposed transducer exhibits an efficiency enhancement of 1.6 to 2 times, compared to the conventional devices driven by a single PZT from the bottom and from the side. Experimental validation of our prototype will be carried out and the results will be reported in the conference.

References

[1] M. Bora and M. Shusteff, *Lab Chip* **15**, 3192 (2015).
[2] W. Qiu, T. Baasch, and T. Laurell, *Phys. Rev. Appl.* **17** 044043 (2022).

Blood cell focusing in simulation optimized molded polymer acoustophoresis chip

Mathias Ohlin[1], Fabian Lickert[2], Sazid Zamal Hoque[2], Anke Urbansky[1], Mikael Evander[1], Agnes Michanek[1], Magnus Hivert[1], Henrik Bruus[2], Pelle Ohlsson[1]*

[1]AcouSort AB, Lund, Sweden www.acousort.com *E-mail: pelle.ohlsson@acousort.com
[2]Department of Physics, Technical University of Denmark (DTU), Kongens Lyngby, Denmark
www.fysik.dtu.dk/microfluidics

Introduction

In bulk acoustophoresis, an ultrasound transducer is used to vibrate a chip so that a standing wave is generated in a channel, pushing cells to one or several pressure amplitude nodes. This is a promising method to automate cell handling, including cell washing, where cells are pushed from one medium to another, concentration where the cells are collected in a smaller volume, and separation where different cell populations are separated from each other, which is useful for a wide range of diagnostic and therapeutic applications [1]. A hurdle for clinical application of this technology is the high cost of cleanroom manufacturing of the silicon and/or glass chips that are typically used. A more cost-efficient alternative for volume production is molding of polymer chips. The less favorable acoustic properties of most polymers with high acoustic damping and low acoustic impedance contrast, compared to water-based samples, typically limits the acoustic field strength, in turn limiting throughput per channel and separation efficiency [2, 3, 4]. Using finite element simulation, we have earlier shown that the acoustic resonances in the whole system are important for polymer chips and that antisymmetric actuation is favorable, and verified this experimentally using a bead model [5, 6]. In this work, we have optimized the chip design using simulation model, verified the function using a bead model and validated the performance by focusing red and white blood cells in 10x diluted whole blood, reducing their concentration to 0.06% and 0.2% of the inlet concentration respectively.

Methods

The chip design was optimized using 2 and 3-dimensional finite element models (fig. 1) implemented in COMSOL Multiphysics (COMSOL AB, Stockholm, Sweden). The material properties were first determined through ultrasound electrical impedance spectroscopy (UEIS) [7]. The chip dimensions were then determined by maximizing the focusing force on a theoretical test particle, while minimizing the out-of-plane force on the particle from unwanted field shapes.

The chip was manufactured through molding and sealed by bonding of a lid made from the same thermoplastic. It was then mounted in a holder with fluidic connectors and a piezoelectric transducer with the top electrode cleaved along the length of the chip to provide antisymmetric actuation. Acoustic contact between the transducer and the chip was made by glycerol applied between the two. The transducer was cooled from below by a Peltier element regulated to hold 20C. For the cell experiments a smaller transducer without Peltier cooling was instead glued in a position avoiding the optical axis to improve imaging.

The function of the chip was verified using a solution of fluorescent 5.0 μm diameter polystyrene beads (Thermo Scientific Fluoro-Max Firefli Fluorescent Green) in Optiprep diluted in purified water to create neutrally buoyant particles to avoid sedimentation during testing. The solution was flushed at 10 μL/min through the chip and the focusing imaged using a fluorescence microscope. The chip was actuated at frequencies from 0.5 to 2.5 MHz in steps of 5 kHz using a function generator supplying 7 V_{pp} to an amplifier.
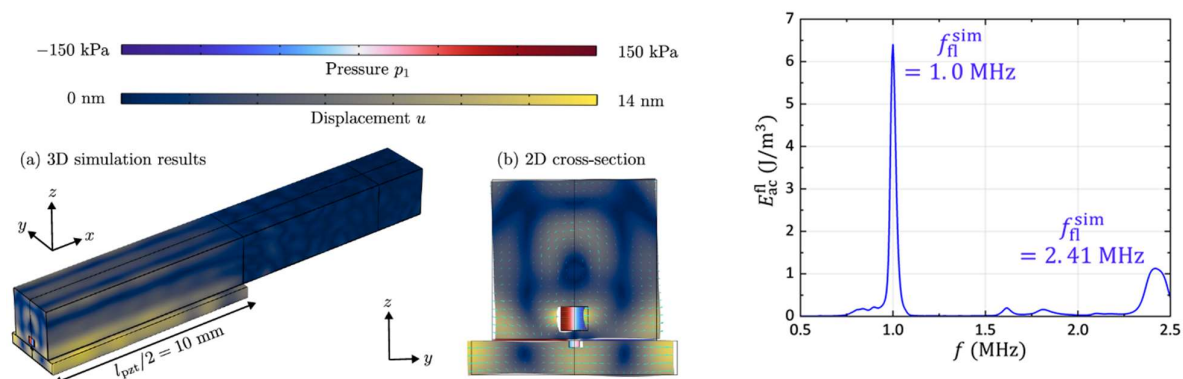

Figure 1: Simulation results for the optimized chip with transducer showing their displacement and the pressure field in the channel (a, b) as well as the acoustic energy in the channel (c).

Finally, focusing of red blood cells was tested. Blood was drawn from healthy volunteers with informed consent and diluted to 10 and 20% in phosphate buffered saline (PBS). The blood was flushed through the channel and ultrasound was used to focus the blood cells towards the centerline of the channel, making it possible to split the flow of cells in the center from the flow of plasma on the sides using a flow splitter at the end of the channel. Input and output samples were analyzed through flow cytometry.

Results

The simulations resulted in a considerably slimmer chip than our earlier design in [6] with a resonance frequency of 0.99 MHz (fig. 1). This design was successfully molded, bonded and tested. Verification with 5µm fluorescent polystyrene beads confirmed efficient focusing at and around 1 MHz at a flow rate of 10 µL/min (fig. 2, 3). The voltage over the transducer and the temperature were measured to vary in the range of 29-32 V_{pp} and 20-37C respectively depending on actuation frequency.
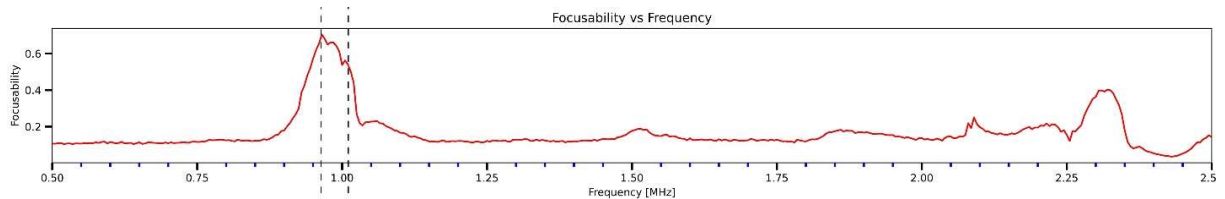
Figure 2: Focusability of 5 µm polystyrene beads in the polymer chip as a function of actuation frequency. Focusability is here defined as the fraction of the total fluorescence intensity that is found in the center 10% of the channel.

Blood cells were efficiently focused from whole blood diluted to 10 and 20% at flow rates of 50 and 40 µL/min respectively (fig. 3). For 10% blood, plasma could be skimmed of through the side outlets of a trifurcation at the end of the chip at 3.5 µL/min. The concentration of blood cells was compared to the inlet sample and determined to be 0.06% and 0.2% for red and white blood cells respectively.
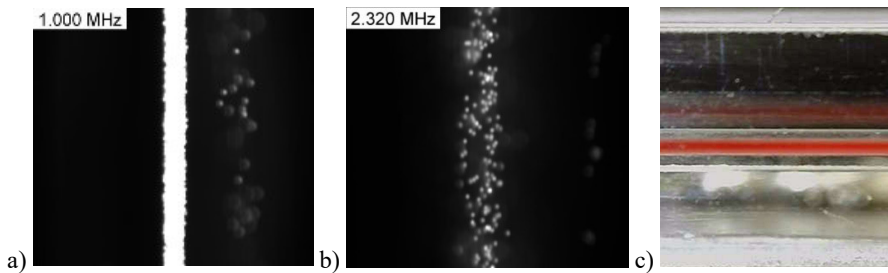

Figure 3: Acoustic focusing of polystyrene beads (a, b) and blood cells from 5x diluted blood (c).

Conclusion

These results confirm that we can design polymer acoustophoresis chips and accurately predict their resonance frequency using our simulation model. The molded thermoplastic chips can efficiently focus polystyrene beads and blood cells, making it possible to from 10x diluted blood skim off a thin layer of very clean diluted plasma with 99.96% of the red blood cells removed.

References

[1] A. Lenshof, C. Magnusson, T. Laurell, *Lab Chip*, **12**, 1210 (2012)
[2] A Mueller, A Lever, T V Nguyen, J Comolli, J Fiering, *J. Micromech. Microeng.* **23** 125006 (2013)
[3] R. Silva, P. Dow, R. Dubay, C. Lissandrello, J. Holder, D. Densmore, J. Fiering, *Biomed Microdevices* **19** 70 (2017)
[4] R. Dubay, C. Lissandrello, P. Swierk, N. Moore, D. Doty, J. Fiering, *Biomicrofluidics* **13**, 034105 (2019)
[5] R. P. Moiseyenko, H. Bruus, *Phys. Rev. Appl.* **11**, 014014 (2019)
[6] F. Lickert, M. Ohlin, H. Bruus, P. Ohlsson, *J. Acoust. Soc. Am.* **149**, 68, (202871)
[7] W. N. Bodé, F. Lickert, P. Augustsson, H. Bruus, *Phys. Rev. Applied* **18**, 064078 (2022)

Localized bulk acoustic traps using milled aluminum devices

Saumitra Joshi[1,*], Dhananjay V. Deshmukh[1], and Mark W. Tibbitt[1]

[1]Macromolecular Engineering Laboratory, D-MAVT, ETH Zurich, Zurich, Switzerland

[*]E-mail: joshis@ethz.ch

Introduction

Owing to the label free nature of acoustofluidics, acoustic traps are particularly useful in biomedical applications to retain different cell types against flow, to study cell–cell interactions and to form microtissues, among others [1]. Acoustic traps in BAW devices are usually created using "whole cavity" resonances, i.e., using the resonant modes of the cavity along multiple axes. But this technique makes it especially difficult to control the location of the traps in 3D [2]. Additionally, such 3D resonances along multiple axes are practically hard to achieve. Both these issues require precise design of the fluid cavity geometry and dimensions, making these devices highly case specific.

As a solution, our devices create localized acoustic traps, i.e. traps that only affect the objects in a certain "area of interest", independent of the fluid cavity dimensions. Localized trapping has been previously demonstrated in capillary devices with localized placement of small transducers to create local standing pressure waves [3] and in certain SAW devices [4]. While the capillary devices increase the electrical design complexity and risk inter-transducer interference when creating multiple traps, the SAW devices are complicated to manufacture and rely on a delicate balance between the acoustic streaming and acoustic radiation force to function. In this study, we show that our devices can be manufactured easily by milling out of aluminum. The milled cavities can then be filled with PDMS, which creates a physical barrier while remaining transparent to acoustics. We validated our numerical study through experiments and observed the effects to be consistent, independent of the cross-sectional profile of the cavity.

Theory and Experimental procedure

We explored multiple surface geometries for aluminum–water–glass BAW devices. The broad geometry type, referred to here as the 'donut' (**Figure 1a**), was further explored along with the geometric variations under this category. All simulations were carried out using COMSOL (v.5.6) with simplified 2.5D axisymmetric models. The base of the aluminum was given a 'prescribed displacement' of 1 μm amplitude and a frequency sweep was performed. For simplicity, the simulations neglected the molded PDMS in the cavity [5].

A few select geometries were milled out of an aluminum base. Most tests were performed on a device with a single circular cross-sectional 'donut' in the fluid chamber (**Figure 1b**) while another device with nine geometries in a larger chamber was tested for interference between shapes. PDMS was molded in the 'donut' valley of the first device to prevent the particles from settling there due to gravity. The devices were tested with two samples—20 μm polystyrene particles in DI water and fixed HepG2 spheroids (Ø 125 μm) in HBSS.

a) 'Donut' cross-sectional view

AA' Cross Section View

b) 'Donut' top view
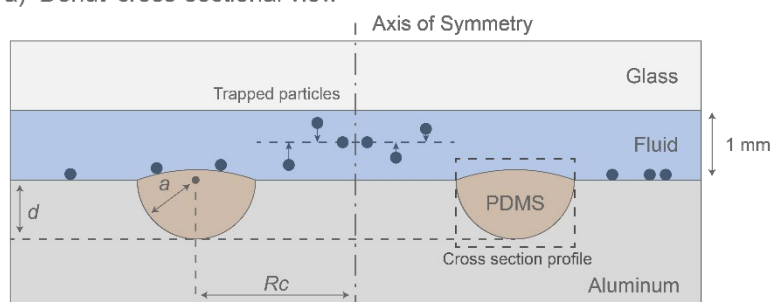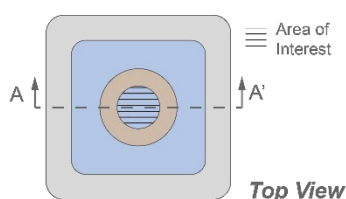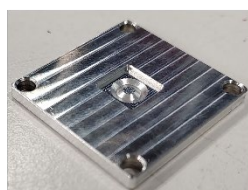
c) Single geometry per chamber

Figure 1: (a) Cross-sectional view of the 'donut' shape along with its features – "area of interest", cross sectional profile, axis of symmetry and geometric parameters (*a, d, Rc*). **(b)** Top view of the 'donut' shape with the "area of interest" highlighted **(c)** Aluminum base with a single geometry (circular cross section) in the chamber.

Results and Discussion

From simulations, we observed that the 'donut' shape forms a planar pressure field in the "area of interest" that sharply falls off as you approach the valley of the shape. The field is much weaker in the surrounding region (outside of the "area of interest") and does not form a planar shape in this region that could cause levitation or trapping (**Figure 2a**); as opposed to the flat shape that would be expected in its λ/2 mode (**Figure 2b**). This specific field shape was observed for multiple cross-section profiles of the 'donut'—parabola, circle, rectangle, and triangle (**Figure 2c**) and different combinations of geometric parameters.
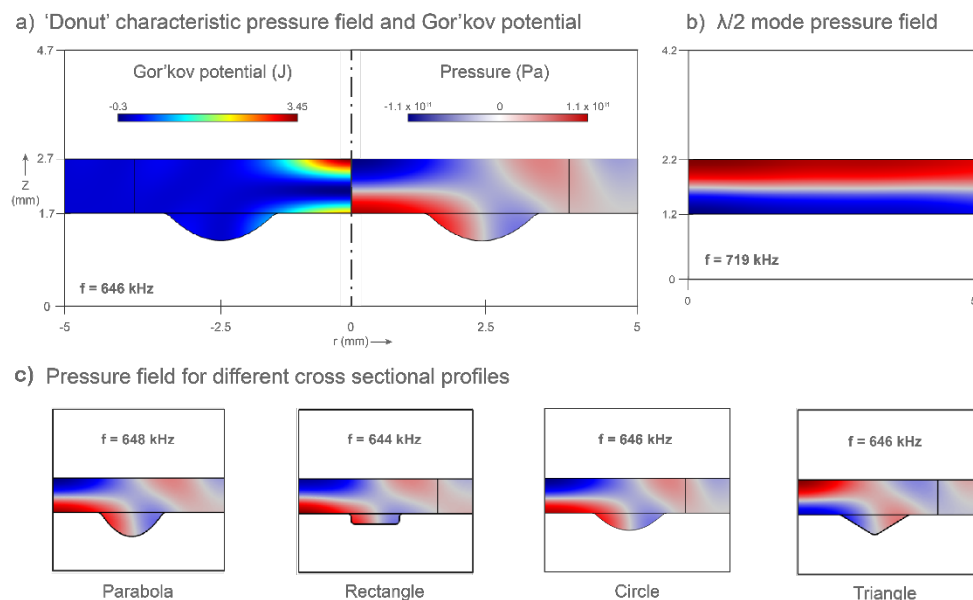

Figure 2: 2.5D axisymmetric simulation results. **(a)** The characteristic pressure field and Gor'kov potential shape formed by the 'donut' geometry. The Gor'kov potential has a minima in "area of interest" and is uniform elsewhere. **(b)** λ/2 mode pressure field for a flat geometry with similar conditions. **(c)** The parabolic, rectangular, circular, and triangular cross-sectional profiles show similar pressure field shapes

Tests with 20 μm polystyrene particles showed strong levitation in the central region and confirmed the effect of 'donut' cavity on the changes in the local field. Proof of concept experiments with HepG2 spheroids also showed selective levitation in the central "area of interest" to a height of 0.3 mm with no levitation in the rest of the chamber (**Figure 3**). Tests with the multi-geometry device confirmed that there was no observable interference between different acoustic traps within the same device.
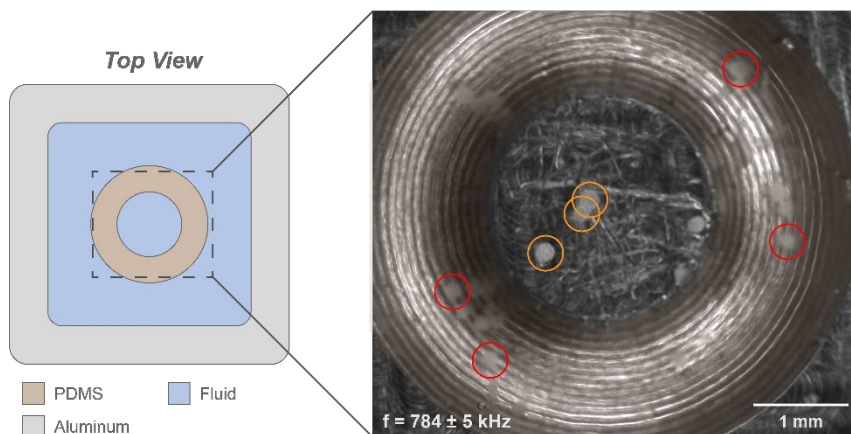

Figure 3: Levitation of fixed HepG2 spheroids in the "area of interest". The frequency was modulated at 200 Hz with a deviation of ±5 kHz. The input signal amplitude was 30V. Orange circles highlight the levitating spheroids, which are confined to the central "area of interest". Spheroids outside the "area of interest", highlighted in red circles, did not levitate.

Conclusion

We demonstrated a new geometry for aluminum BAW devices that can be milled easily and behaves as a localized acoustic trap, levitating objects selectively within the "area of interest". Future work would explore the limits of the shape, width, and depth of the trap, while performing analytical studies to understand the physical phenomenon. We will also study the crosstalk between multiple traps to optimize the device design. Eventually we would also like to test its applications in trapping microtissues for histology and live imaging.

References

[1] Evander, Mikael, and Johan Nilsson. 2012 *Lab on a Chip* **12.22**: 4667-4676
[2] Johnson, Keith E., *et al.* 2023 *Materials & Design* **232**: 112165
[3] Fornell, Anna, *et al* 2019 *Biomicrofluidics* **13.4**
[4] Hongwei, Cai *et al.* 2020 *Biofabrication* **12** 035025
[5] Leibacher, Ivo *et al.* 2013 *Lab on a Chip* **14** 463-470

Array of piezoelectric micromachined ultrasonic transducers (PMUTs) for the acoustofluidic manipulation of particles and spheroids

Emilie Vuille-dit-Bille[1,2], Sarah Heub[1], Dara Zaman Bayat[1], Marc-Alexandre Dubois[1], Thomas Overstolz[1], Michel Despont[1], Mahmut Selman Sakar[2] and Gilles Weder[1]

[1] CSEM SA, Neuchâtel, Switzerland
 e-mail: emilie.vuille-dit-bille@csem.ch
[2] Institute of Mechanical Engineering, EPFL, Lausanne, Switzerland.

Introduction

Integrated solutions for precise manipulation of microscale biological entities are often desired in life science applications. Particularly, the demand is increasing for innovative tools to manipulate large (typically 50 to 500 µm) entities such as spheroids, microtissues or organoids both in 2D and 3D. [1] Piezoelectric micromachined ultrasonic transducers (PMUTs) as source of pressure waves holds great potential. They allow the miniaturization of high-resolution ultrasonic transducer arrays while offering good acoustic matching and easy integration in lab-on-chip devices.[2] The existing platforms based on PMUTs are limited to the manipulation of small silica beads (4 µm). [3] In this work, a MEMS-based platform is developed to investigate the use of PMUTs to dynamically manipulate particles and spheroids with diameters ranging from 30 to 150 µm in a physiological environment. To maximize the generated acoustic forces, the resonant membrane-based acoustic transducers were fabricated from a material that exhibits a high piezoelectric coefficient, Al0.7Sc0.3N. The performances and vibrational modes of the PMUTs were characterized to understand the general behavior of the platform. The movement of particles and cell hepatocellular carcinoma spheroids (HepG2) in the acoustofluidic platform were studied experimentally and through finite element method (FEM) simulations.

Experimental Setup and Methods

The acoustic platform is composed of a silicon chip containing two PMUTs covered by an acoustofluidic chamber made of aluminum (Figure 1a,b). Each PMUT is composed of a silicon membrane and a piezoelectric stack using Al0.7Sc0.3N as a piezoelectric layer (Figure 1c). The PMUT design was tuned to display a resonance frequency in water around 750 kHz, and the top electrode was divided in an inner circle and outer ring to generate stronger acoustic forces. The frequency response of PMUTs were characterized using a laser Dopler vibrometer (LDV). The maximal displacement and vibration modes of the PMUTs were measured on the unpackaged and packaged chip in air and water environments. For particle manipulation, the packaged PMUTs were activated at their fundamental resonance frequencies with a continuous sinusoidal signal. The acoustofluidic chamber was filled with water-based solutions containing one of the following samples: polystyrene beads (30 µm diameter), polydimethylsiloxane (PDMS) beads (40 µm diameter) and HepG2 spheroids (150 µm diameter).
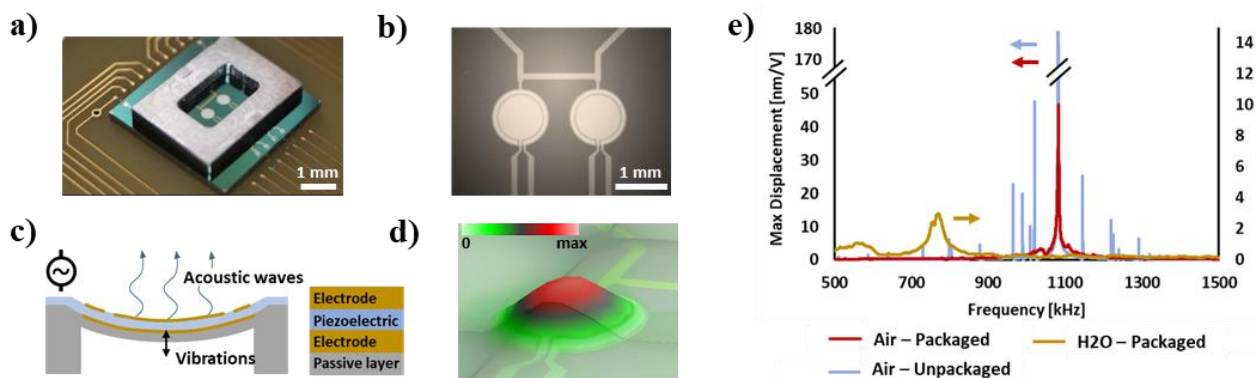

Figure 1: (a) Picture of the PMUT-based acoustofluidic platform mounted on a printed circuit board (PCB). (b) Micrograph of PMUTs. (c) Schematics of a PMUT's cross-section illustrating acoustic waves generation principle. (d) Surface maximal displacement of PMUT at 1.08 MHz in air. (e) Frequency response of PMUTs vibration in air and water.

Characterization of PMUTs

PMUTs located on an unpackaged chip showed a complex frequency response in air, exhibiting several sharp peaks, and a maximum displacement of 178 nm/V (Figure 1e). Once mounted on a PCB and bearing an acoustofluidic chamber, the PMUTs showed only one remaining peak at 1.08 MHz with a reduced amplitude of 48 nm/V. This peak was confirmed to be the fundamental vibration mode by scanning the surface using LDV (Figure 1d). We hypothesized that the adjacent peaks present on the spectrum of the unpackaged chip were induced by the movement of the whole chip, which disappeared once the chip was physically constrained. The diminution of the maximum amplitude showed that packaging can significantly dampen the vibration of the PMUTs and should be carefully optimized. Finally, the fundamental resonance frequency in water was shifted from 1.08 MHz to 770 kHz. The vibration amplitudes were greatly reduced to 3 nm/V and the peaks exhibits a low-quality factor due to the damping nature of water. An input voltage of around 50 V is needed to generate sufficient acoustic forces and manipulate particles in water.

Particles Manipulation

Particles with positive and negative acoustic contrast factors are expected to go to regions of low and high Gor'kov potential, respectively. The HepG2 spheroids and PS particles have a positive acoustic contrast factor, while PDMS particles have a negative acoustic contrast factor. HepG2 spheroids and PS beads were patterned on the side of the PMUTs, while PDMS beads formed a circle at the center of the PMUTs (Figure 2a-c). FEM simulations confirmed that the positions of the particles corresponded to regions of low and high Gor'kov potential (Figure 2e). Different transducer configurations repeatedly showed the expected results for in plane patterning. Notably, PDMS particles were levitated above the surface demonstrating the formation of vertical acoustic standing waves (Figure 2d). Levitation was promoted by the high acoustic contrast factor of PDMS enhancing the acoustic force.
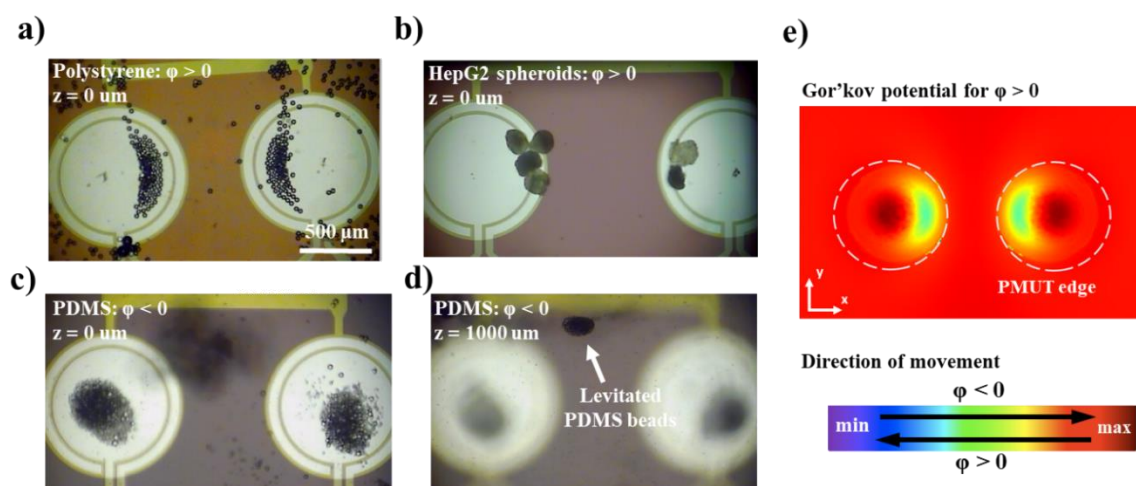

Figure 2: Patterning of (a) PS beads, (b) HepG2 spheroids, and (c) PDMS beads on top of the PMUTs. (d) PDMS beads are levitated on a plane above the surface. (e) FEM simulation of the Gor'kov potential of the xy plane 20 μm above the surface coincides with the particle behavior

Conclusion and Outlook

Experimental and numerical investigations validated the capability of a PMUT-based acoustofluidic platform to manipulate both particles and spheroids, making the first-time demonstration of spheroid manipulation using this technology. In plane manipulation of particles with opposite acoustic contrast factors resulted in patterning in distinctive regions of the chamber. Additionally, the creation of standing waves leading to the levitation of PDMS particles was demonstrated. These results highlight the potential of PMUTs-based platform to manipulate large biological objects for life science applications such as organoid-on-chip engineering for disease modeling and drug testing.

The characterization of the PMUTs highlighted their sensitivity to the device assembly. Therefore, a follow-up study has started with the aim to optimize the packaging strategy to minimize energy losses caused by interfaces, excitation of unwanted resonances or acoustic damping in materials.

References

[1] Vuille-Dit-Bille E *et al.,* Tools for manipulation and positioning of microtissues. Lab Chip., 2022.
[2] Y. He *et al.*, Piezoelectric Micromachined Ultrasound Transducer Technology: Recent Advances and Applications, Biosensors, 2023.
[3] C. Y. Cheng *et al.*, Thin Film PZT-Based PMUT Arrays for Deterministic Particle Manipulation, IEEE Trans. Ultrason. Ferroelectr. Freq. Control, 2019.